Center for Gas Turbines and Power
The Pennsylvania State University
University Park, PA 16802

Final Report

INVESTIGATION OF TIP CLEARANCE FLOW FIELDS AND METHODS OF DESENSITIZING TIP CLEARANCE EFFECTS IN TURBINES

X. Xiao, B. Lakshminarayana,
A. McCarter, A. Chernobrovkin,

Center for Gas Turbines and Power

July 2000

Center for
GAS TURBINES
and
POWER

College of Engineering
The Pennsylvania State University

DISTRIBUTION STATEMENT A
Approved for Public Release
Distribution Unlimited

PENNSTATE

1855
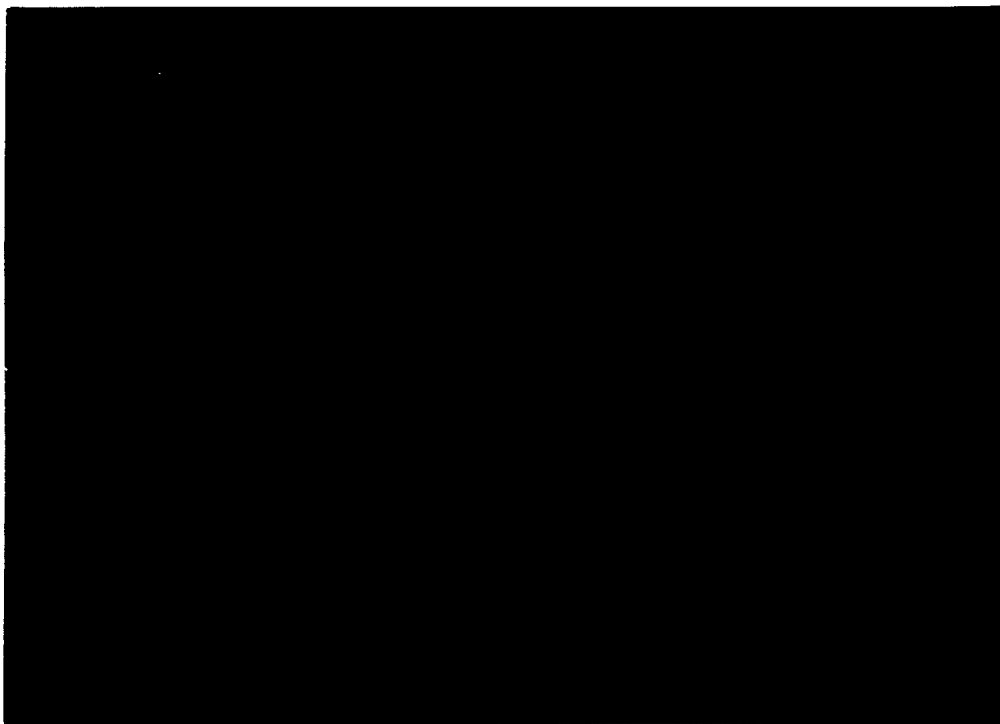
REPORT DOCUMENTATION PAGE

Form Approved
OMB NO. 0704-0188

Public reporting burden for this collection of information is estimated to average 1 hour per response, including the time for reviewing instructions, searching existing data sources, gathering and maintaining the data needed, and completing and reviewing the collection of information. Send comment regarding this burden estimates or any other aspect of this collection of information, including suggestions for reducing this burden, to Washington Headquarters Services, Directorate for information Operations and Reports, 1215 Jefferson Davis Highway, Suite 1204, Arlington, VA 22202-4302, and to the Office of Management and Budget, Paperwork Reduction Project (0704-0188), Washington, DC 20503.

1. AGENCY USE ONLY (Leave blank)	2. REPORT DATE JULY 2000	3. REPORT TYPE AND DATES COVERED MAY 1,95 TO FEB, 1999

4. TITLE AND SUBTITLE
Investigation of Tip Clearance Flow Fields and Methods
of Desensitizing Tip Clearance Effects in Turbines

6. AUTHOR(S)
B. Lakshminarayana, X. Xiao, A. Chernobrovkin, A. McCarter

5. FUNDING NUMBERS
DAAH04-95-1-0179

7. PERFORMING ORGANIZATION NAMES(S) AND ADDRESS(ES)

The Pennsylvania State University
Center for Gas Turbines and Power
153 Hammond Building
University Park, PA 16802

8. PERFORMING ORGANIZATION REPORT NUMBER

PSU CGTP 2000-08

9. SPONSORING / MONITORING AGENCY NAME(S) AND ADDRESS(ES)

U.S. Army Research Office
P.O. Box 12211
Research Triangle Park, NC 27709-2211

10. SPONSORING / MONITORING AGENCY REPORT NUMBER

ARO 33527.5-EG

11. SUPPLEMENTARY NOTES

The views, opinions and/or findings contained in this report are those of the author(s) and should not be construed as an official Department of the Army position, policy or decision, unless so designated by other documentation.

12a. DISTRIBUTION / AVAILABILITY STATEMENT

Approved for public release; distribution unlimited.

12 b. DISTRIBUTION CODE

13. ABSTRACT (Maximum 200 word An experimental and computational investigation was carried out during this reporting period to derive the flow field information at various axial and radial locations from the leading to the trailing edge in the tip clearance region of the rotor, and the casing static pressure was measured to derive the trajectory of the leakage vortex and the horseshoe vortex. The data provided here indicates that the tip leakage flow originates at approximately 50% of the chord and is confined to the tip clearance region due to the relative motion between the blade and the wall, as well as the secondary flow in the tip region. Both of these effects are responsible for keeping the tip vortex closer to the suction surface corner of the tip. The leakage flow losses are high, but are confined to an extremely small region near the tip of the suction surface as opposed to the secondary flow, which tends to increase the losses spread over a substantial portion of the passage. Therefore, the information provided here is substantially different from that derived on the basis of cascades testing. Numerical investigation of the flow field in the Penn State rotor based on the utilization of the Navier-Stokes solver has been carried out to gain a better understanding of the secondary and the tip leakage flow development. Analysis of the leakage flow development shows that the relative motion of the blade and the casing wall reduces the propagation of the leakage flow into the mainflow. The tip leakage vortex is confined to the suction surface corner of the casing. Most of the leakage losses are due to the mixing of the tip leakage vortex downstream of the trailing edge.

14. SUBJECT TERMS
Fluid Dynamics, Turbomachinery, Tip clearance effects,
Laser velocimetry

15. NUMBER IF PAGES

16. PRICE CODE

17. SECURITY CLASSIFICATION OR REPORT	18. SECURITY CLASSIFICATION OF THIS PAGE	19. SECURITY CLASSIFICATION OF ABSTRACT	20. LIMITATION OF ABSTRACT
UNCLASSIFIED	UNCLASSIFIED	UNCLASSIFIED	UL

NSN 7540-01-280-5500

Enclosure 1

Standard Form 298 (Rev. 2-89)
Prescribed by ANSI Std. 239-18
298-102

PSU CGTP 2000-08

Center for Gas Turbines and Power
The Pennsylvania State University
University Park, PA 16802

Final Report

INVESTIGATION OF TIP CLEARANCE FLOW FIELDS AND METHODS OF DESENSITIZING TIP CLEARANCE EFFECTS IN TURBINES

X. Xiao, B. Lakshminarayana,
A. McCarter, A. Chernobrovkin,

Center for Gas Turbines and Power

July 2000

PREFACE

This report covers the progress in research for the period May 1, 1995 to Feb 28, 1999, and was carried out under the contract DAAH 04-95-1-0179. The following information is with regard to publications, presentations, and theses completed during this period.

Publications:
1. Ristic, D., Lakshminarayana, B., and Chu, S., 1999, "The Three-Dimensional Flow Field Downstream of an Axial Flow Turbine Rotor," Journal of Propulsion and Power, vol. 15, No. 2, pp. 334-344, March-April, 1999

2. Xiao, X., McCarter, A., and Lakshminarayana, B., 2000, "Tip clearance Effects in a Turbine Rotor, Part I: Pressure and Loss Fields," ASME 2000-GT-0476, accepted for publication in ASME Journal of Turbomachinery

3. McCarter, A., Xiao, X., and Lakshminarayana, B., 2000, "Tip clearance Effects in a Turbine Rotor, Part II: Velocity Field and Flow Physics," ASME 2000-GT-0477, accepted for publication in ASME Journal of Turbomachinery

Presentations:
1. Ristic, D., Lakshminarayana, B., and Chu, S., 1999, "The Three-Dimensional Flow Field Downstream of an Axial Flow Turbine Rotor," AIAA 98-3572, AIAA/ASME/SAE/ASEE Joint Propulsion Meeting, Cleveland, Ohio.

2. Xiao, X., McCarter, A., and Lakshminarayana, B., 2000, "Tip clearance Effects in a Turbine Rotor, Part I: Pressure and Loss Fields," ASME 2000-GT-0476, ASME TURBO EXPO 2000 Meeting in May, in Munich, Germany

3. McCarter, A., Xiao, X., and Lakshminarayana, B., 2000, "Tip clearance Effects in a Turbine Rotor, Part II: Velocity Field and Flow Physics," ASME 2000-GT-0477, ASME TURBO EXPO 2000 Meeting in May, in Munich, Germany

Thesis's:
1. Chernobrovkin, A., 1999, "Numerical Simulation of Complex Turbomachinery Flow," Ph.D. Thesis in Aerospace Engineering, Pennsylvania State University (Partially Supported)

2. McCarter, A., 2000, "Investigation of Tip Clearance Flow Fields in a Turbine Rotor Passage," M.S. Thesis in Aerospace Engineering, Pennsylvania State University

3. Xiao, X., 2000, "Tip Clearance Flow Fields and Methods of Desensitizing Tip Clearance Effects in Turbines," Ph.D. Thesis in Aerospace Engineering, Pennsylvania State University (in Preparation)

ABSTRACT OF THE PROPOSED PROGRAM

The main focus of the proposed research program is to carry out a systematic study of the tip clearance flow fields and methods of desensitizing their effects in turbines. The objective is to understand the flow physics; origin, nature and effects of leakage flow and their dependency on blade and flow geometry and then carry out an investigation to minimize their effects through flow control and design. The investigation will be carried out in the Axial Flow Turbine Facility at The Pennsylvania State University. The diameter of the facility is 91.4 cm and it has 23 nozzle and 29 rotor blades followed by outlet guide vanes. The blades and vanes were designed by the General Electric Aircraft Engine group to simulate the flow in modern HP turbines. The flow field will be measured using a miniature (1 mm) five-hole probe or a three-sensor hot-wire probe, and a laser doppler velocimeter. Measurements include static pressure on blades and endwall, stagnation pressure and three components of velocity, turbulence intensity and stresses at various radial, tangential (one passage), and axial locations inside and at the exit of the rotor passage in the tip clearance region. A rotating probe traversing mechanism will be used to acquire the data in the relative frame of reference. A three-channel laser doppler velocimeter will also be used to acquire the flow data and compliment the results from the three-sensor hot-wire or the miniature (1 mm) five-hole probe. The data will be correlated and synthesized with several analytical approaches presently used and the cascade (with simulated tip clearance) data available. In addition, an existing three-dimensional Navier-Stokes code, which includes various higher order turbulence models, will be used to validate the code, carry out additional simulation such as the effect of blade and tip geometry and flow control devices. The code has compressible flow formulation; and hence, the high temperature and high speed effects will be simulated using this code. In the second phase of the program, an attempt will be made to reduce the effect of leakage flow through flow control and desensitization. Several approaches, including the tip slots, will be discussed with industry personnel before deciding on the final approach. Close collaboration will be maintained with their industrial turbine group during this investigation. These investigations will be carried out using an integrated experimental and computational program.

ABSTRACT OF THE FINAL REPORT

An integrated experimental and computational investigation was carried for the proposed research project to derive the flow field information at various axial and radial locations from the leading to the trailing edge in the tip clearance region of the rotor. The static pressure on the blade surfaces and on the casing wall was measured to derive the trajectory of the leakage vortex and the horseshoe vortex. The numerical investigation of the flow field is based on the utilization of the Navier-Stokes solver. The experiment is carried out in the Axial Flow Turbine Research Facility (AFTRF) at the Pennsylvania State University.

The following measurements were completed:

1. Static pressure measurement on the blade surfaces from tip to hub, including hub surface. This brings the total number of static pressure taps on the rotor blade (hub-to-tip) to 11 x 22 (radial, chordwise) locations. Four group static pressure data was acquired separately along the 11 radial stations at 100%, 94%, 83% and 60% design rotating speed. A comparison of the design data and the corresponding CFD predictions shows good agreement. And the transient pressure measurement on the casing wall from the leading edge to the downstream using semiconductor Kulite probe.

2. Laser Doppler measurements at 20%, 30%, 40%, 500/o, 60%, 70%, 80%, 90%, and 101% of chord, at approximately 8 radial locations. This represents a measurement matrix of about 3,600 grids inside the turbine facility in the tip clearance region. The data includes the axial, tangential, and radial velocities, and the six stress correlations.

3. Rotating five-hole probe measurement to derive the losses. This has provided information on the stagnation pressure losses and static pressure characteristics in the tip clearance region, both inside the passage and downstream of the rotor.

4. Comprehensive numerical investigation was carried out using a steady state Navier-Stokes solver with optimized artificial dissipation, as well as a large number of grid points. This has provided valuable information on the physics of the leakage flow as well as the structure of the leakage vortex.

The data provided here indicates that the tip leakage flow originates at approximately 50% of the chord and is confined to the tip clearance region due to the relative motion between the blade and the wall, as well as the secondary flow in the tip region. Both of these effects are responsible for keeping the tip vortex closer to the suction surface comer of the tip. The vortex is very confined and very strong. The losses due to the secondary flow dominate compared due to the losses due to the leakage flow. The leakage flow losses are high, but are confined to an extremely small region near the tip of the suction surface as opposed to the secondary flow, which tends to increase the losses spread over a substantial portion of the passage. The casing pressure shows the presence of the scraping vortex, which originates near the leading edge, as well as the trajectory of the leakage vortex, which originates approximately at 50% of the passage. Therefore, the information provided here is substantially different from that derived on the basis of cascades testing. To some extent, it invalidates the cascade data that has been prevalent hith-

erto. This is the first set of data taken in a rotating turbine rig, and it seems to indicate that the modeling and the effects are quite different in the turbine rotor where the influence of the relative motion between the blade and the wall, as well as the influence of the secondary flow, have to be considered in modeling this flow. Most of the leakage losses are due to the mixing of the tip leakage vortex downstream of the trailing edge.

Numerical investigation of the flow field in the Penn State rotor based on the utilization of the Navier-Stokes solver has been carried out to gain a better understanding of the secondary and the tip leakage flow development. Pressure gradient across the blade tip clearance results in the development of the jet-like tip clearance flow. Its interaction with the main stream leads to the development of the tip vortex and modification of the casing secondary flow and vortex. The vortex interaction and mixing result in additional losses. One of the objectives of this simulation was to identify features affecting the development of secondary and tip leakage vortices, as well as sources of secondary flow losses. Analysis of the leakage flow development shows that the relative motion of the blade and the casing wall reduces the propagation of the leakage flow into the main stream. The tip leakage vortex is confined to the suction surface corner of the casing. Most of the leakage losses is due to the mixing of the tip leakage vortex downstream of the trailing edge.

TABLE OF CONTENTS

NOMENCLATURE

C	Chord
c_μ, $c_{\varepsilon 1}$, $c_{\varepsilon 2}$	Constants in low Re turbulence models
C_{ax}	Blade chord at mid-span
C_m, C_r	Blade chord at mid span
C_p	Static pressure coefficient
Cp_{pitch}	Pitch pressure coefficient of five-hole probe
Cp_{Static}	Static pressure coefficient of five-hole probe
Cp_{total}	Total pressure coefficient of five-hole probe
Cp_{yaw}	Yaw pressure coefficient of five-hole probe
C_x	Rotor axial chord
e	Internal energy per unit mass
G, g	Amplification factor
h	Spanwise distance $(R - R_h)/(R_t - R_h)$
H	The distance between the hub and the casing $(r - r_h)/(r_t - r_h)$
H_b	Blade height
k	Turbulent kinetic energy, wave number
p	Static pressure on rotor surface
P	Turbulent kinetic energy production
$\overline{P}$	Average of pressures 2 through 5 sensed by five-hole probe
P_1 - P_5	Pressures 1 through 5 sensed by the five-hole probe
P_{atm}	Atmospheric pressure
$P_{corrected}$	Pressure corrected for centrifugal force
P_{ij}	Production rate of Reynolds stress
$P_{measured}$	Experimentally measured pressure
P_o	Stagnation pressure
PS	Pressure surface
P_{static}	Mean static pressure

P_{total}	Absolute mean total pressure
Q	Vector of conservative variables
r	Distance in the radial direction
R	Residual, Radius of cylinder
$\overline{\overline{R}}, R_{ij}$	Rotation rate tensor
Re	Reynolds number, based on chord and outlet velocity
Re_t	Turbulent Re number, $k^2 / \nu\varepsilon$
Re_y	Turbulent Re number, $\sqrt{k}\, y/\nu$
R_{gc}	Gas constant
r_h	Radius of the hub
r_{probe}	Radius of five-hole probe hole pressure holes
r_t	Radius of the blade tip
r_{trans}	Radius of ESP-32 sensor array
s	Blade pitch
S	Rotor blade spacing
SS	Suction surface
t	Time
T_b	Period
U	Total velocity
u''	Fluctuation component of velocity
U_i	i-component of velocity
U_m	Blade speed at mid-span
V	Absolute total velocity
$\overline{V}$	Magnitude of flow velocity
V_θ	Absolute tangential velocity
V_b	Velocity measured by the LDV blue beam
V_g	Velocity measured by the LDV green beam
V_r	Radial velocity
V_v	Velocity measured by the LDV violet beam

V_x	Axial velocity
W	Relative total velocity
W_θ	Relative tangential velocity
W_r	Relative radial velocity
W_x	Relative axial velocity
w'	Fluctuating velocity component
x	Axial length measured from leading edge
y^+	Inner variable, $u_\tau y/\nu$
Zg	Normalized gap distance $Zg = (r-r_{tip})/(r_{cas}-r_{tip})$

Greek

ρ	Density
Ω	Rotor angular velocity
α	Flow angle measured in the radial direction
β	Relative flow angle measured in the tangential direction
γ	Specific heat ratio
δ	$\delta = \Delta\tau/\Delta t$
Δ	Normalized gap distance $Zg = (r-r_{tip})/(r_{cas}-r_{tip})$
ε	Turbulence dissipation rate
ζ	Loss coefficient
θ	Angle in the tangential direction
σ	Von Neuman number
τ	Pseudo time, stress
ϖ	Wake passing frequency
ω	Vorticity, wake width parameter, rotation vector
Ω	Rotor angular velocity
μ, μ_l	Molecular viscosity
ψ_{03}	Absolute pressure drop coefficient $(\overline{P}_{01a}-P_{03a}) / (0.5\,\rho\,Um^2)$
ψ_{03R}	Relative pressure loss coefficient $(\overline{P}_{02r}-P_{03r}) / (0.5\,\rho\,Um^2)$

Ψ_{3Rotor}	Rotor static pressure drop coefficient $(\overline{P}_2 - P_3) / (0.5\ \rho\ Um^2)$
Ψ_{3Stage}	Absolute stage pressure drop coefficient $(\overline{P}_1 - P_3) / (0.5\ \rho\ Um^2)$
δ_{ij}	Kronecker delta
ε_{ij}	Alternating tensor
$\sigma_k, \sigma_\varepsilon$	Turbulent Prandtl numbers
μ_t	Eddy viscosity coefficient
ω_x	Axial vorticity

Superscript

-	Time averaged, ensemble averaged
h	Hub
1	Inlet
o	Total
r	Rotor
ref	Reference condition
t	Tip
x	Axial direction

Subscript

1	Inlet of nozzle
2	Nozzle/Rotor gap
3	Exit of Rotor
ARSM	Based on Algebraic Reynolds Stress Model
a	Absolute frame of reference
cas	Casing
j	Jet
k-ε	Based on k-ε model
max	Maximum outside rotor wake
r	Relative frame of reference

t	Turbulent
tip	Blade tip
vis	Viscous
w	Quantity at the wall
x	Axial
y	Projection on y direction

ACKNOWLEDGEMENTS

XIII

1. INTRODUCTION

A tip clearance exists in all turbomachinery rotors for mechanical reasons. In modern high-pressure turbines, unshrouded tip design is beneficial due to structural reasons. Leakage flow occurs through the tip clearance gaps driven by the pressure difference that exists across the blade tip. Although the leakage mass flow may be insignificant when compared with the main stream, this leakage flow has major effects on the turbine efficiency. Once the tip clearance is larger than about 1% of the blade height, the efficiency usually drops by about 1.5% for every 1% increase of the blade height in tip clearance. Schaub, et al. (1993) have reported that up to 45% of the losses in a rotor and 30% of the losses in a stage can be attributed to the tip leakage flow in a modern, high performance, high pressure turbine stage. This is particularly applicable to smaller sized turbines. With increased size, the percentage of losses may be somewhat lower, but is still a dominant effect. In addition, the tip leakage also changes the lift of the blade due to the unloading in the tip region; and decreases the pressure and temperature drop across a stage, which represent a deterioration in performance. This modifies outlet angles, and introduces radial flows. This results in three-dimensionality and off-design conditions downstream of the blade row. The modified outlet angles results in a less work output. Transverse and radial flows result in an intense mixing, high turbulence production, and losses in this region.

Furthermore, the heat transfer near the tip clearance region of the blade and the casing is affected by the leakage flow. The most difficult zone to be cooled in an unshrouded axial flow turbine rotor is the area located near the tip corner on the pressure surface. This creates a barrier in improving turbine performance through higher inlet gas temperatures. The leakage flow and its vortex cause flow unsteadiness, structure vibration, flutter, and noise in the following rows which may result in a shortened engine life. Evidently, it is extremely important to understand the physics and effects of the tip leakage. The trend towards higher loading, higher temperature, and lower aspect ratio intensifies the importance of tip leakage flow for turbine designers. But, unfortunately, the flow field in the rotor tip region remains one of the least understood phenomena due

to complexities of the flow physics, the measurement system needed, and the operational rotating turbine facilities.

2. LITERATURE REVIEW

The complexity of the leakage flow physics is governed by numerous geometry and flow variables. Height of the tip clearance, blade thickness, blade turning angle, space-chord ratio, shape of the blade, and end wall near the tip are all important geometrical parameters. Aerodynamic parameters involves blade speed, blade pressure distributions, Mach number, Reynolds number, inlet boundary layer thickness, inlet vorticity distribution, unsteadiness, and possible shock wave occurrence in the gap flow.

Much of the present knowledge of the flow field in the tip clearance region is based on simplified analysis and testing of compressors and turbine cascades. For example, Dean (1954), Lakshminarayana and Horlock (1967), Lakshminarayana (1970), Storer and Cumpsty (1991) among others have reported detailed structure of flow in a compressor cascade with simulated tip clearance. Lakshminarayana et al. (1982, 1983, 1984, 1995), Pandya and Lakshminarayana (1983), Inoue and Kuroumaru (1984, 1986, 1988), Hunter and Cumpsty (1982), Schmidt et al. (1987), and Stauter (1992) have provided detail data in the tip clearance region of compressor rotors. These investigations reveal that the tip clearance effects in a rotor are substantially different from those in a cascade. The presence of the blade motion, secondary flow, unsteady flow, and blade boundary layers from upstream blade row substantially alters the structure, losses, and three-dimensionality induced by the tip clearance.

The tip clearance flow field in a turbine is much more complex than that in compressors due to higher loading coefficient, higher turning angles, thicker blading, larger leakage velocities, high temperatures, etc., but much less attention is paid to the investigation in turbines than that in compressors. Until today, most of the work done in turbines focuses on linear cascades without any blade motion. Bindon (1987, 1990), Dishast and Moore (1989), Moore et al. (1989), Graham (1986), Moore and Tilton (1988), Yaras and Sjolander (1988, 1990, 1991), Yamamoto et al. (1982, 1987a, 1987b,

1988), Wadia and Booth (1982), Booth et al. (1985) and others have provided detailed information on the flow field at the exit of turbine cascades. The presence of the secondary and leakage vortex, and the location and strength have been measured. The flow field is dominated by the vortices. Its effects downstream on outlet angles, losses, and span wise and cross flows is found to be substantial. It is believed that the decay of the leakage vortex, formed by the mixing of the leakage flow with the main stream and blade boundary layer, accounts for the majority of this loss, and about 20% of span from tip is influenced by the tip clearance. The magnitude of these effects depends on the tip clearance height, blade thickness, inlet flow angle, Reynolds number, and Mach number.

Very little information is available in the open literature on tip leakage flow in rotors. In a rotor, the effects of the relative motion between the blade and the end wall remains unknown. It may tend to reduce the leakage flow in a turbine due to opposing relative motion between casing and blades, but no data has been acquired to confirm this. In addition, the radial flow is also very strong in the tip region of a turbine rotor. It results in substantially different leakage flow and vortex structure in a turbine rotor as compared to a cascade. The radial flow inside the blade boundary layer, due to centrifugal and coriolis forces, tends to energize the tip leakage flow. The wall boundary layers and turbulence intensities are much different in the tip clearance region compared to a cascade. Hence, it is anticipated that leakage flows and vortices in a rotor will be substantially different from those in a cascade. Although tip leakage vortex has been observed in turbine cascades, but it may not have a chance to roll up into a discrete vortex in a turbine rotor. Recent investigations in a compressor rotor (Lakshminarayana et al., 1995 and Stauter, 1992) suggest that the leakage flow diffuses before it has had a chance to roll up into a discrete vortex. In summary, there has been no systematic investigation of tip clearance effects in turbine rotors, and this is the objective of the proposed research.

3

3. OBJECTIVE OF THE RESEARCH

The objectives of the present research program are as follows:

A. To investigate the flow physics and effects of the tip leakage. The emphasis is on the flow field inside the rotor passage and the pressure distribution of the rotor blade surface. No attempt will be made to obtain the flow field inside the tip gap of the rotor. The reason for this emphasis lies in two aspects. The first reason is because most of losses come from the interaction between the tip leakage flow and the main stream. The second is because the height of the tip gap is extremely small (0.75 mm) in the Penn State research turbine rotor and the turbine configurations used in industry. The pressure distribution on the blade surface is directly related to the turbine blade loading.

B. To explore some basic ideas for desensitizing the effects of the tip clearance in order to increase the performance of a turbine stage. One of these methods is to induce a jet to impede the formation of the tip clearance vortex in order to decrease the loss due to the interaction between the tip leakage vortex and the main stream flow.

4. EXPERIMENTAL FACILITY AND INSTRUMENTATION DESCRIPTION

4.1 Experimental Facility Description

The Axial Flow Turbine Research Facility (AFTRF) of the Pennsylvania State University is an open circuit turbine research rig with 91.4 cm in diameter, a hub-to-tip radius ratio of 0.73, and one advanced blading stage (Figure 4.1). In general, it consists of a bellmouth inlet, a turbulence generating grid, a test segment with two rows of 23 nozzle guide vanes and 29 rotor blades, an acoustic absorber to decrease noise, and a variable through flow propeller consisting of two auxiliary, adjustable pitch, axial flow fans with an aerodynamically designed throttle. To filter the air flowing into the AFTRF, an enclosure cover with wire mesh and a thin layer of rubber foam is installed around the bellmouth inlet.

The two fans in series provide a mass flow of 10 m^3 per second with a pressure rise of 74.7 mm Hg (40 " of water) under nominal operation conditions. The power generated by

the experimental turbine rotor assembly is absorbed using an eddy-current brake, which is capable of absorbing up to 60.6 KW (90 Hp). With the help of a dynamic control system, the speed of the rotor can be varied from 175 to 1695 rpm while rpm deviation within +/- 1 rpm and normal fluctuations in line voltage, and a closed loop chilled water cooling system is selected to cool this eddy current brake.

The configurations of the vane and blade are designed by the GE Aircraft designers and represent the features of a current or near-future HP turbine stage (Fig. 4.3). The peak total-to-total isentropic efficiency is 89.3% at a rotational speed of 1300 rpm. At this peak efficiency point, the total pressure and temperature ratios are $P_{03}/P_{01} = 0.928$ and $T_{03}/T_{01} = 0.981$ (For more details, see Lakshminarayana et al., 1996). The experiment was conducted at a corrected rotational speed of 1300 rpm and a mass flow rate ($\dot{m}$) of 10.53 kg/sec. Design features of the AFTRF are shown in Table 4.1.

On the blade surfaces of the suction side and pressure side and the hub surface of the rotor, nearly 500 static pressure holes are drilled at carefully selected locations as follows:

- 16 static holes for performance measurements on the outer casing and inner casing of the rig at 4 axial planes. A circumferential average at each plane will be used for performance calculations.
- 43 static holes on the nozzle endwall in one passage
- 43 static holes on the annulus wall of the same nozzle passage
- 154 static pressure holes at several axial and chordwise locations on both surfaces of nozzle blades (one passage) (Figs. 4.4, 4.5, & 4.6)
- 52 static holes on the hub surface of one rotor pasage
- 154 static pressure holes at several radial and chordwise locations of rotor blade on both surfaces (one passage)

Static pressure measurements in the rotating frame are taken by a 32-channel electronic pressure scanner located in the rotor frame. The output signal, after multiplexing in the rotor frame, is passed through a slip ring unit for processing in a computer controlled data acquisition system (Fig. 4.2).

The data acquisition system is called MODEL 780B/T electronically scanned Pressure Measurement System (PSI). It is a fully integrated measuring instrument consisting of Electronically Scanned Pressure (ESP) sensors and a microcomputer based data

5

acquisition system. It offers one transducer per port to provide high data rates for multiple static pressure measurement applications. The PSI system chooses an on-line three-point pressure calibration of all transducers, up to 20,000 measurements can be sampled per second with inaccuracies less than +/-0.01% of span.

Table 4.1 Facility parameters

Tip radius (m)	0.4582
Chord (m)	0.1287
Hub-to-tip ratio	0.7269
Solidity	1.2519
Turning angle at tip (degree) 0.12513442	95.42
Maximum thickness-to-chord ratio	17.1%
Mean tip gap-to-span ratio	0.78%
Maximum tip gap-to-span ratio	0.90%
Minimum tip gap-to-span ratio	0.65%
Reynolds number based on inlet relative velocity	$(0.25\sim0.45)\times10^6$
Reynolds number based on exit relative velocity	$(0.50\sim0.70)\times10^6$
Tip relative maximum mach number	0.240
Pitchline loading coefficient[1]	3.4
Pitchline reaction	0.4~0.5

4.2 Static Pressure Acquisition on Blade Surfaces

All blade static pressure data in this experiment were acquired by using a pressure scanner system controlled by an IBM 486 compatible microcomputer system. As mentioned earlier, this system can acquire 20,000 samples for each port of as many as 1024 ports per second with an accuracy of +/- 0.01% span.

One of the major difficulties in this experiment is the reference pressure. Because the pressure sensor array ESP-32 used IN this experiment is a differential pressure transducer, a precise reference pressure is required for an accurate absolute static pressure. But the pressure array ESP-32 is installed on a point between the turbine axis and the hub inside the turbine rotor and rotates at the same speed as the turbine rotor. It

---

[1] Definition of pitchline loading coef. is $\dfrac{\Delta h_0}{0.5\rho U_m^2}$, where Δh_0 is the total enthalpy drop across stage.

can be expected that there are other factors that influence the accuracy of the reference pressure data. We consider the majority of these factors:

Firstly, the effect of centrifugal force is considered. Since the ESP-32 and the static pressure hole are located at different radii, the following centrifugal force correction is incorporated:

$$a_c = \frac{1}{2}\rho\omega^2 r_2^2 - \frac{1}{2}\rho\omega^2 r_1^2$$

where

a_c	centrifugal acceleration
ρ	average density of the gas inside the tubes connecting the ESP-32 and the static pressure holes on the turbine rotor blade
ω	rotating angular speed in radians
r_2	radius of the point where static pressure holes are located
r_1	radius of the point where ESP-32 sensor arrays are located

Secondly, the temperature changes affect the accuracy of the data through this temperature drift of ESP-32 pressure transducers. This error is eliminated by acquiring data after the temperature has reached equilibrium conditions.

It is nearly impossible to calibrate the sensor on line in a rotating coordinate system at the present time because we can not connect a gas with standard pressure to flow from the stationary casing to the turbine rotor passage while rotating. We have resolved the problem by calibrating the ESP-32 sensor using gas, a known pressure before the run. If it is good or its reading is zero, we operate the turbine and acquire the data. The sensor is checked again at the end of the experiment for zero drift.

There are 22 static pressure holes in the chordwise location at 11 different radius as shown in Fig. 4.4, 4.5, & 4.6. Five of them are located at 90%, 70%, 50%, 30% and 10% of the radius from the hub-to-tip. Another five of them are located very close to the tip at 93%, 95%, 96%, 98% and 99% span from the hub, for the investigation of the secondary and leakage flow in near tip region. The last location is at edges close to the suction side and the pressure side of the blade in the tip region (inside the gap).

All data were acquired under the following conditions:

inlet temperature:	24 °C
inlet atmosphere pressure:	988 mbar
corrected rotation speeds:	1330, 1225, 1100 and 800 rpm
relative humidity:	about 50%

Since all the data are acquired under the same conditions, one of these data is chosen as the reference pressure.

4.3 Transient pressure acquisition on casing wall using Kulite probe

The transient pressure distribution on the end wall due to the rotor was investigated by using a dynamic pressure sensor, model XCS-093-5D developed by the Kulite Semiconductor Products, Inc. The sensing area is very small. Its diameter is less than 1 millimeter, or about 1% of the axial chord length of the rotor. This small size guarantees a good space resolution for the data to be acquired. The Kulite transducer is installed on the casing of the turbine facility. The pressure field on the end wall is measured by this configuration. Data was acquired at eleven axial locations uniformly spaced from the leading edge to the trailing edge of the rotor along the axial direction, and two more locations are chosen at 30% upstream and 20% downstream of the rotor, respectively. A shaft encoder with 6000 line per resolution is used as a clock in the data acquisition procedure. With its starting or trigger location known, the actual tangential position for each data point is thereby defined. Some turbomachinery- related literature refers to this as a phase locked technique.

4.4 Three Dimensional LDV Instrumentation System

In addition to the investigation of the pressure distribution on the surfaces, the flow fields inside the rotor passage are also investigated. These flow field parameters include the velocity distribution, turbulence intensities and shear stresses, vortex development, and interactions inside the rotor passage near the tip region, which are effected by the tip leakage flow. Since the space in the tip region is very limited, the scales of fluid flow structures are very small, and the measurement in the region is extremely difficult.

A non-invasive LDV system with a tiny measuring volume (0.112 millimeter in diameter) is therefore chosen to perform this research. A TSI Model 9100-12 three-dimensional LDV system was used in this research. This system is capable of acquiring three velocity components concurrently. Menon (1987) gave a detailed description of this system and its application in the aerodynamic research field inside a turbomachinery. Ristic, Lakshminarayana, and Chu (1998) provide details of the Penn State system and data acquisition process. The light source is a 7-watt Argon-Ion Laser of the Coherent Model Innova 300. This laser operates in its multi-line mode. A light splitting lens is used to divide the multi-line laser source beam into three beams with green, blue and violet colors, respectively (Fig. 4.10). Then for each beam, a Bragg cell element is used to divide it into two beams, one of these two beams is 40 megahertz shifted in frequency. So after these divisions, six beams with three colors are present. For each two beams with the same color, the frequencies are 40 megahertz divided. The purpose for the frequency shifting is to remove the ambiguity of the flow direction, in order to measure the reverse flow.

These three pairs of beam have different functions. The green beams and blue beams are aligned to one axis. The axis of violet beams intersects at a angle of 30.14 degree with the axis of the green and blue beams. The plane formed by the green beams is kept horizontal so as to measure axial velocity component V_x. The plane formed by the blue beams is kept vertical in order to measure tangential velocity components V_θ, The plane formed by the violet beams is also horizontal. Since the violet beams have an angle with the green beams, the radial velocity components can be calculated from the velocities measured by the green beams and violet beams. All these six beams intersect at one point exactly. The higher the accuracy of the intersection, the lower the signal to noise ratio, and the higher the data rate. Table below shows some important parameters of the LDV system used in this experiment.

Green wave length (nm)	514.0
Blue wave length (nm)	488.0
Violet wave lenth (nm)	476.5
green fringe spacing (microns)	4.656
blue fringe spacing (microns)	4.417
violet fringe spacing (microns)	4.432

9

diameter of meas. Volume (mm)	0.11
shaft encoder resolution	6000
typical green freq. Shifting (Mhz)	2
typical blue freq. Shifting (Mhz)	5
typical violet freq. Shifting (Mhz)	2
coincidence window size (μs)	10

All six beam are introduced into the flow field through a glass window on the turbine casing. The axis of the green and blue beams is perpendicular to the glass window. The displacement caused by passing a light beam at an incidence angle through a glass window is accounted for by placing a similar glass in the optical path when the beam crossing alignment is being made. Thus, the three dimensional velocity can be calculated from:

$$V_x = \frac{V_G \sin \gamma_1 + V_V \sin \gamma_2}{\sin(\gamma_1 + \gamma_2)} \tag{4.1a}$$

$$V_r = \frac{V_G \cos \gamma_1 - V_V \cos \gamma_2}{\sin(\gamma_1 + \gamma_2)} \tag{4.1b}$$

$$V_\theta = V_B \tag{4.1c}$$

where V_B, V_G, and V_V are the velocities sampled by the blue, green and violet light beams, respectively and γ_1 and γ_2 are the angles of the green and violet optical paths. In the present investigation $\gamma_2 = 30.14°$ and $\gamma_1 = 0$

The receiving optics are arranged off-axis, i.e. the photo multiplier for the violet beam receives scattered light from the seeding particles in the blue and green transmitting optical rail, and vice versa. This arrangement substantially reduces noise from internal refection and light reflected and scattered from the glass window. The whole LDV system is mounted on an optical table, and a hydraulic system is provided for the table movement in x, y, and z directions, plus a tilting. Thus, traversing of the LDV probe volume in radial, tangential and axial directions can be readily achieved.

A 6-jet atomizer, TSI Model 9306, is chosen to generate seeding particles for the LDV system. The Propylene Glycol is used as the working liquid for the jet atomizer, which can generate particles with a nominal mean size of 0.6 micrometer in diameter. The advantage of the Propylene Glycol is its low toxicity and water solubility. This is

especially helpful for the investigation of the tip leakage flow, since the seeding particles directly contaminate the glass window, and the water solubility allows for a quick clean up during the experiments procedure. Seeding liquid particles are introduced into the flow field at the bellmouth inlet of the facility.

4.5 Rotating Five Hole Probe System

Five hole probe measurements are taken using the area traverse installed in the rotating frame in order to acquire instantaneous pressure and velocity data. The traverse mechanism allows a detailed traverse of over 1-1/4-blade passages downstream of the rotor. A special probe attachment was designed and manufactured to allow the five-hole probe to be extended into the rotor passage to obtain measurements using the area traverse mechanism. The probe extension allows the probe to rotate along a radial axis. This allows the angle of the probe to be rotated relative to the turbine axis to match the angle of the rotor blade at a given axial location. In this way the probe angle can be aligned with the flow relative to the blade.

The probes are traversed by stepper motors driven by an IBM compatible-486 using a Kiethley Metrabyte MSTEP-3 Stepper Motor Driver and MSTEP-3 Stepper Motor Driver Board. The computer controls these boards using a QuickBasic program. The program controls both the motion of the probe and acquisition of data. The probe is traversed tangentially in one passage (about 54 points) at 7 radial locations up to about 25% of the span measured from the tip, and at seven axial locations, inside the passage and downstream of the trailing edge. This area traverse provides detailed information on the three instantaneous velocity components and total and static pressures. The average tip clearance for the five-hole probe tests was 0.97mm.

4.5.1 Probe calibration and measurement technique

The five-hole probe is capable of measuring three orthogonal components of velocity and mean total pressure. The diameter of the probe tip is 1.67 mm. The probe was calibrated in the Garfield Thomas water tunnel of the Pennsylvania State University at a Reynolds number, $Re_d = 16460$. The five-hole probe was calibrated over a +/- 30° range in both pitch and yaw in 10° increments with a 0.5° alignment accuracy.

A complete description of the five-hole probe calibration and data reduction technique is given in Treatster and Yocum (1979). Some of the basic concepts of the technique are given here. Four pressure coefficients are first defined in equations (4.2a – e).

$$Cp_{yaw} = \frac{P_2 - P_3}{P_1 - \overline{\overline{P}}} \qquad (4.2a)$$

$$Cp_{pitch} = \frac{P_4 - P_5}{P_1 - \overline{\overline{P}}} \qquad (4.2b)$$

$$Cp_{total} = \frac{P_1 - P_{total}}{P_1 - \overline{P}} \qquad (4.2c)$$

$$Cp_{static} = \frac{P_1 - P_{static}}{P_1 - \overline{\overline{P}}} \qquad (4.2d)$$

where

$$\overline{P} = \frac{1}{4} (P_2 + P_3 + P_4 + P_5) \qquad (4.2e)$$

The important issue is that the calibration of the probe removed any aerodynamic effects associated with the probe tip and/or body. The five-hole probe was designed to have a standard geometry (for example each of the four planes on which the static pressure is read is designed to be at 45° to the angle of the plane of the stem of the probe). This means that two different five-hole probes will respond slightly differently to the same flow and this is the reason to calibrate the probe.

4.5.2 Five-Hole Probe Data Processing Algorithm

This section describes the computer algorithm that has been written to precisely process the five-hole probe data when the probe is used in nonnulled mode. The program uses the three-dimensional calibration maps, and compressible flow equations given below with the pressures measured at each of the five-hole probe holes and the stagnation temperature measured behind the rotor to obtain the direction and magnitude of the measured velocity vector.

12

The algorithm determines, P_{static}, P_{total}, and the magnitude and direction of the velocity for the experimental data using equations (4.2) and the compressible flow relations in equations (4.4) to (4.7) in an iterative process.

The first step in the algorithm is to correct the measured pressures in the five-hole probe for centrifugal forces. Since the probe and the transducer are mounted in a rotating frame and the radius of the pressure ports for the probe and the transducer diaphragm are different, we need to correct the pressure data for centrifugal force which develop. Before the acquired pressure data for each of the five-hole probe pressure holes can be processed it is corrected to account for this centrifugal acceleration as shown in the following equation

$$P_{corected} = P_{measured} + [\frac{1}{2}\rho\Omega^2(r^2_{\text{Pr}obe} - r^2_{Trans})] \tag{4.3}$$

For the first iteration the density was assumed atmospheric. Using the corrected pressures, the next step is to calculate Cp_{yaw} and Cp_{pitch} for the experimental data with equations (4.2a) and (4.2b). Next the calibration maps for Cp_{yaw} and Cp_{static} are fit with a spline curve for each set of yaw angles in the calibration set. The values of Cp_{yaw} and Cp_{static} calculated from the experimental data is used in a double interpolation procedure using the spline fit calibration maps to obtain the local yaw and pitch angles (α and β respectively) of the data thus defining the direction of the velocity vector.

With the direction of the velocity vector determined, the magnitude is calculated. The values of the yaw and pitch angle previously determined are used in a double interpolation procedure using the calibration maps of Cp_{static} and Cp_{total} to determine the values of Cp_{static} and Cp_{total} for the experimental data. From these values, P_{static}, P_{total}, and the magnitude of the velocity for the experimental data can be calculated using equations (4.2c) and (4.2d).

Then the Mach number is calculated with equation (4.4). The static temperature is calculated from equation (4.5) using the Mach number just determined with the stagnation temperature measured downstream of the rotor. Finally the density is

13

determined from equation (4.6). The new density is placed back into centrifugal force correction equation (4.3) and the process is repeated until the calculations converge.

$$M = \left\{ \frac{2}{\gamma - 1} \left[\left(\frac{P_{Total}}{P_{Static}} \right)^{\frac{\gamma - 1}{\gamma}} - 1 \right] \right\}^{1/2} \tag{4.4}$$

$$T_{static} = T_{stag} \left\{ 1 + \frac{\gamma - 1}{2} M^2 \right\} \tag{4.5}$$

$$\rho = \frac{P_{static}}{R_{gc} T_{static}} \tag{4.6}$$

Once the compressible flow equations converge, the total velocity magnitude of the flow is determined using the equation as follows.

$$V = M \sqrt{\gamma R_{gc} T_{static}} \tag{4.7}$$

The velocity vector is then resolved into a coordinate system relative to the turbine using equations (4.8a-c) below.

$$V_x = V \cos(\alpha) \cos(\beta) \tag{4.8a}$$

$$V_r = V \sin(\alpha) \tag{4.8b}$$

$$V_\theta = V \cos(\alpha) \sin(\beta) \tag{4.8c}$$

4.5.3 Data Acquisition and Processing

The five hole probe pressure measurements in the rotating frame were carried out using Pressure System Inc. (PSI), Model-780B pressure measurement system. This has a range from 0 to +/- 1.0 psi and contains 32 separate channels. The PSI system is controlled on-line by a PC-486 computer using a Keithley Metrabyte Das-20 board. The accuracy of the PSI System was specified by the manufacturer as +/-0.0027 psi.

The PSI System measures a differential pressure referenced to the pressure inside the rotor hub where the transducer is mounted. To obtain absolute pressures, this reference pressure is measured using a separate sealed Data Instuments model XCX absolute transducer with a range from 0 to 15 psia. This equipment allows the absolute pressure within the flow field to be calculated.

This section outlines the procedures that are followed to correct several discrepancies with the instrumentation used to acquire five-hole probe data. The temperature of the transducers is of importance for the accuracy of the ESP-32 pressure sensor array. According to our experience in this experiment, temperature will increase nearly 10°C after running for one half hour in the Turbomachinery Laboratory of the Penn State and will then reach a steady state. As the temperature increases , the ESP-32 reading will begin to shift. Fortunately, we can nearly eliminate the temperature effect by allowing the turbine to run until a steady state temperature is reached in the room and in the turbine rig before taking any measurements.

Because the length of the tube connecting the static pressure hole of the probe to the ESP-32 inlet can sometimes be long, transient pressures may develop in the lines as the probe is moved within the flow field. Because we are measuring static pressure, some length of time is needed for the gas inside the tube to gain equilibrium. We found this length of time is about ten seconds by acquiring data continuously and immediately after running conditions are changed. Theoretically, this length of time should be proportional to the length and oppositely proportional to the square diameter of the connecting tube. Therefore we pause for a minimum of fifteen seconds after changing the position of the probe before pressure measurements are taken.

Using the traverse mechanism in the rotating frame, the five-hole probe was traversed at an axial location of 1.10 chords downstream measured from the rotor leading edge at midspan. All measurements were taken in a single blade passage. Data was taken at seven radii from 60% to 97% of the blade span. The exact radii are given in table 4.1. The probe was traversed across one complete blade passage with data being taken at 54 equally spaced points.

Table 4.1: Radial Location for measurements at x/C$_r$ = 1.10

H=	0.60	0.75	0.80	0.85	0.90	0.93	0.95	0.97
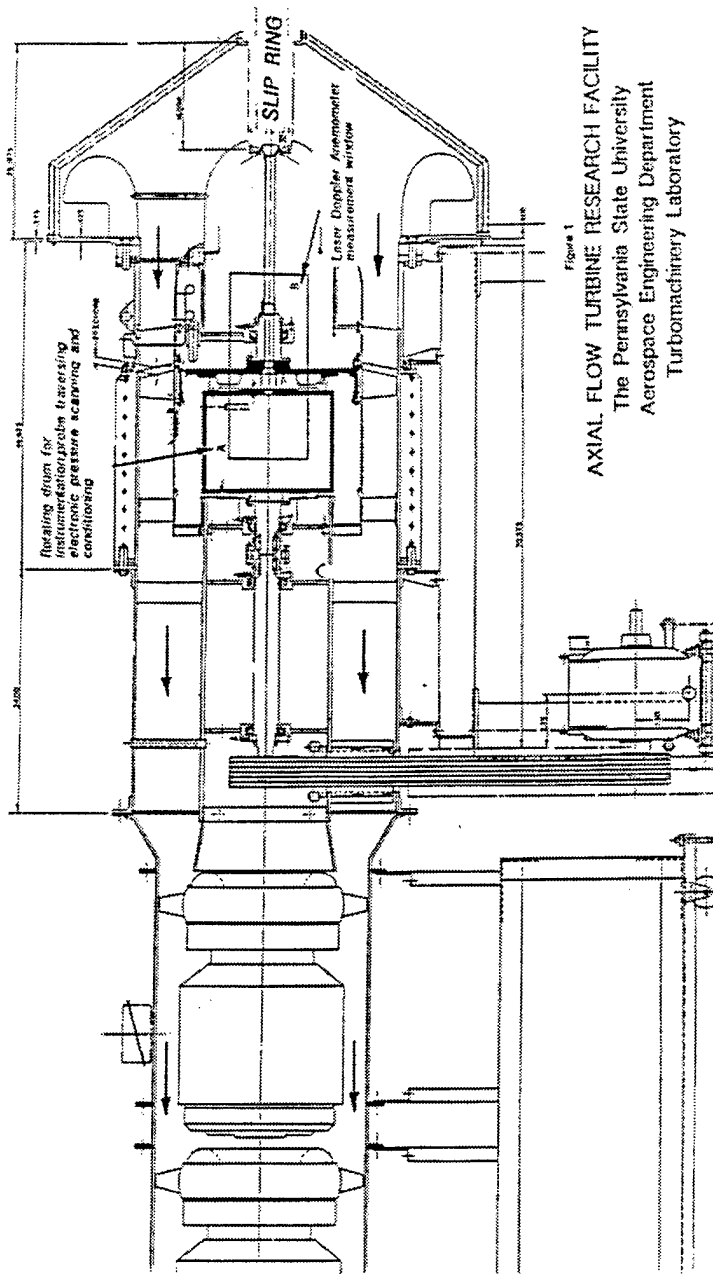
Figure 4.1   Schematic and flow path of the AFTRF
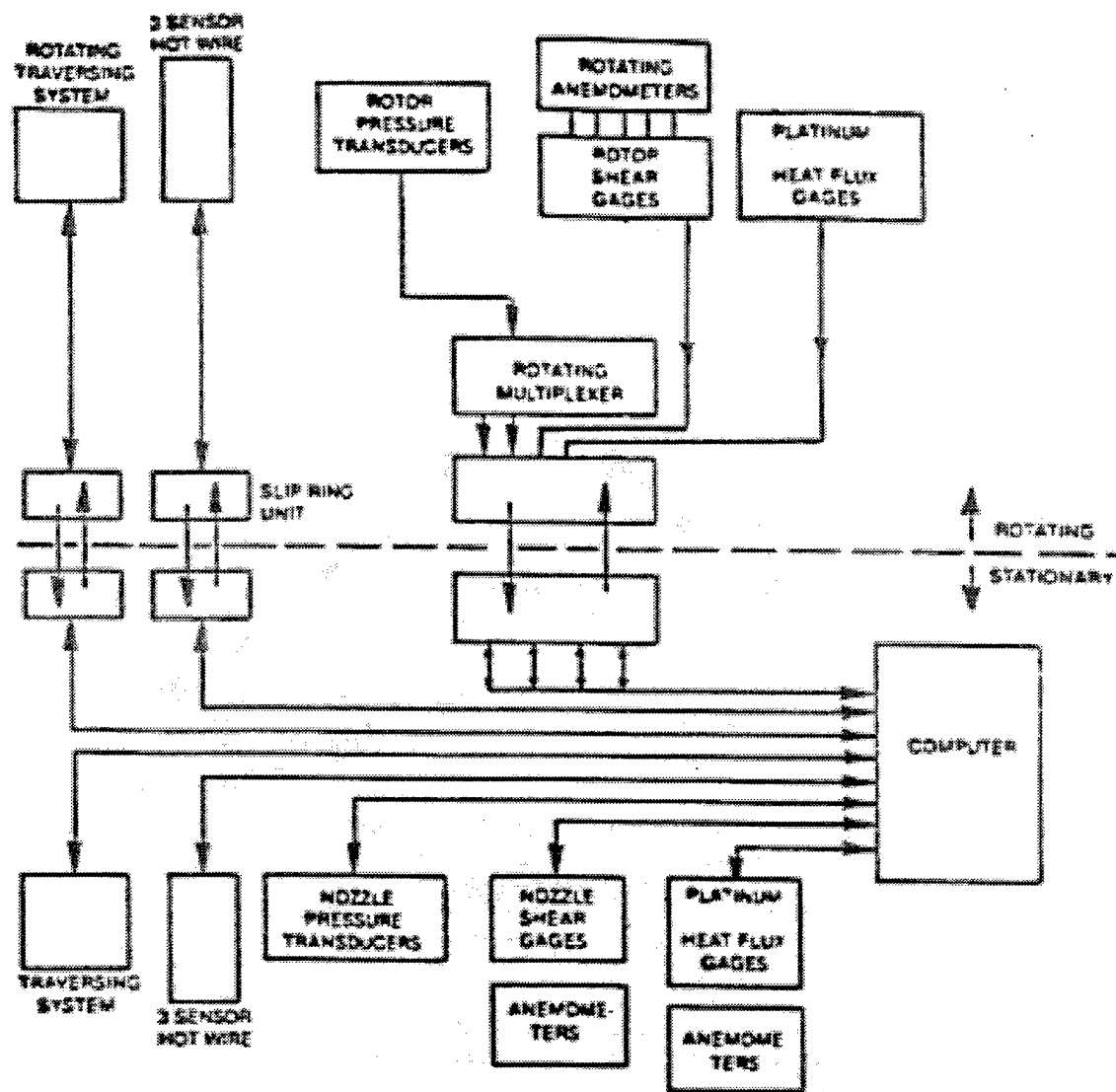
Figure 4.2 Layout of the slip ring used in AFTRF

17
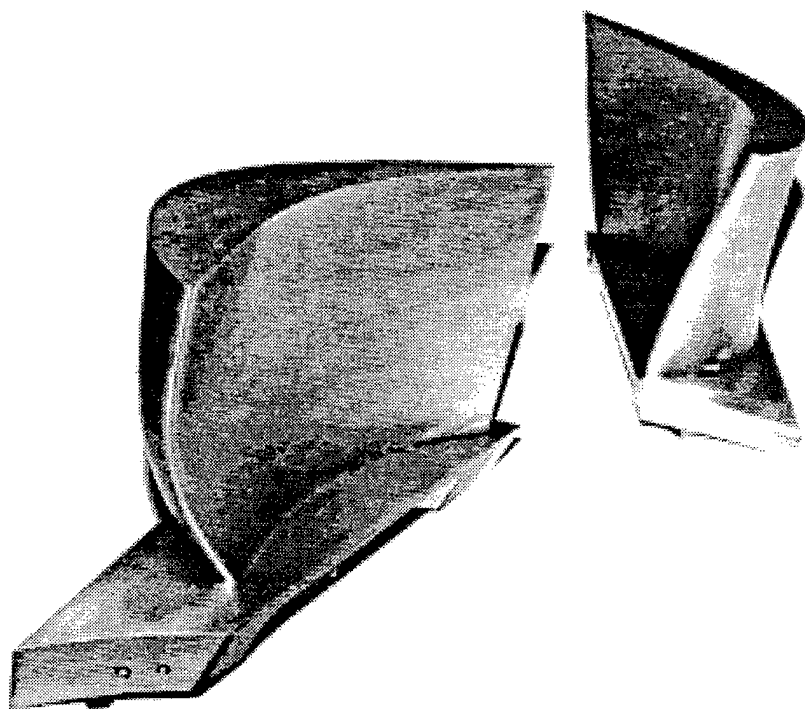
Figure 4.3 blade of the nozzle and rotor of turbine in this experiment

passage A

STATIC PRESSURE
HOLES

suction side
pressure side
endwall
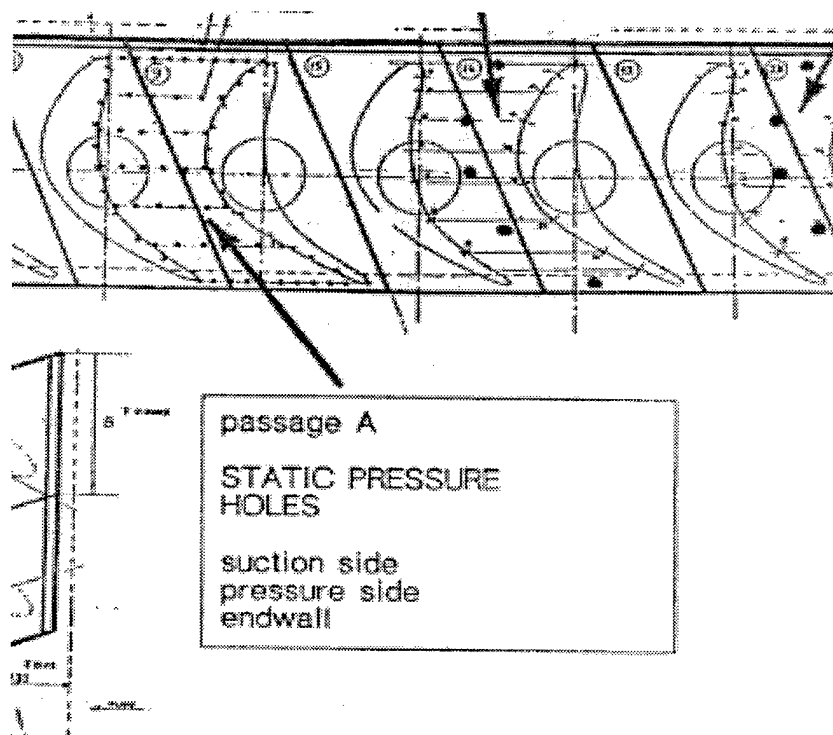
Figure 4.4 static pressure holes location layout 1
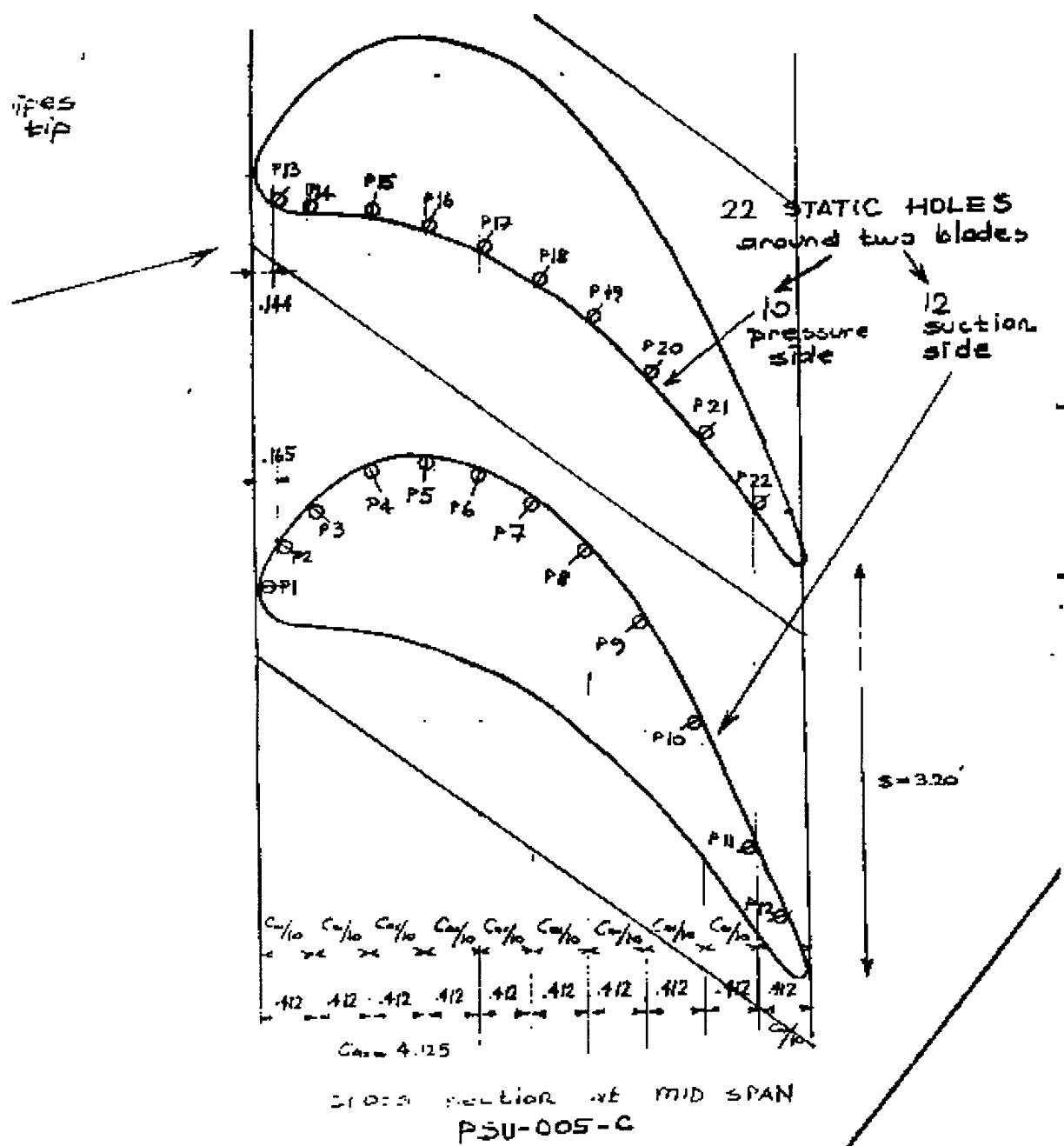
Figure 4.5 static pressure holes location layout 2
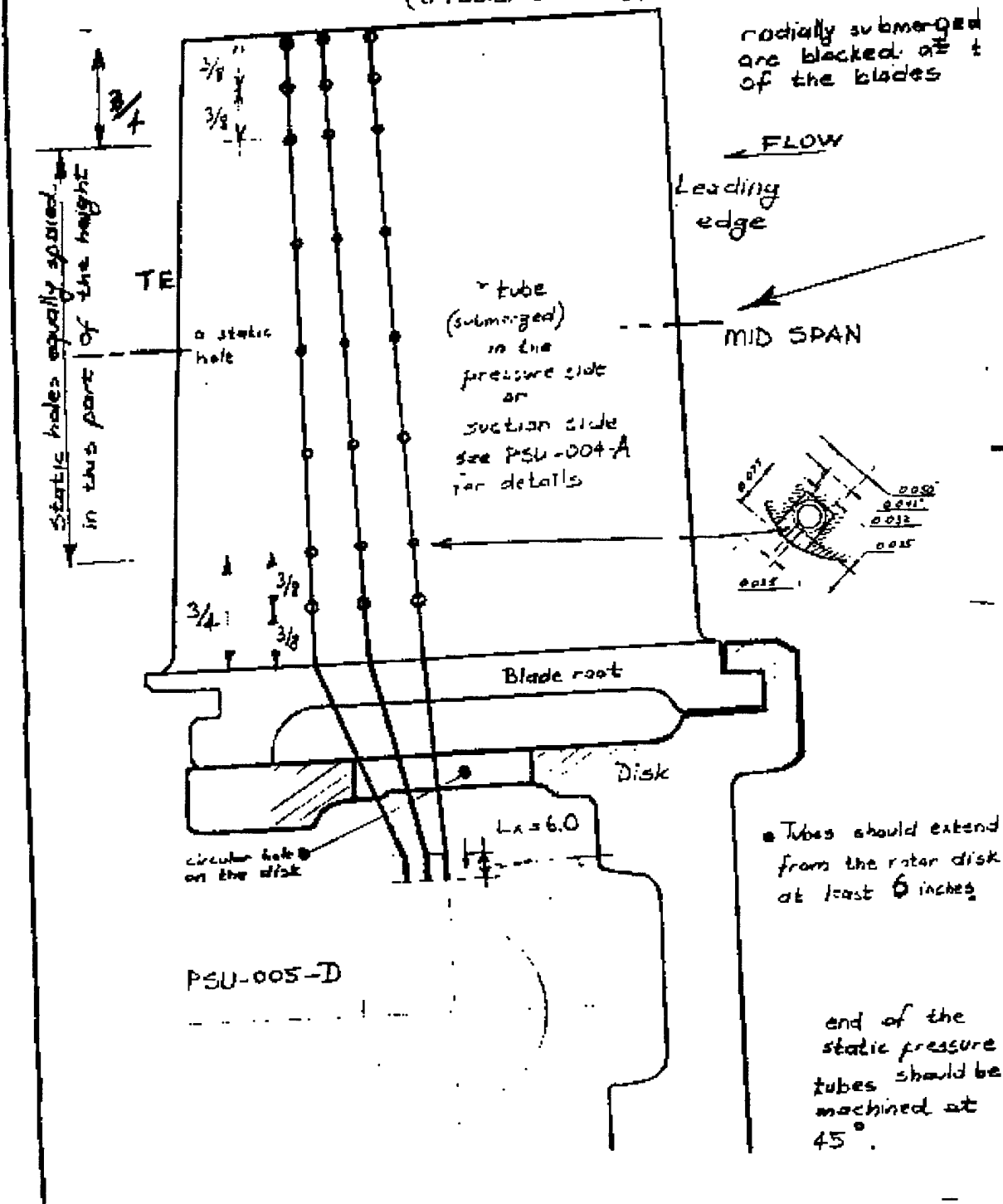
Figure 4.6 static pressure holes location layout 3
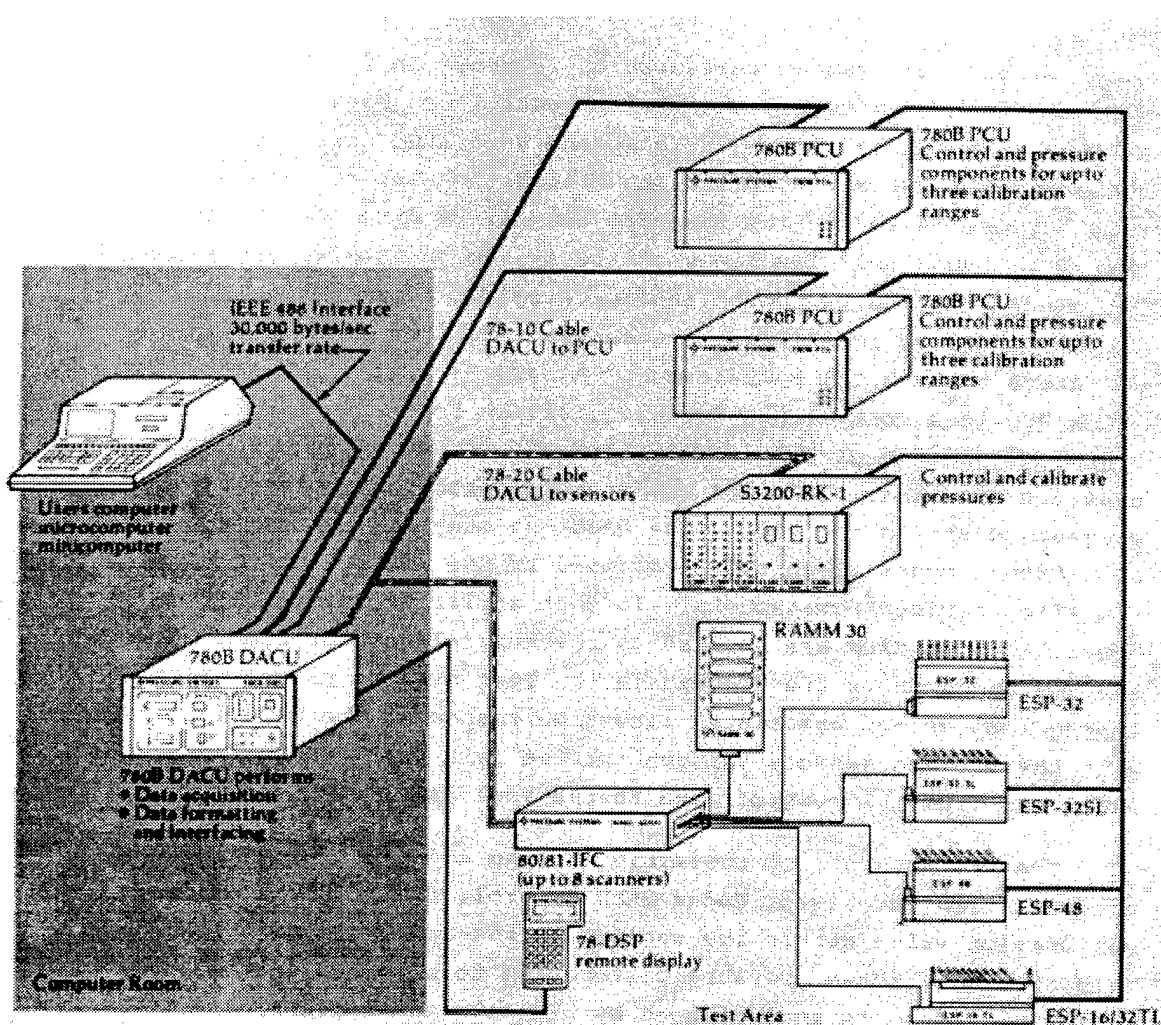
Figure 4.7 layout of the measurement system used in this experiment
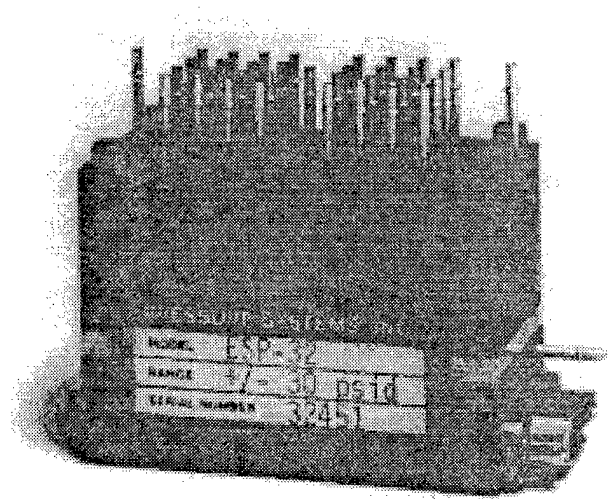
Figure 4.8 photo of ESP-32
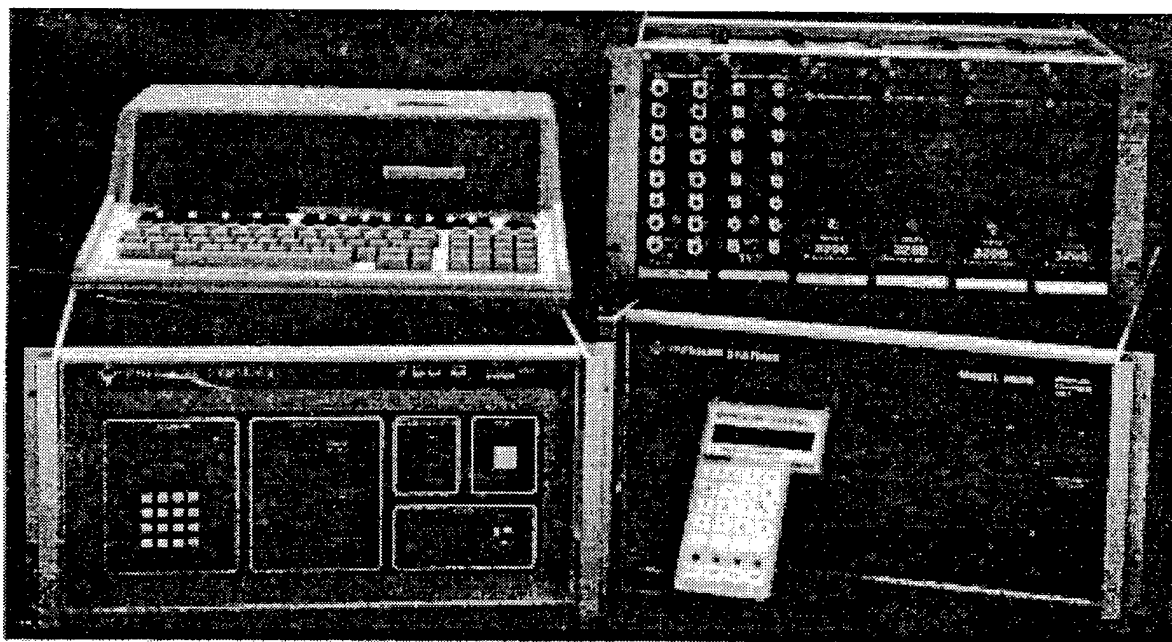
Figure 4.9 photo of instrument
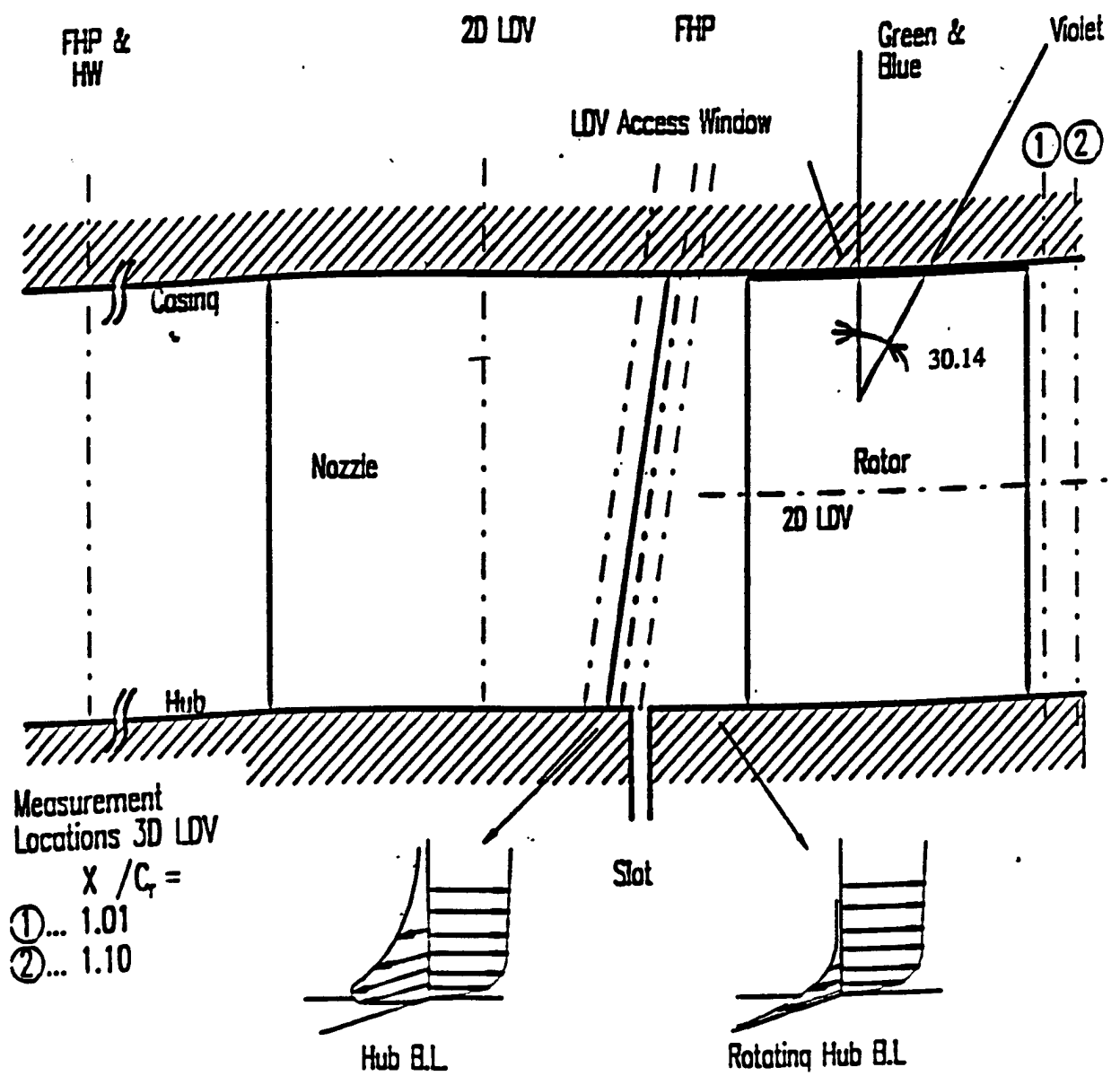
Figure 4.10   Schematic of the LDV system
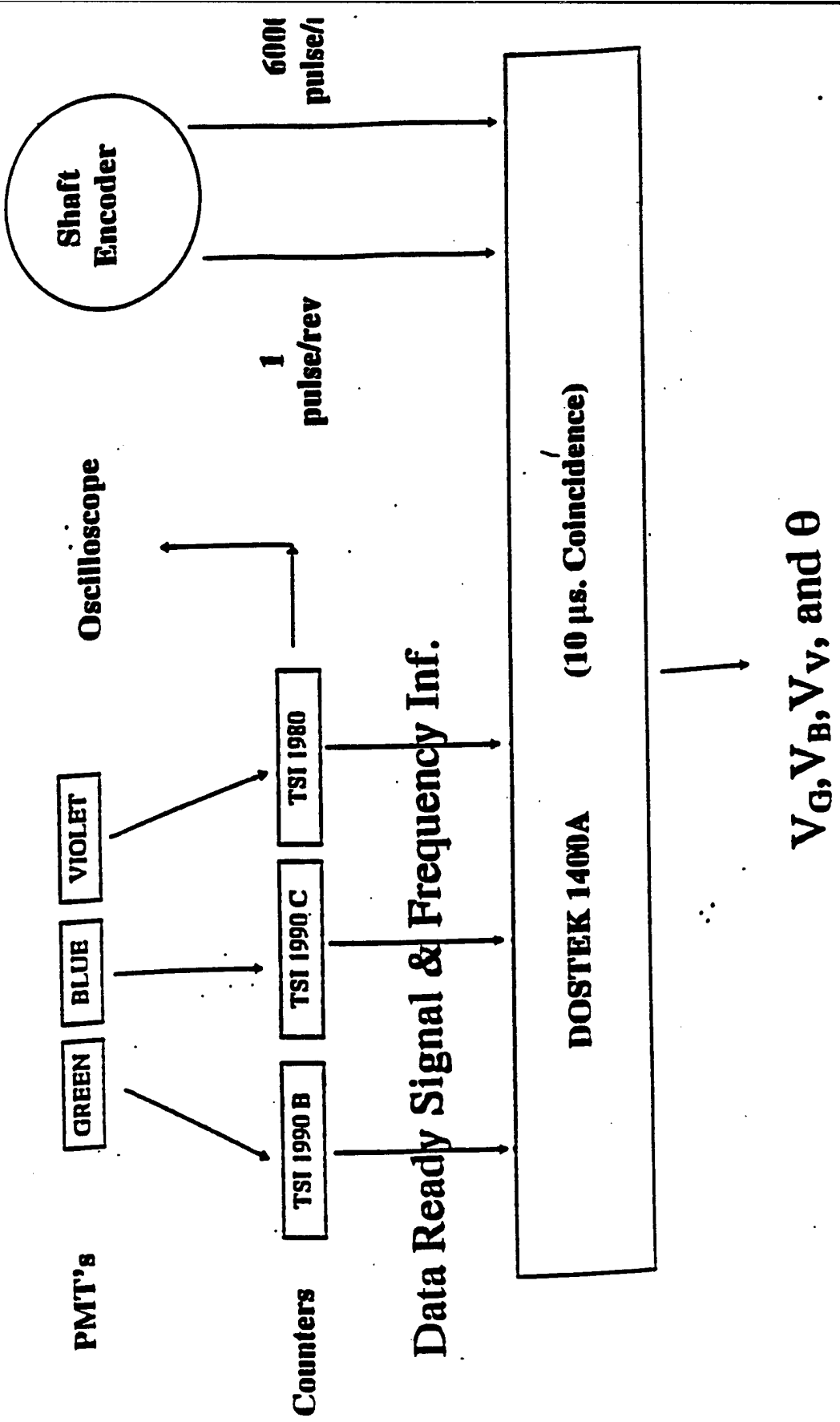
Figure 4.11   Schematic of the test section with locations of previous measurement

24

5. INVESITAGION OF STATIC PRESSURE ON BLADE SURFACES AND TRANSIENT PRESSURE ON CASING WALL

5.1 Static pressure distribution on blade surfaces and comparison with design and computation

The blade static pressure acquired experimentally is compared with the design data provided by the GE Aircraft Engine Company and predictions from the computational fluid dynamics (CFD) techniques (Chapter 8).

In the legends for the figure in this section, "pre" denotes pressure surface, "suc" denotes suction surface, "D" designates design data from GE Aircraft Engine Company, "E" denotes the experiment data obtained by us, and "C" designates the computational results. Percentage represents height from hub. For example, 90.3% in Fig. 5.1 represents the station where its height is 90.3% of the total height of the rotor. Other notations are defined in the nomenclature.
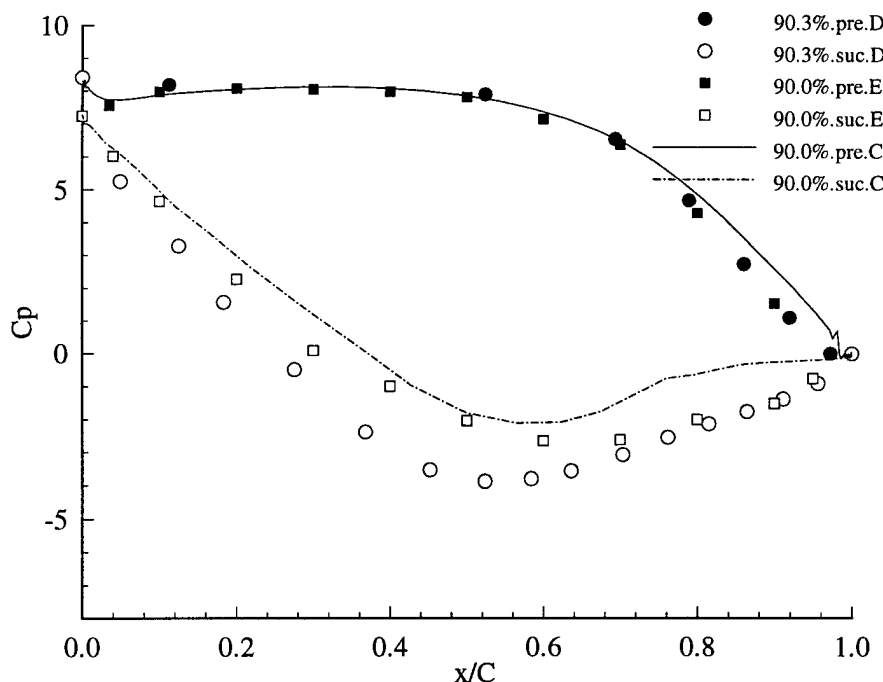
Figure 5.1. Experimental, design, and computational data comparison at 90% location from hub
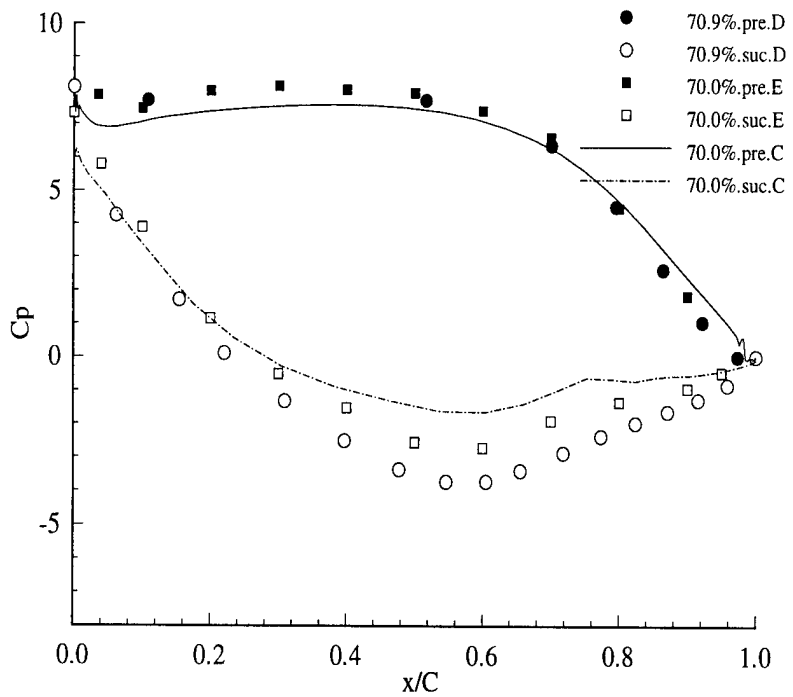
Figure 5.2. Experimental, design, and computational data comparison at 70% location from hub
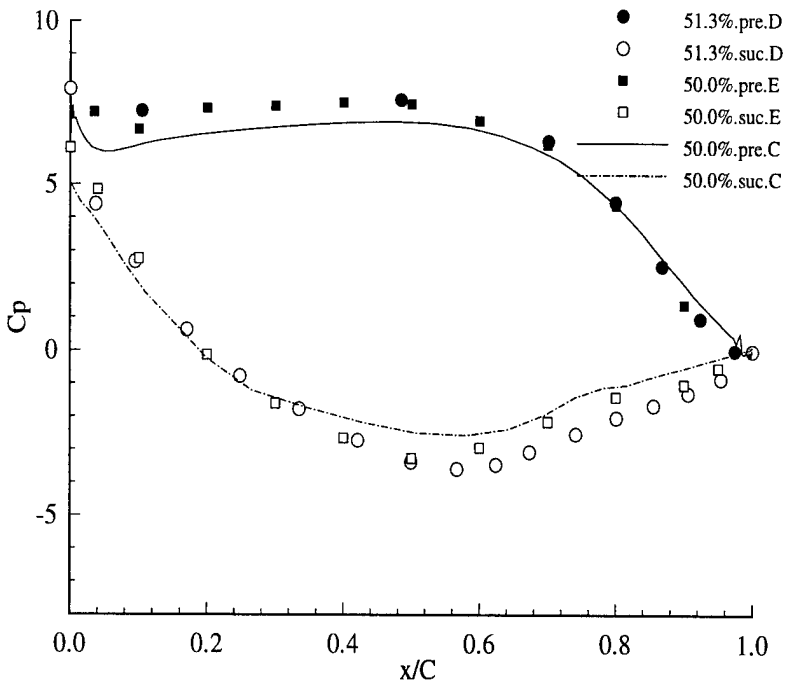
Figure 5.3 Experimental, design, and computational data comparison at 50% location from hub
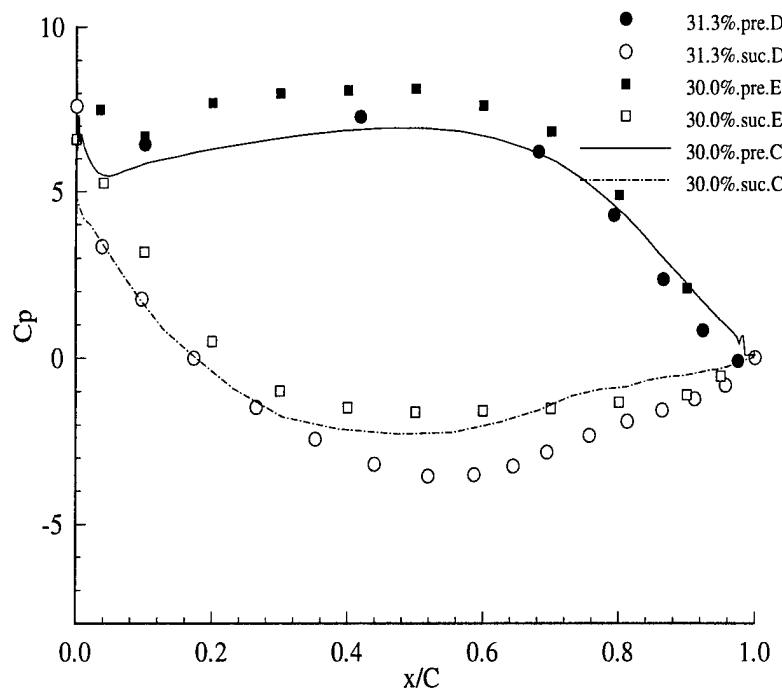
Figure 5.4 Experimental, design, and computational data comparison at 30% location
from hub
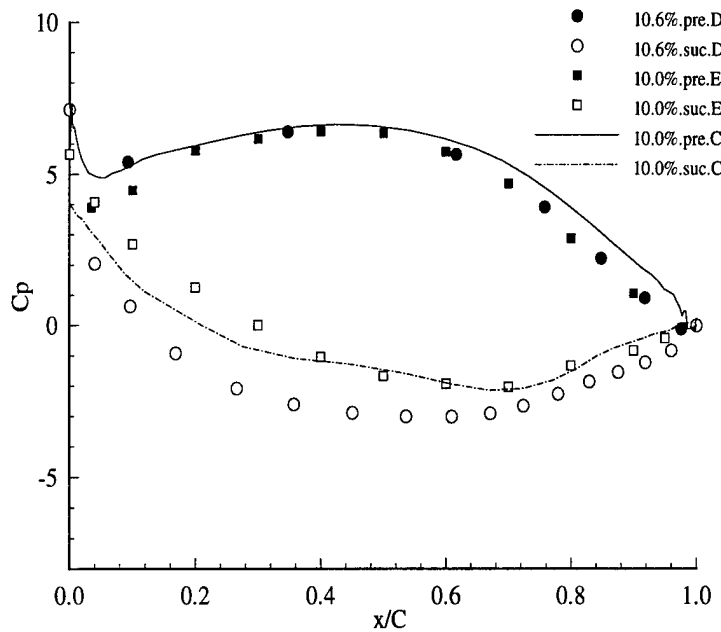
Figure 5.5 Experimental, design, and computational data comparison at 10% location
from hub

27

A comparison between the data, design, and computation away from the hub and endwall (10% to 90% span) are shown in Figs. 5.1 to 5.5. In the middle span, shown in Fig. 5.3, the data agrees very well with the design. The predictions agree well except near the trailing edge of the suction surface. The maximum discrepancy between the experiment and design occurs at 70% and 90% span; middle third of the chord on the suction surface. This is caused by the endwall and secondary flow, which results in underturning (overturning near the wall) of the flow. This accounts for lower loading on the blade. The computational results, which are closer to the experiment, confirm the source of discrepancy.

The secondary flow in the hub region is also strong (Ristic et al., 1997) and this accounts for the discrepancy between the design and experiment and lower loading distribution near the hub region. The predictions are in good agreement with the data.
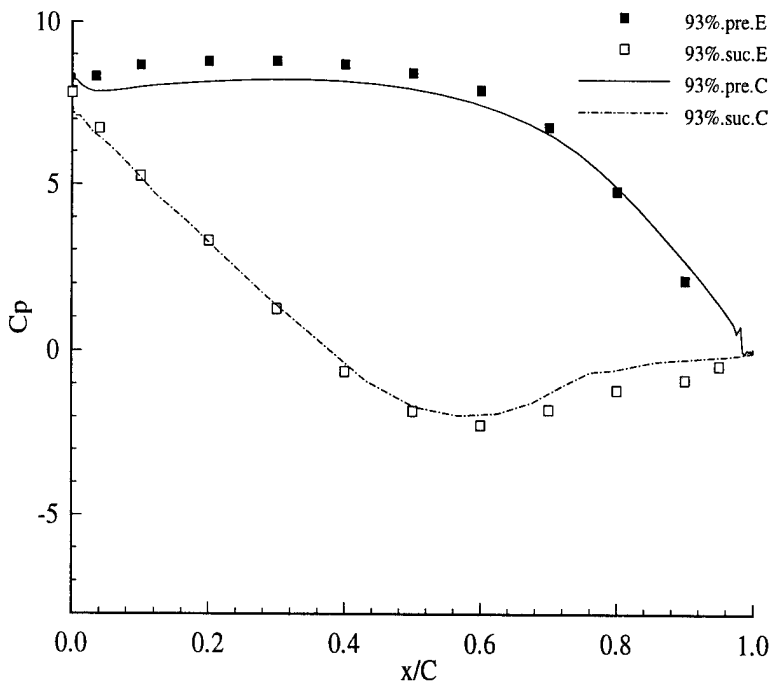
Figure 5.6 Experimental and computational data comparison at 93% location from hub
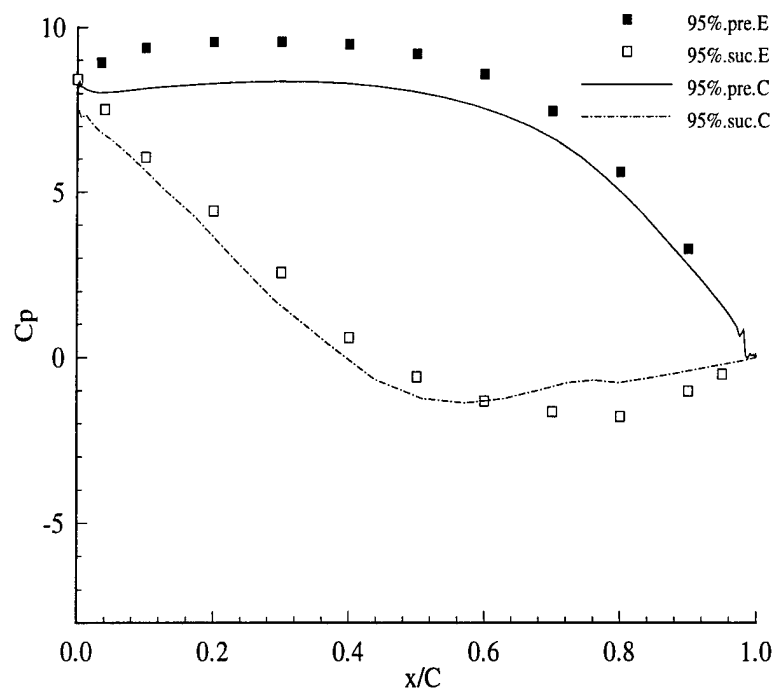
Figure 5.7 Experimental and computational data comparison at 95% location from hub
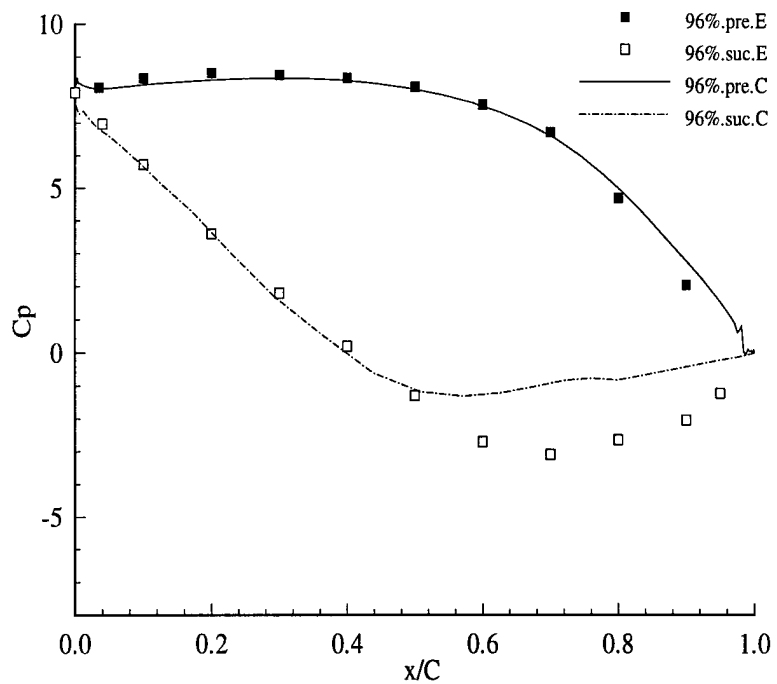
Figure 5.8 Experimental and computational data comparison at 96% location from hub

The data at 93% span (Fig. 5.6), 95% span (Fig. 5.7), and 96% span (Fig. 5.8) shows good agreement between the data and predictions except near the trailing edge on the suction surface. This is mainly caused by blade unloading due to tip clearance flow and pressure of the tip leakage vortex. The other possible causes are flow separation due to the interaction of the leakage flow, the secondary flow, and the blade surface boundary layer. The computational results is in excellent agreement at 93% span and slowly deteriorates as the tip is approached. This seems to indicate that the prediction of tip clearance has to be improved through finer grid and turbulence modeling.

The 96% span wise location shows an indication of tip clearance effects. All the cascade data indicate that the tip clearance effects are felt up to 90-95% span. The rotor data indicate that the influence of leakage flow is not as extensive as that observed in cascades.

The outer 4% of the span (98% to 100% span) is dominated by leakage flow. At 98% of span (Fig. 5.9), the pressure surface is not affected by leakage flow, but the suction surface undergoes a major change in the pressure distribution. The suction peak is located at 60% chord (compared to 50% in regions away from the tip) and the suction peak is substantially higher. This is caused by the presence of leakage vortex as it moves inward as the trailing edge is approached (Lakshminarayana, 1970). The leakage flow effects are mainly confined to the region beyond X/Cx=0.5. It is interesting to note that predictions are qualitatively similar, but the effects are under-predicted. The leakage vortex location is predicted accurately, but the predicted vortex is not as strong as the measured one.

The blade static pressure data at 99% span is very similar to those observed at 98%, except that the pressure surface also perceives major effects of tip leakage flow, resulting in reduced pressure. The suction surface has much lower pressures (compared to 98%) beyond X/Cx=0.4. The suction peak is almost at the same location.

The pressure on the tip of the blade (100% span, located on the blade surface inside the gap) shows a major influence on the leakage flow. The roles of the pressure and suction surfaces are reversed. Due to flow separation on the tip near the pressure surface, the pressures were lower than those observed near the suction surface. This is

mainly caused by the leakage flow. The maximum effect is again observed at 60% chord. The prediction has not captured this flow accurately; suggesting the need to improve the grid and other effects in this region.
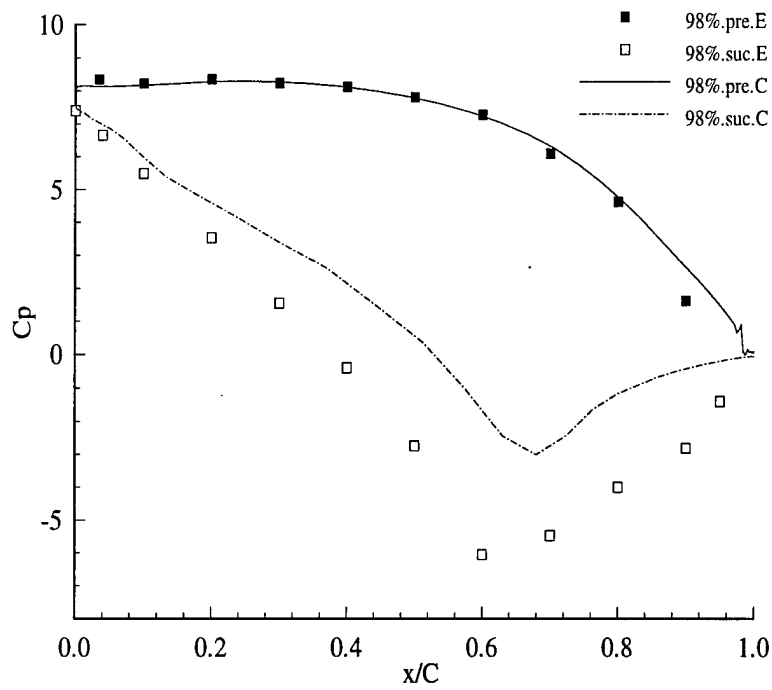
Figure 5.9 Experimental and computational data comparison at 98% location from hub
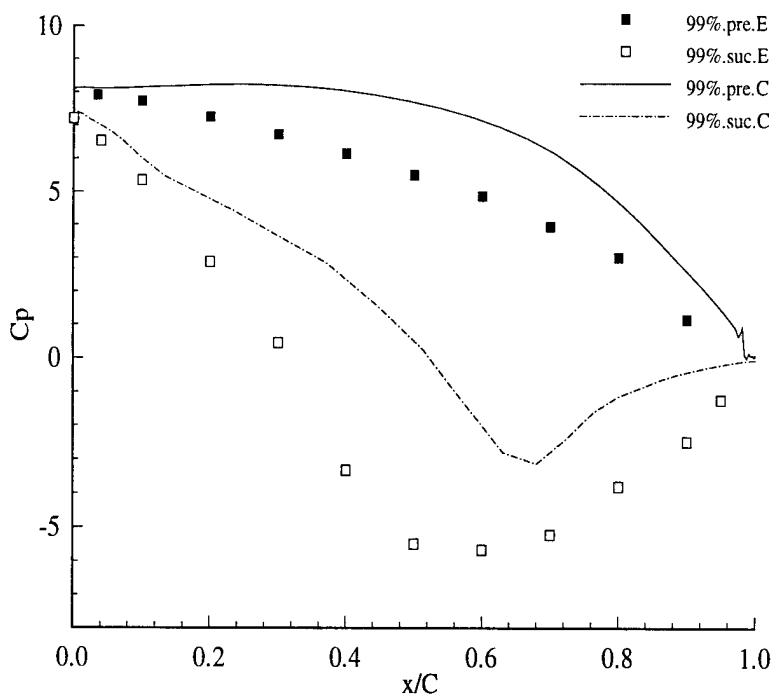
Figure 5.10 Experimental and computational data comparison at 99% location from hub
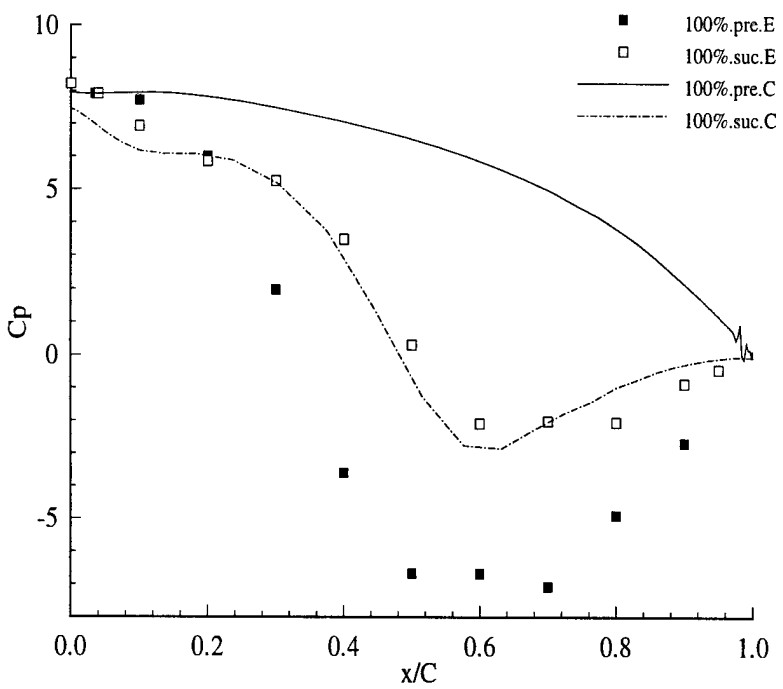
Figure 5.11 Experimental and computational data comparison at 100% location from hub

5.2 Blade surface off-design pressure distribution with RPM 1250, 1100 and 800

The blade static pressures at three off-design rotating speeds were also acquired. These three off-design rotating speeds are 1250, 1100 and 800, which correspond to 94.0%, 82.7%, and 60.2% of the design speed (1330 rpm), respectively. These blade distributions at off-design conditions are interpreted in this section.
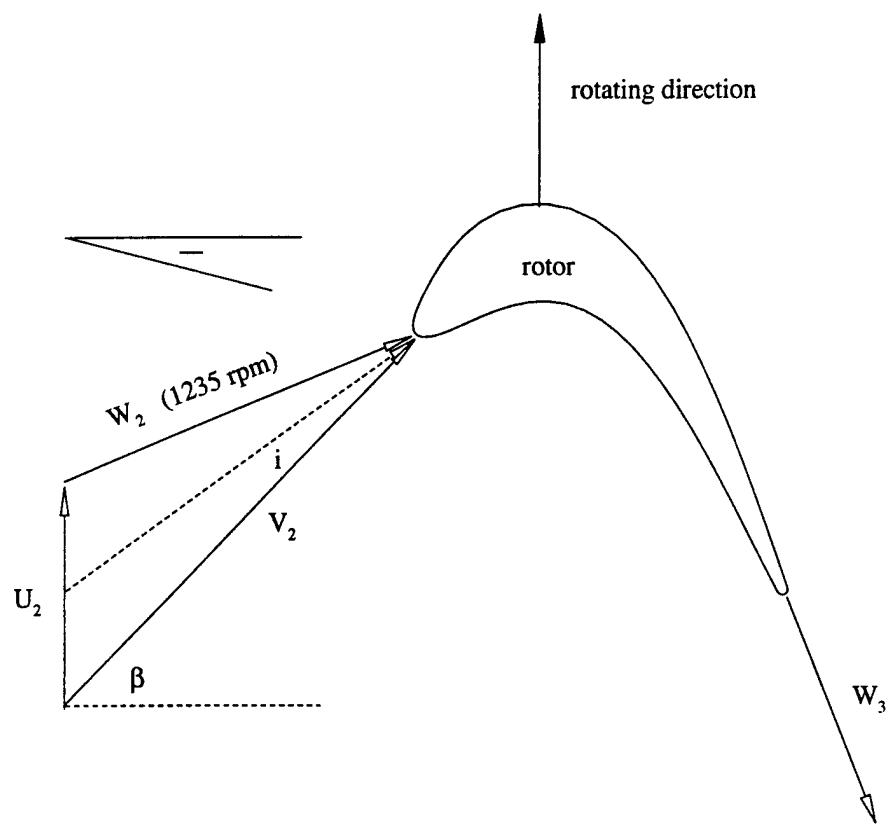
	1330 rpm	1235 rpm	1100 rpm	800 rpm
β (Degree)	41.0°	44.9°	-4.75°	+33.39°
i (Degree)	0.0°	+3.9°	-45.75°	-7.6°

Figure 5.12   Velocity triangles at different rotating speeds
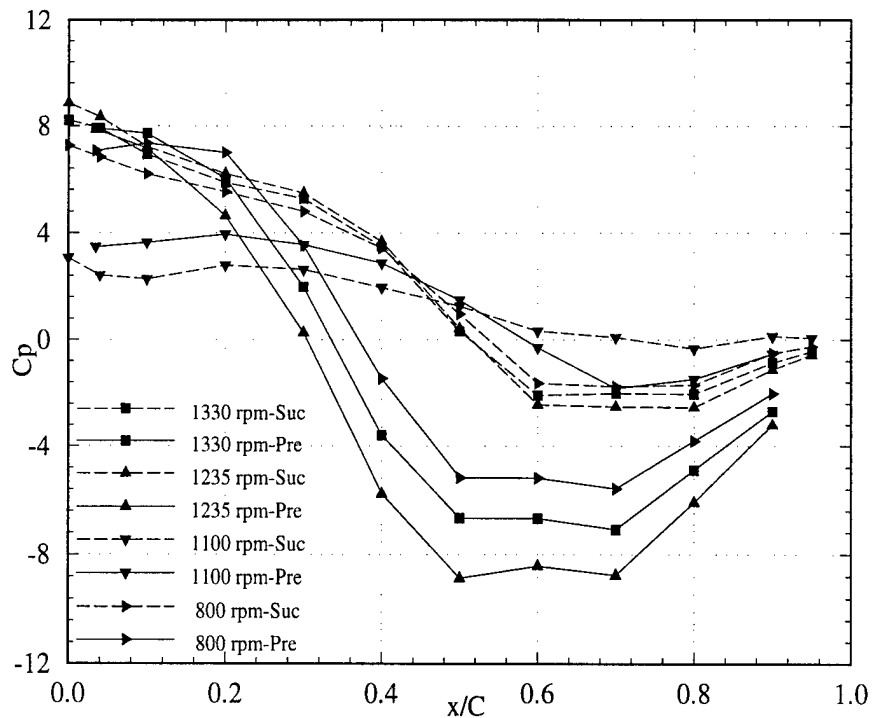
Figure 5.13. Pressure coefficient distribution at 100% location from hub at four speeds
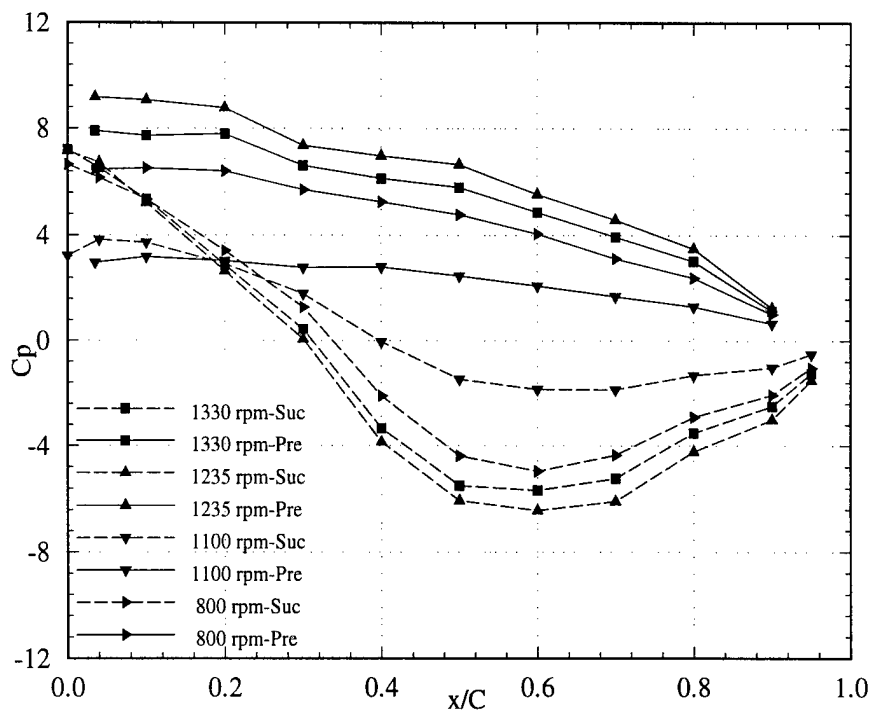
Figure 5.14. Pressure coefficient distribution at 99% location from hub at four speeds
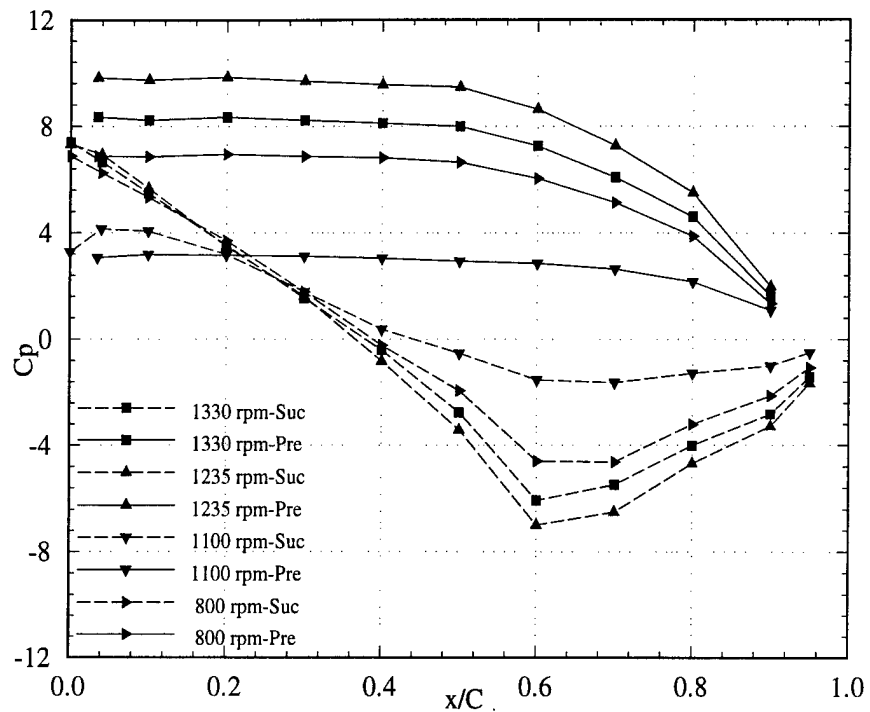
Figure 5.15 Pressure coefficient distribution at 98% location from hub at four speeds
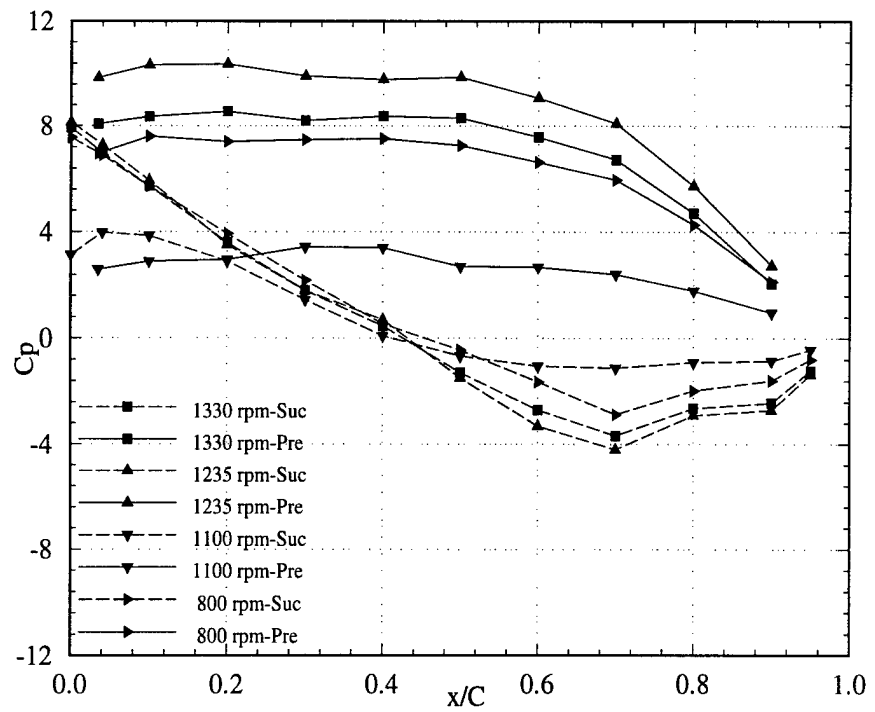
Figure 5.16 Pressure coefficient distribution at 96% location from hub at four speeds

35
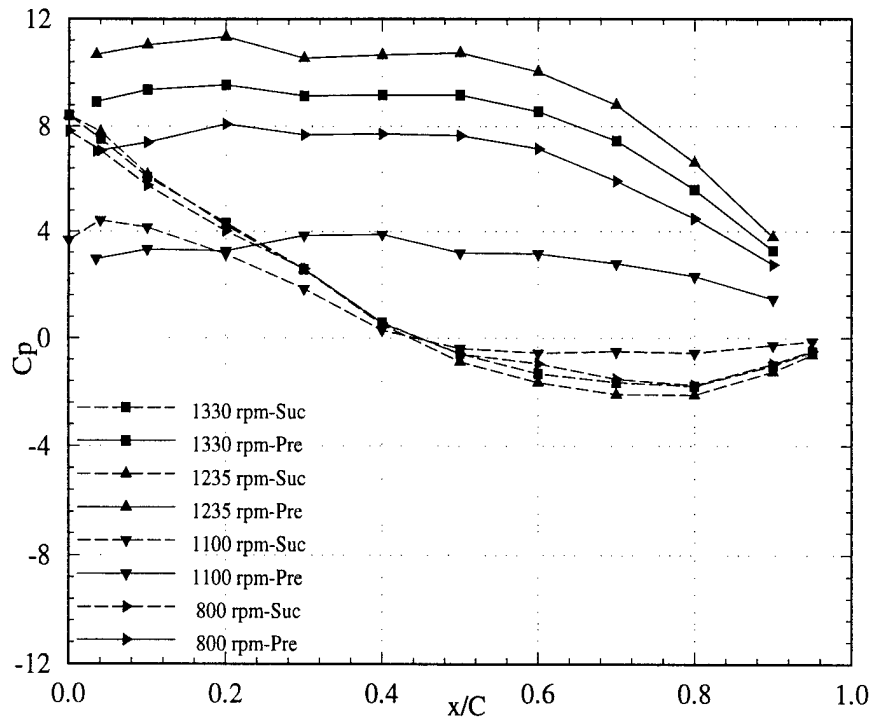
Figure 5.17 Pressure coefficient distribution at 95% location from hub at four speeds
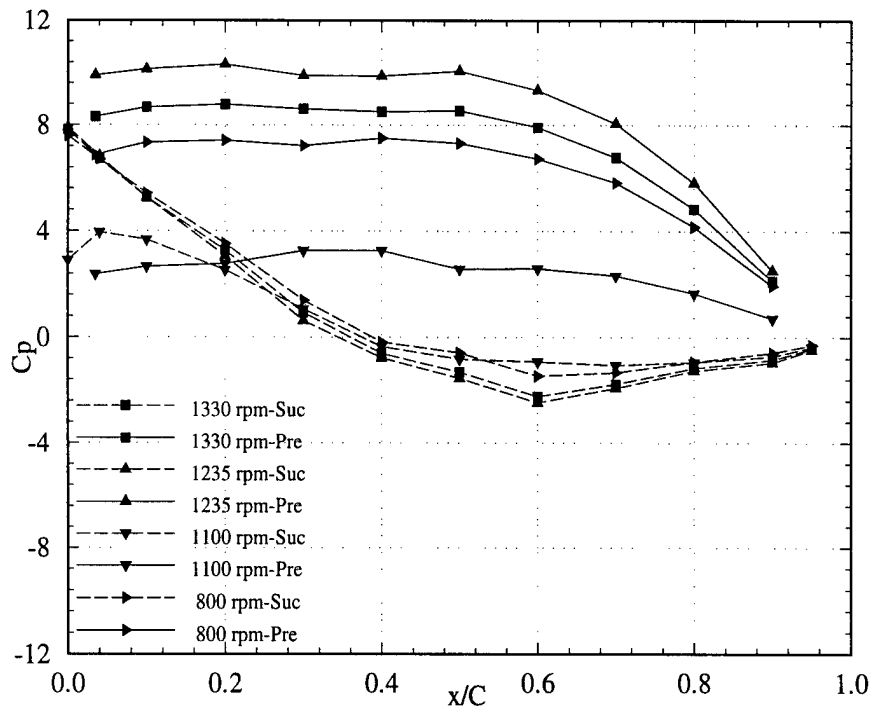
Figure 5.18 Pressure coefficient distribution at 93% location from hub at four speeds
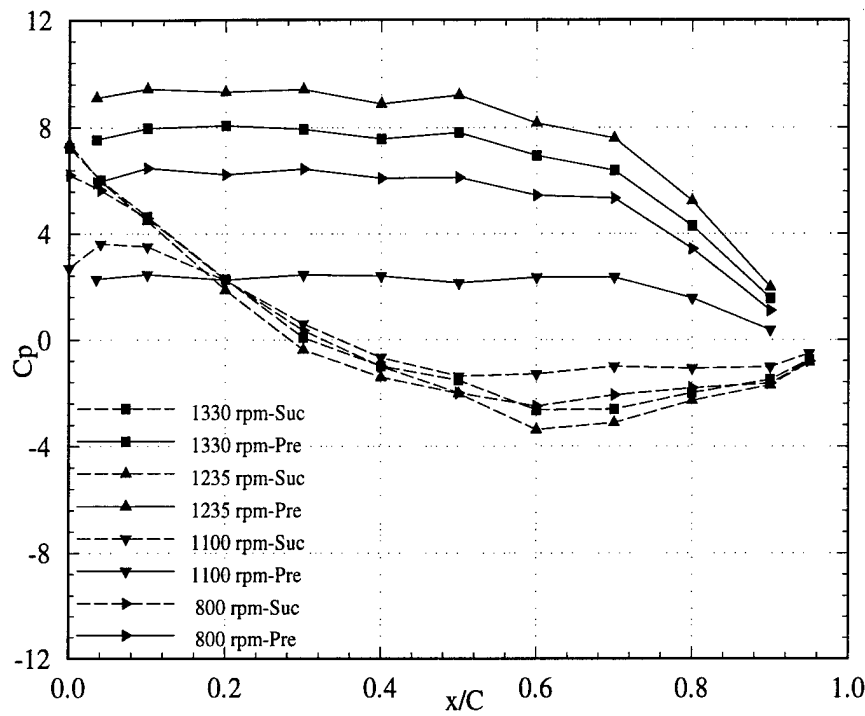
Figure 5.19 Pressure coefficient distribution at 90% location from hub at four speeds
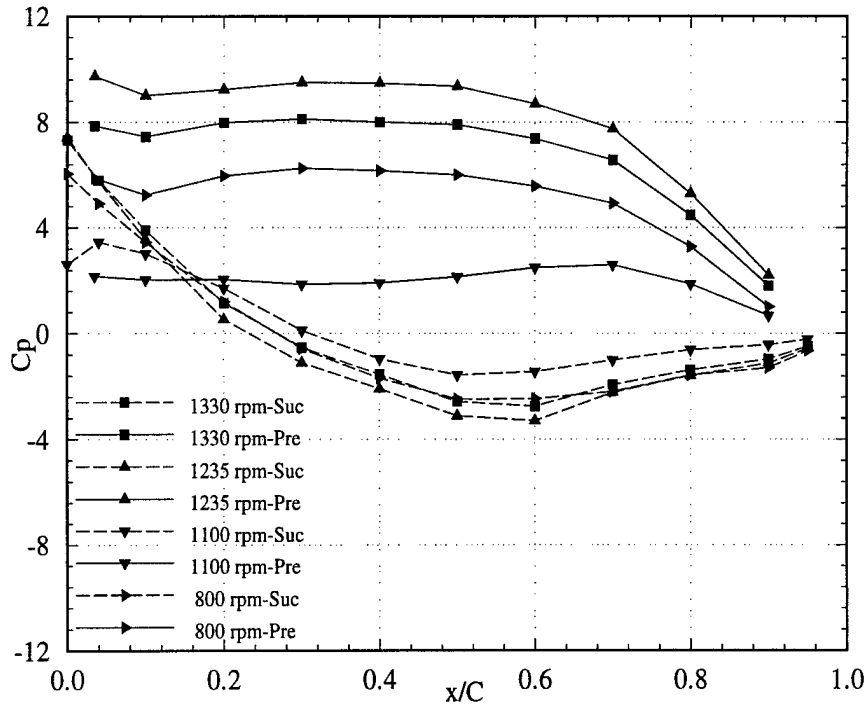
Figure 5.20 Pressure coefficient distribution at 70% location from hub at four speeds
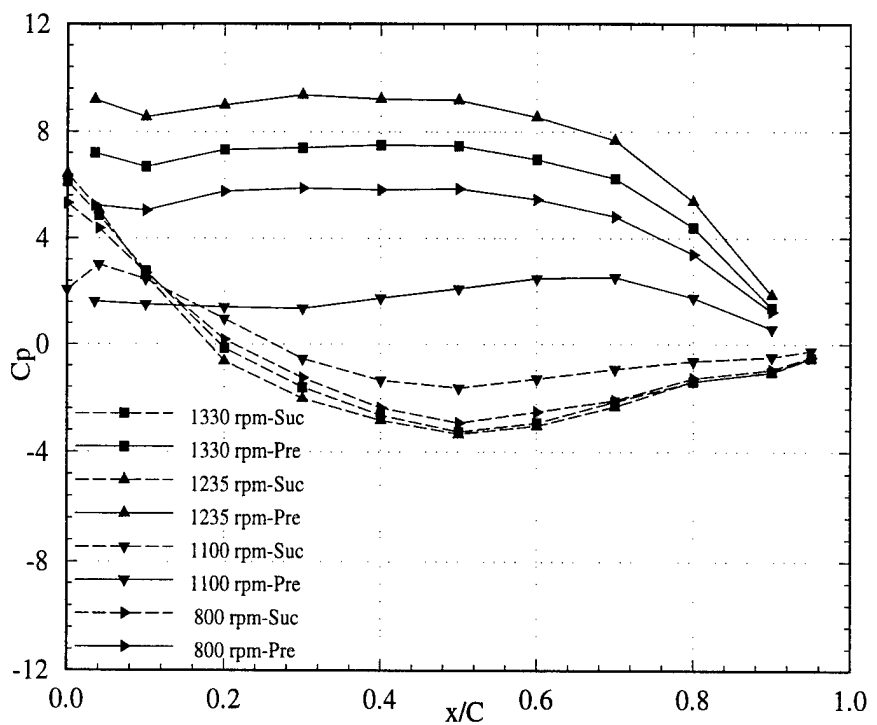
Figure 5.21 Pressure coefficient distribution at 50% location from hub at four speeds
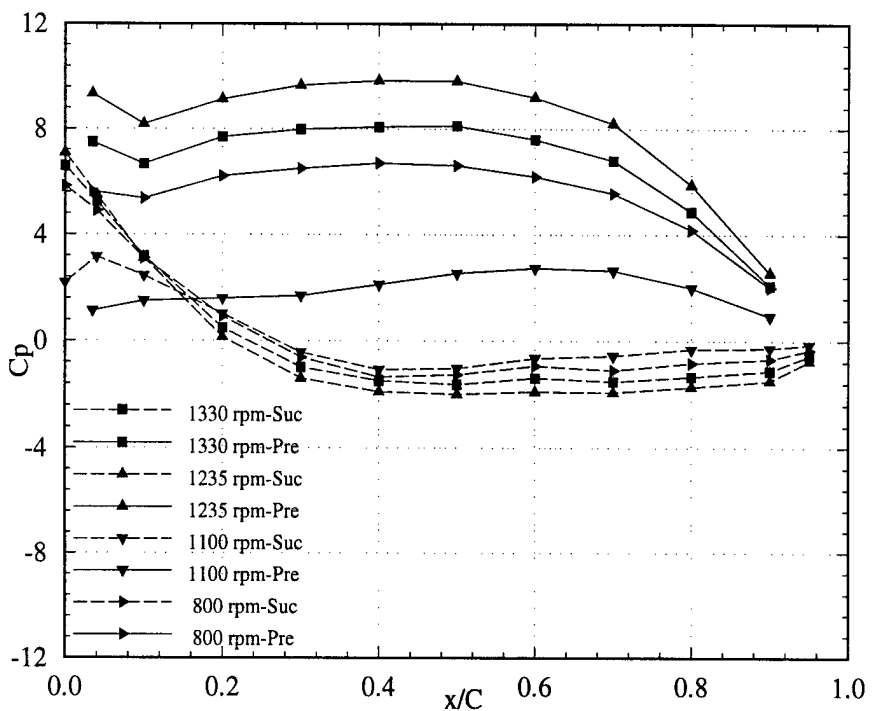
Figure 5.22 Pressure coefficient distribution at 30% location from hub at four speeds
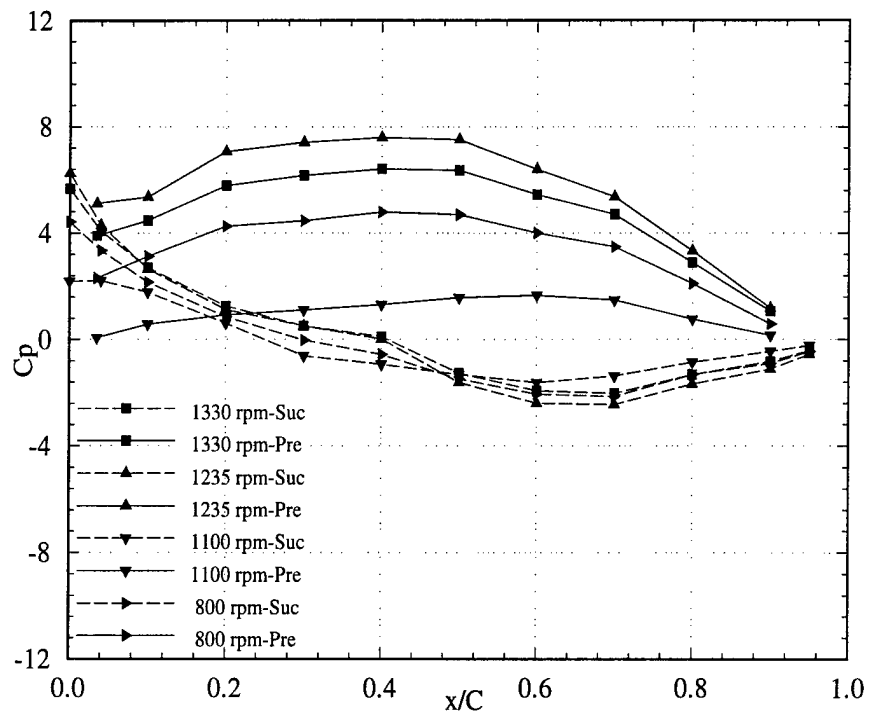
Figure 5.23 Pressure coefficient distribution at 10% location from hub at four speeds
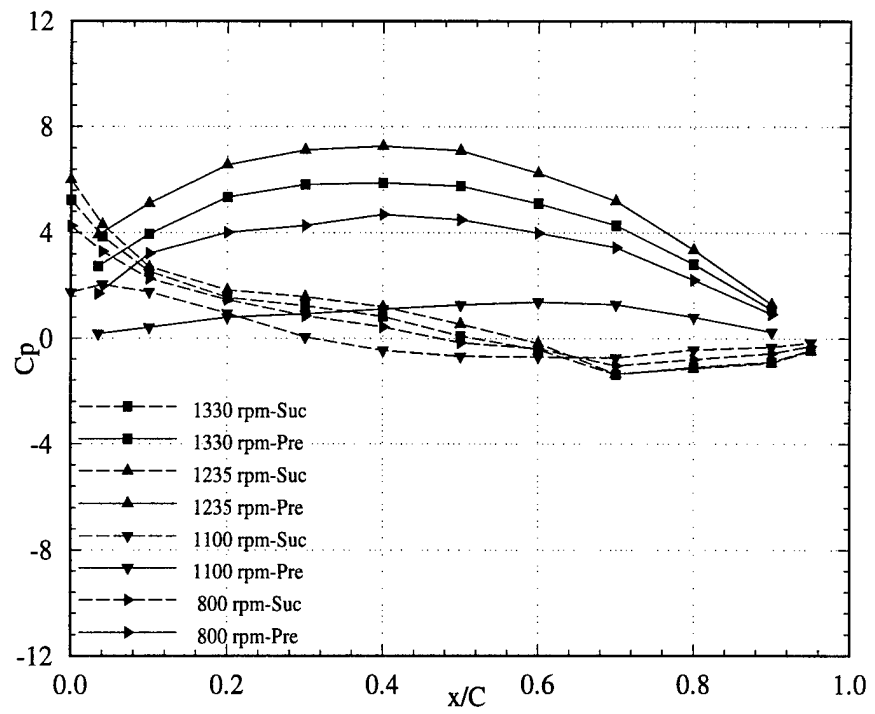
Figure 5.24 Pressure coefficient distribution at 5% location from hub at four speeds

The data at 100%, 99%, 98%, 96%, 95%, 93%, 90%, 50%, 70%, 30%, and 10% locations are shown in Figs. 5.13 – 5.24. respectively; and are compared with the design conditions. As indicated in Fig. 5.12, the speed 1235 represents higher incidence and the speed at 1130 represents lower incidence.

Consider the pressure distribution at 50% span (Fig. 5.21). The pressure on the suction surface is nearly identical for all speeds, except 1100 rpm, which is at a very high negative incidence. The blade pressure on the pressure surface undergoes dramatic changes. This is expected from the changes of incidence angle. The stagnation point moves toward the suction side at lower speeds (800, 1100 rpm). The plot shown in Fig. 5.12 represents only the incidence effect with highest loading at 1235 rpm and lowest loading at 1100 rpm. The data at 1100 rpm shows that the initial part of the blade (up to X/Cx=0.15) behaves like a compressor with several of the pressure and suction surfaces. Similar trends are observed at all locations up to 95% span.

Beyond 95% span, the leakage flow seems to substantially influence the pressure distribution on the suction side. For example, the blade pressure distribution at 1235 rpm shows the highest suction peak, followed by those at 1330, 800, and 1100 rpm. This is consistent with the loading distribution. Similar distribution is observed at 100% span (Fig. 5.13). It is interesting to note that the loading is lowest at 1100 rpm, and this results in nearly zero pressure difference across the tip

.

5.3 Hub surface static pressure distribution

To investigate the flow on the rotor hub surface, 52 static pressure taps were drilled at carefully selected locations shown in Fig. 5.25.
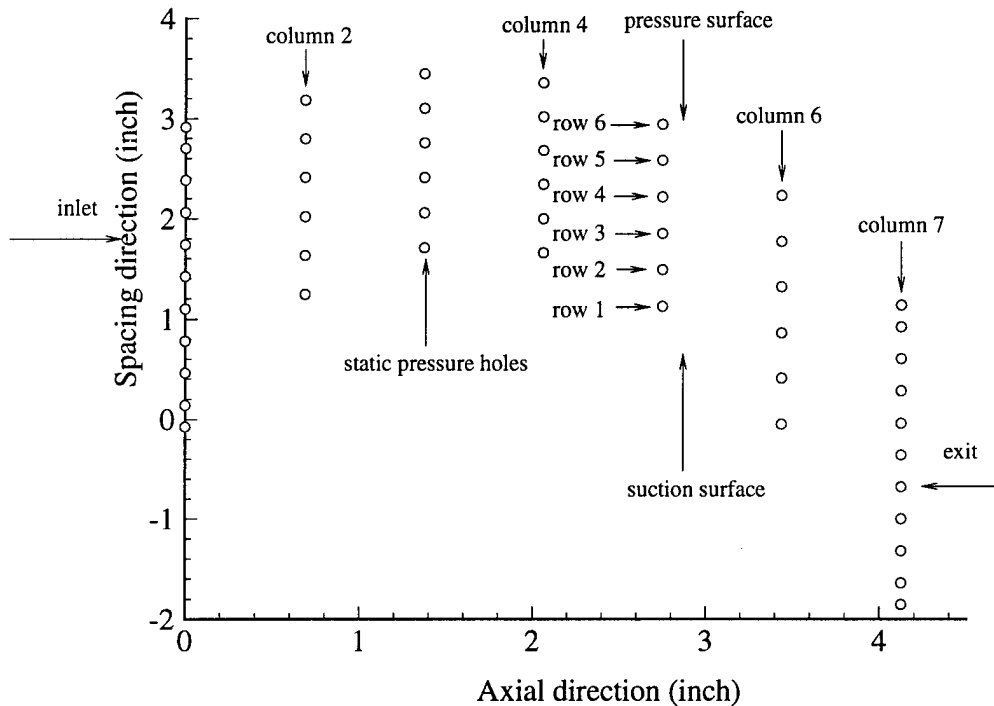
Figure 5.25 Hub surface static pressure taps distribution

All of these holes are distributed on seven columns. The first (inlet) and last (exit) columns consists of 11 holes, and the others consist of 6 holes. Pressure surface is located on the top of the holes, where row 6 is actually located in the corner between the hub surface and the pressure surface. For row 1, the location is similar; it lies in the corner between the hub surface and the suction surface of the rotor.

The seven columns are located equally spaced in the axial direction, and the distance between each of the two adjacent columns is one-sixth of the rotor axial chord. Except for the inlet and exit columns, 6 holes are also equally distributed along the tangential direction. The distance between each two adjacent holes is one-fifth of the local spacing. For the two columns at the inlet and the exit, 18 holes are equally spaced along the tangential direction.

All of the hub static pressure data is acquired at a corrected speed of 1300 rpm and an inlet atmospheric total pressure of about 0.988 bar. The pressure data is shown in Figs. 5.26 - 5.28.
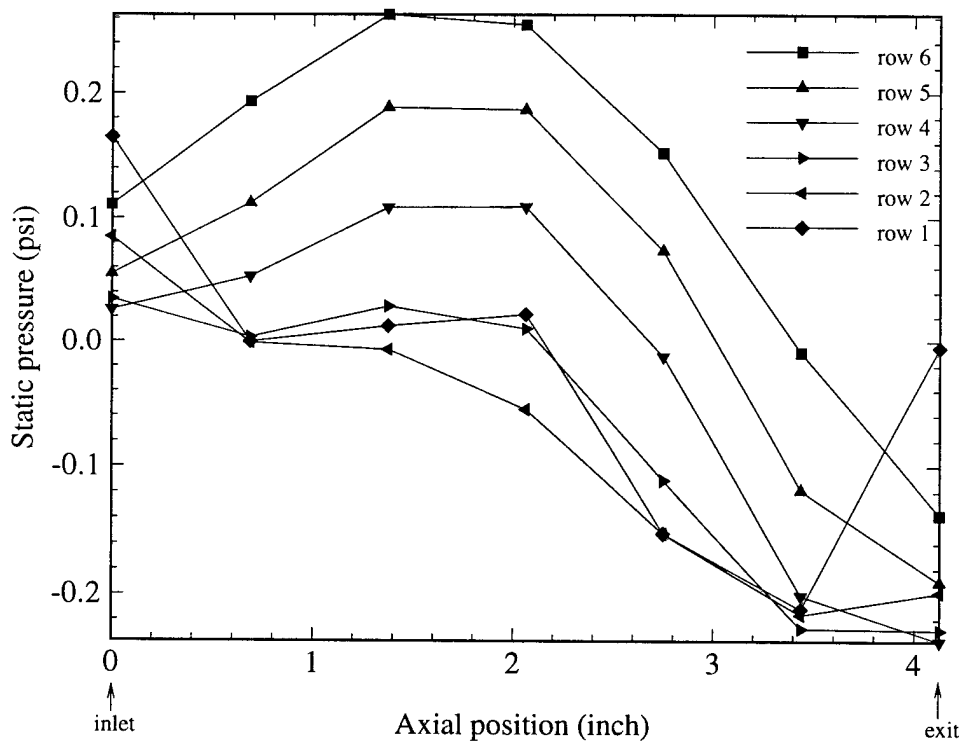
Figure 5.26 Static pressure distribution for each row

Data in Fig. 5.27 shows the expected static pressure increase from the suction surface (row 1) to the pressure surface (row 6) in most region on the hub. The pressure variation near the leading edge and the trailing edge regions show substantial variations. In column 1, relatively high static pressure is achieved in two locations close to the leading edge adjacent to the suction surface and the pressure surface. A similar variation is observed in column 7, which is located at the trailing edge.   The blade-to-blade variation in static pressure is shown in Fig. 5.26.
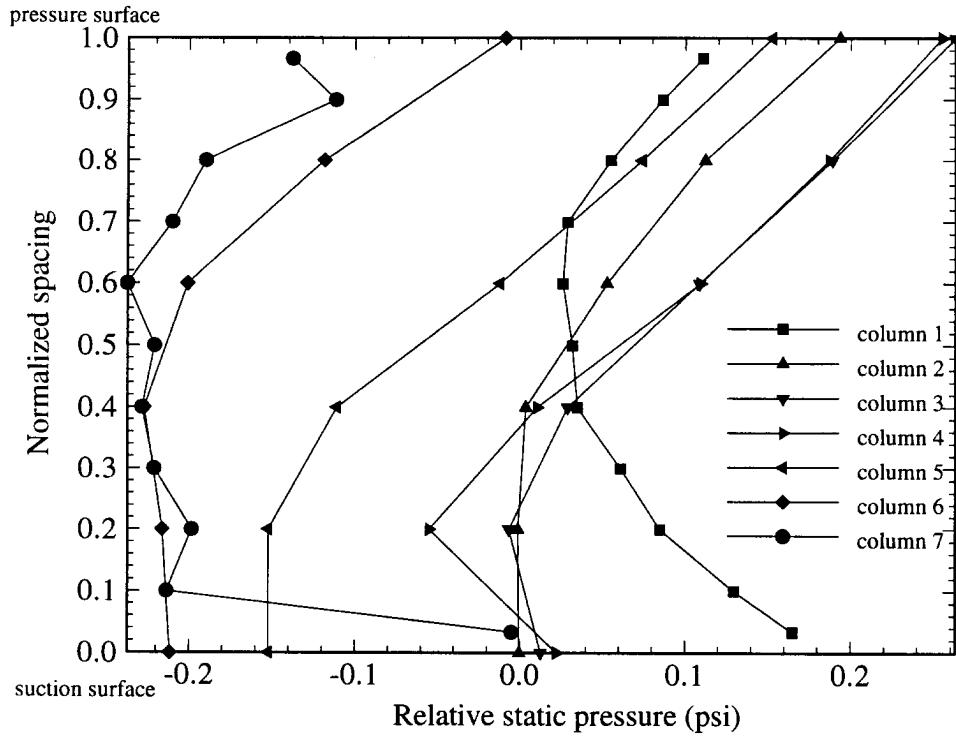
Figure 5.27 Static pressure distribution for each column

On the hub surface, leading edge is not the point with the highest pressure. The highest pressure is located on the point of the pressure surface where the largest flow direction variation occurs (Figure 5.28).

The flow is complex at the corner of the suction surface hub where the secondary flow dominates. This is also evident from contour plots shown in Fig. 5.28.
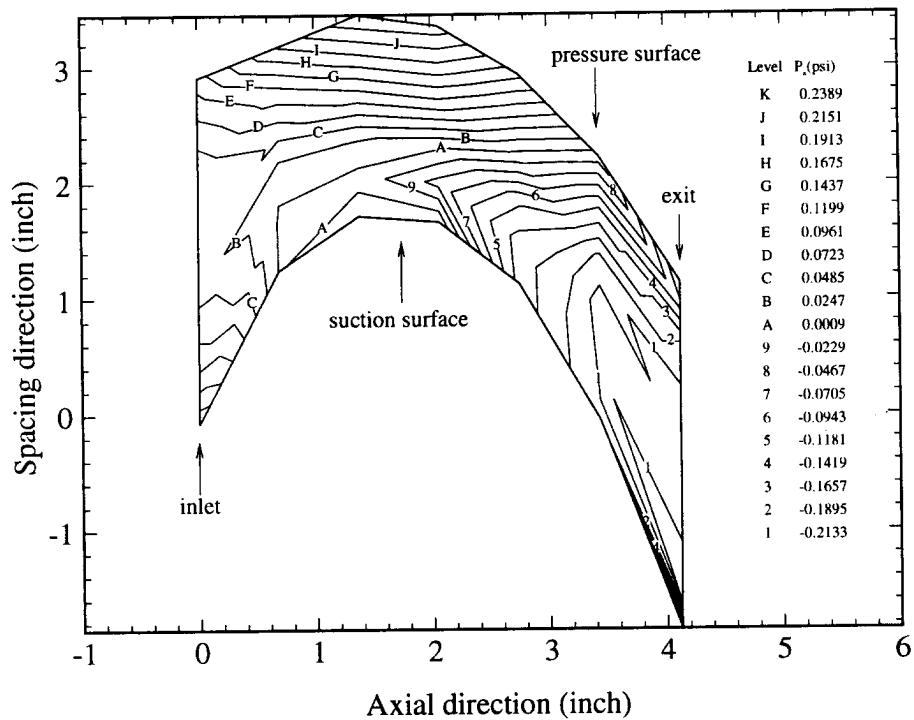
Figure 5.28 Static pressure contour for whole hub

The static pressure validation shown in Fig. 5.28 shows relatively smooth distribution near the pressure surface. The secondary flow/vortex region, marked A, clearly shows a low pressure region, which increases in size as it travels downstream. The region "B" is marked by corner flow separation, with nearly constant pressure. The LDV data at the exit shown in Lakshminarayana et al. (1995) clearly reveal the pressure of a strong secondary flow vortex and corner separation in the hub region at the exit.

5.4 Data acquisition and reduction method for the transient pressure

For the present configuration of the turbine rotor, the tip clearance gap height is only 0.75 mm or 1% of the blade height in the static case, and this height can decrease while the turbine rotor is running. It would be extremely difficult to access the flow field inside the gap. The static pressure distribution on the wall of the blade tip and the casing can provide valuable information on flow field inside the gap. The pressure distribution on the casing of the turbine rotor will be presented in this section. The casing pressure can provide valuable information on leakage velocity, vorticity, and pressure of the respective zone inside the gap.

At 1300 rpm, and 29 rotor blades, the dynamic probe on the casing senses 628 blade passages per second. The dynamic probe has a frequency of more than 50 kilohertz, so this probe has the ability to capture most of the pressure variation across the passage. The signal is amplified 100 times before it is fed into a microcomputer system. This microcomputer system couples with a DAS-50 data acquisition system, which can acquire 1024x1024 sample per second. The position for each sample is determined by using a shaft encoder as the clock for the DAS-50 data acquisition system. This shaft encoder is installed axially and it rotates synchronously with the turbine rotor passage. The shaft encoder can produce 6000 pulses per rotation to define very accurately the position for each data sample. This means the angle between each two neighboring sample points on the casing is 360/6000=0.06 degree, or the distance between these two neighboring points is 0.4582x2x3.14159/6000 = 0.48×10^{-3} meter or 0.48 millimeter. This distance is about 1/207 of the spacing of the turbine rotor. The shaft encoder can also generate a starting impulse for each rotation. This starting impulse is used as the trigger signal for the DAS-50 system to define the starting position. Hence the current instrumentation and data acquisition system has good accuracy to capture the flow physics of the gap flow. The calibration shows excellent linearity between the input pressure and the output electronic voltage of the Kulite instrumentation system. During experiment, the temperature is maintained at the calibration temperature.

A phase-locked ensemble averaging method is used to reduce to the data acquired. Because each raw data point includes both the voltage and the position, the

45

ensemble averaging can be performed for all of the raw data at same angular position. And the starting position of the data and the turbine rotor can be aligned to determine the absolute tangential position of each data point.

5.5 Transient pressure result interpretation and discussion

The blade periodic values of casing static pressure are shown in figure 5.29. The Cp values are ensemble-averaged. Figure 5.30 shows the Cp values at the corresponding locations to the blade edges compared with the blade surface pressure. Three low-pressure cores are obvious. The first one exists inside the tip gap. This is probably due to throat section. This throat section may be generated due to the sharp edge of the blade in the corner near pressure side. From the cascade data, a similar separation bubble and a throat section are concluded. We can also conclude that a separation bubble may exist on the blade tip surface in a turbine rotor.

The second low-pressure core is probably due to the vortex formed by the interaction between tip leakage flow and main stream. This tip leakage vortex is generated at 50% of the axial chord. The trace of the tip leakage vortex left one the casing shows that the core of the tip leakage vortex is at an angle with the blade surface and is nearly straight. This type of projection of the tip leakage vortex is also observed in both the turbine and compressor cascade situations. The effect of this tip leakage vortex is significant. Usually an adverse pressure gradient exists near blade surface on suction side of turbine, the boundary layer in this region is thick and viscous effect is strong. Since the tip leakage vortex also exists from about 50% of the chord until wake region, these two regions with high vorticity interact even more strongly and have stronger viscous dissipation and result in more energy loss than the sum of the losses generated by each separate region.

The third low-pressure core is probably due to the horse shoe vortex. The horse shoe vortex may be generated because of the interaction of the incoming casing boundary and blunt leading edge of the turbine blade. From the leading edge, this horse shoe vortex is divided into two legs. One lies in the suction side of the turbine blade, another lies in the pressure side of the turbine blade. The leg on the pressure side can not survive for a long path and disappears just after the leading edge. The leg on the suction side develops,

46

but it gradually reduces and disappears at nearly 50% of the chord due to the viscous diffusing effect. The effects of the horse shoe vortex could have less strong effect than that due to the tip leakage vortex.
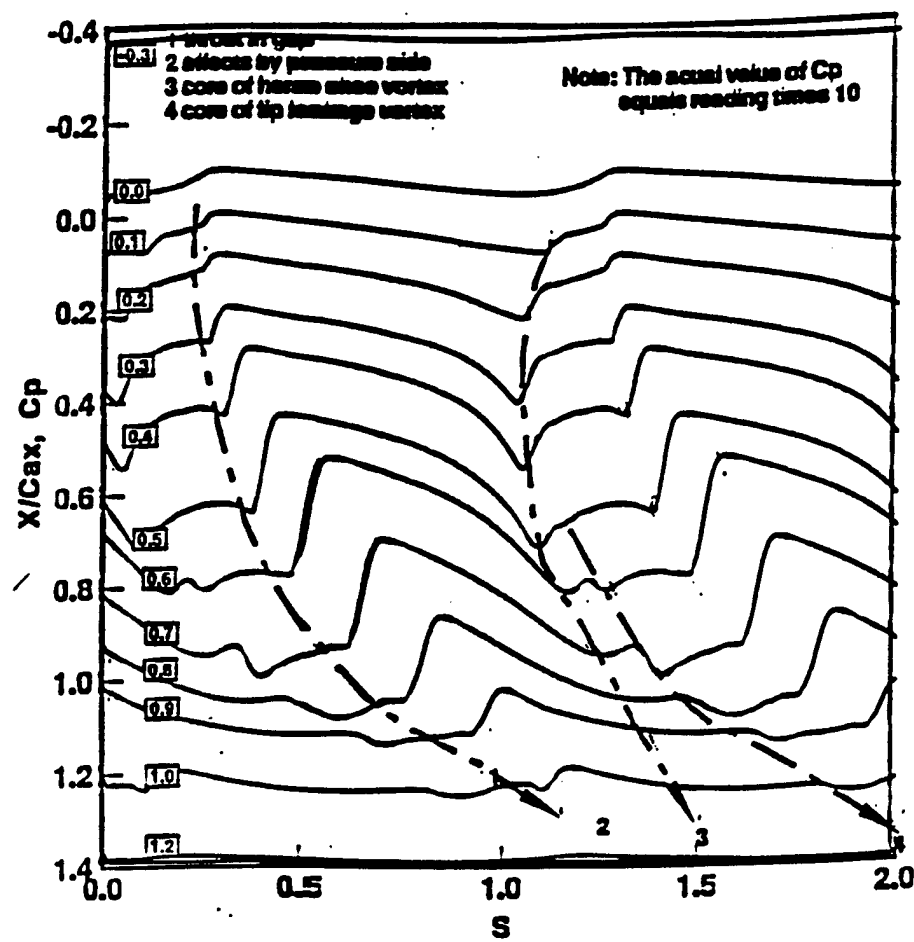
Figure 5.29 Static pressure distribution on casing wall
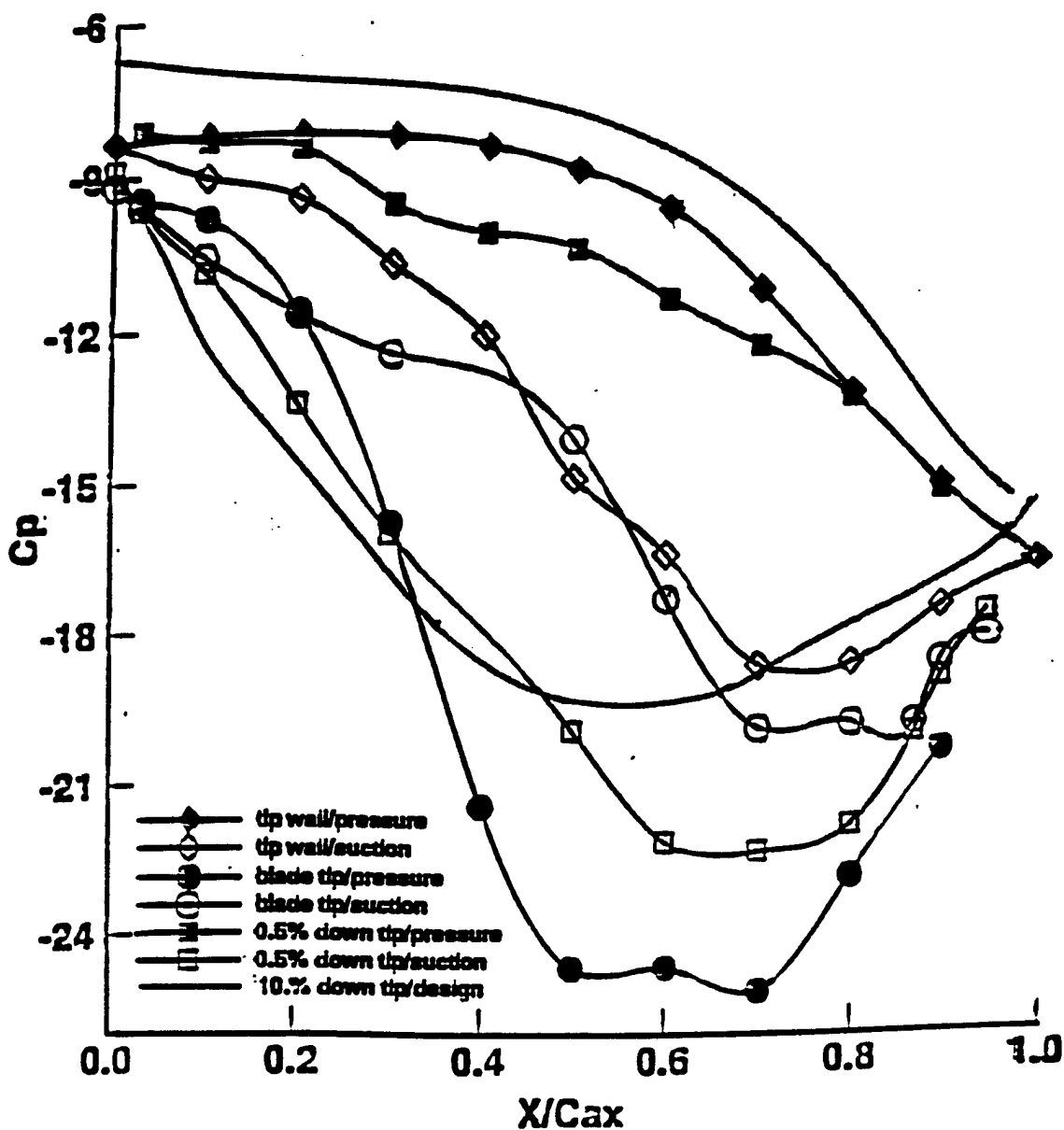
Figure 5.30   Comparison of static pressure on casing wall with that on blade surface

6. LDV DATA IN THE TIP REGION

6.1 Data acquisition and reduction procedure

The current LDV set-up, with the violet beam inclined at $30.14°$ from the perpendicular on the downstream side of the blue and green beams is arranged ideally to acquire data inside and downstream of the passage of the rotor for the least shadow effect from the blade. A PC-based interface (Dostek Model 1400A) records the data on three velocity components, along with the rotor orientation from the shaft encoder (6000 pulses per revolution for clocking and 1 pulse per revolution for triggering). In this configuration, each data sample consists of four data components: velocity by green beam V_G, velocity by blue beams V_B, velocity by violet beams V_V and the tangential position determined by the shaft encoder. After this, three velocity components of V_x, V_θ, V_r (cylinder coordinate system) are therefore calculated by equation (4.1). All measurements were acquired with the facility operating at the peak efficiency.

The data reduction is accomplished by ensemble averaging and then by passage-to-passage averaging the data according to the recorded tangential location. The entire rotor is discretized into 1450 bins (50 per blade passage) and the corresponding measurements are averaged over the individual bins to yield the ensemble average velocity. One of the main limitations of the LDV technique is apparent in the non-uniform distribution of measurements across the individual blade passages. A fairly low seeding density in the blade boundary layer, wake, end wall boundary layer, secondary flow, and tip leakage vortex regions require an enormous amount of samples to resolve the blade-to-blade variations accurately. To determine the minimum data number of data points per window required for a sufficient passage averaging, we examined the mean velocity and the turbulence intensity (the rms value of the instantaneous velocity minus the passage-averaged mean) at various stations with sample sizes from 50,000 to 200,000. The passage-averaged properties were computed and compared for a variety of individual bin measurements and found to be essentially constant for samples larger than 100 measurements per bin.

In addition, the actual number of data windows per blade passage, each representing a finite time interval, was varied to determine the optimal size. If within this time interval, there exists appreciable variation in velocity, especially in the wake region, artificial

fluctuations may influence the averaging procedure and result. The number of bins per blade passage was varied between 50 and 100 at a few selected stations with large velocity gradients and negligible variations were seen between the two temporal discretizations. A sample size of 50 was chosen to keep the overall data sample size manageable, while at the same time ensuring measurement accuracy.

The following data are presented, derived, and interpreted in this report.

1. Three components of mean velocities in cylindrical co-ordinate system (W_x, W_θ, W_r), and the total mean velocity (W_s).

2. Relative yaw angle and pitch angle of the flow (measured from the axial direction).

3. Three components of turbulence intensity and shear stresses cylindrical co-ordinate system ($T_{W_xW_x}$, $T_{W_\theta W_\theta}$, $T_{W_rW_r}$, $T_{W_xW_\theta}$, $T_{W_\theta W_r}$, $T_{W_rW_x}$). These turbulence intensity components are based on local total velocity W.

4. Secondary velocity vectors and axial vorticity. Any deviation from the design angle is the secondary flow represented by

$$W_{sec} = W_{measured} - W_{design} \qquad (6.1)$$

The mean velocities presented in this report are based on the "averaged passage" derived from averaging the ensemble averaged velocity across all the blade passages. This procedure is considered valid for the investigation of single-stage flow field of the Axial Flow Turbine Research Facility. To verify that the averaging procedure is valid, the procedure developed by Suder et al. (1987) to decompose the instantaneous velocity measurement in a multi-stage environment was used at a few selected measurement stations. The decomposition is based on the following:

$$V = \overline{V} + V_{BP} + V_{BA} + V_{RA} + v' \qquad (6.2)$$

where: is the time mean, V_{BP} is the blade periodic, V_{BA} is blade aperiodic, V_{RA} is the revolution aperiodic, and v' is the unresolved unsteadiness due to turbulence and revolution-to-revolution variations. The summation of V_{BP} and V_{BA} represents the revolution periodic (V_{RP}) component. The general procedure in the computation of the individual components involves computation of the time mean ($\overline{V}$) and the ensemble

50

average (V_e) over the entire turbine rotor. The revolution aperiodic (V_{RA}) component is computed as the average variation of the difference between the time mean and ensemble averaged velocity over the individual blade passage. For a single-stage facility the V_{RA} component is essentially zero. The revolution periodic (V_{RP}) component is computed by subtracting the V_{RA} component from V_e - $\overline{V}$ at each bin location. The V_{RP} component can now be decomposed into the blade periodic (V_{BP}) and blade aperiodic (V_{BA}) components. The blade periodic velocity is representative of the flow as seen by the "average" blade passage and the blade aperiodic component is a measure of the blade-to-blade passage variation. The blade aperiodic component is relatively small over most of the blade passage except in the wake region. The procedure is illustrated for typical data set in figure 6.1.

The flow field inside the rotor passage in tip clearance region is measured at various axial stations from 20% of the axial chord from leading edge to 101% near trailing edge. Figure 6.2 and 6.3 shows these locations in the blade to blade and hub-to-tip planes. The measurement locations are 20%, 30%, 40%, 50%, 60%, 70%, 80%, 80%, 90%, and 101% of the axial chord length, respectively. Eight radial stations are traversed at each axial location. A denser distribution near the tip clearance region is chosen to provide higher resolution in the tip leakage vortex region. The relative position for each station is tabulated below. (also figure 6.2).

Table 6.1. Measurement locations in the radial direction

No.	1	2	3	4	5	6	7	8
H	80.0%	84.6%	88.3%	91.3%	93.6%	95.5%	97.0%	98.3%

6.2 Flow field in the first half chord

Figures 6.4 to 6.48 show the blade-to-blade distribution of the flow properties at various axial and radial locations. These flow properties include relative total velocity (W), yaw angle (β), three relative component velocities (W_x, W_θ, W_r), turbulence intensities ($T_{W_xW_x}$, $T_{W_\theta W_\theta}, T_{W_rW_r}$), and turbulent shear stresses ($T_{W_xW_\theta}$, $T_{W_\theta W_r}$, $T_{W_xW_r}$) in cylindrical coordinate system. During the first half chord, the flow field is dominated by

invicid effects, and observed to be relatively uniform. The secondary flow, tip leakage flow, and other viscous phenomena have not fully developed and are not very strong yet to be observed.

The flow is observed to follow the blade profile very well near the blade surfaces. No separation or reverse flow occurs in the first half chord. However, the present research uses a high turning turbine blade (turning angle is 125.69° at hub and 95.42° at tip), and most of the turning is distributed in the first 20% of the axial chord. It is difficult for the flow to smoothly follow such a high turning blade. This may be the reason for the flow in the front 20% of the axial chord to be under-turned along most of the spacing from the pressure side to the suction side. Near the suction side, the under-turning is much stronger than that near the pressure side. This is probably due to the much higher turning on the suction side of the blade surface. Due to the tip wall boundary viscous effects, the under-turning near the tip wall is not as strong as that in the main stream. At X/Cx=20% for example, the flow at the radial station H=0.98 is less under-turned than the flow at H=0.80. The under-turning tends to increase away from the tip wall. Similar phenomenon is observed in the pressure distribution on the casing (figure 5.29). Under-turning is changed to over-turning near the central passage at X/Cx = 0.30, and then changed back to under-turning again at X/Cx=0.40 and 0.50. The highest-pressure region is located near X/Cx=30% on the pressure side for the current turbine. The flow tends to move toward the suction side by pressure gradient. This may be the reason for the over-turning of the flow angles at X/Cx=0.30. In general, the flow field in the first half chord is smooth, turbulence intensity is about 4 to 7%. No secondary flow or tip leakage vortex is clearly observed. The flow is mainly inviscid, except in the boundary layers near wall. Potential flow theory can probably give a good prediction for the flow field in this part. The boundary layer has not fully developed yet in the first half chord, its thickness is thin on both pressure and suction sides.

The turbulence intensities of the radial velocity component are relatively high from X/Cx=0.20 to 0.40. The upstream nozzle wake, nozzle rotor interaction, tip wall boundary, or radial mixing may be the reason. The gap between the nozzle and the rotor is only about 18.9% of the axial chord of the nozzle. This distance is too short for the nozzle wake to fully decay. There must exist a strong rotor-nozzle interaction by nozzle

wake. Since the presented flow field are near the tip wall (H=0.80 to 0.98), the casing wall boundary layer and the secondary flow from the upstream nozzle are also strong.

6.3 Flow field in the second half chord

Tip leakage flow is observed from the distribution of the total velocity, yaw angle, turbulence intensity, and shear stresses beyond X/Cx=0.60 (figures 6.4 to 6.48). Figures 6.49 to 6.52 show the passage-averaged total velocities, flow yaw angles, axial velocity components, and tangential velocity components at every axial location in the second half chord. The contour plot for the axial velocity is shown by figure 6.53. The flow field is divided into two different regions. One is the inviscid main stream core with high velocity, the other is the viscous region near blade surface which is affected by the tip vortex. The velocity in this viscous region is relatively low. The mean value of W_x decreases beyond the mid-chord because the passage expands from the mid-chord to the trailing edge. As the size of the tip leakage vortex grows, the main stream core region becomes smaller and tends to locate toward the pressure side. A sharp displacement of the main stream core region is observed from 80% to 90%. This displacement is related to the boundary layer development on the suction side. A region with low velocity near the corner between the suction side and the casing is observed at all axial locations from 60% to 100% of the axial chord. This low velocity distribution suggests the presence of a tip leakage vortex. The velocity inside the center of the tip leakage vortex is relatively low, a part of the translation energy is converted into rotating energy of the vortex due to the formation of the tip leakage vortex. The inception location of the tip leakage vortex is about 60% of the axial chord.

The vortex is small and attached to the surface on the suction side at 60% of the axial chord, but its size increases rapidly beyond 90% chord. The last station investigated is 101% chord. The largest pressure difference across the blade tip is observed between 60% to 80% of the axial chord from the pressure distribution investigation (Lakshminarayana and Xiao, 1998). Therefore the strongest tip leakage flow should occur near 60% to 80% too. The pressure difference across the blade tip decreases rapidly beyond 80% of the chord. There are at least two reasons for this phenomenon. One is due to the thickness of turbine blade. Turbine rotors usually have thick blade. Although the

biggest pressure difference exists from 60% to 80%, the leakage flow starting from the pressure side at 60% chord may reach further down stream at 80% of the chord on the suction side. The leakage flow originally at 80% chord on the pressure side may reach at 90% chord or further location on the suction side. Another reason is probably due to the interaction between the tip leakage vortex and the boundary layer on the suction side. This interaction is probably very strong. The tip leakage vortex entrains portions of the boundary layer fluid. Since a locally adverse pressure gradient exists beyond 80% chord on the suction side, the boundary layer thickness increases sharply. This sharp increase of the boundary layer thickness pushes away the main stream core and the tip vortex. At the same time, the tip vortex entrains much more fluid hence develops very rapidly.

The development of the axial component of the vorticity is shown in figure 6.54. The diffusion of the tip leakage vortex becomes very fast beyond 80% of the axial chord. Strong interaction between the tip leakage vortex and the boundary layer probably accounts for this diffusion. Another opposing vortex is observed beyond 80% chord. This is probably the passage vortex. The tip leakage vortex and the passage vortex strongly interact with each other. The development of the passage vortex is probably the third reason for pushing the tip leakage vortex away from the suction side. The interaction between the passage vortex and the boundary layer can not be discerned in the plot, the hot film investigation will complete this investigation.
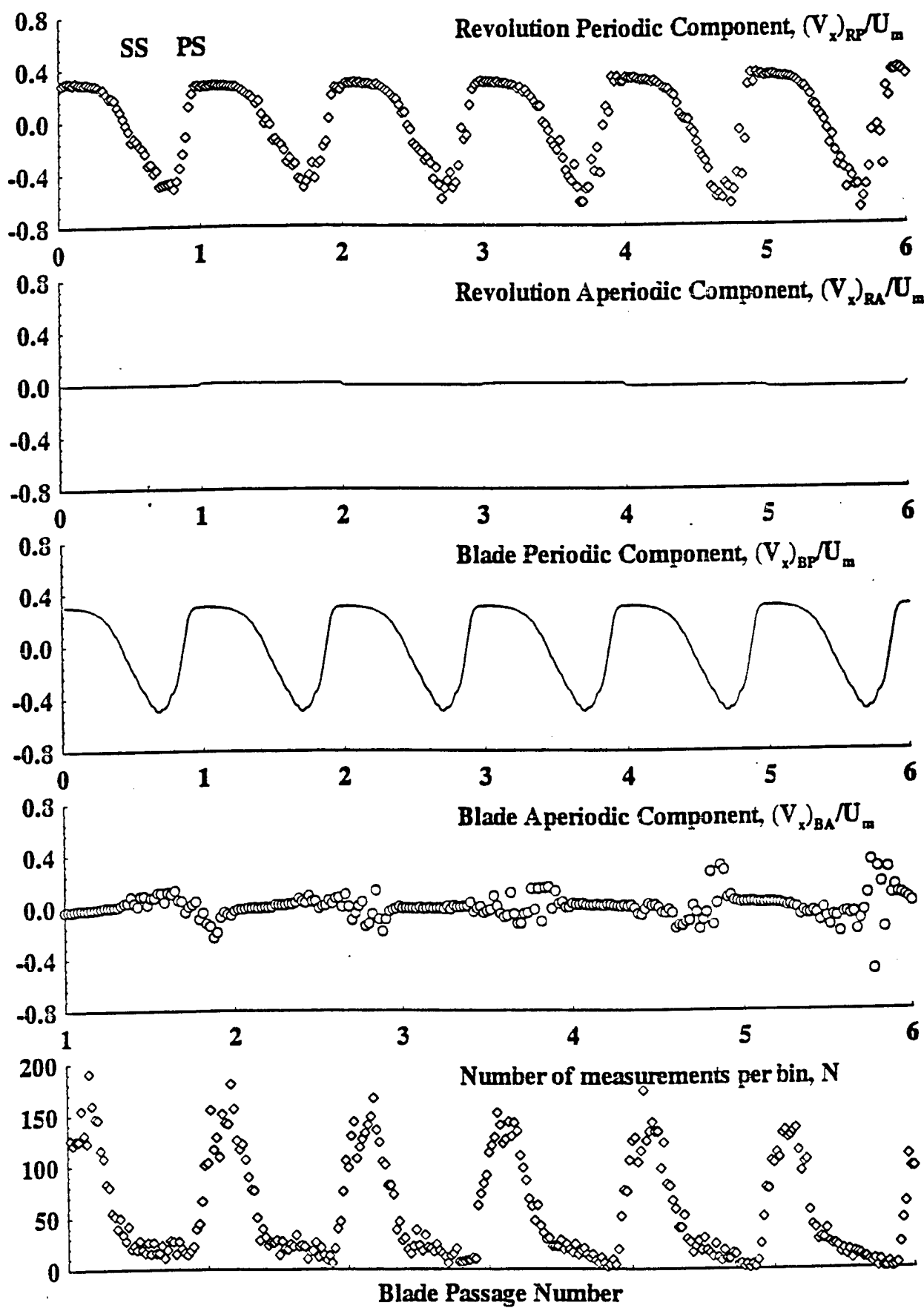
Figure 6.1 The blade periodic, blade aperiodic, revolution periodic, and revolution aperiodic components at the $x/c_r=1.01$ (1% chord from trailing edge) and H=0.93 position.

20%

BLADE 1   BLADE 2   BLADE 3

101%

Y
Z
x: rot
y: r
z: a
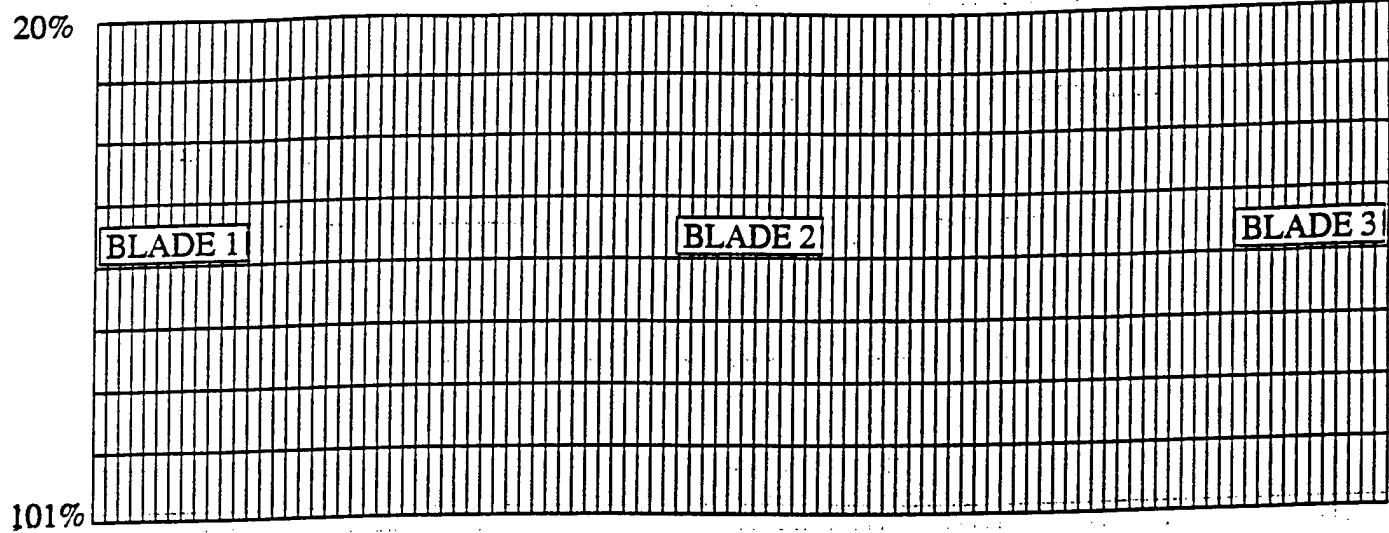
Distribution of locations in axial direction (-Z axis direction) are
20%, 30%, 40%, 50%, 60%, 70%, 80%, 90%, 101% of axial chord
in the tip of rotor from leading edge

Y
Z

Front View from axial direction

99.2%

80.0%
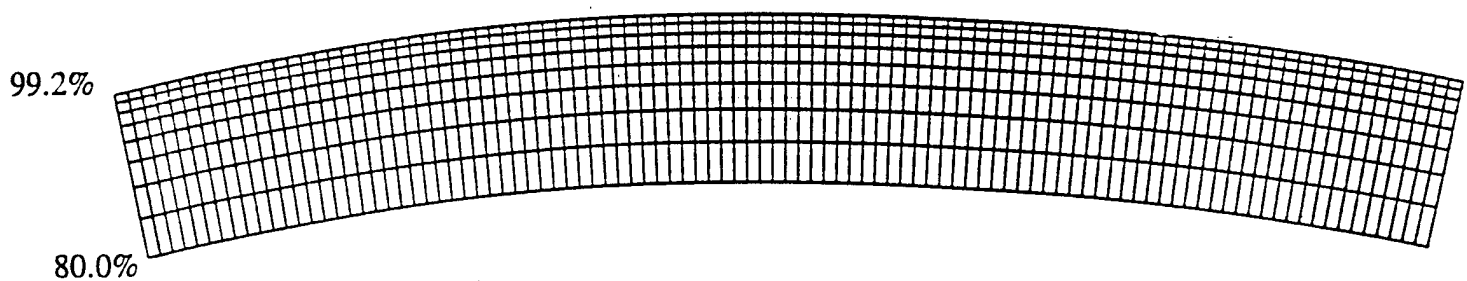
Distribution of locations in tangential direction (X axis direction) are
80.0%, 84.6%, 88.3%, 91.3%, 93.6%, 95.5%, 97.0%, 98.3%, 99.2% of
the height of blade starting from hub

Figure6.2Grid for three dimensional LDV measurement
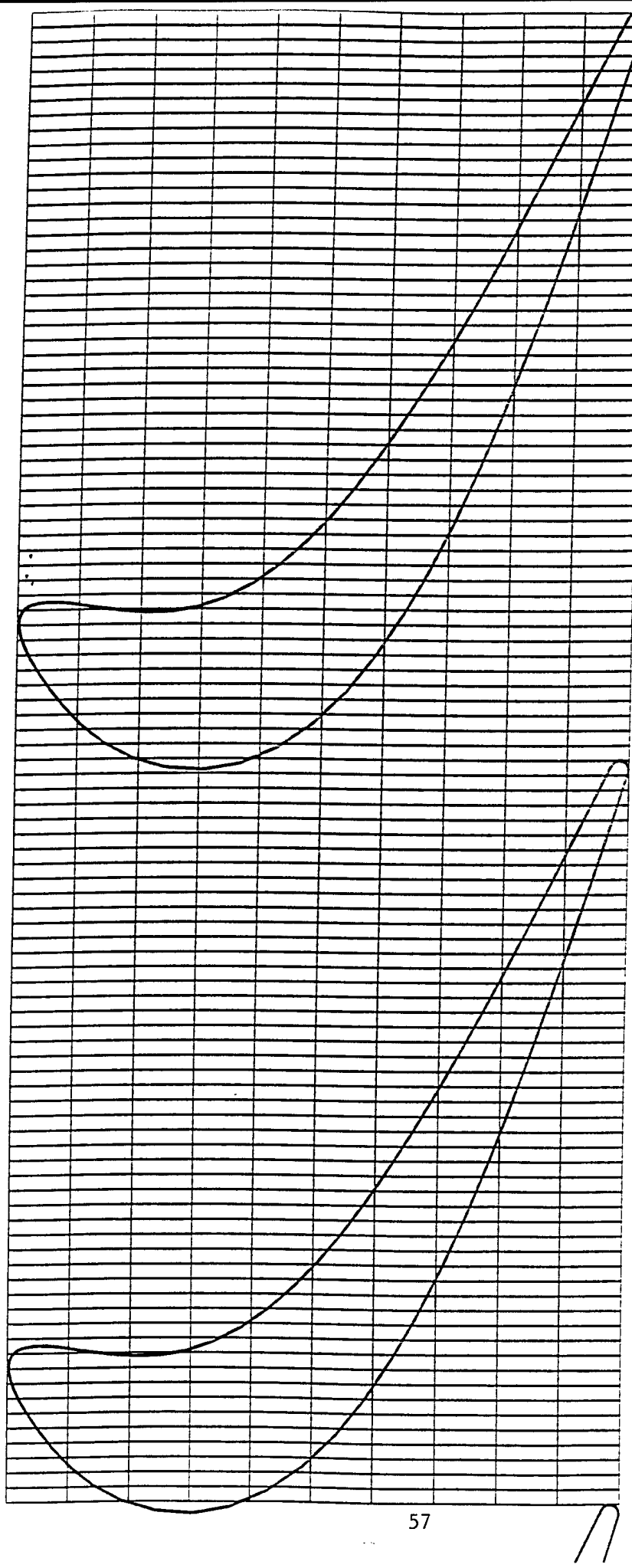
6.3 LDV measurement locations in axial and radial direction
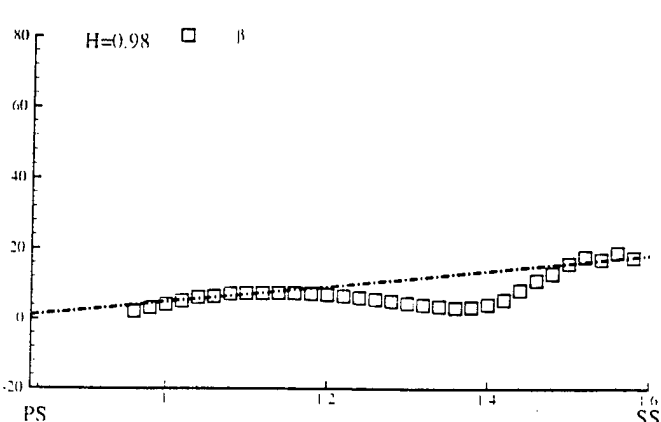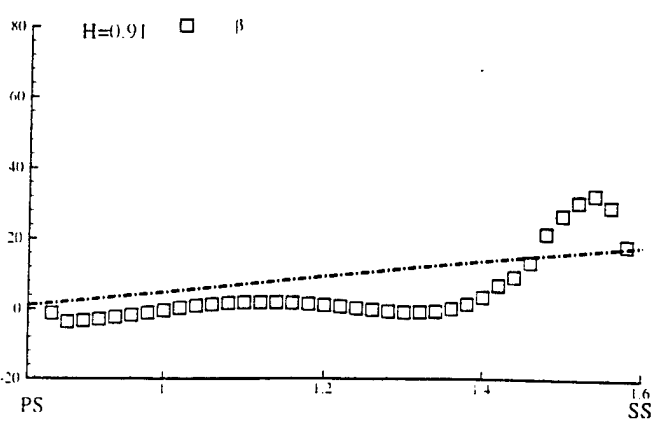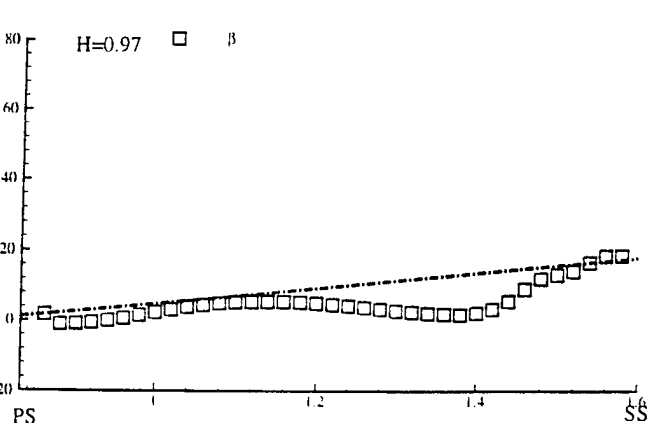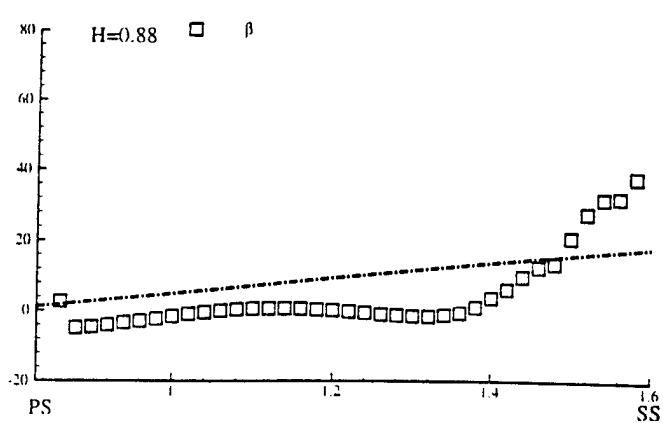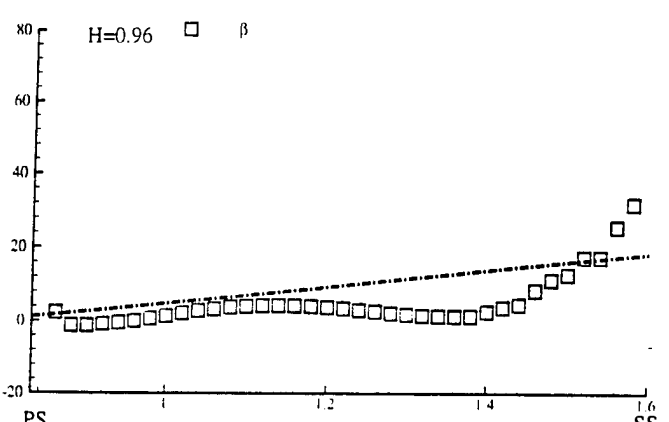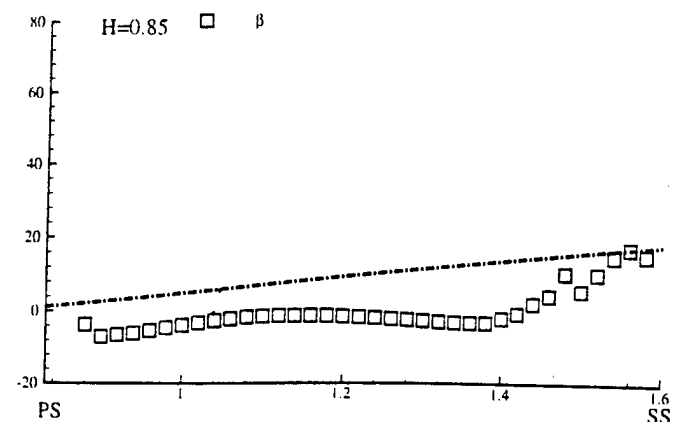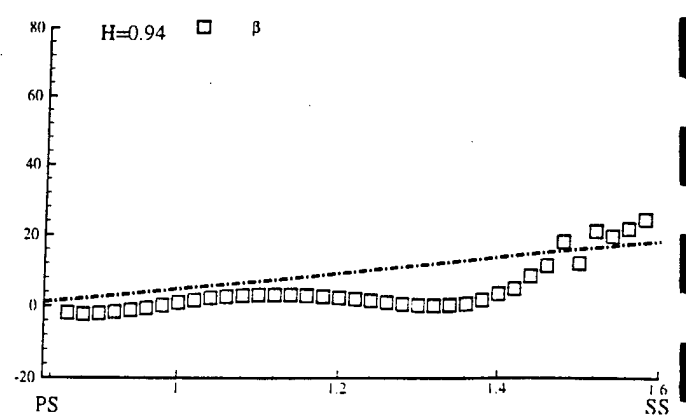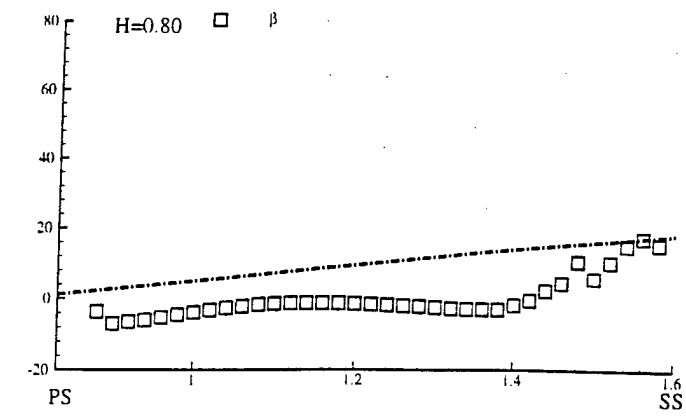
Figure 6.4 The distribution of total velocity angle from pressure surface to suction surface at the $X/C_{ax}=0.20$
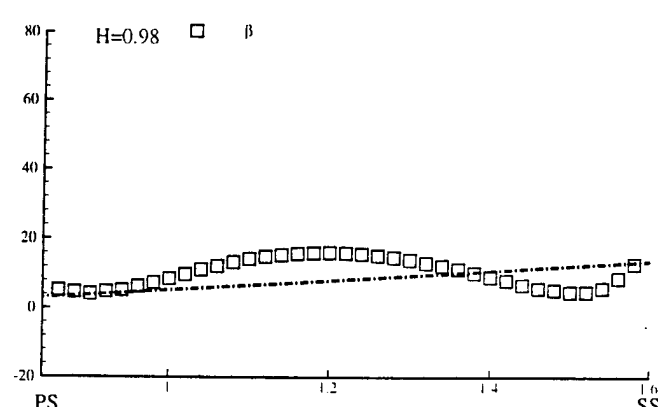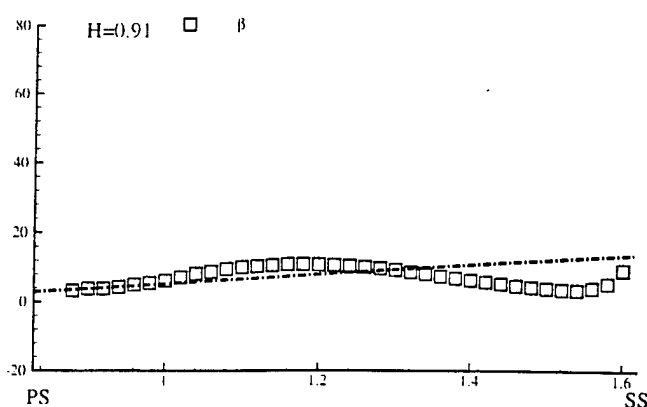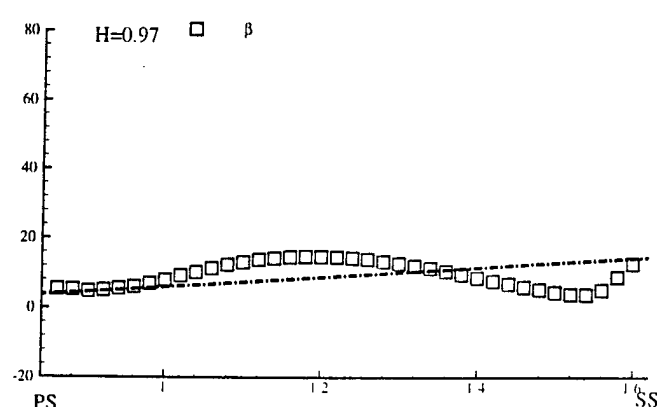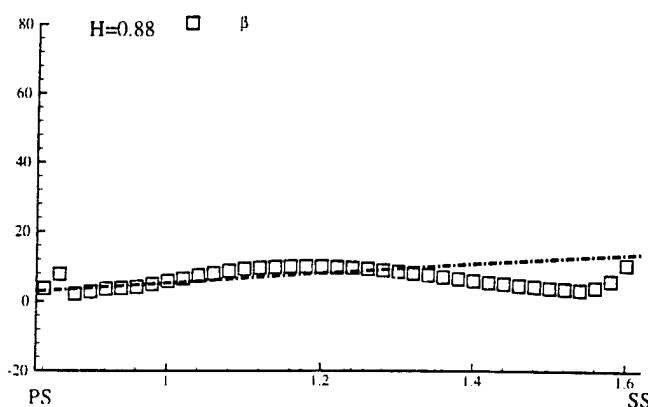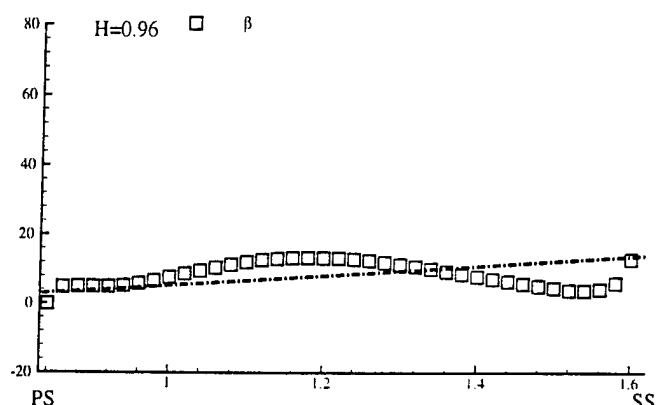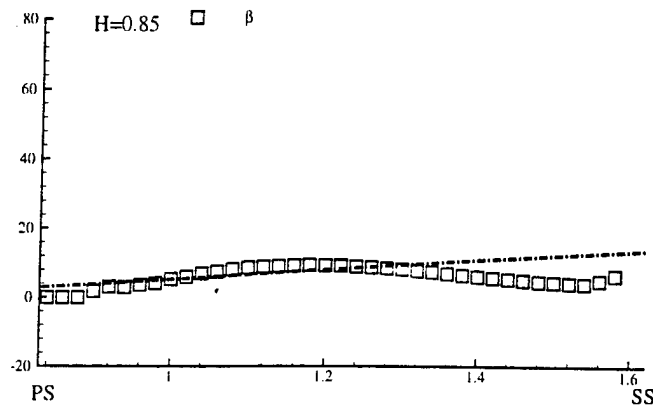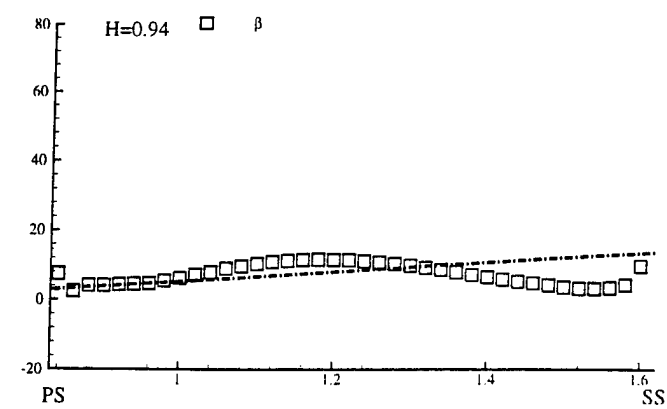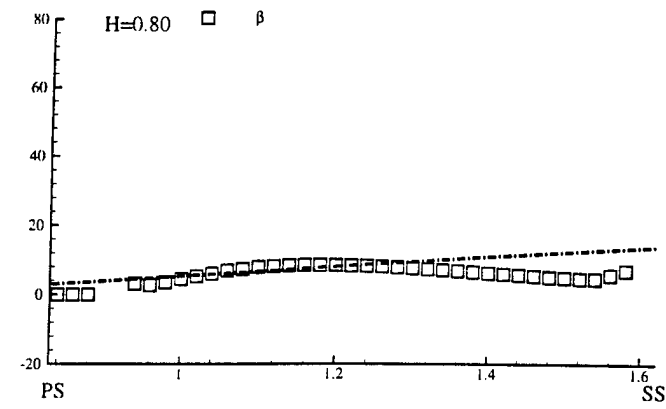
Figure 6.5 The distribution of total velocity angle from pressure surface to suction surface at the $X/C_{ax}=0.30$

59
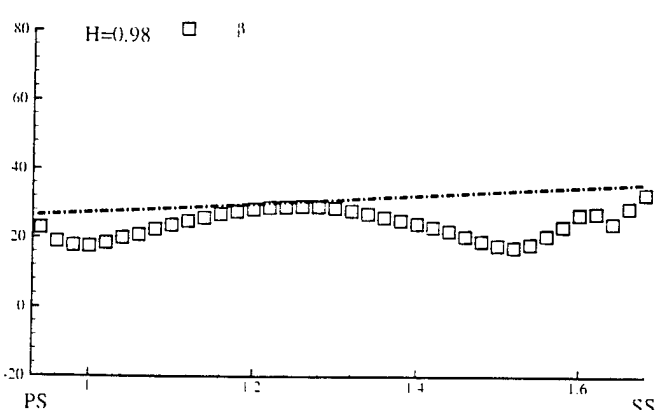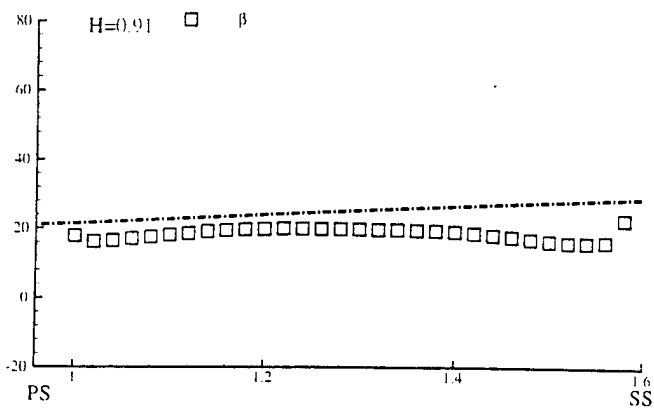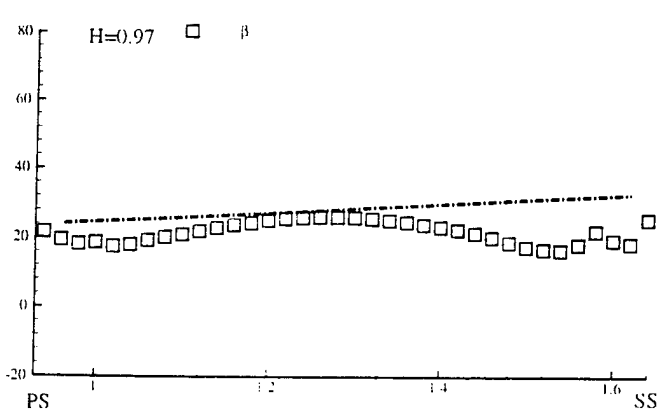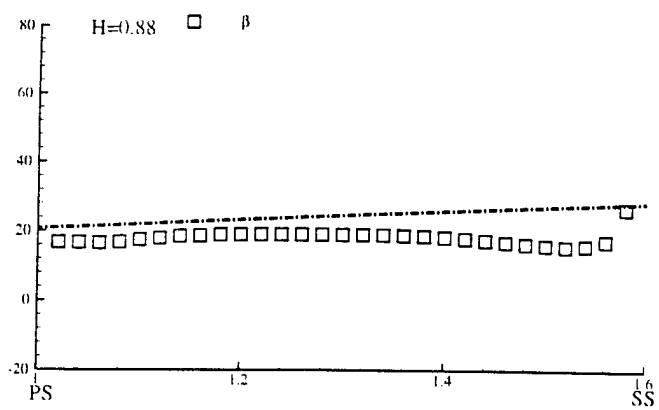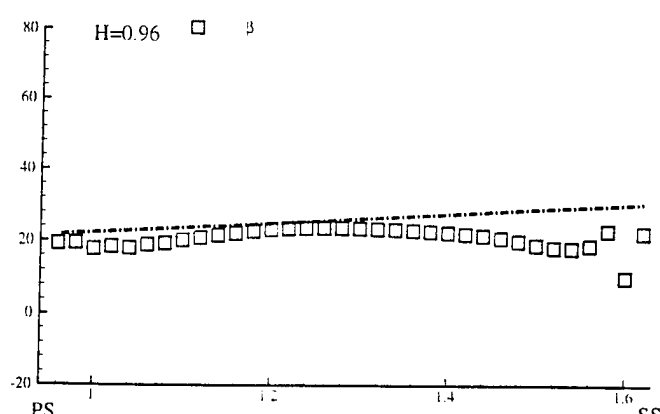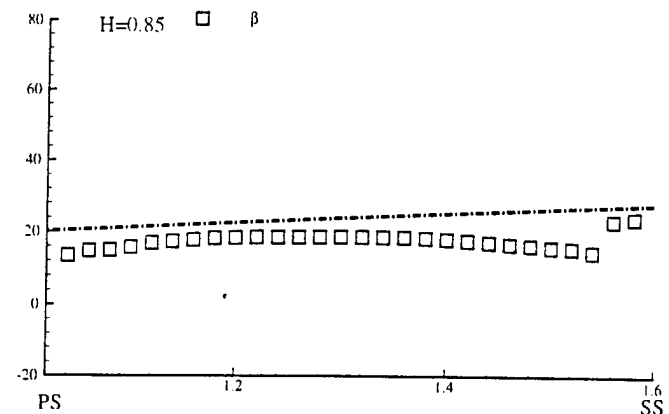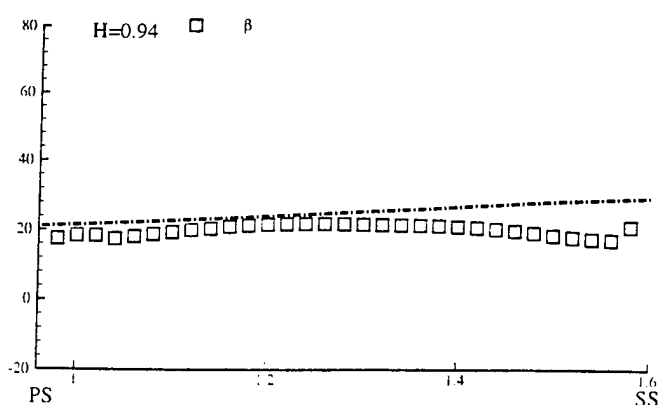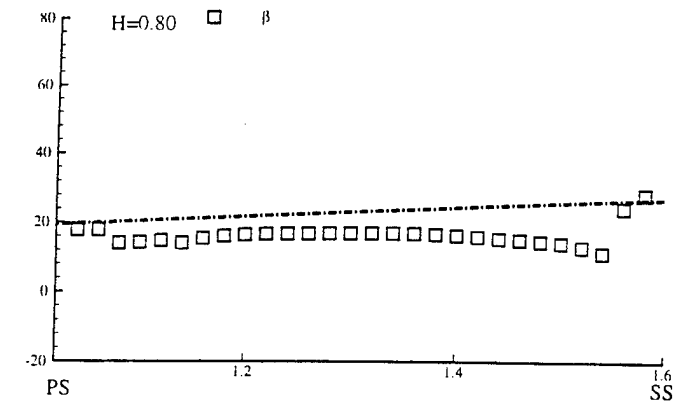
Figure 6.6 The distribution of total velocity angle from pressure surface to suction surface at the $X/C_{ax}=0.40$

60
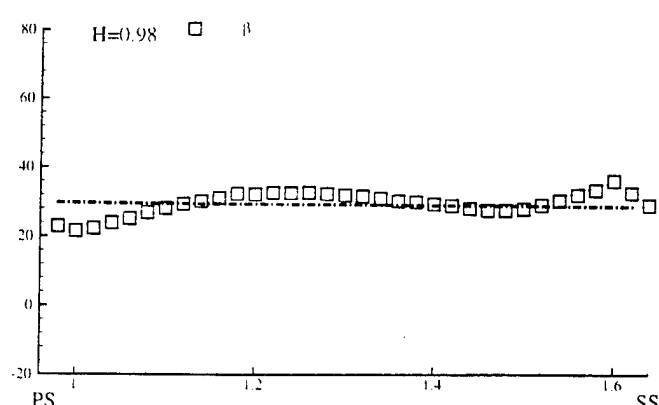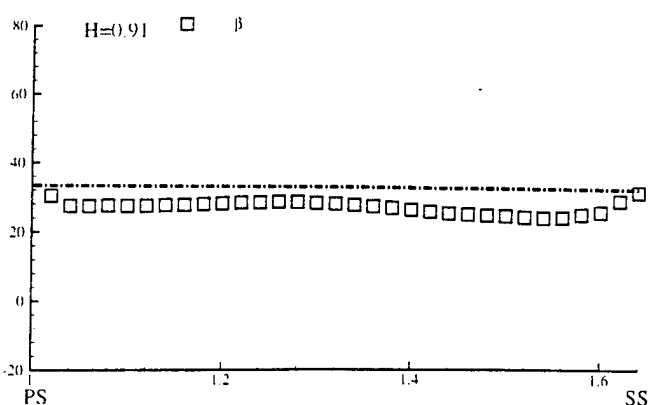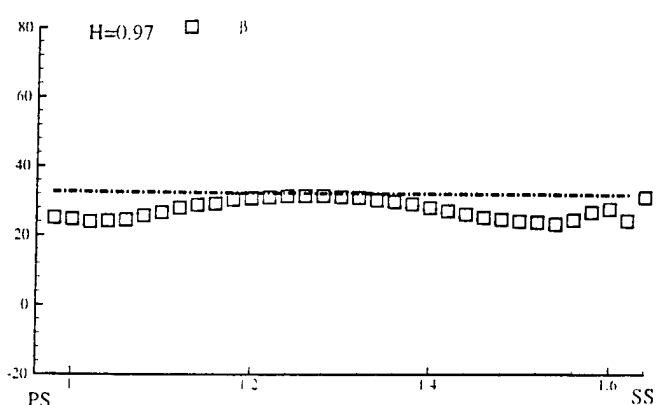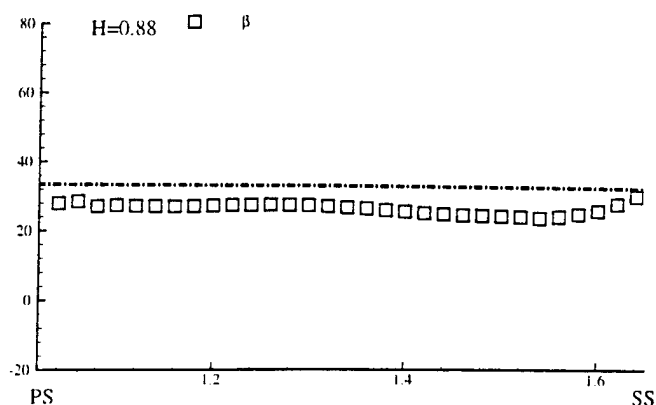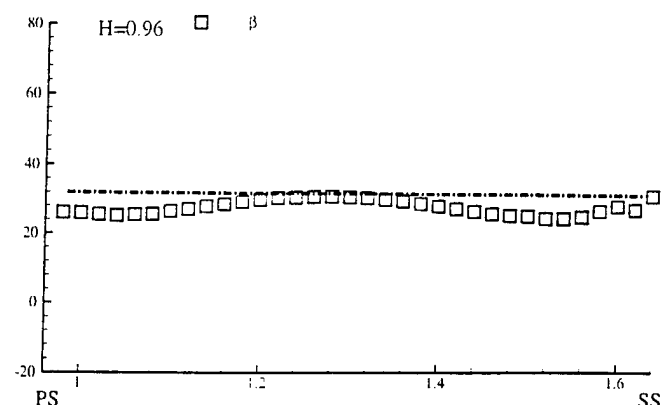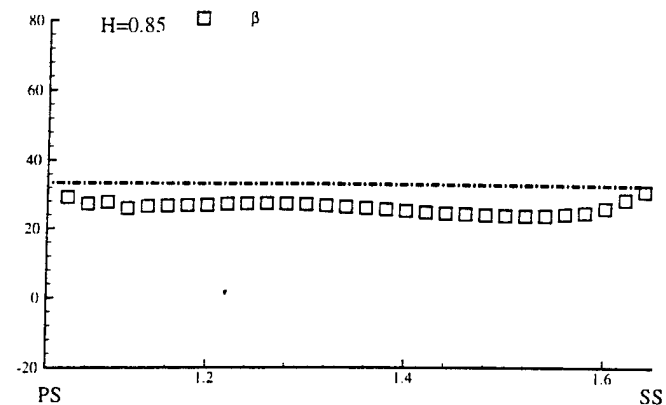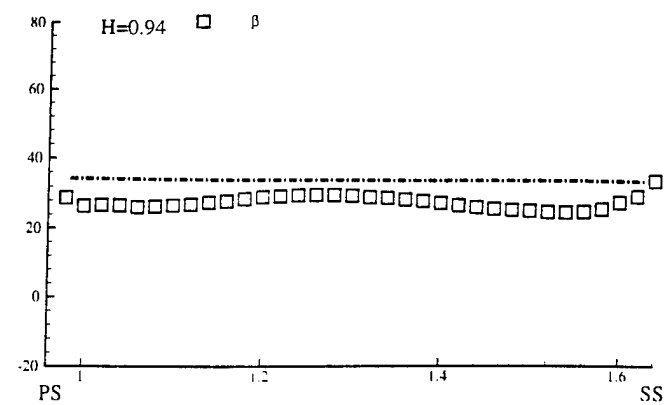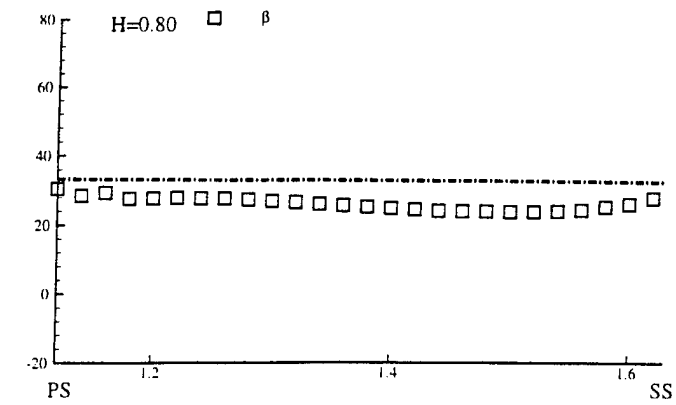
Figure 6.7 The distribution of total velocity angle from pressure surface to suction surface at the X/C_{ax}=0.50
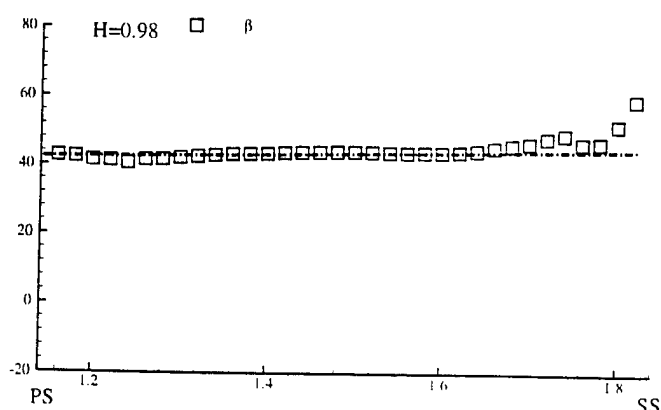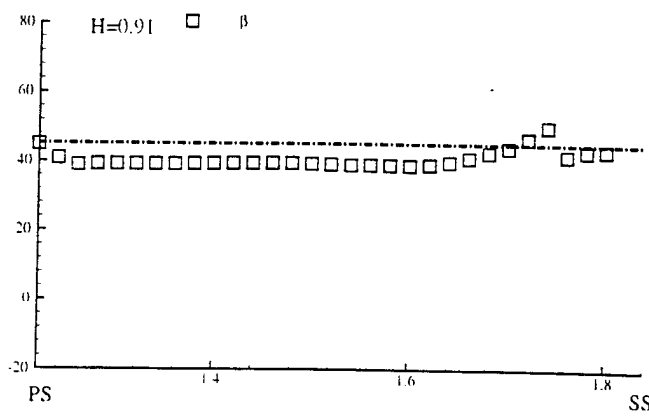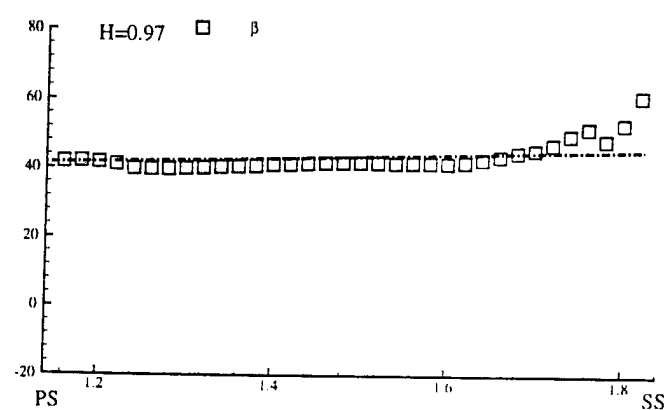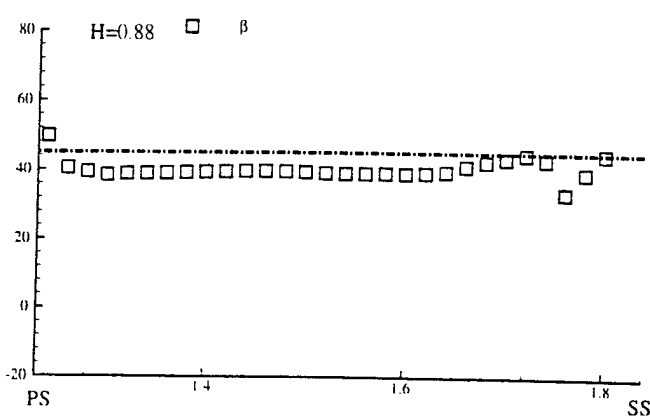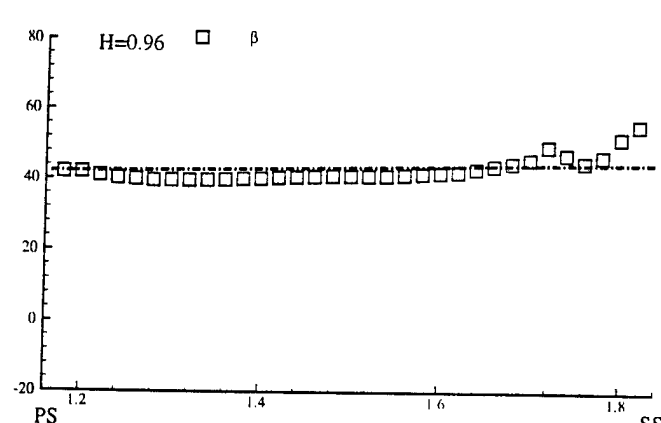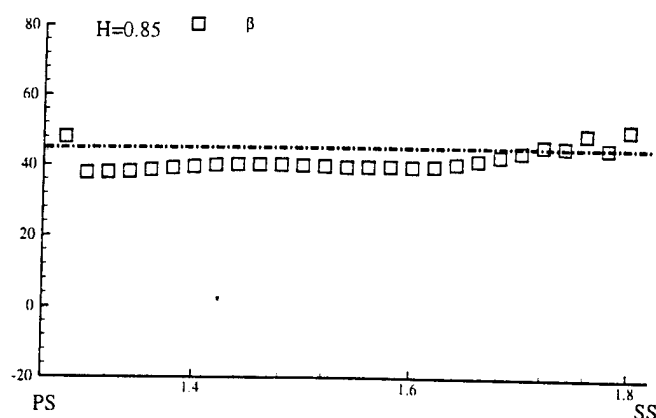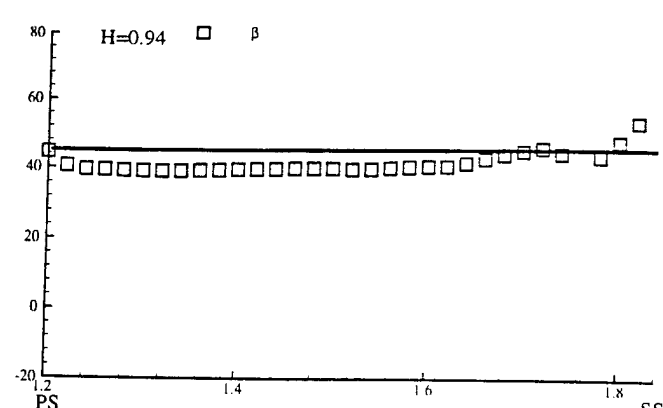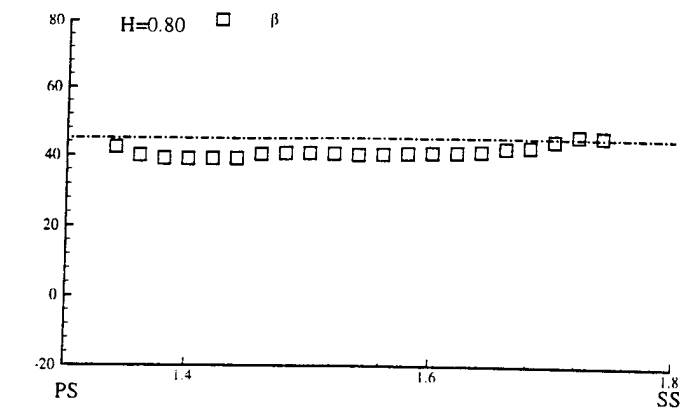
Figure 6.8 The distribution of total velocity angle from pressure surface to suction surface at the X/C_{ax}=0.60

62
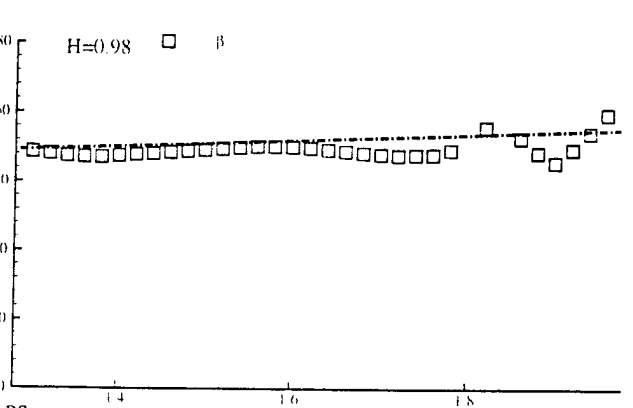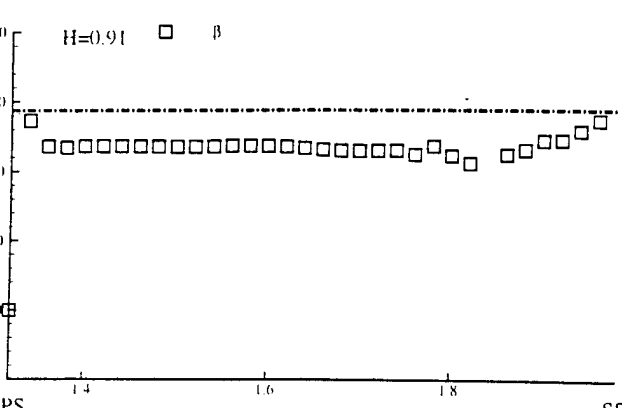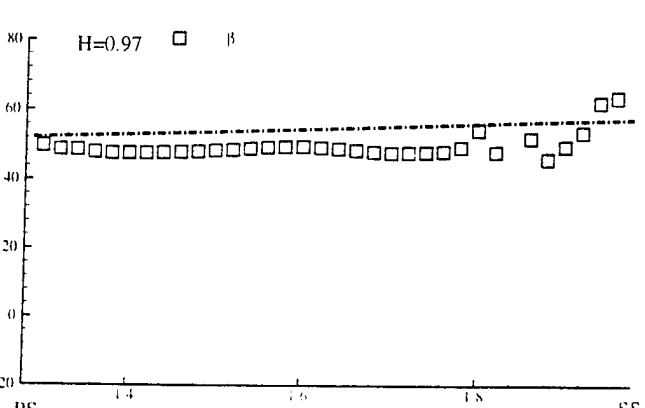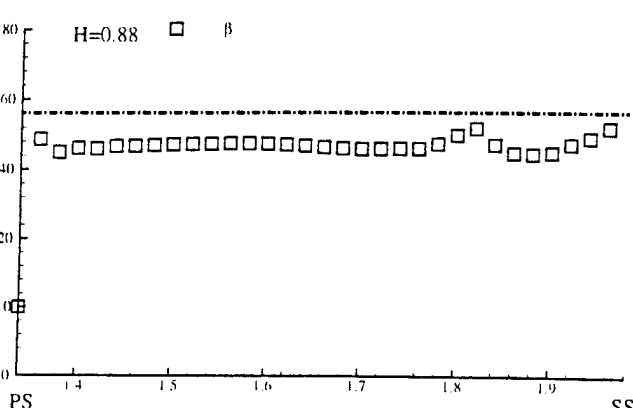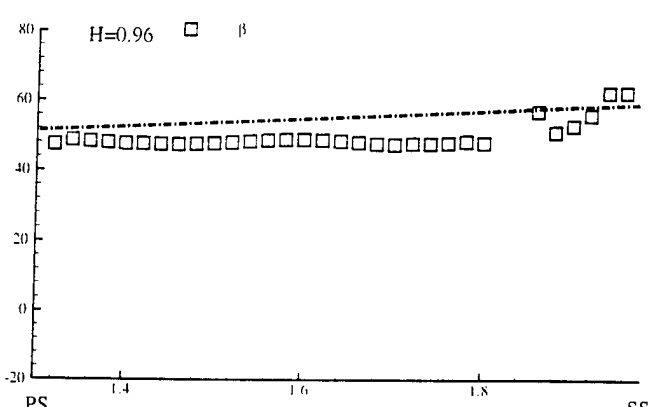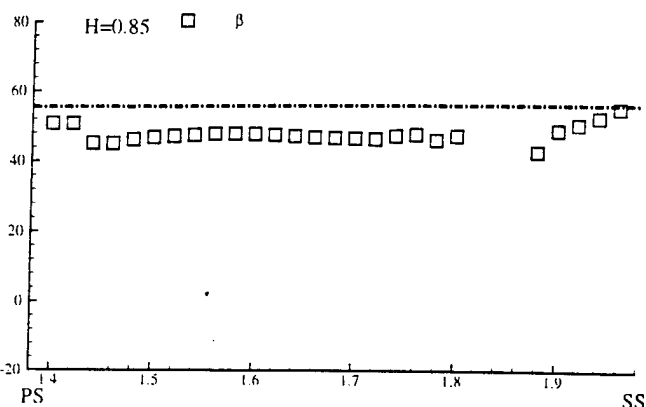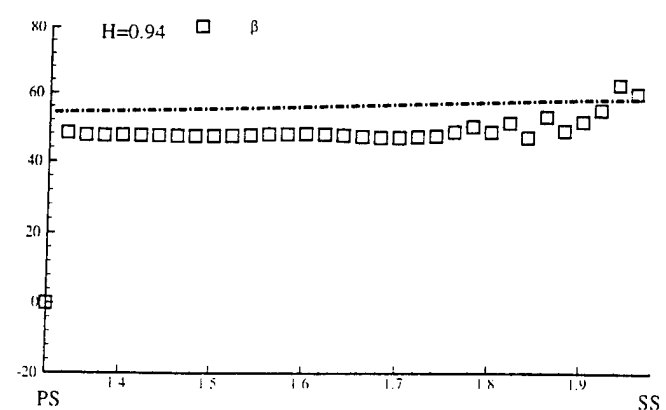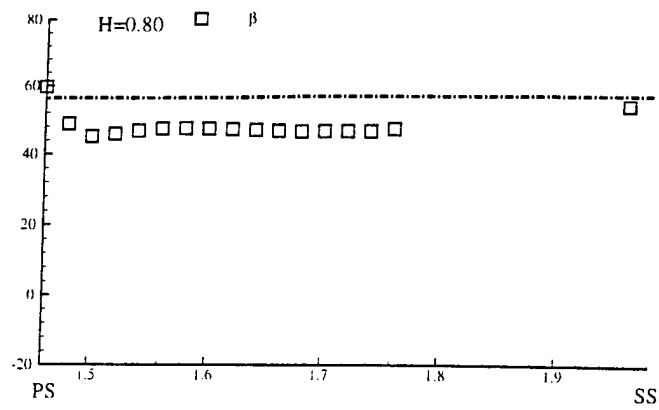
Figure 6.9 The distribution of total velocity angle from pressure surface to suction surface at the $X/C_{ax}=0.70$

63
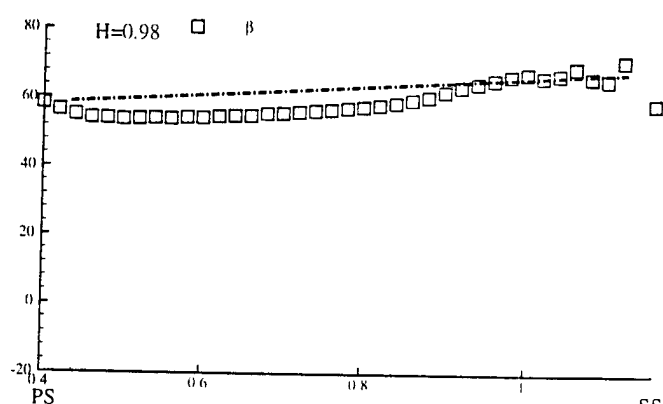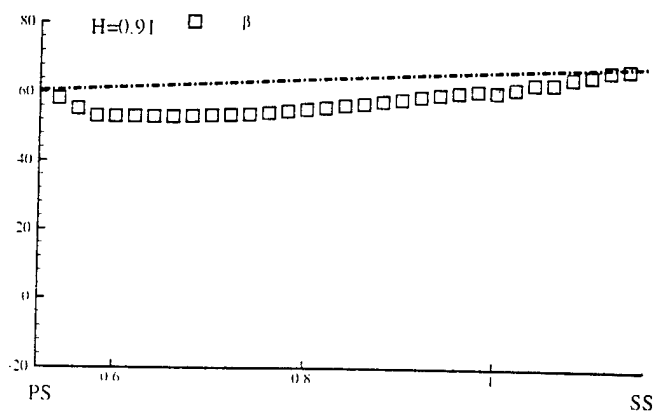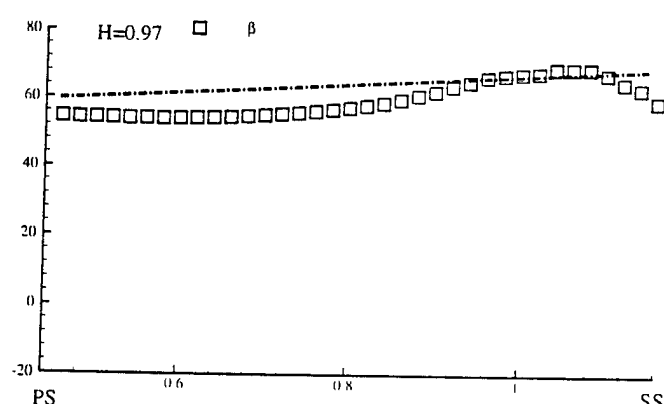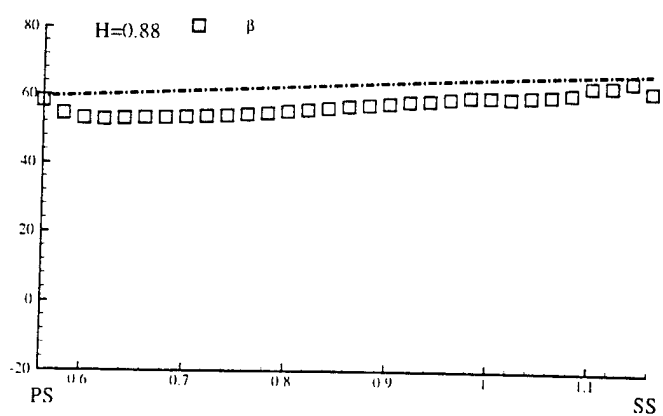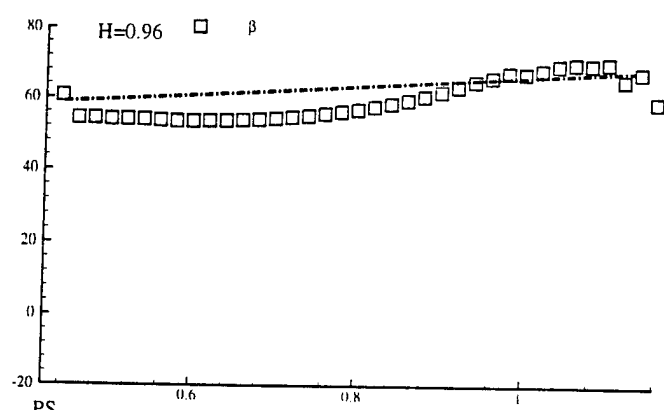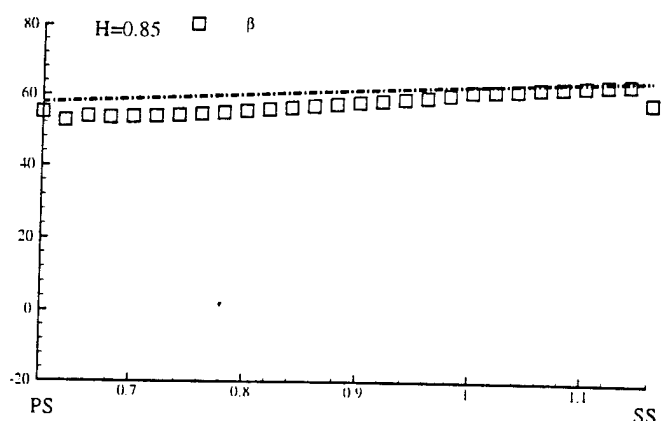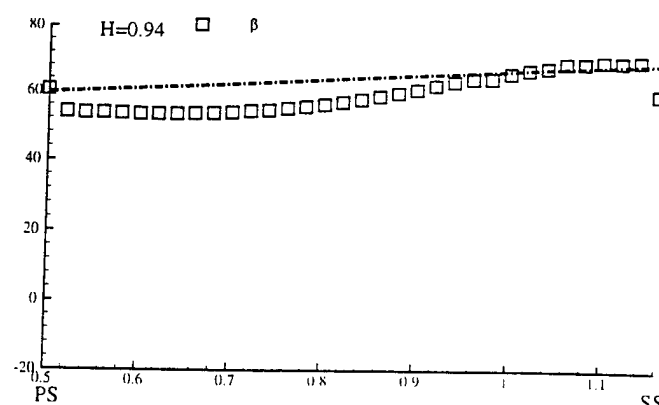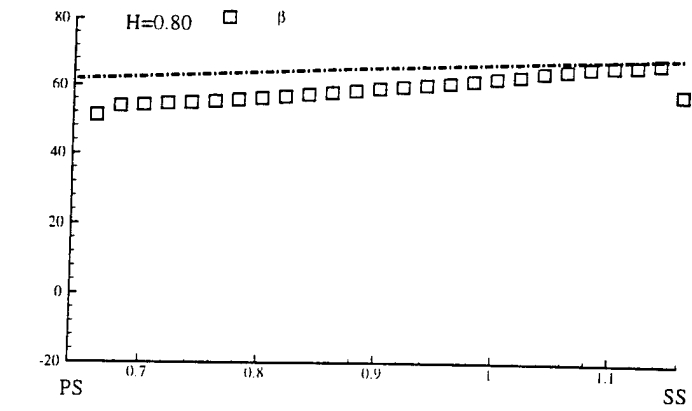
Figure 6.10 The distribution of total velocity angle from pressure surface to suction surface at the $X/C_{ax}=0.80$
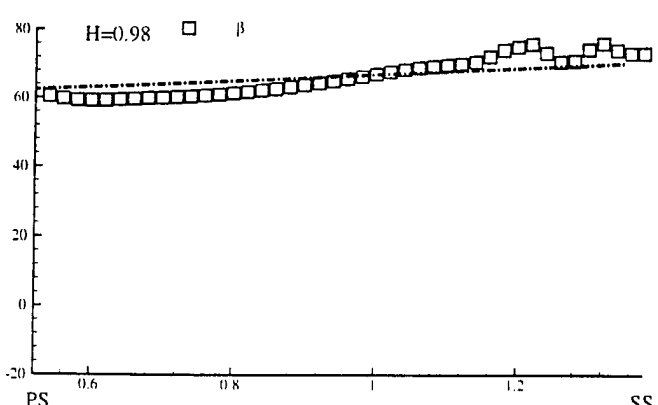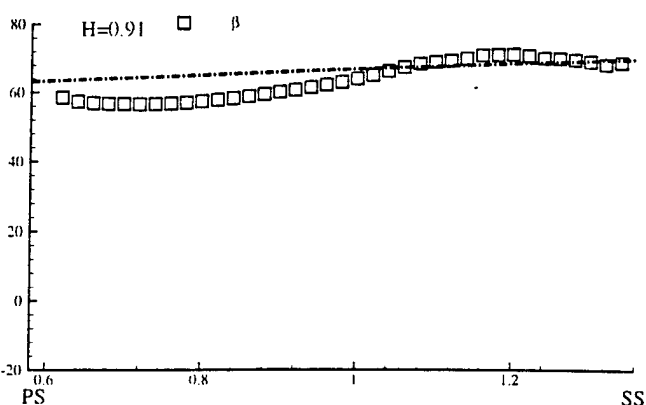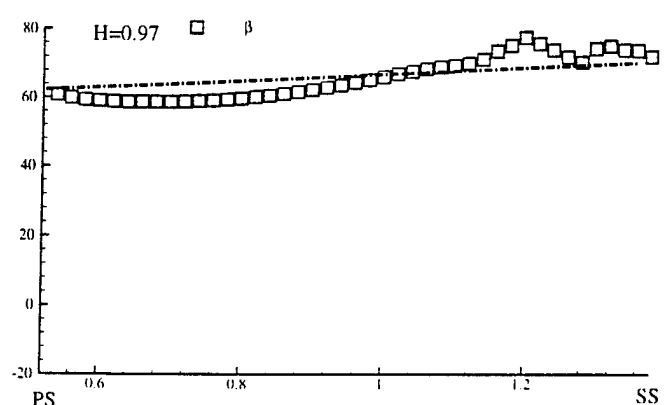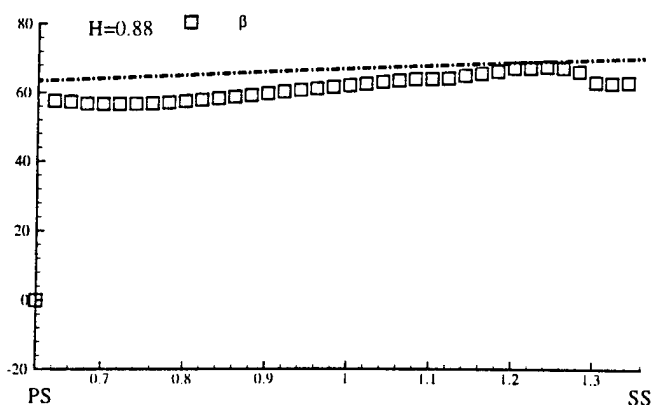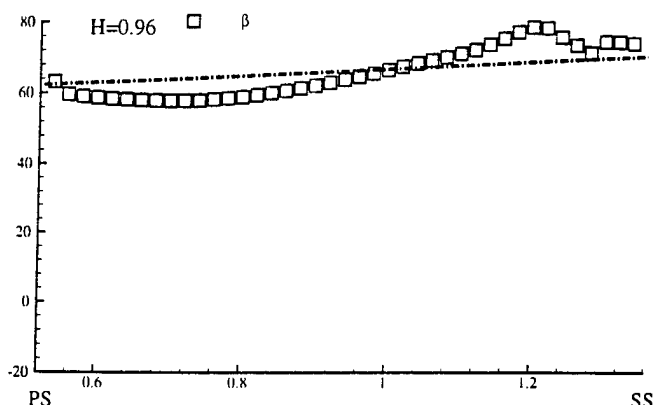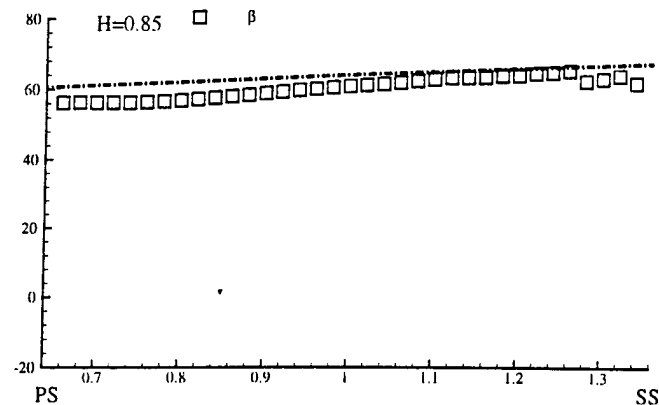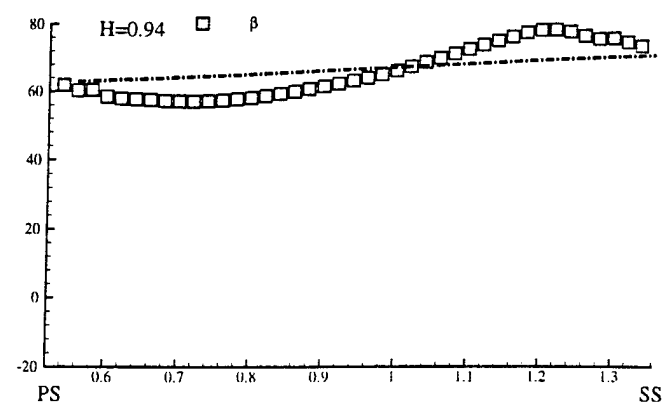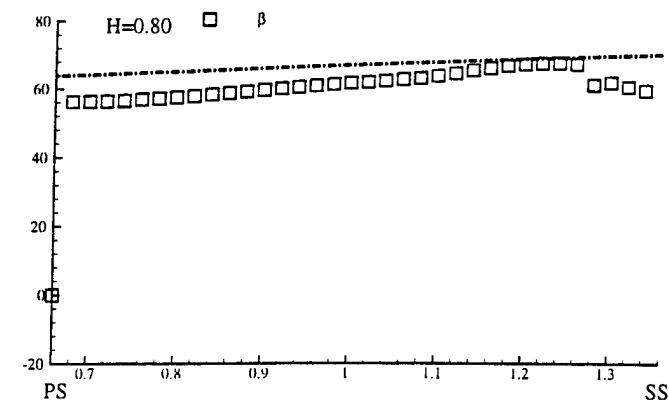
Figure 6.11 The distribution of total velocity angle from pressure surface to suction surface at the X/C$_{ax}$=0.90
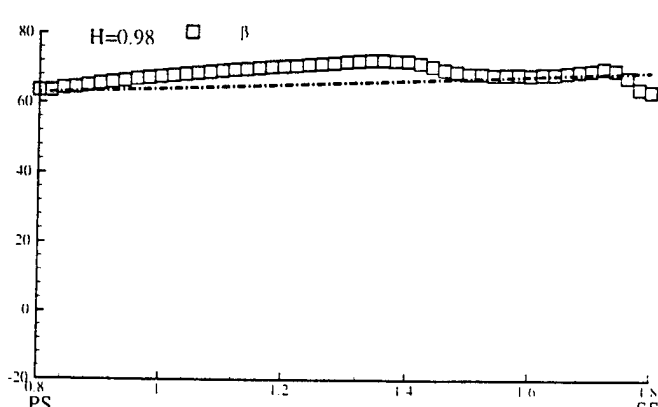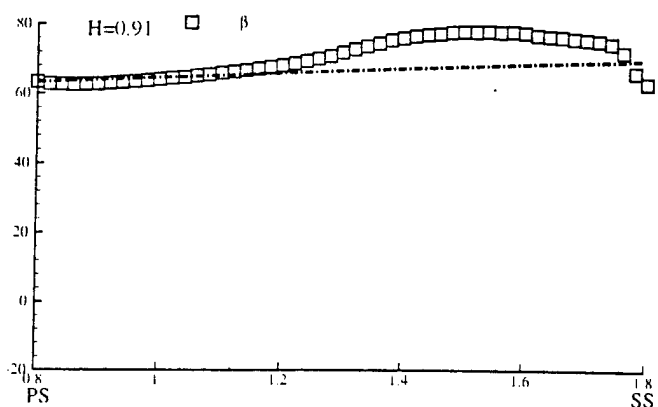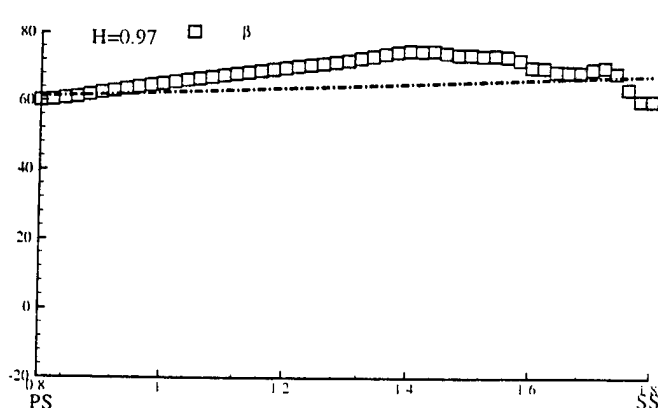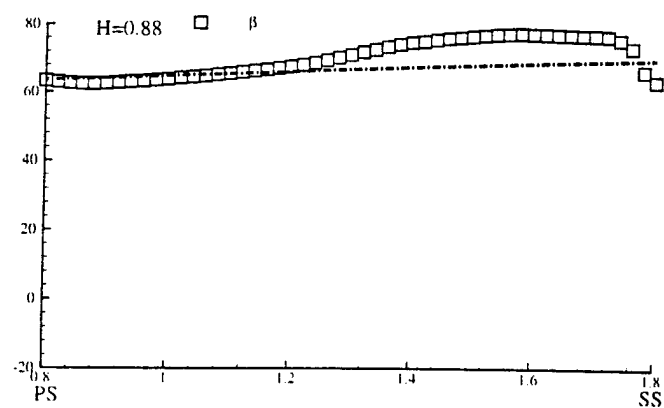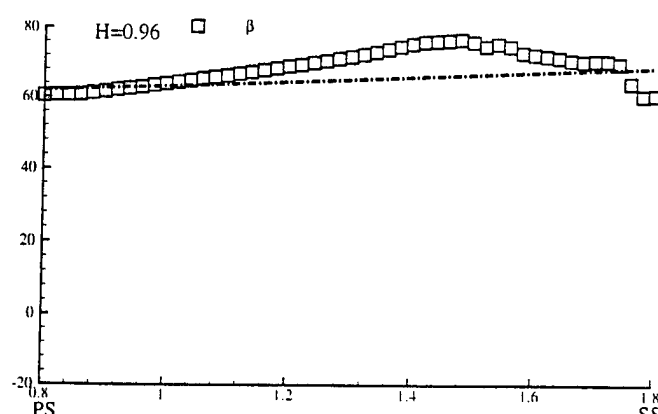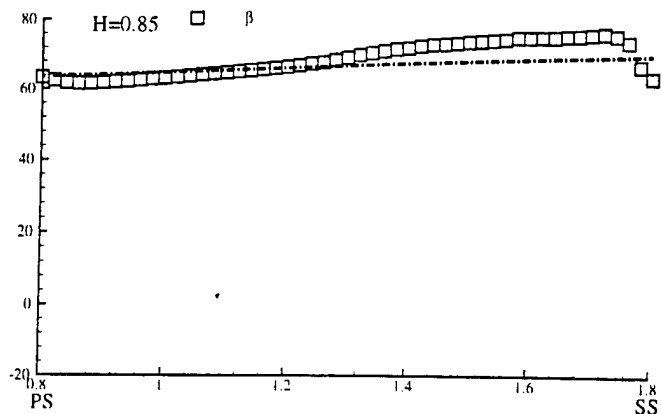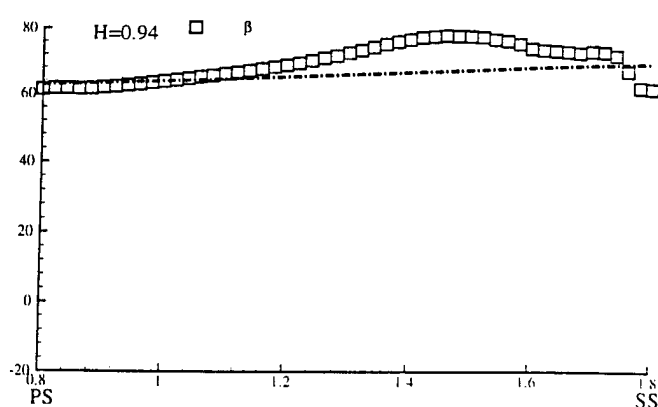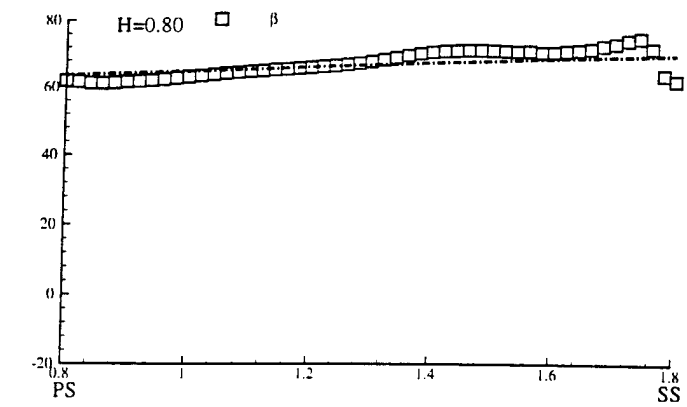
Figure 6.12 The distribution of total velocity angle from pressure surface to suction surface at the X/C$_{ax}$=1.01
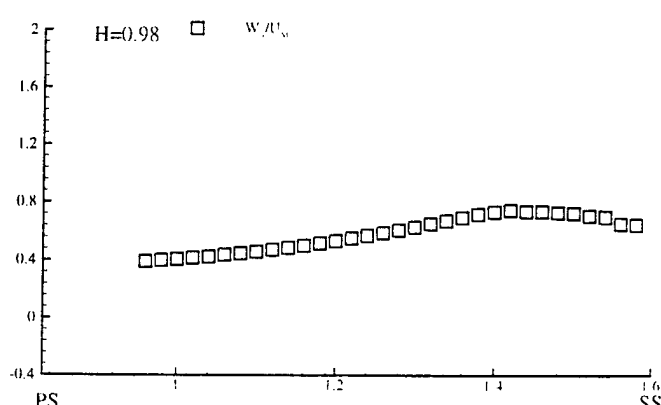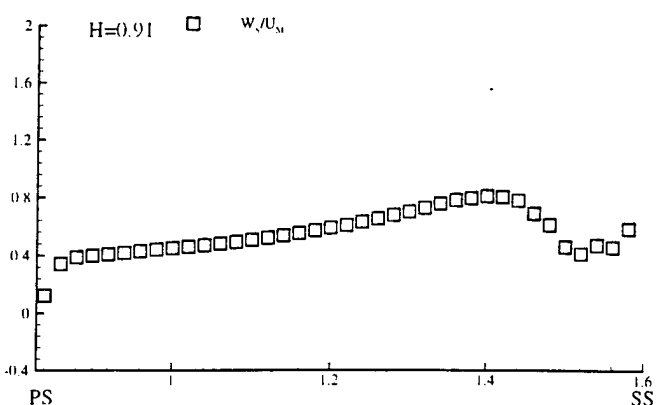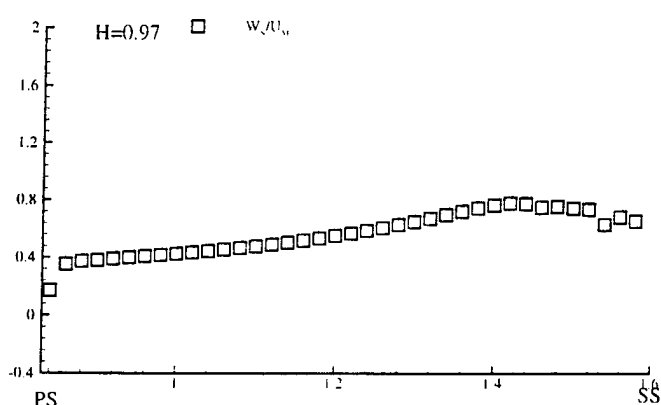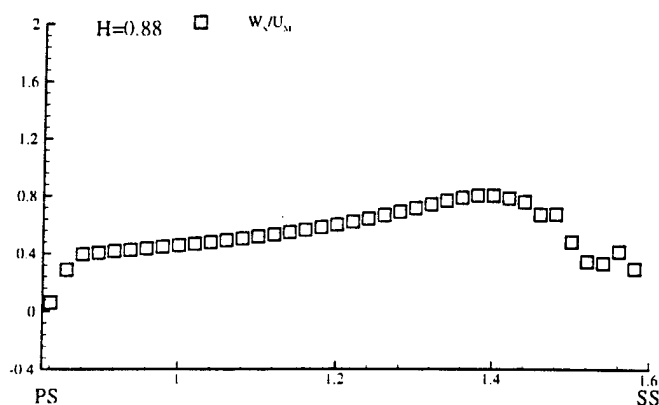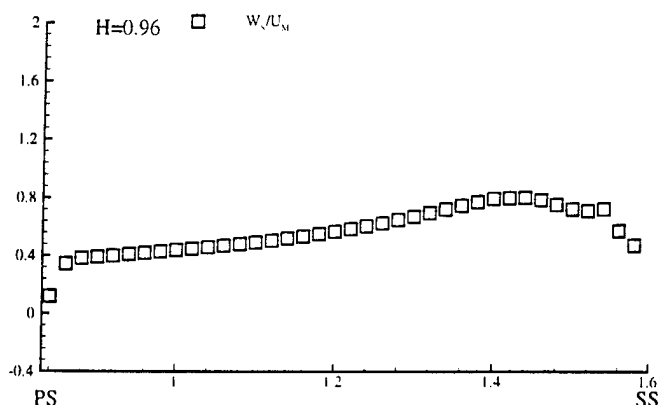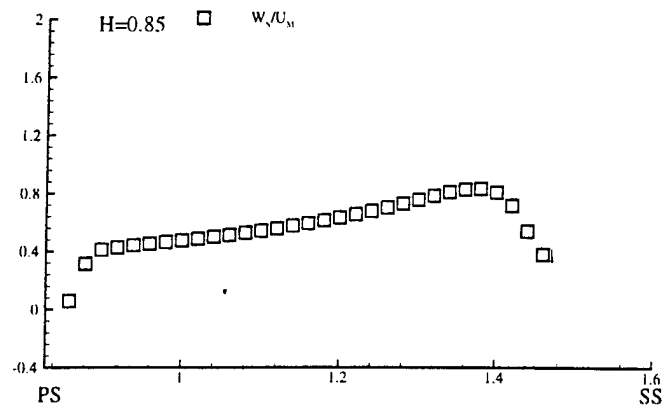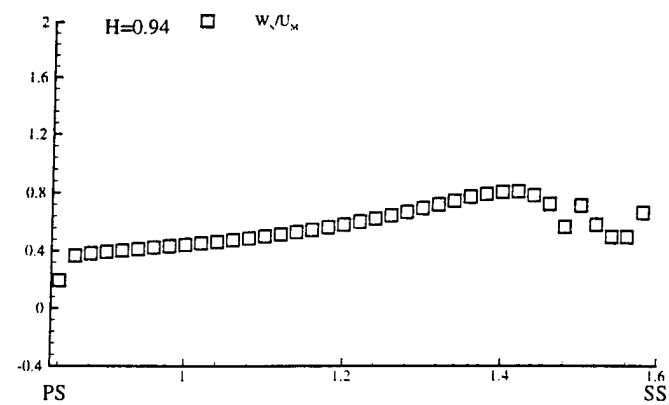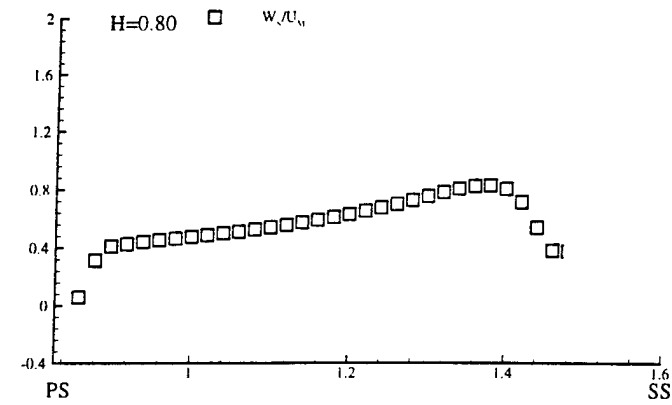
Figure 6.13 The distribution of total velocity from pressure surface to suction surface at the X/C$_{ax}$=0.20

67
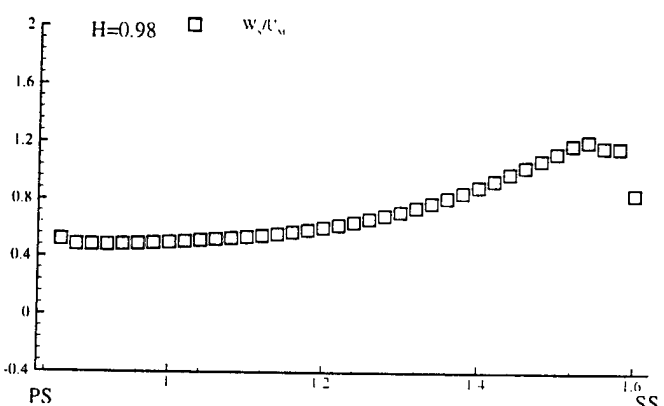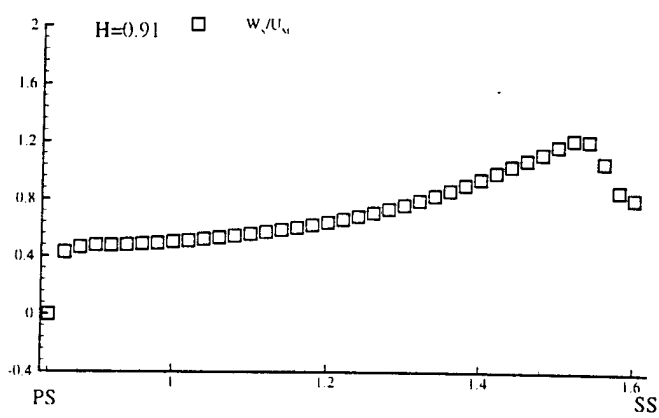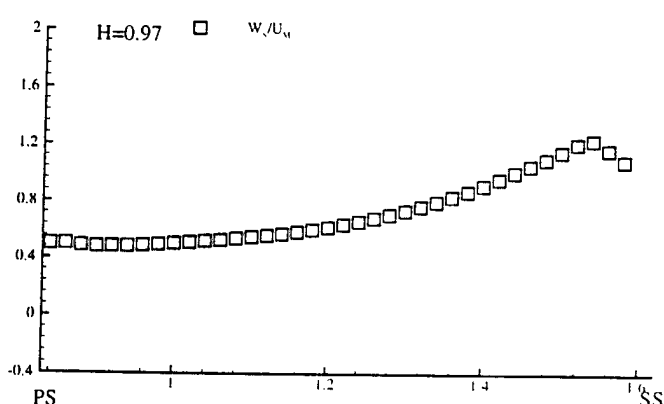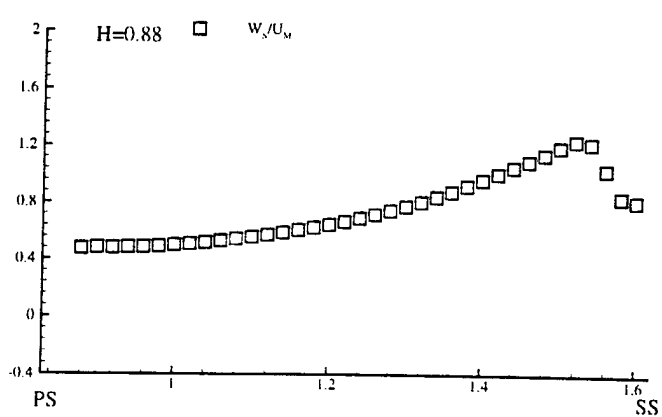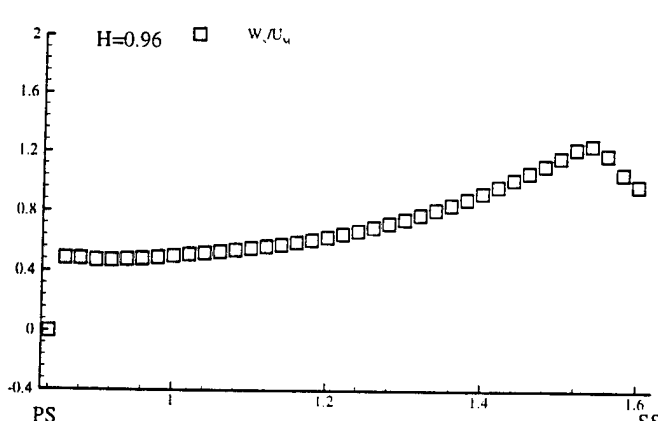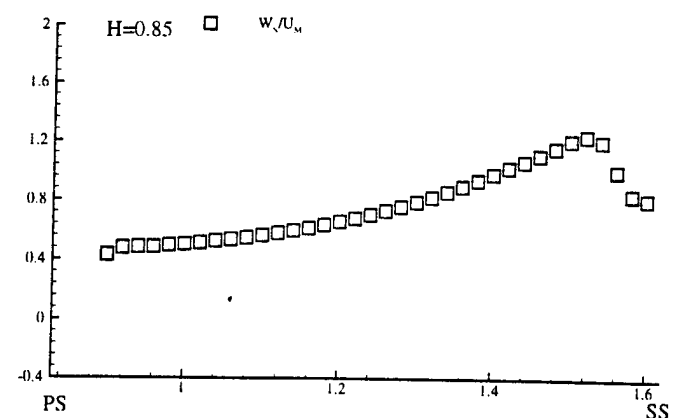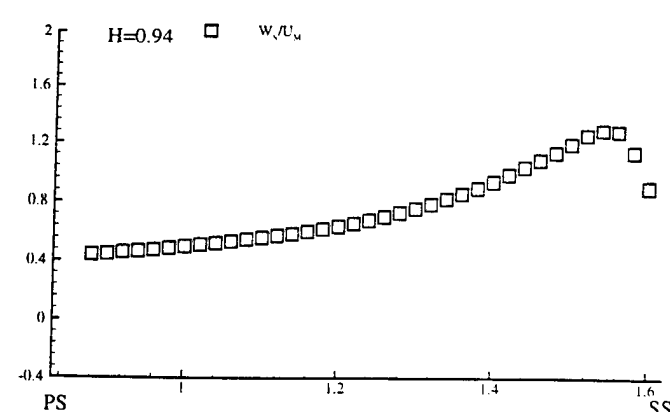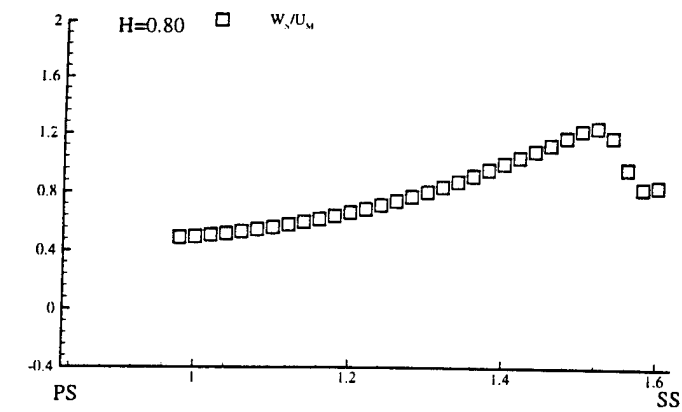
Figure 6.14 The distribution of total velocity from pressure surface to suction surface at the X/C$_{ax}$=0.30

68
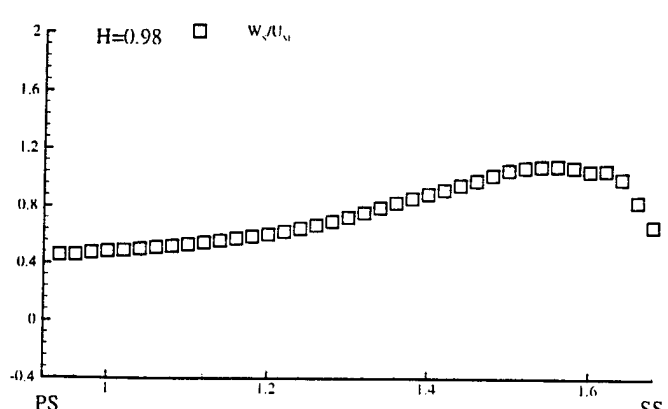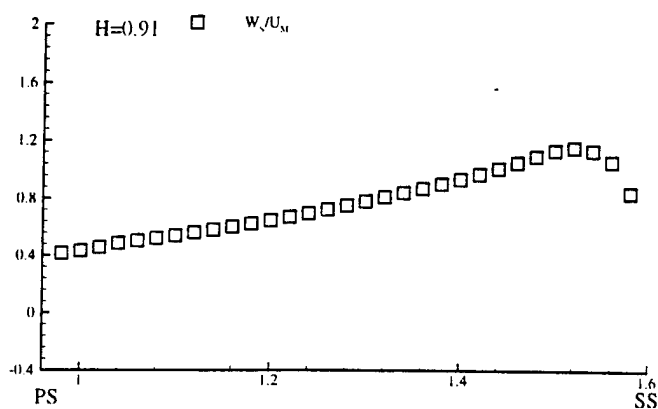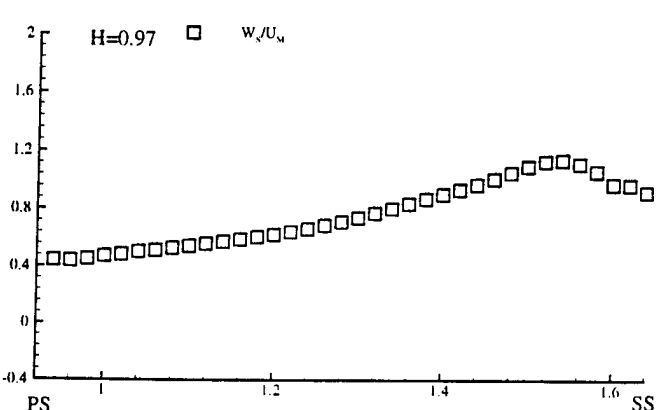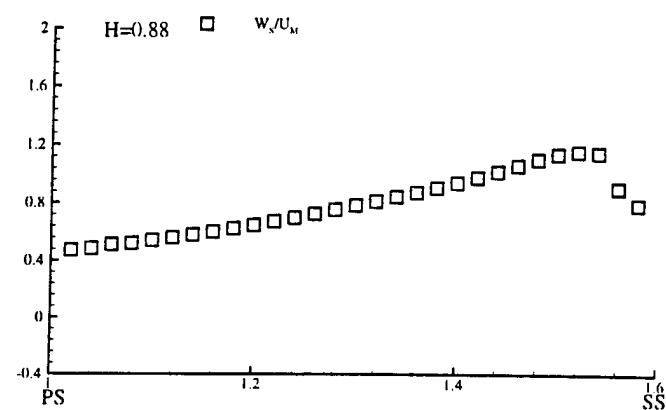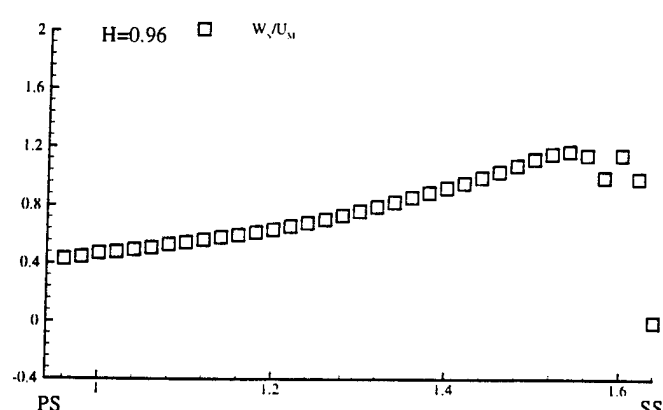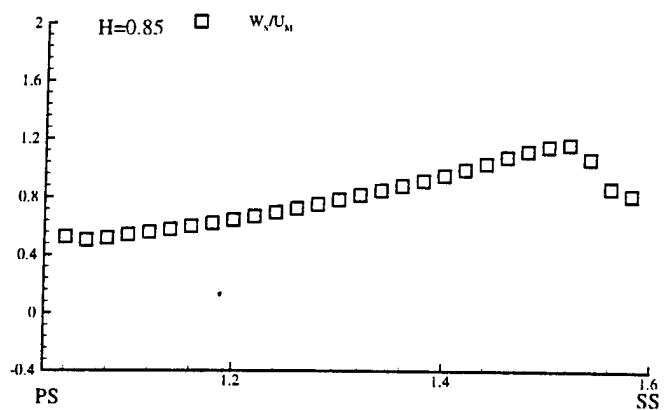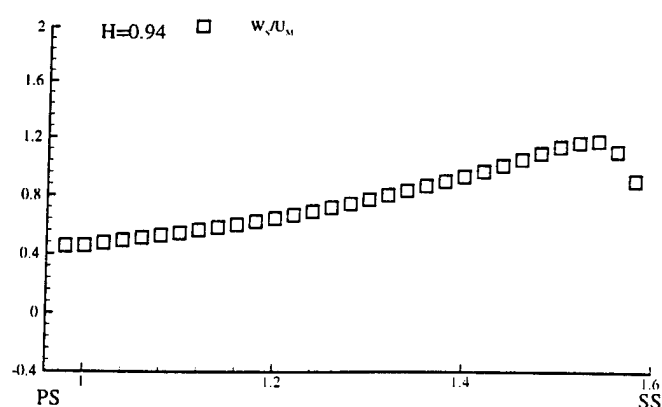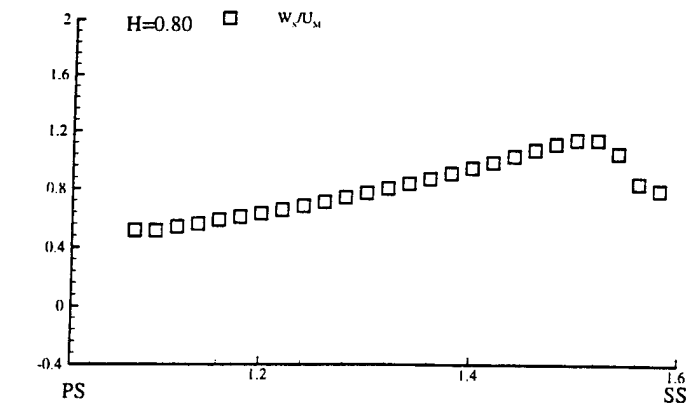
Figure 6.15 The distribution of total velocity from pressure surface to suction surface at the $X/C_{ax}=0.40$
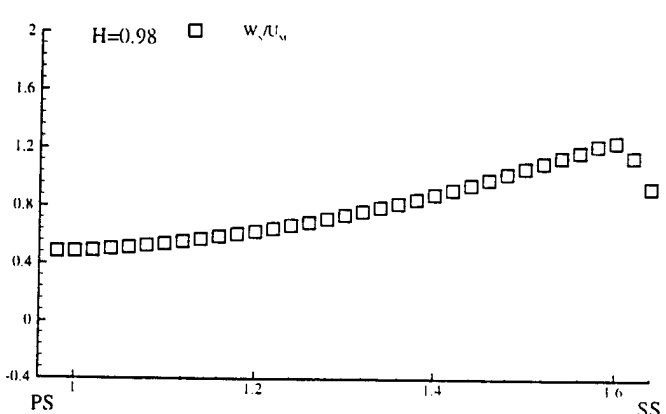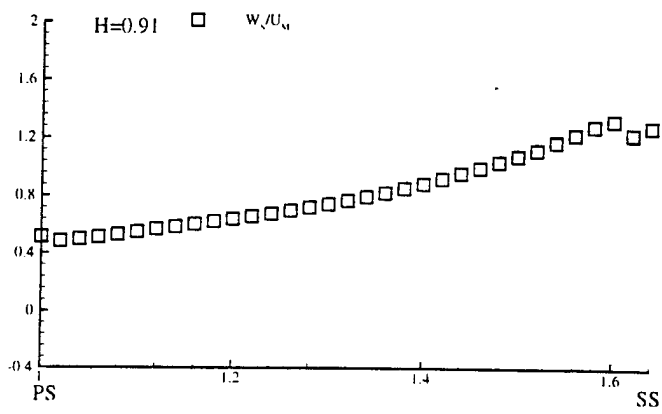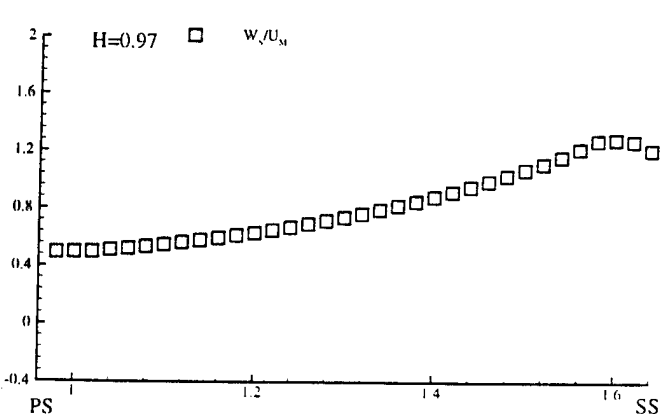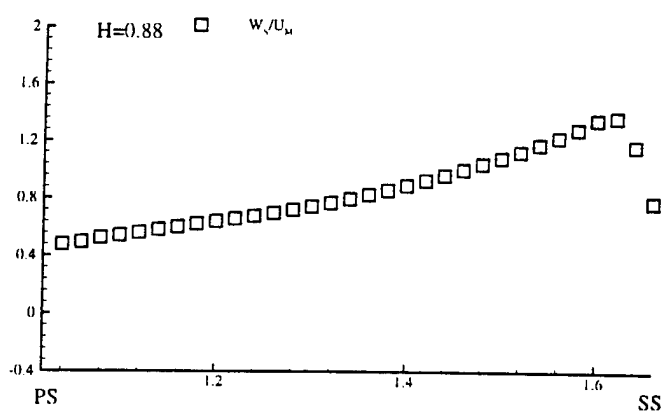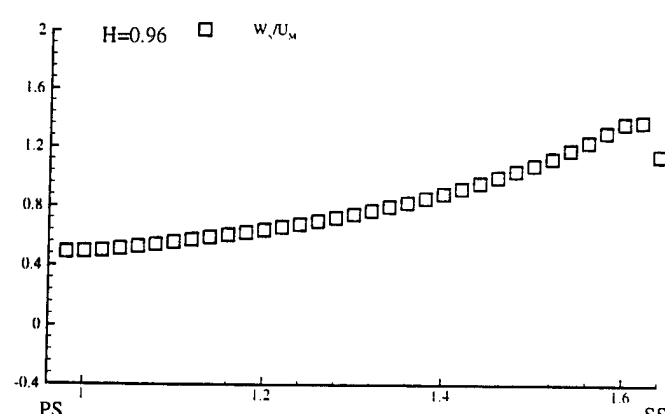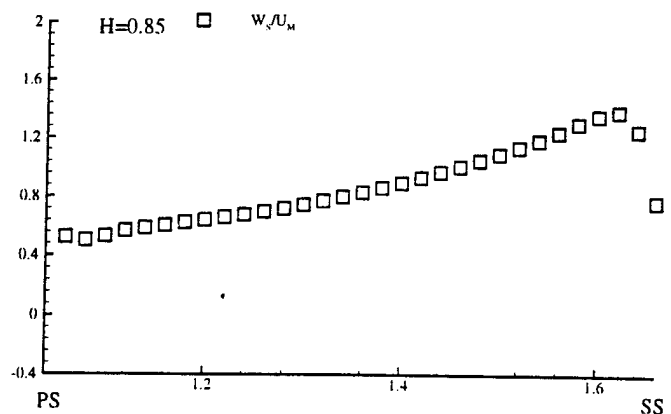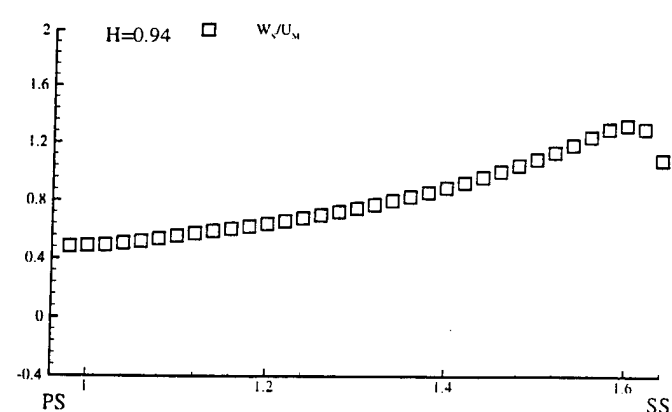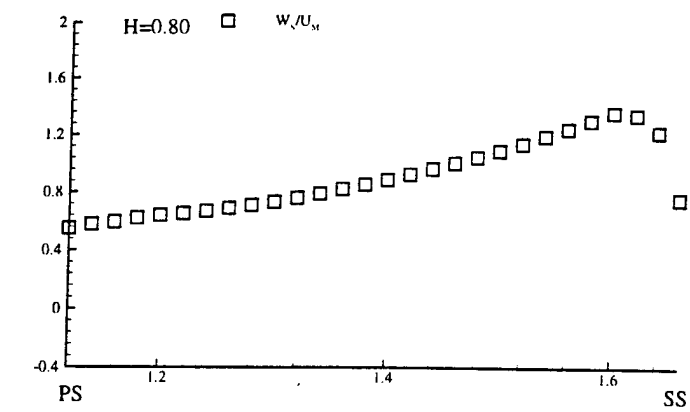
Figure 6.16 The distribution of total velocity from pressure surface to suction surface at the X/C$_{ax}$=0.50
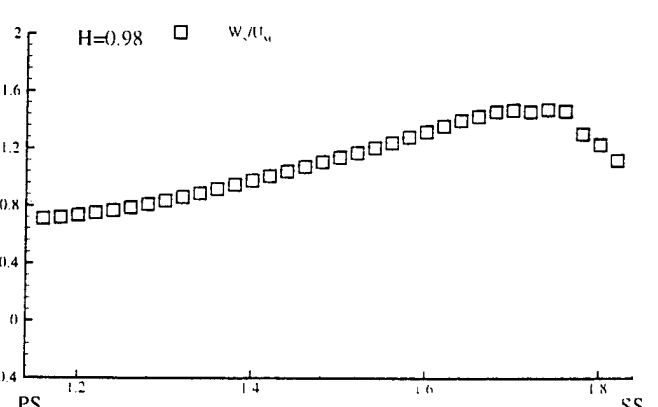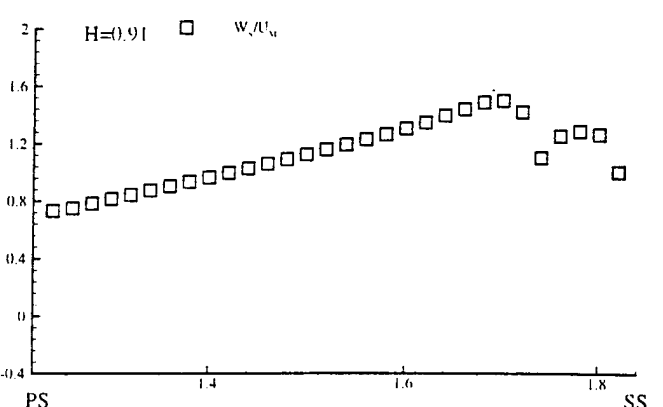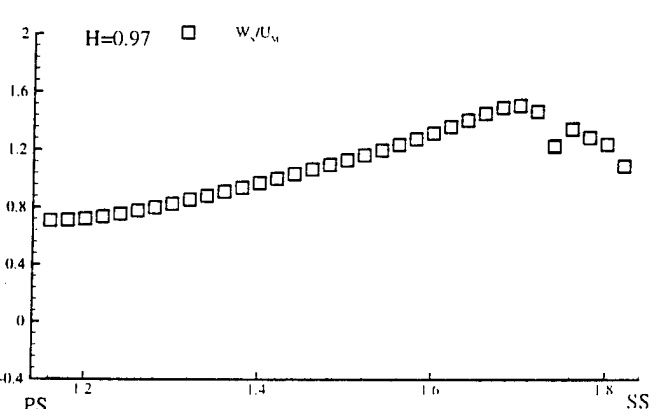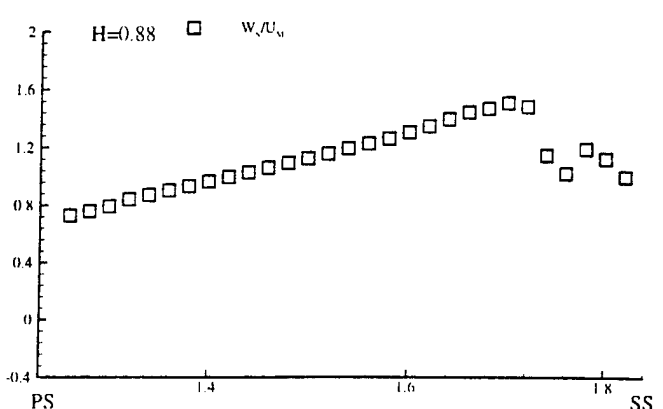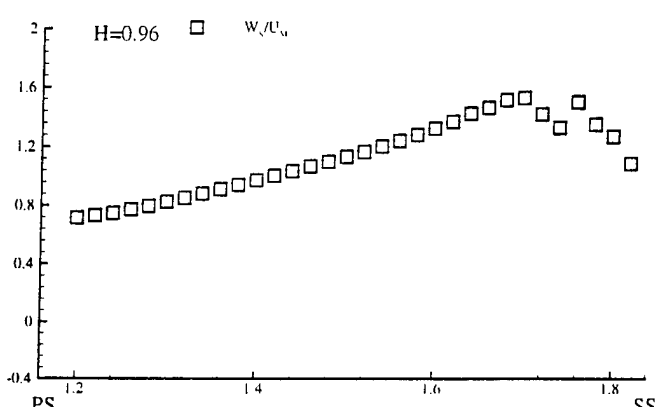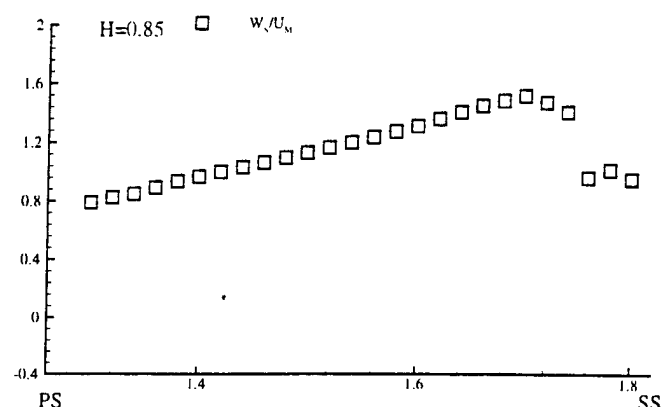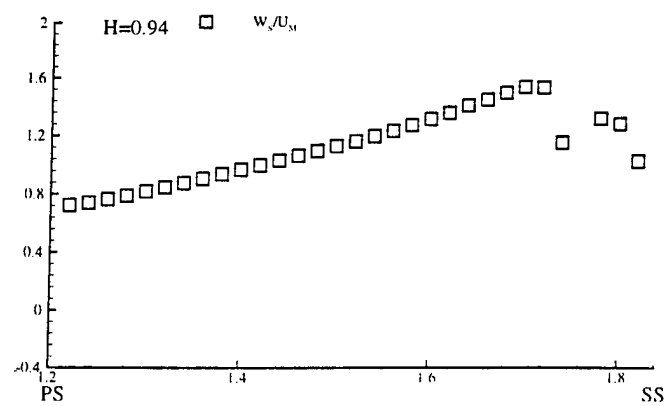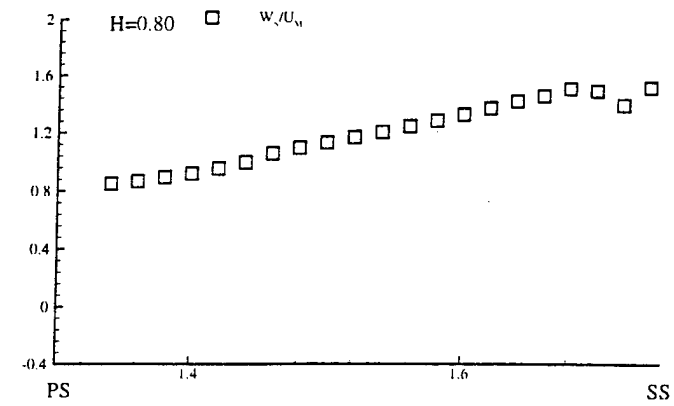
Figure 6.17 The distribution of total velocity from pressure surface to suction surface at the X/C$_{ax}$=0.60

71
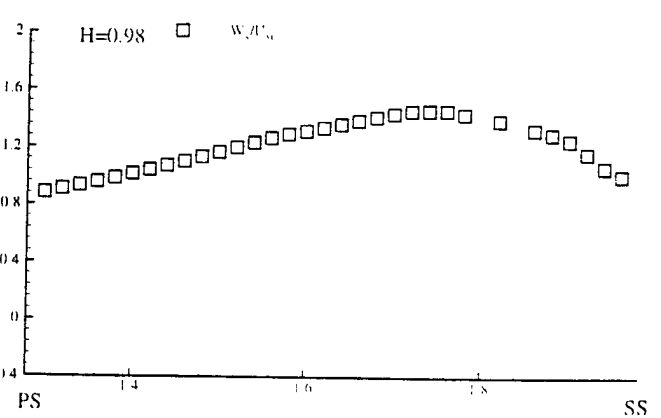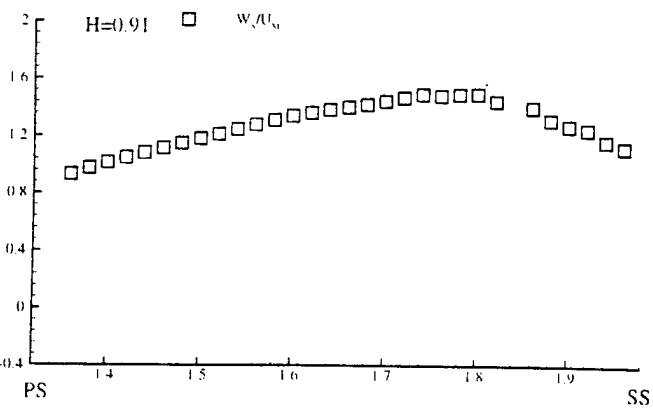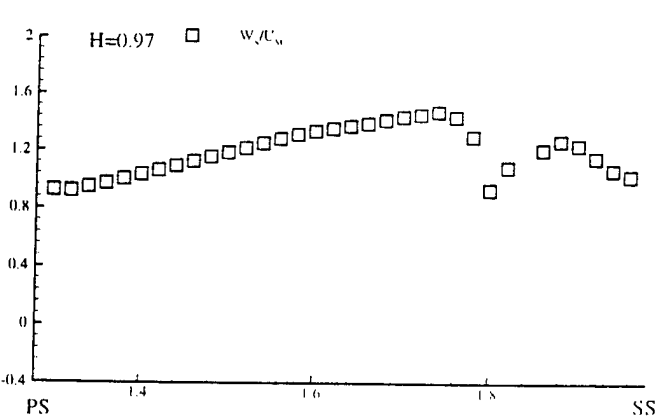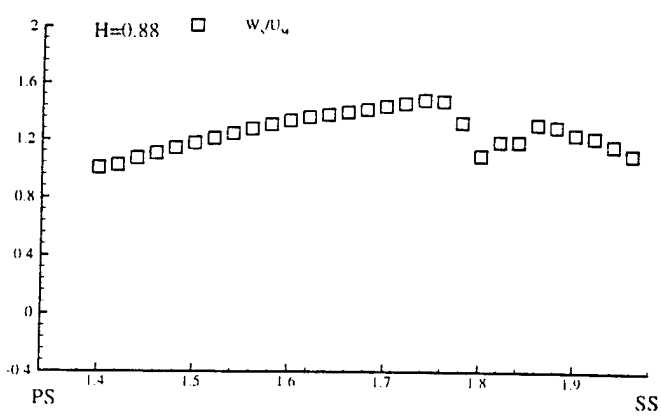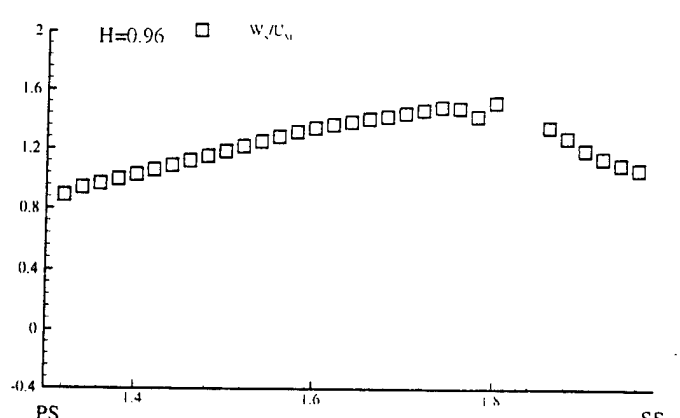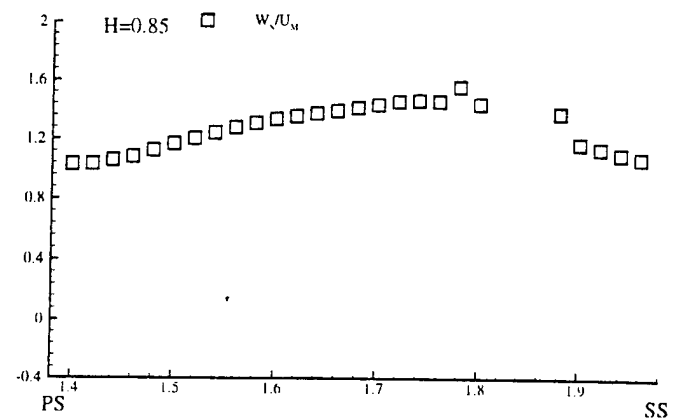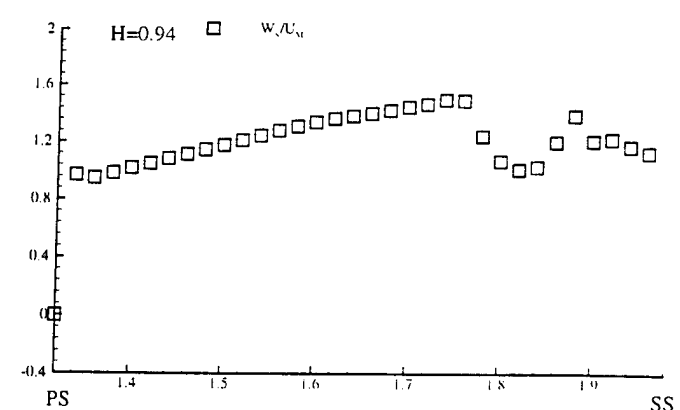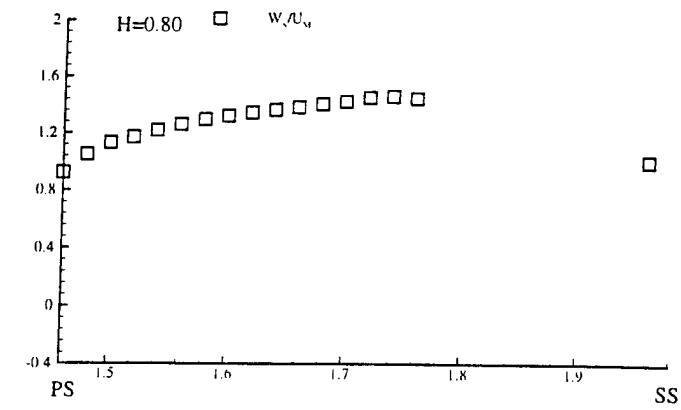
Figure 6.18 The distribution of total velocity from pressure surface to suction surface at the $X/C_{ax}=0.70$
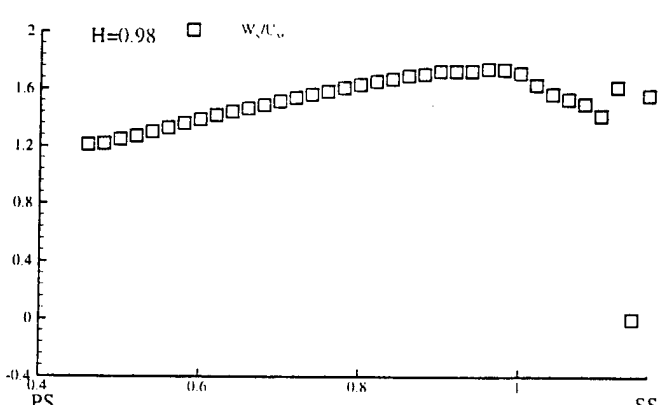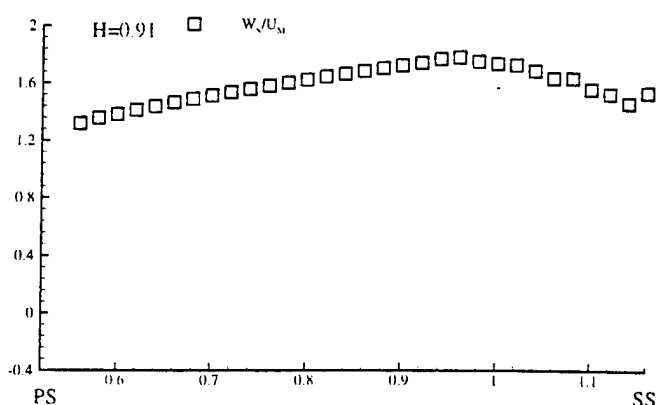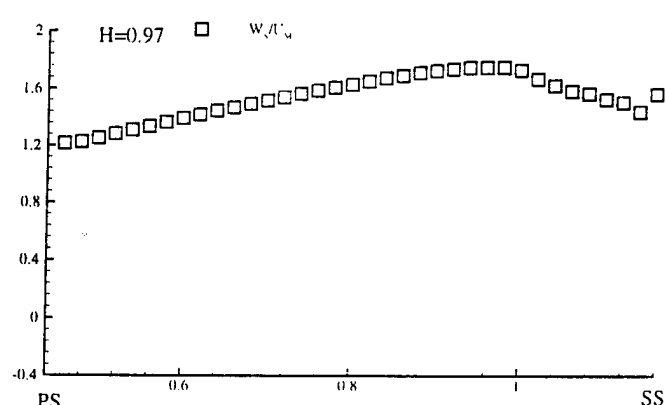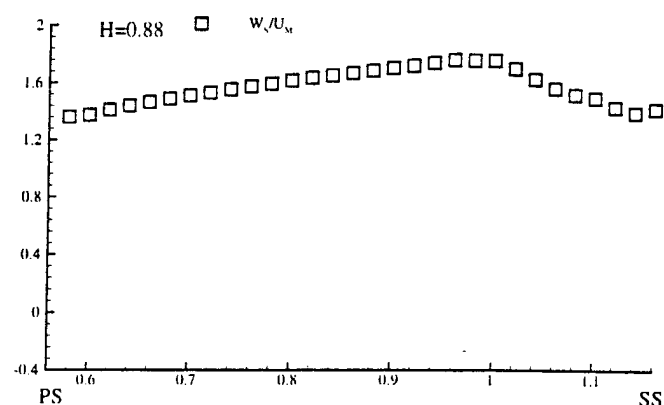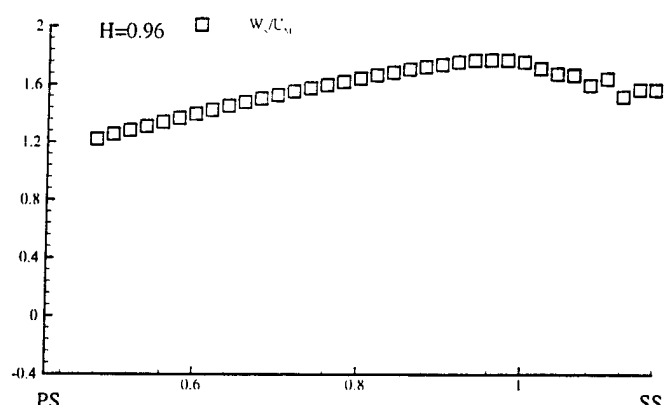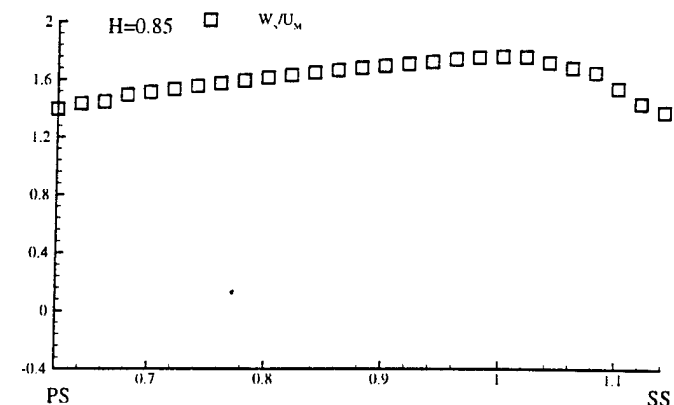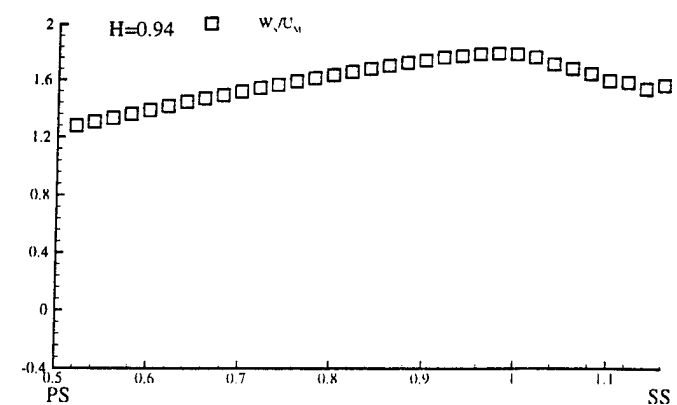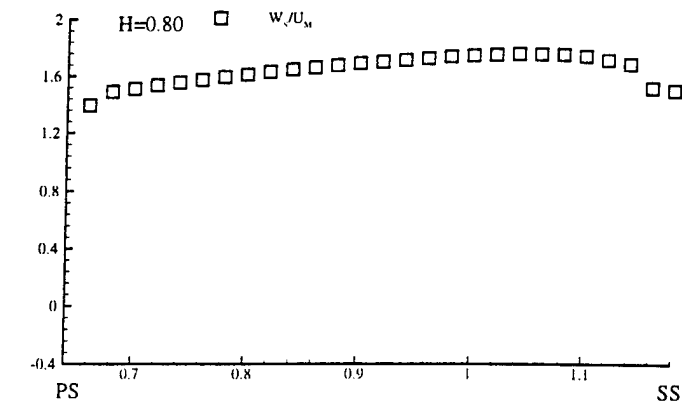
Figure 6.19 The distribution of total velocity from pressure surface to suction surface at the X/C$_{ax}$=0.80

73
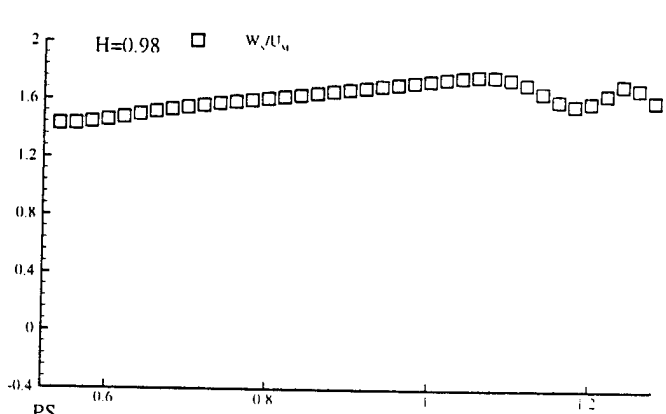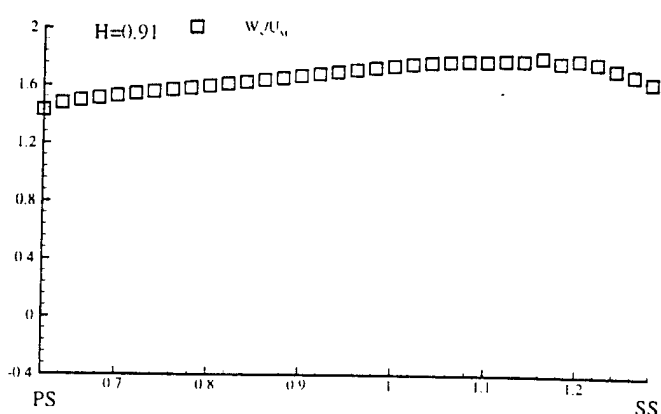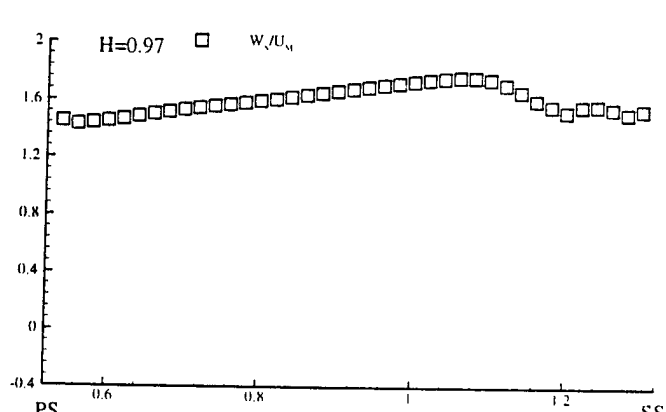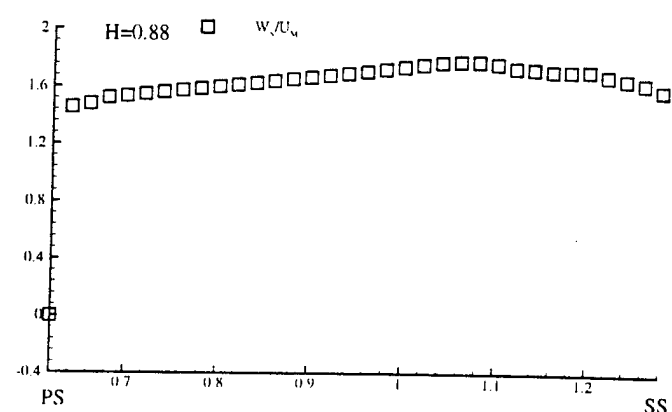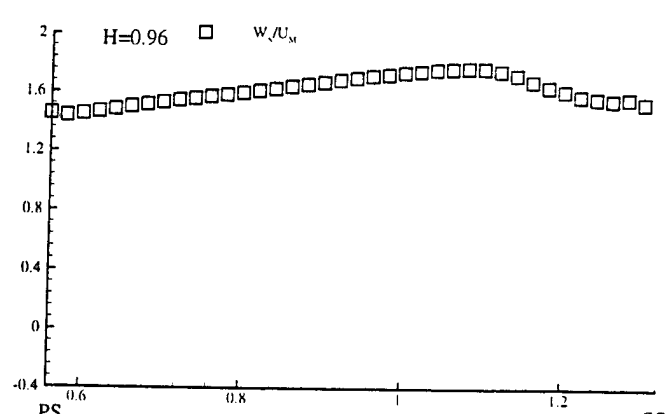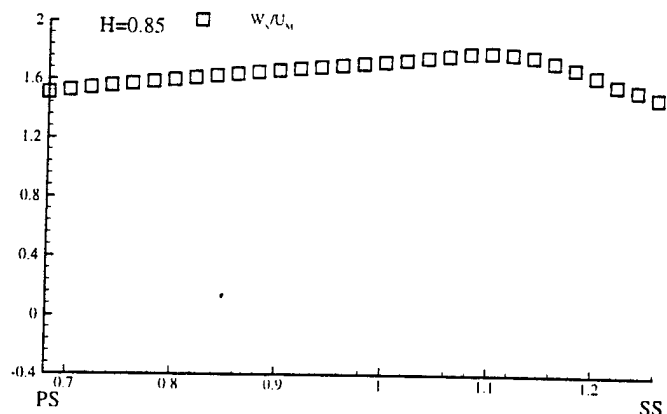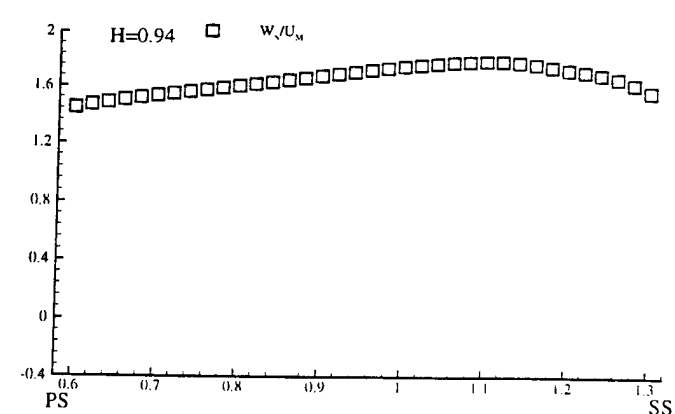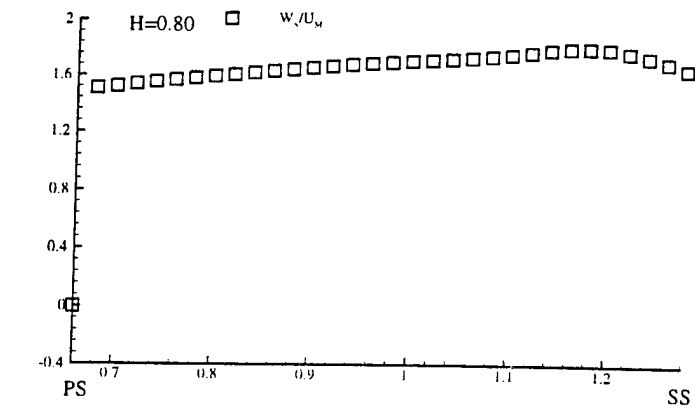
Figure 6.20 The distribution of total velocity from pressure surface to suction surface at the X/C$_{ax}$=0.90
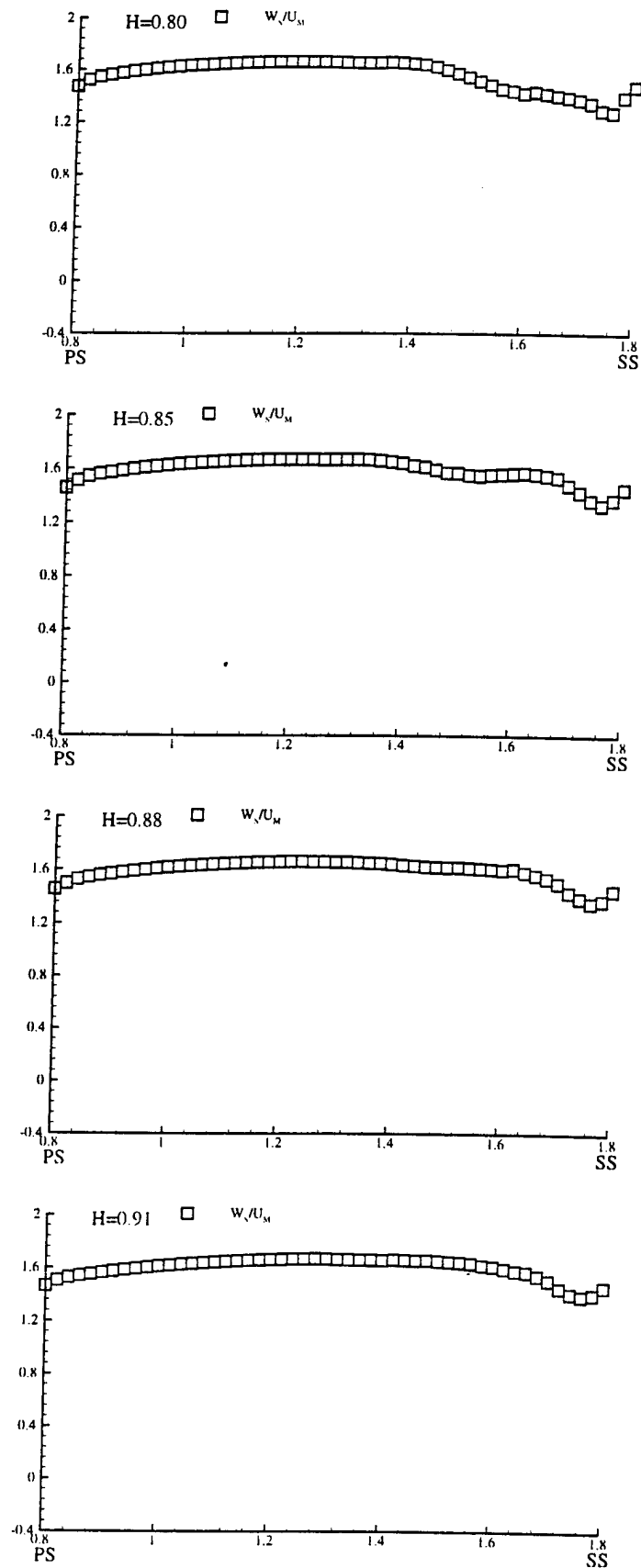
Figure 6.21 The distribution of total velocity from pressure surface to suction surface at the $X/C_{ax}=1.01$

75
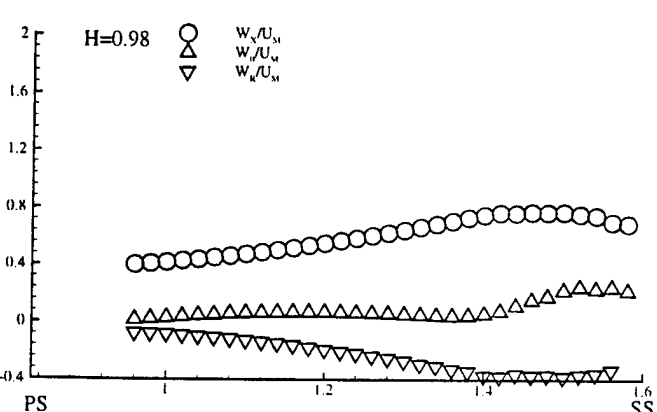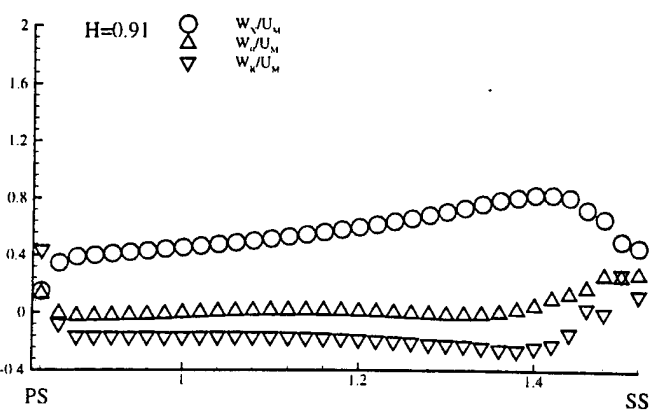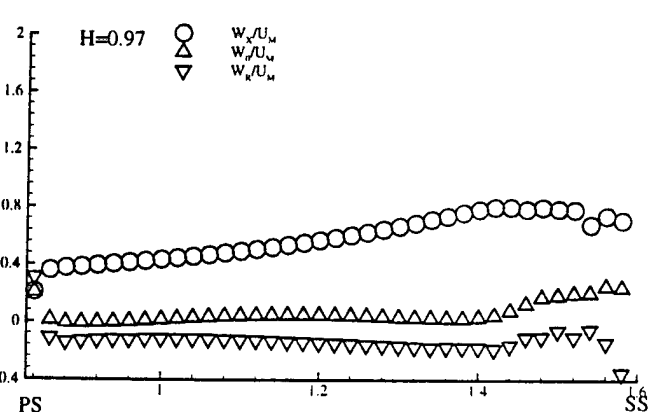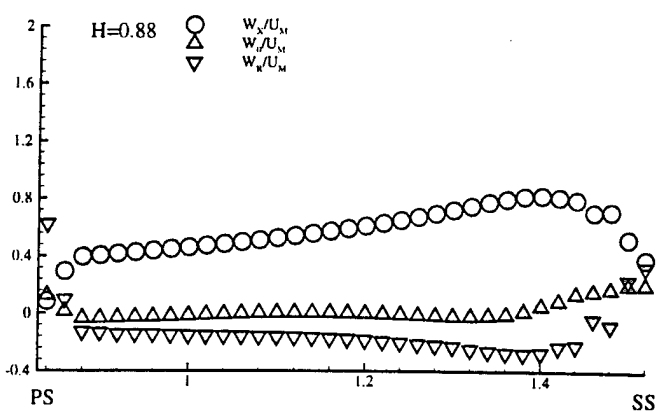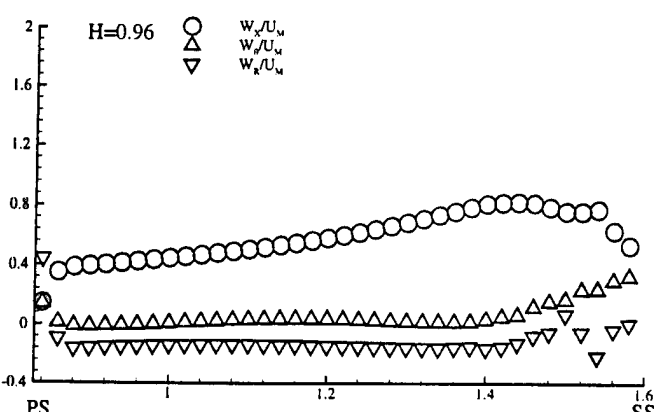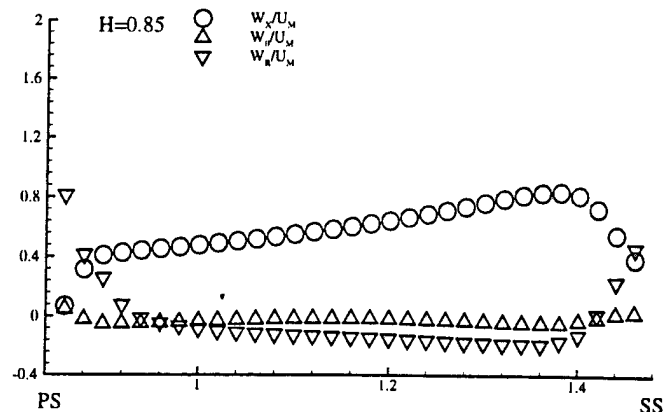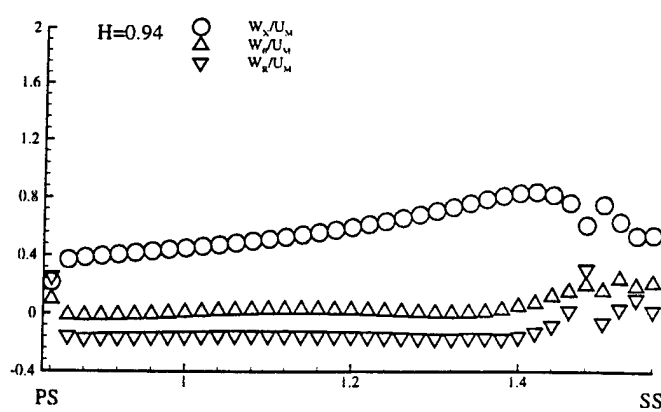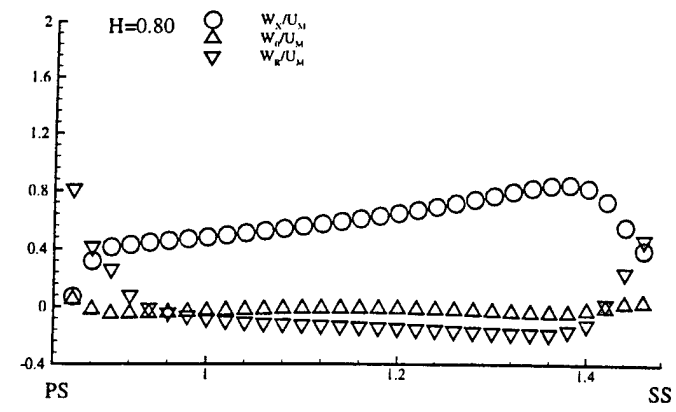
Figure 6.22 The distribution of relative velocity components from pressure surface to suction surface at the X/C_{ax}=0.20
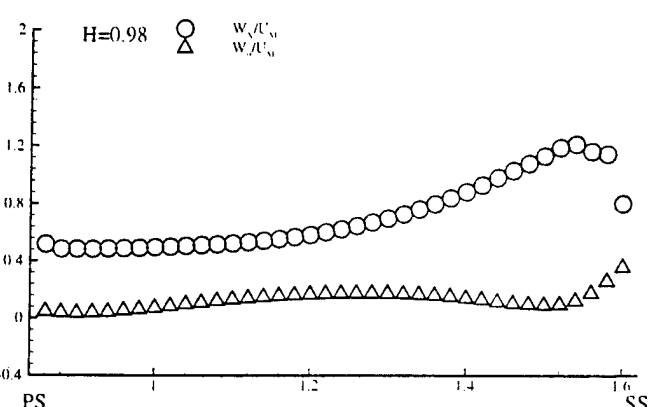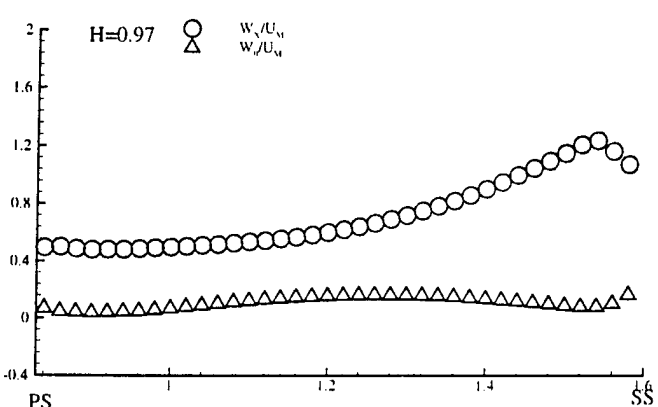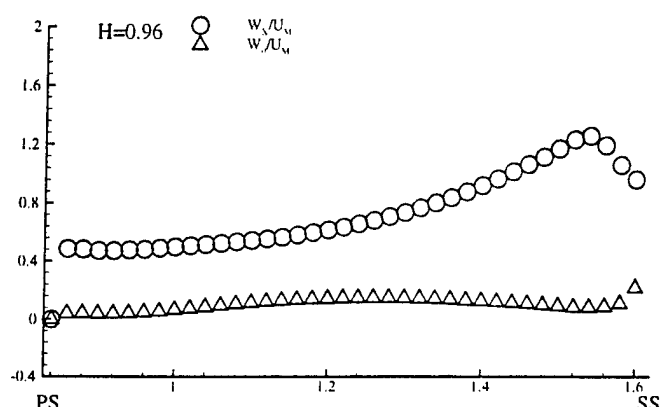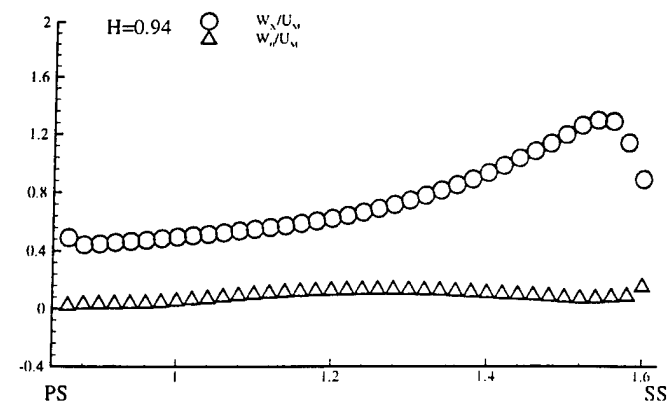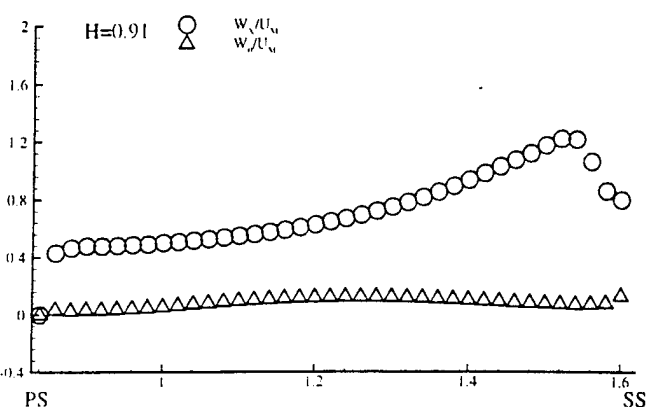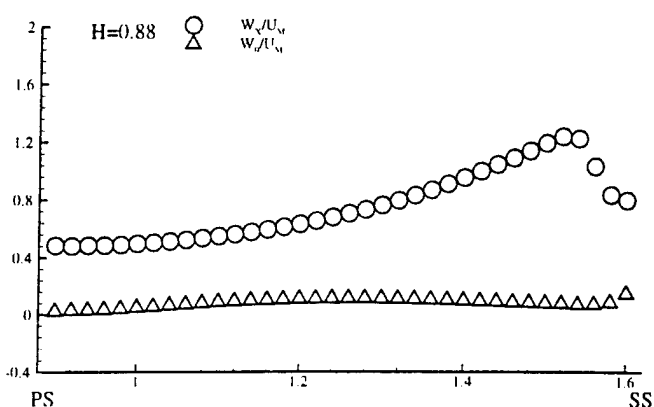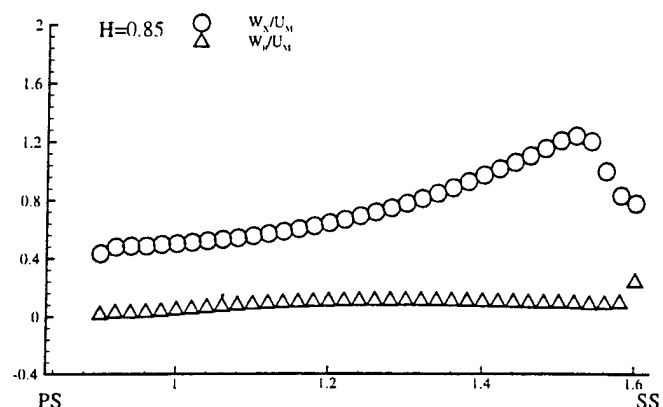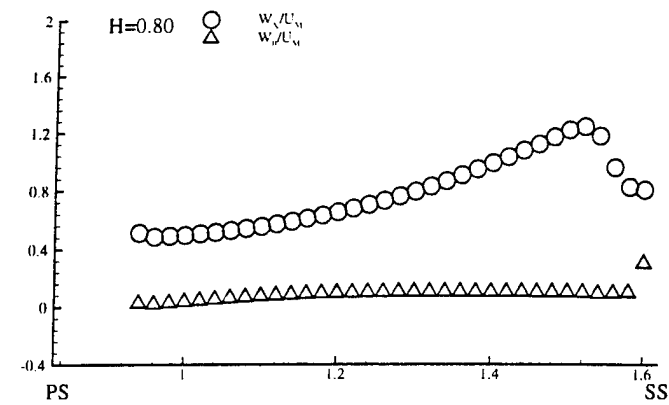
Figure 6.23 The distribution of relative velocity components from pressure surface to suction surface at the $X/C_{ax}=0.30$
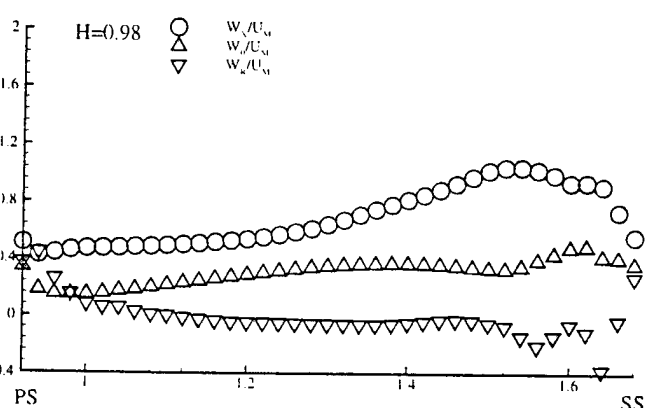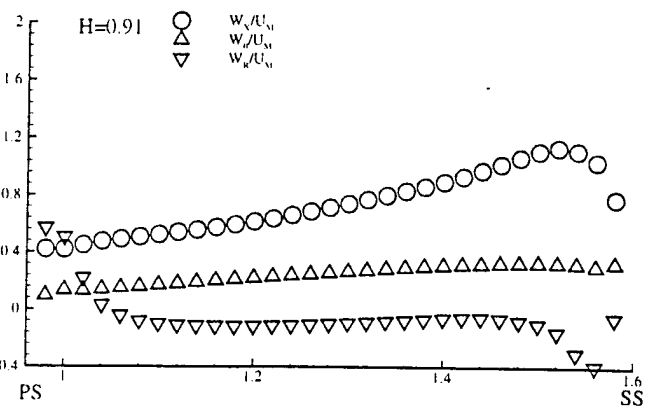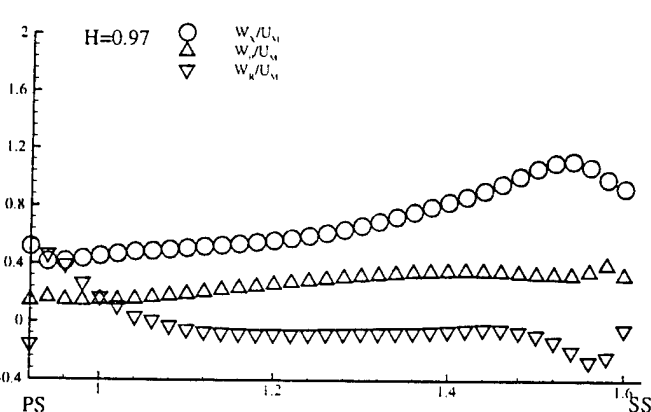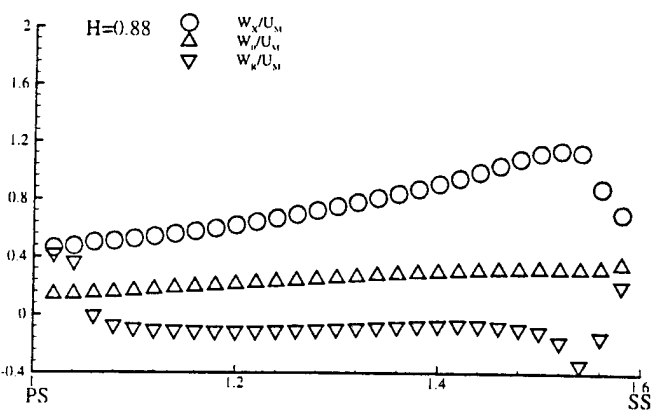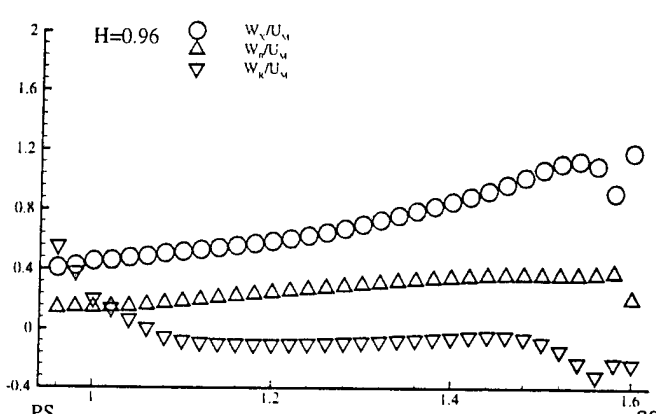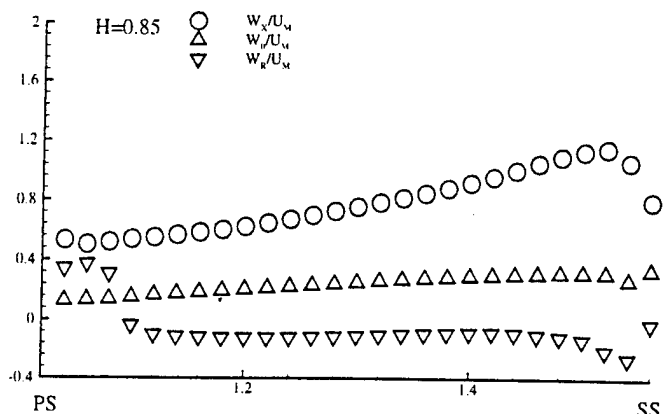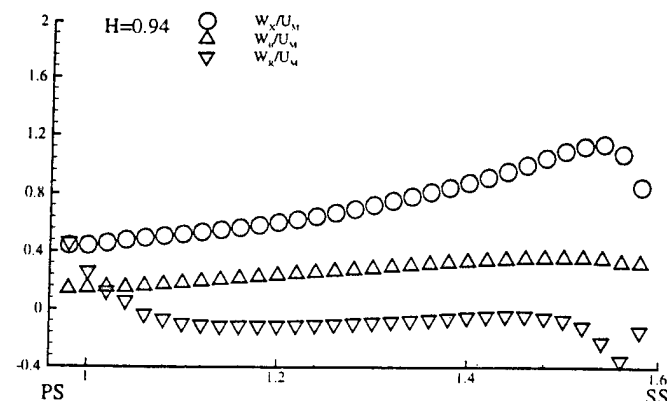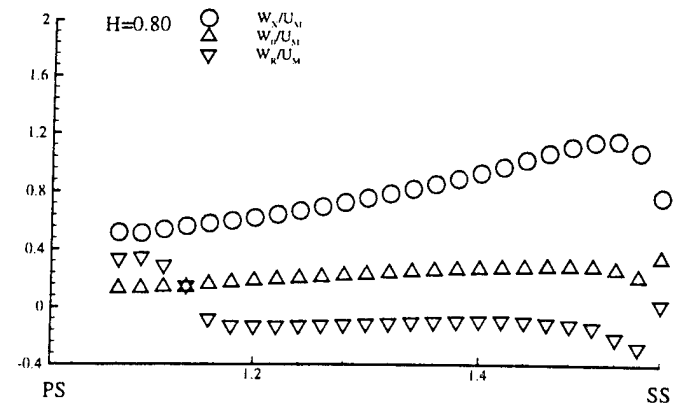
Figure 6.24 The distribution of relative velocity components from pressure surface to suction surface
at the X/C$_{ax}$=0.40

78
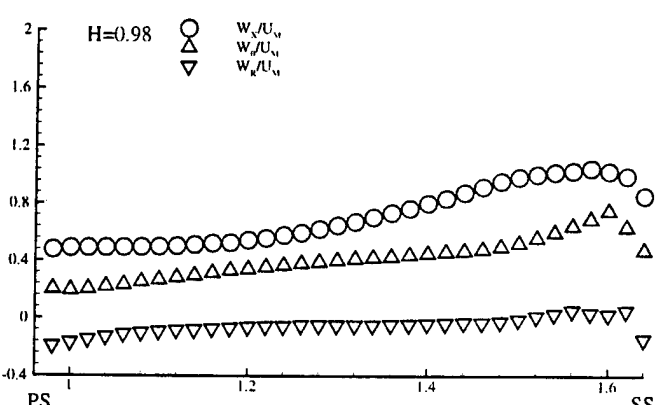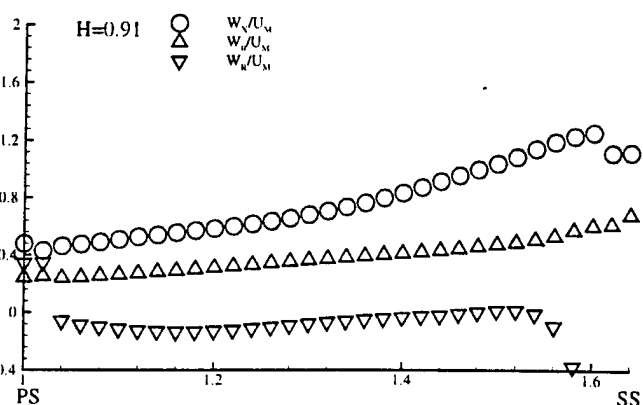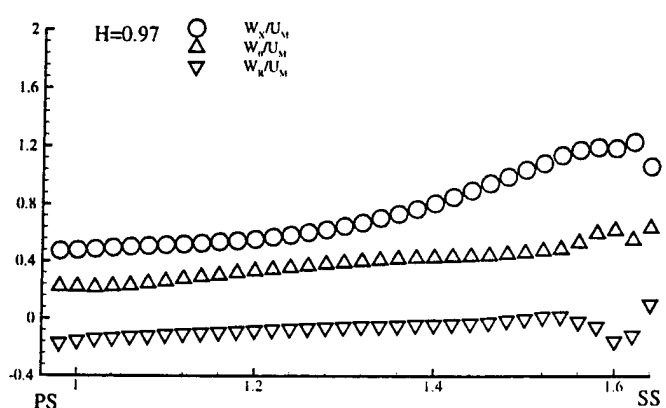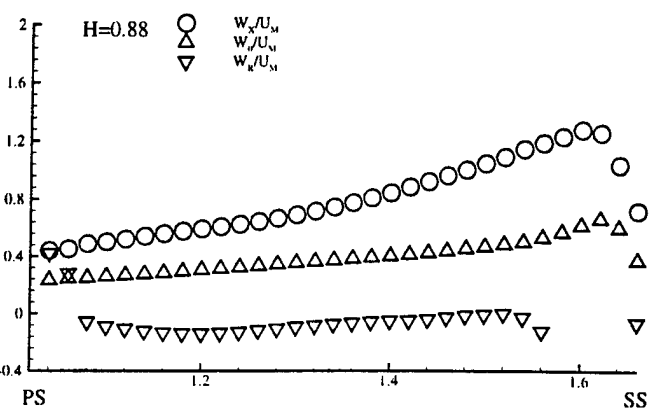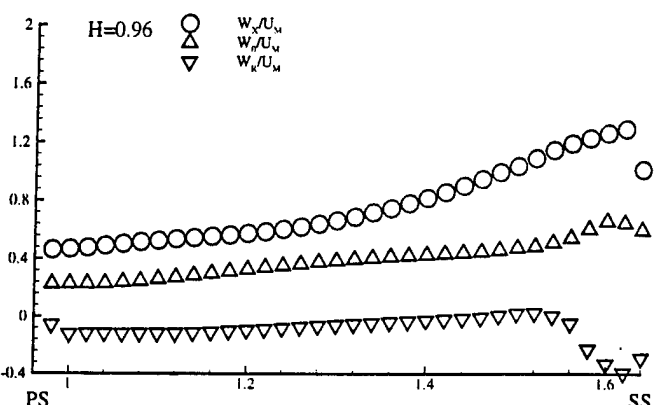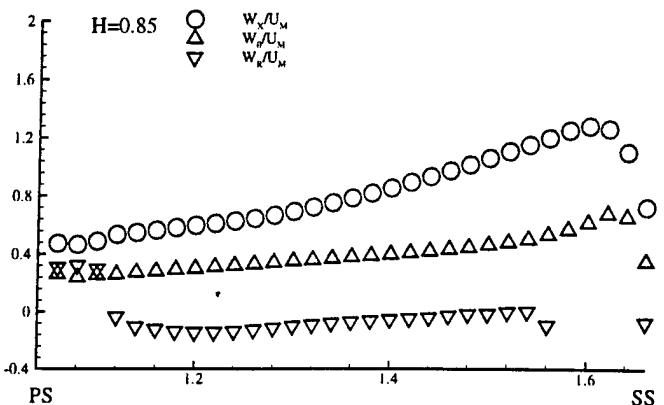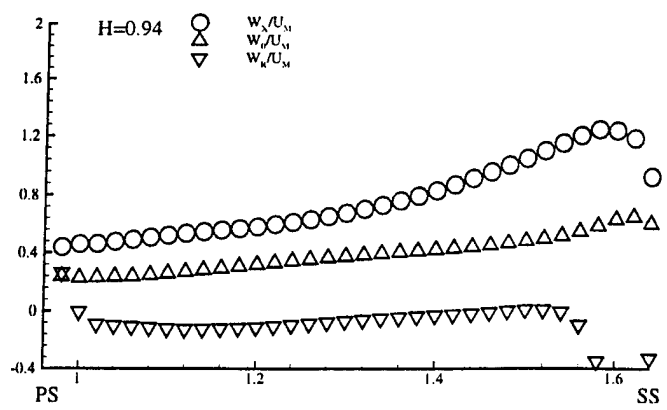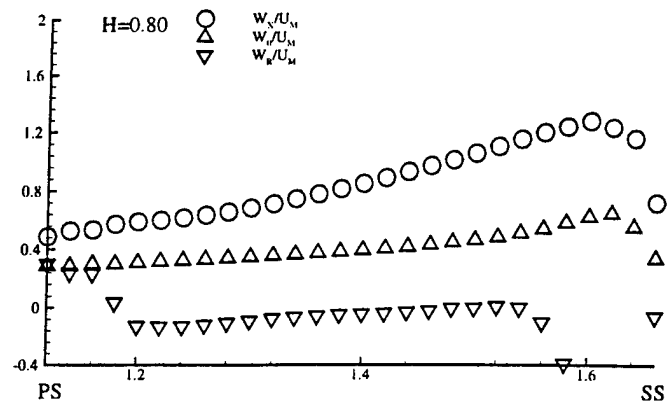
Figure 6.25 The distribution of relative velocity components from pressure surface to suction surface at the X/C$_{ax}$=0.50
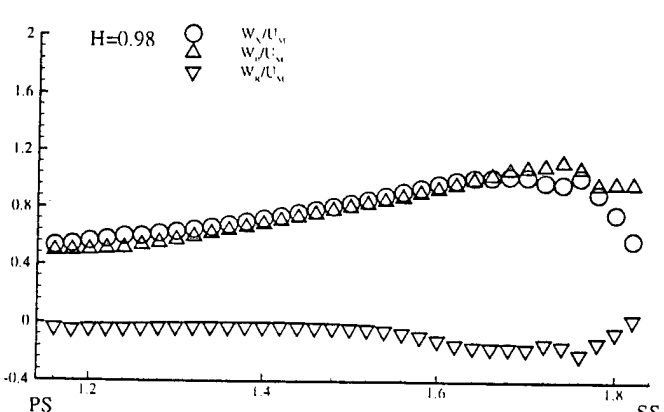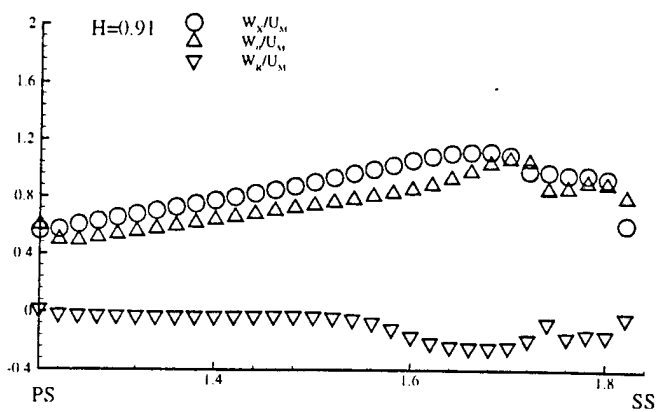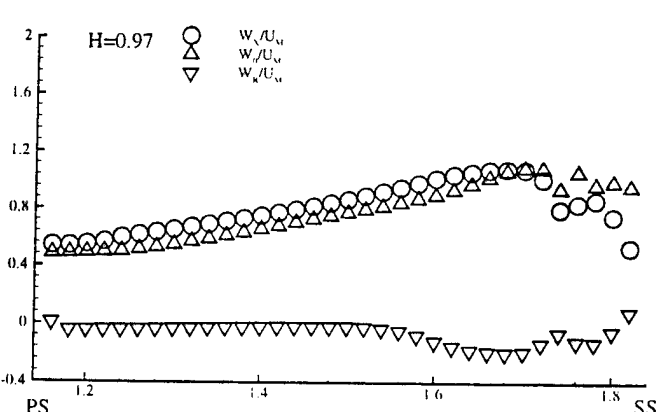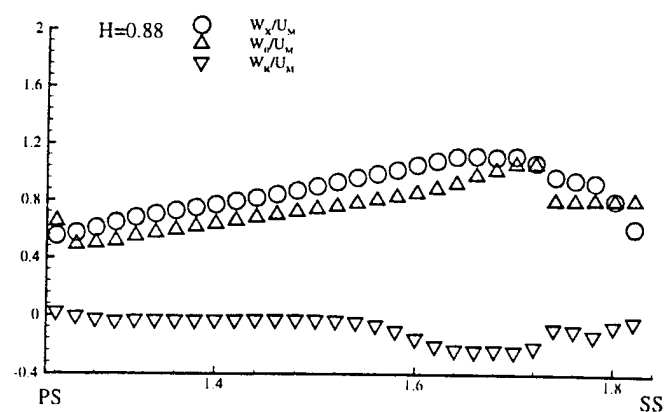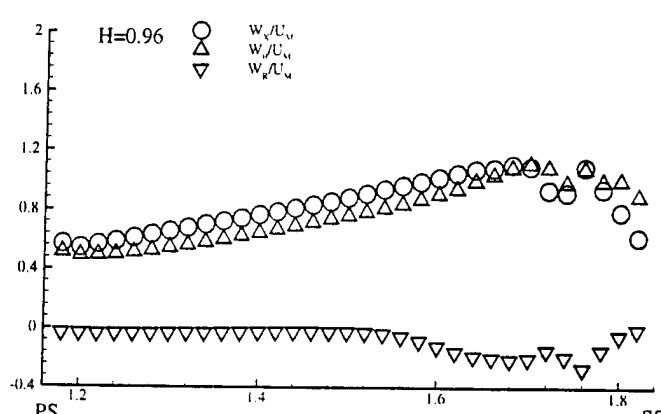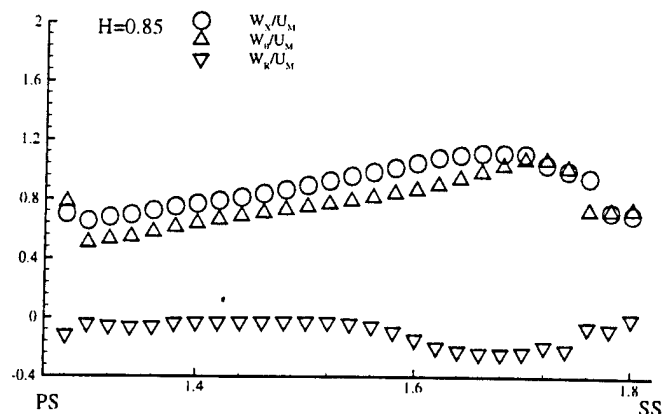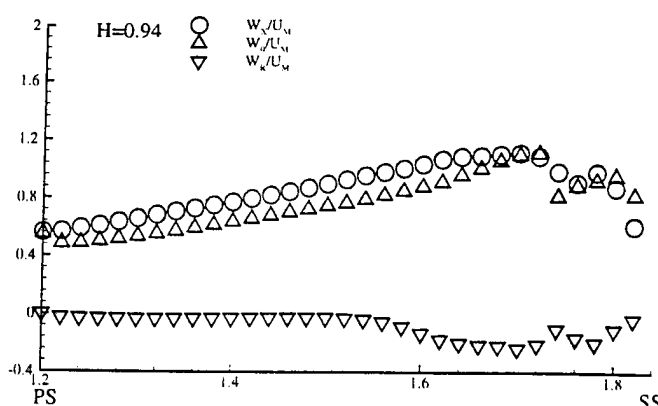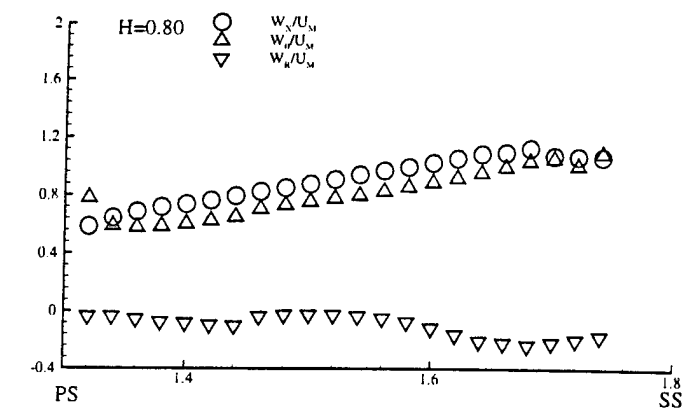
Figure 6.26 The distribution of relative velocity components from pressure surface to suction surface at the X/C$_{ax}$=0.60
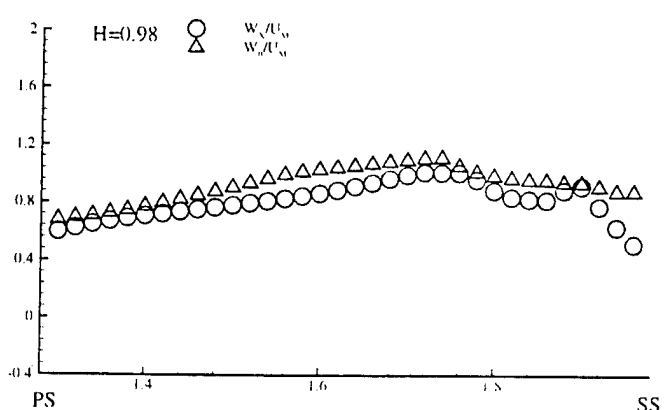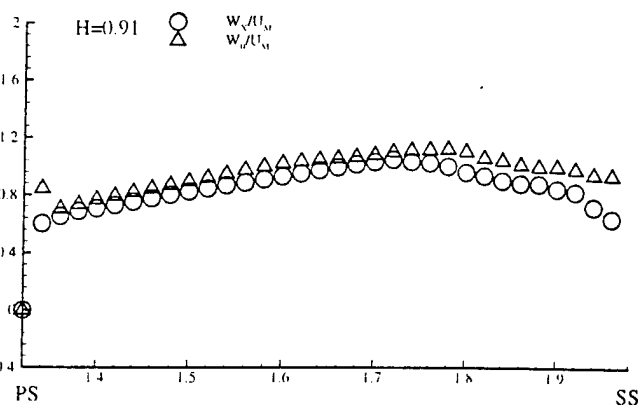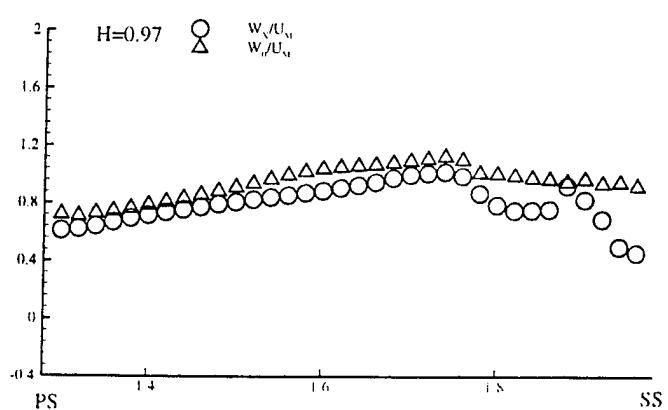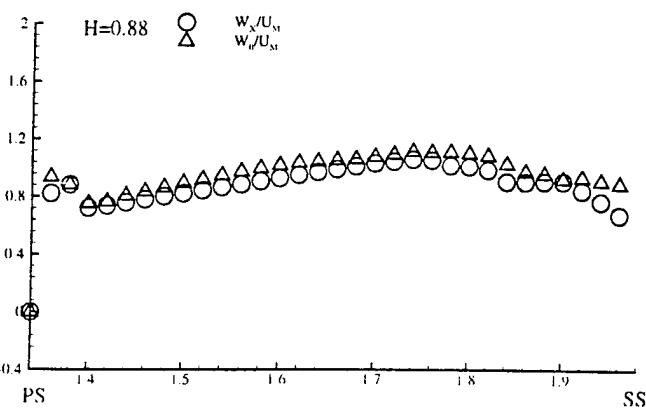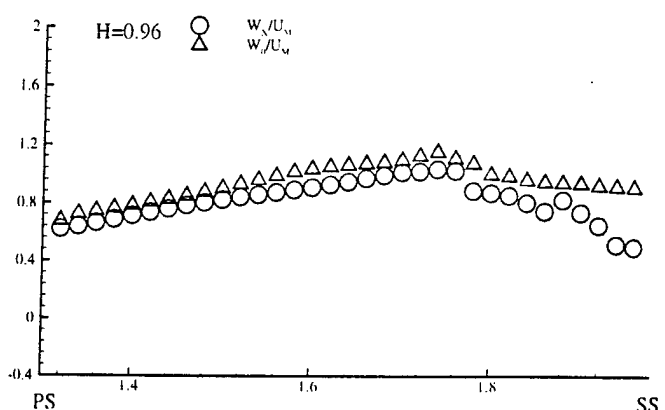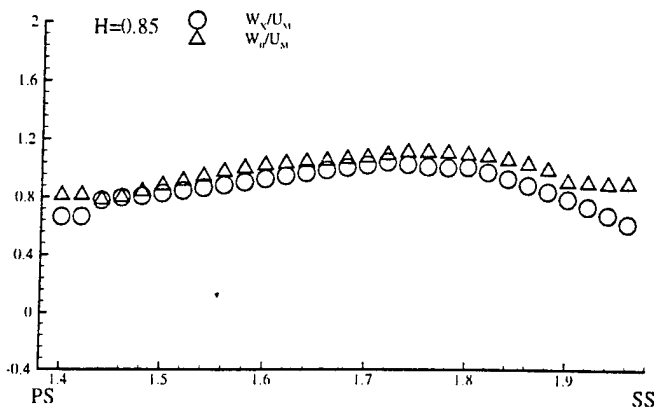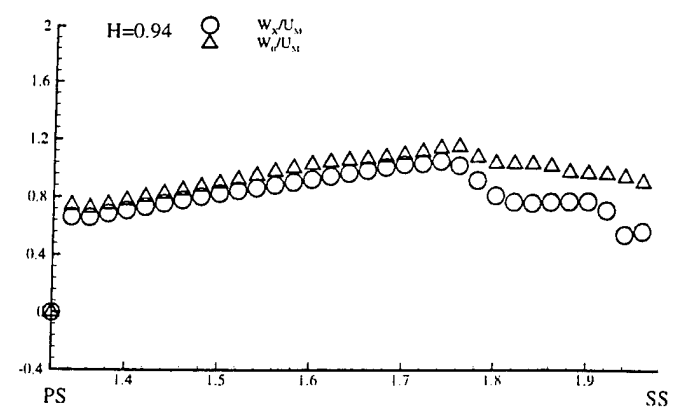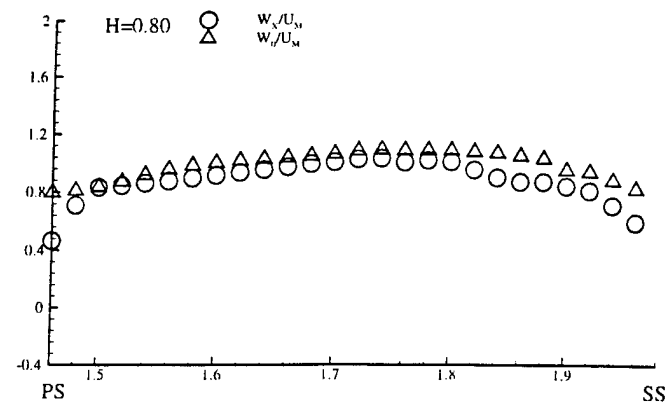
Figure 6.27 The distribution of relative velocity components from pressure surface to suction surface at the X/C$_{ax}$=0.70
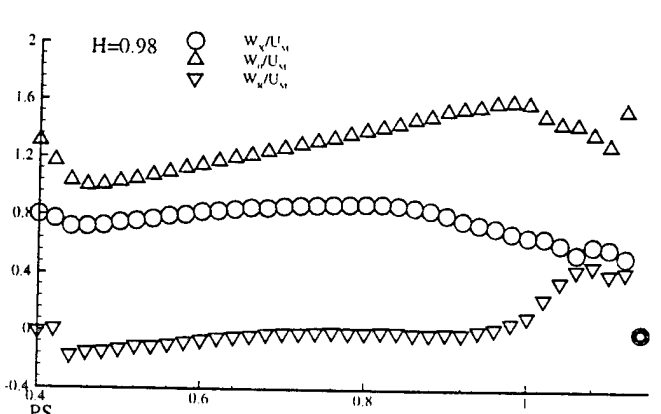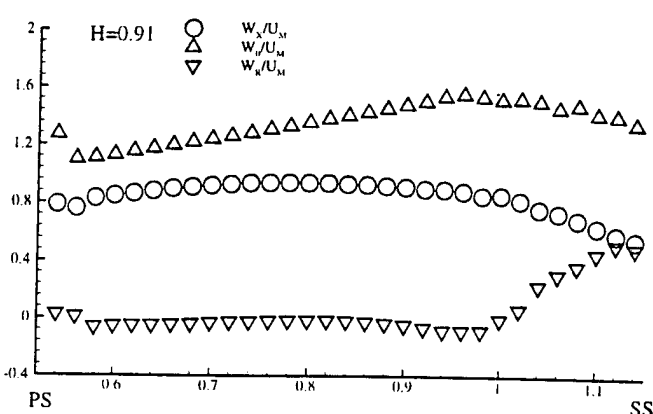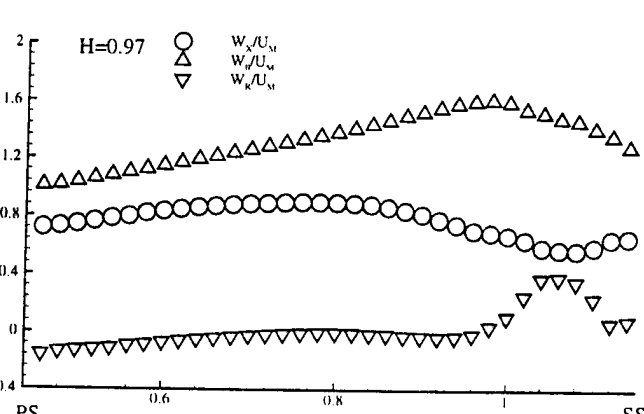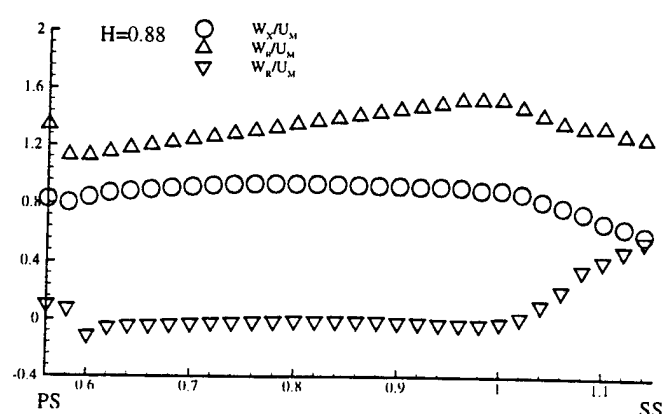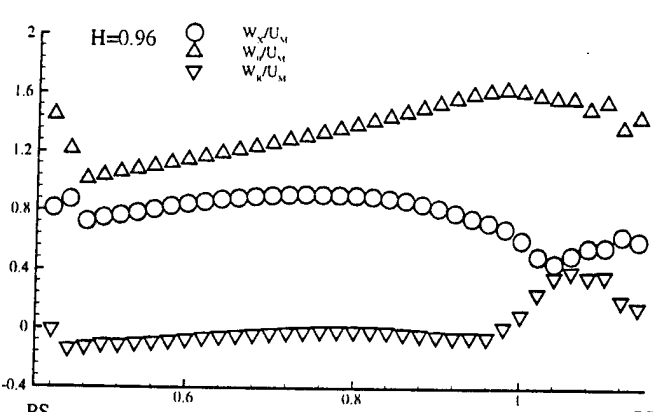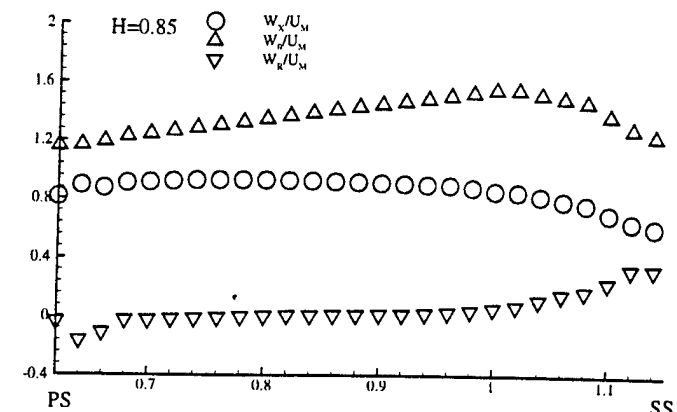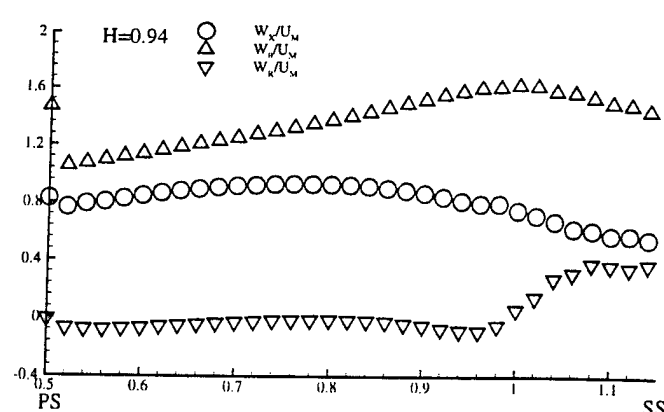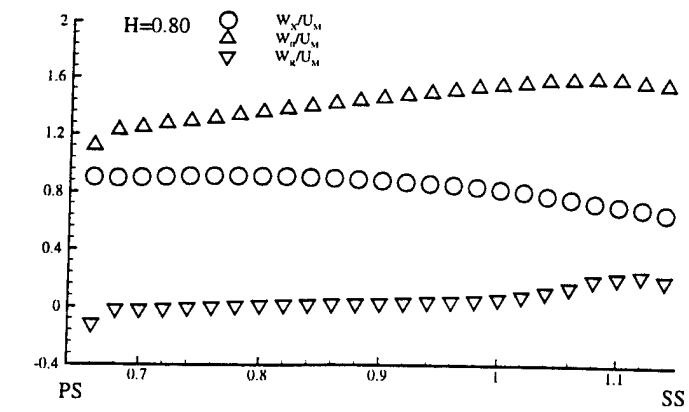
Figure 6.28 The distribution of relative velocity components from pressure surface to suction surface at the $X/C_{ax}=0.80$
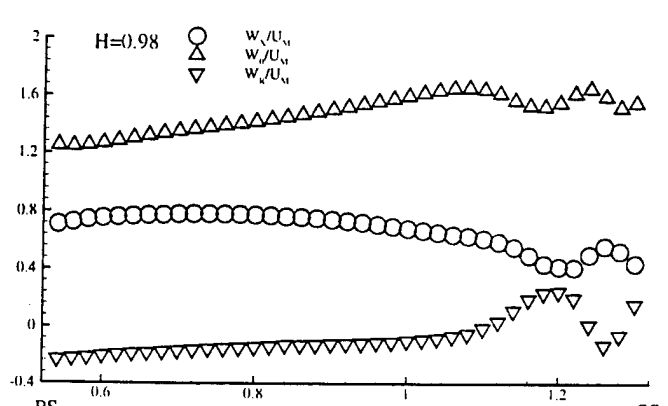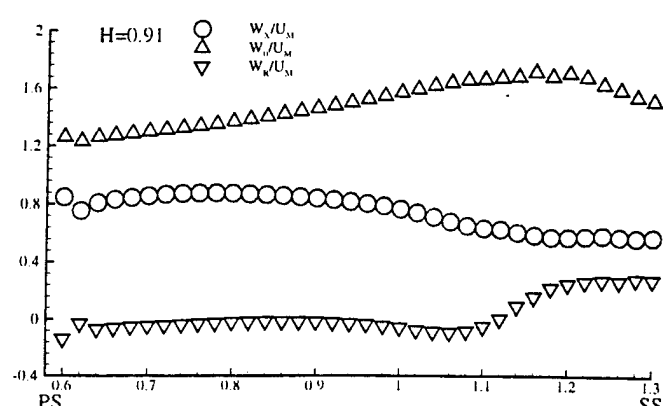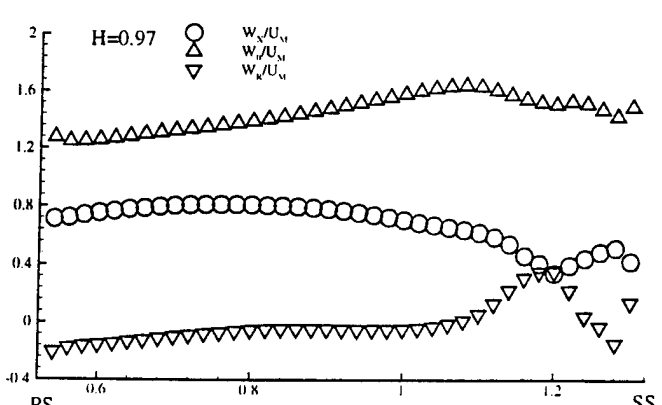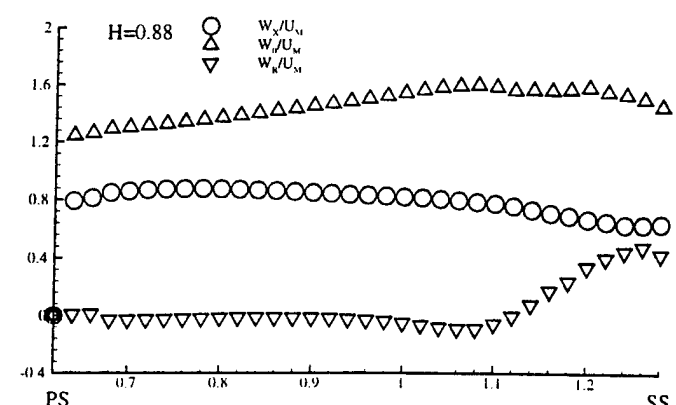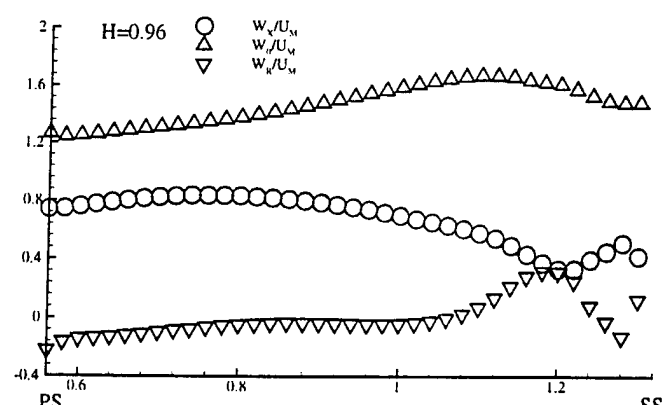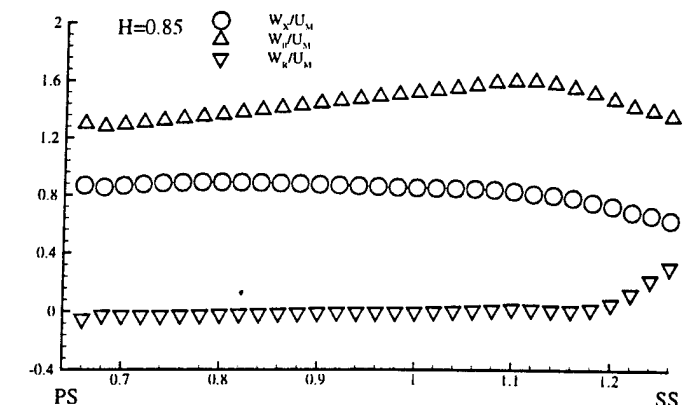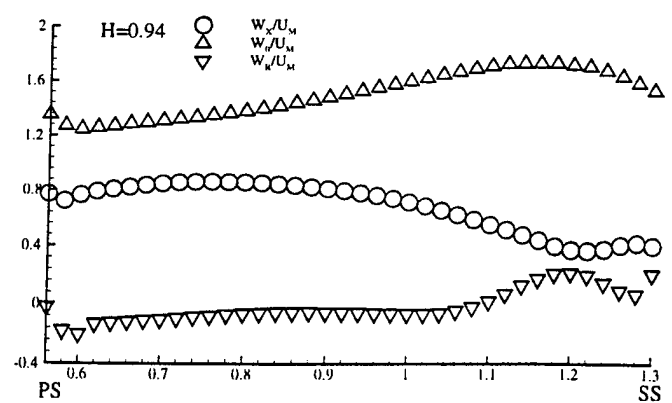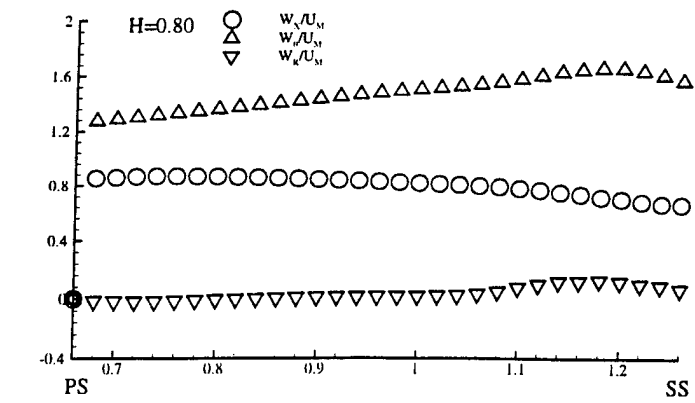
Figure 6.29 The distribution of relative velocity components from pressure surface to suction surface at the X/C$_{ax}$=0.90

83
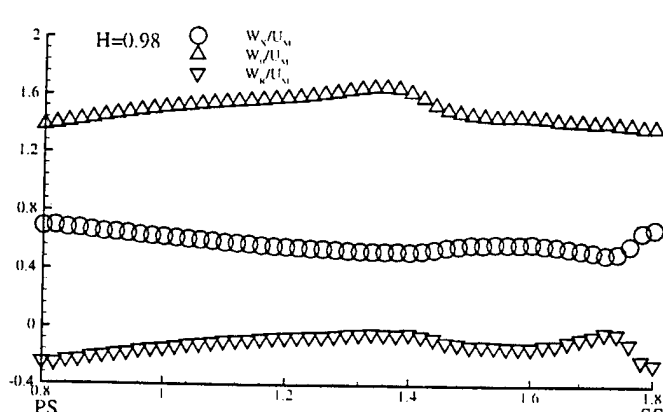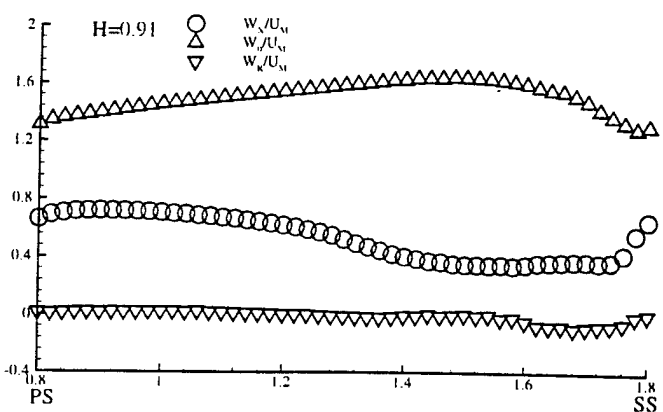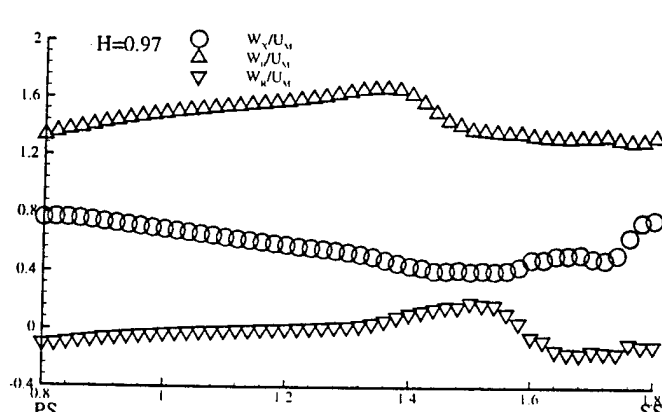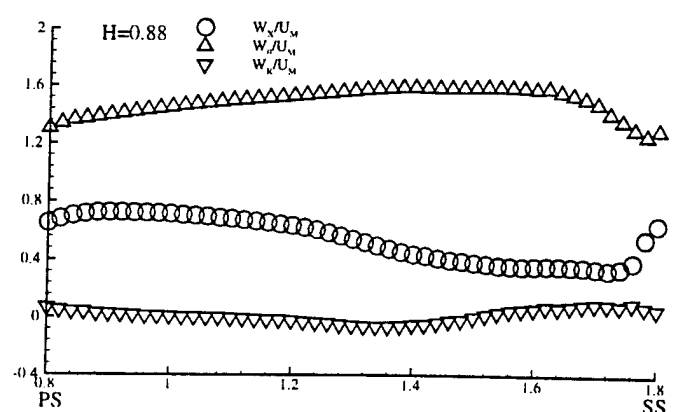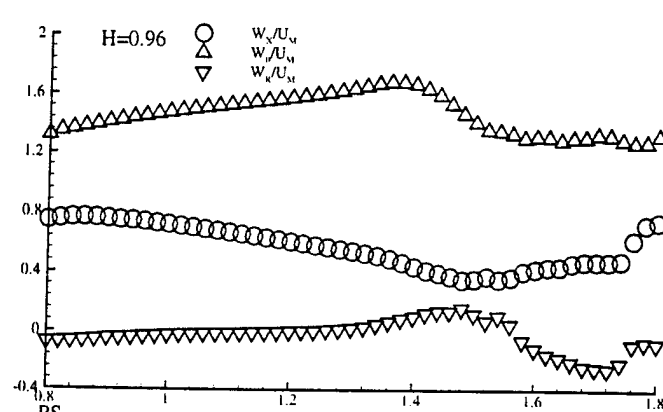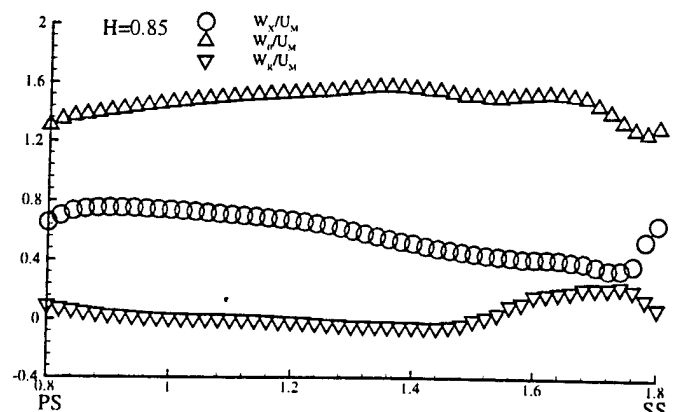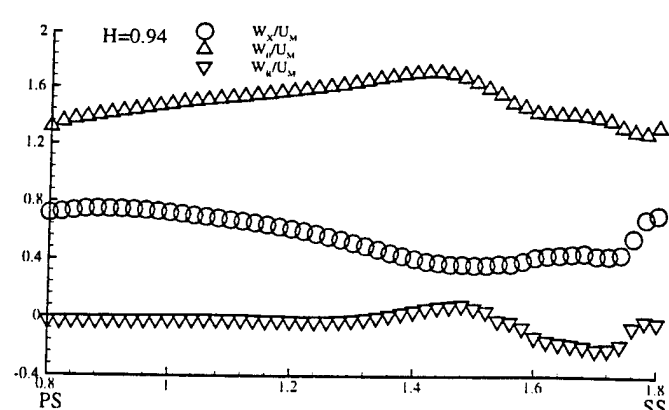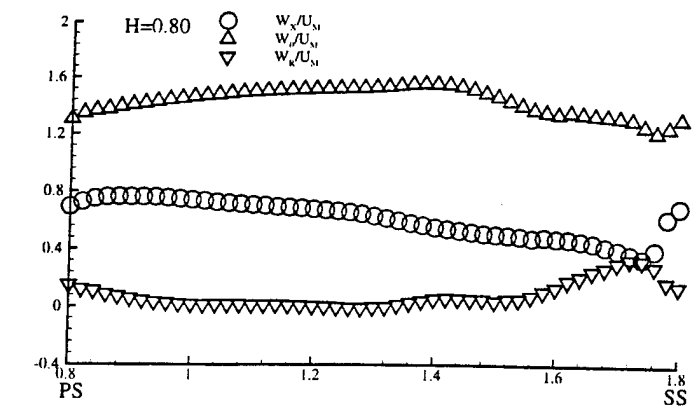
Figure 6.30 The distribution of relative velocity components from pressure surface to suction surface at the $X/C_{ax}=1.01$
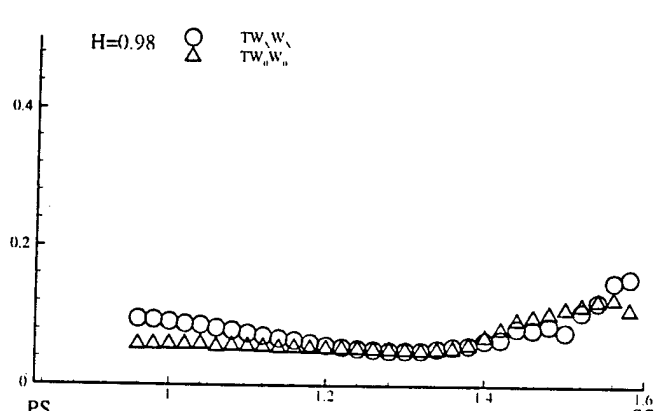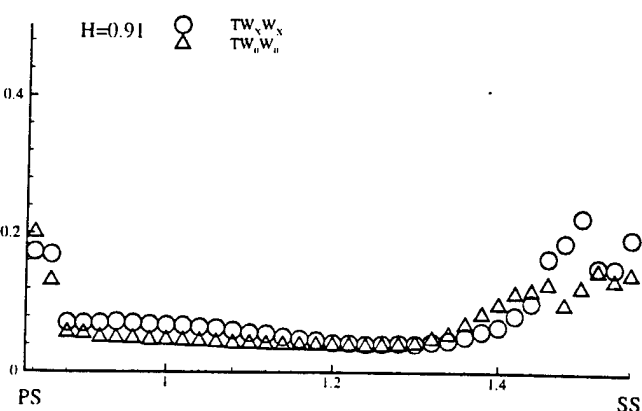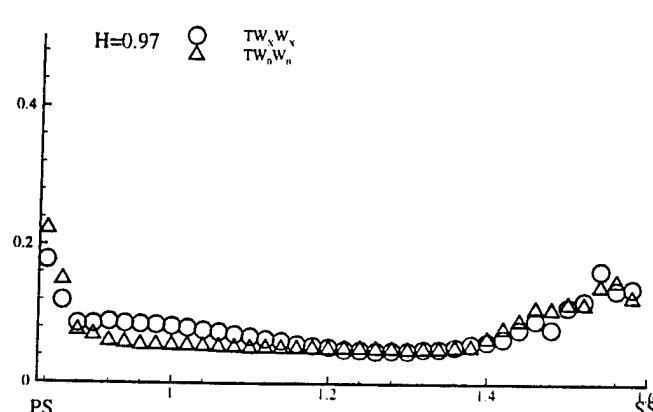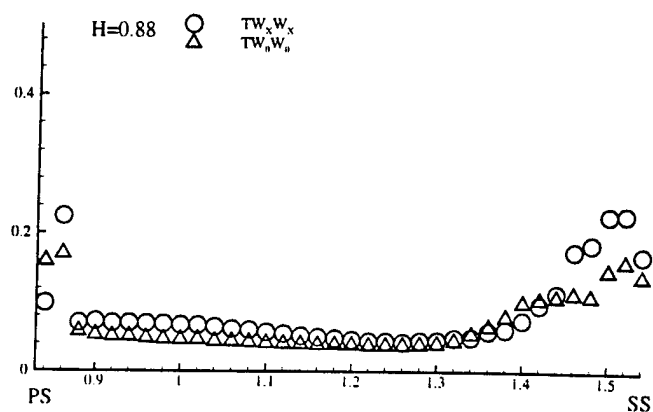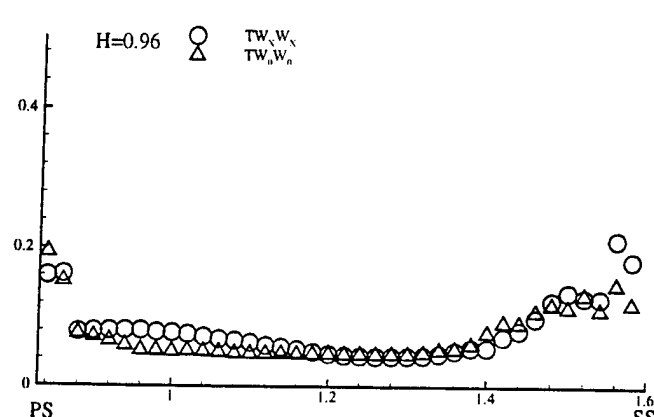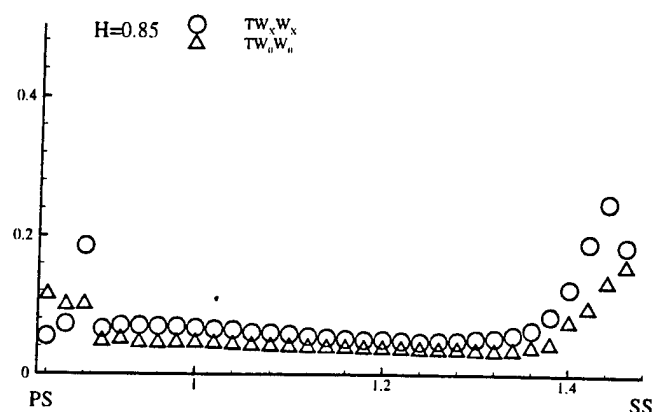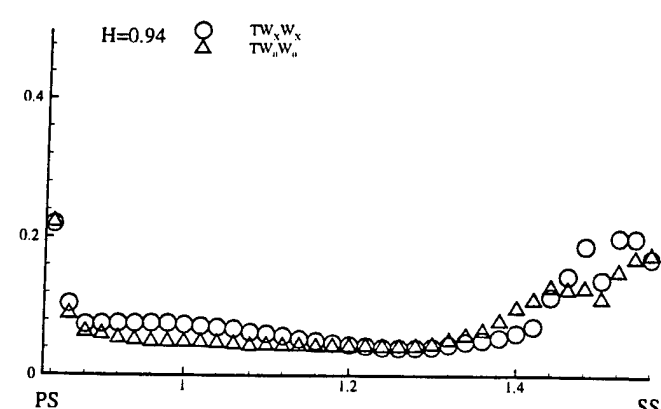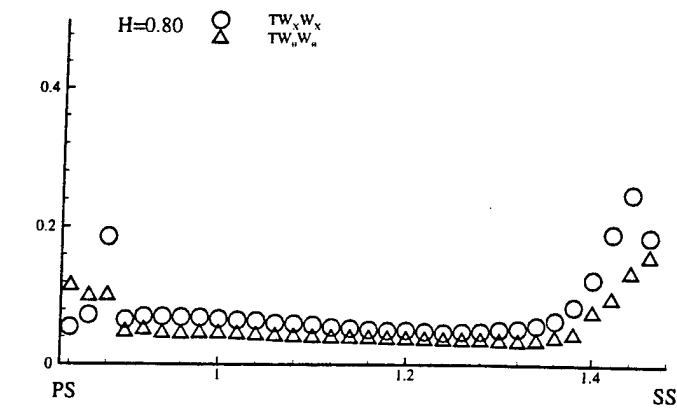
Figure 6.31 The distribution of the velocity fluctuation correlations from pressure surface to suction surface at the X/C_{ax}=0.20
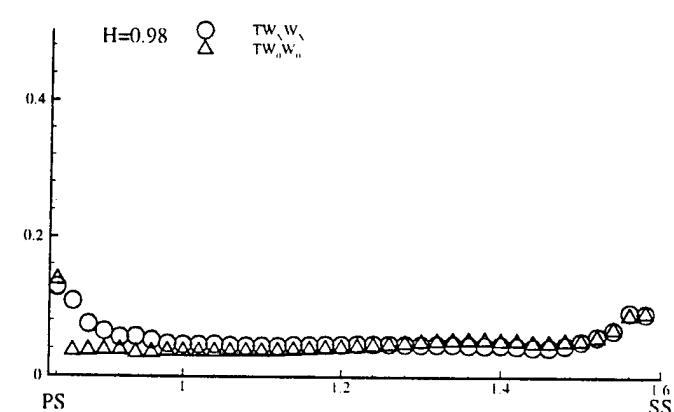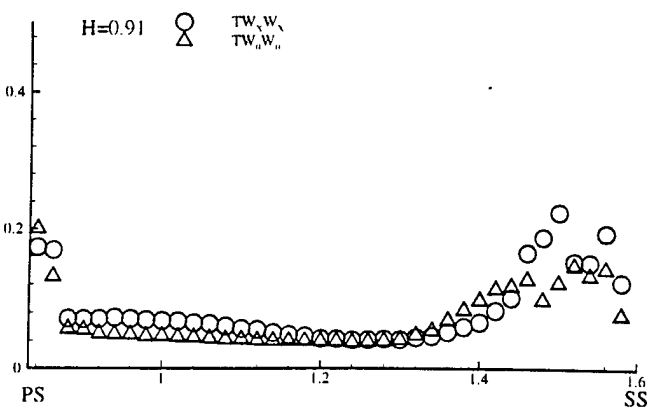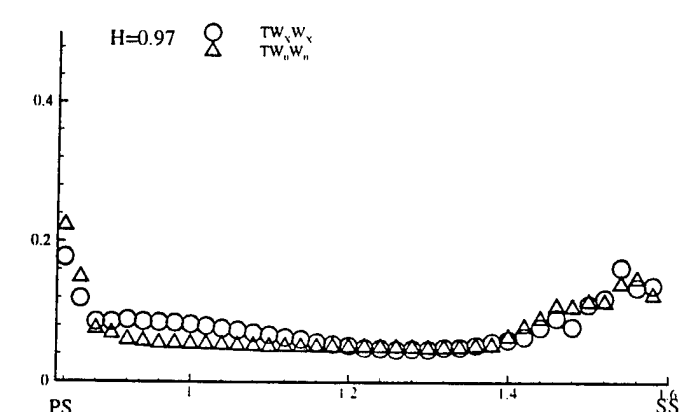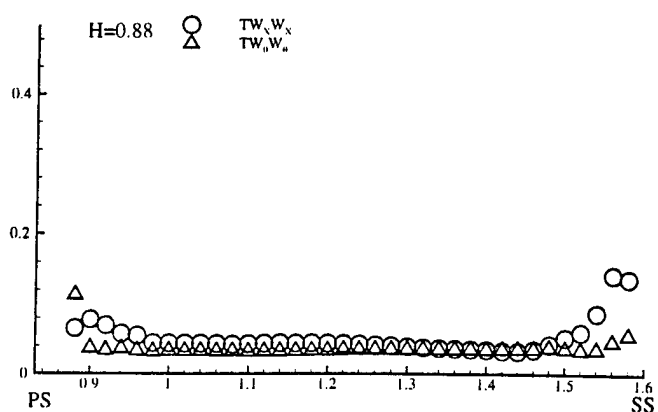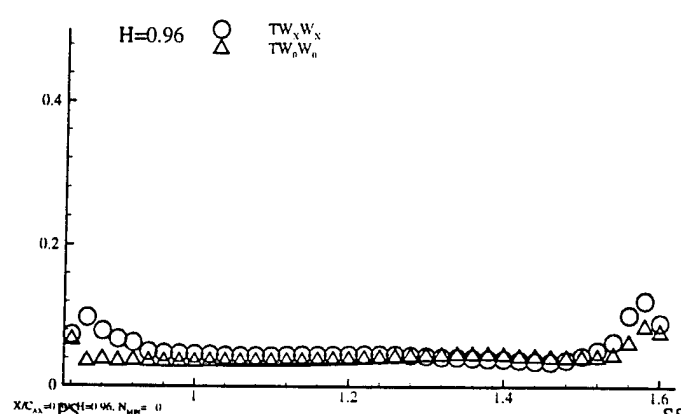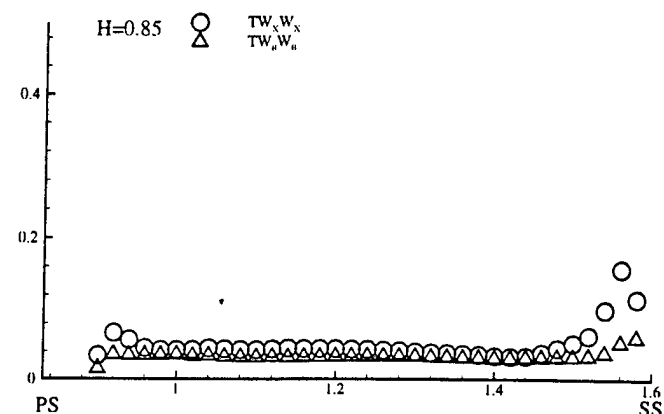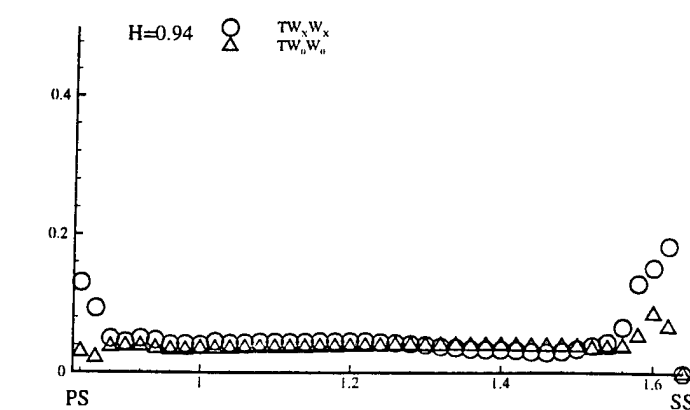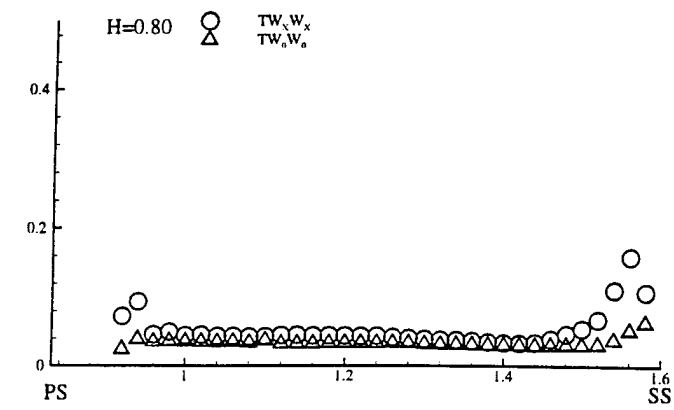
Figure 6.32 The distribution of the velocity fluctuation correlations from pressure surface to suction surface at the X/C$_{ax}$=0.30
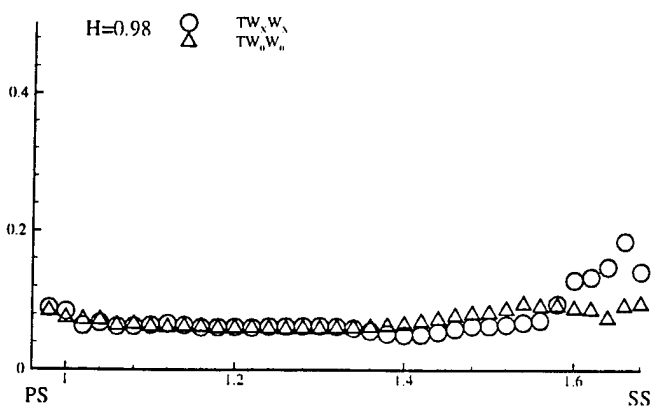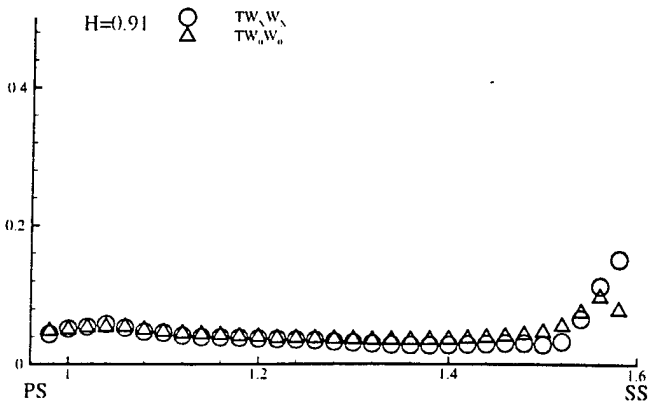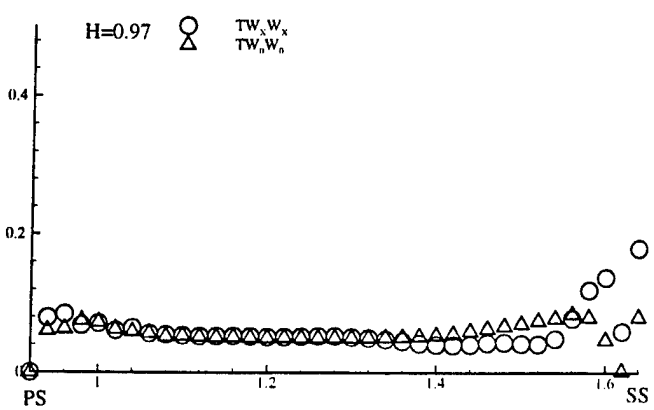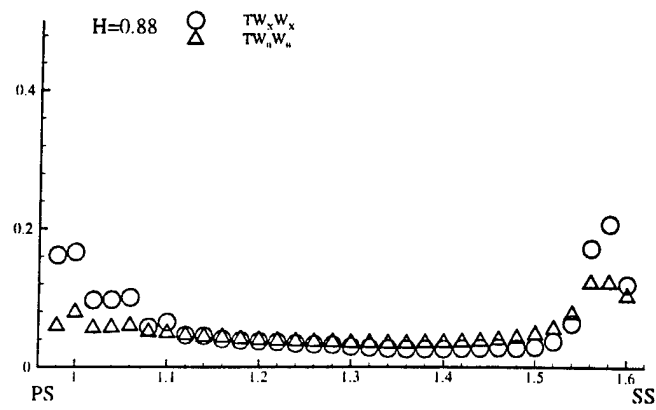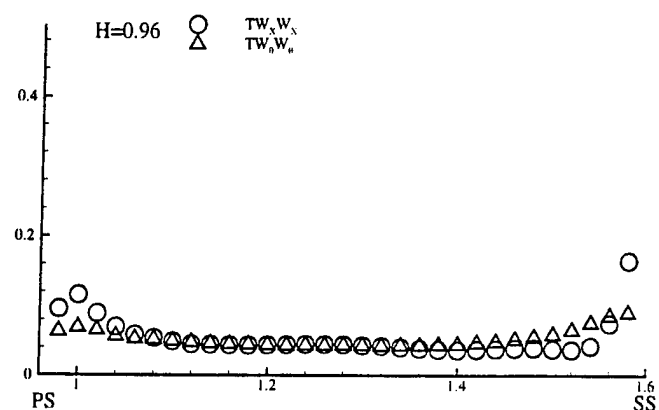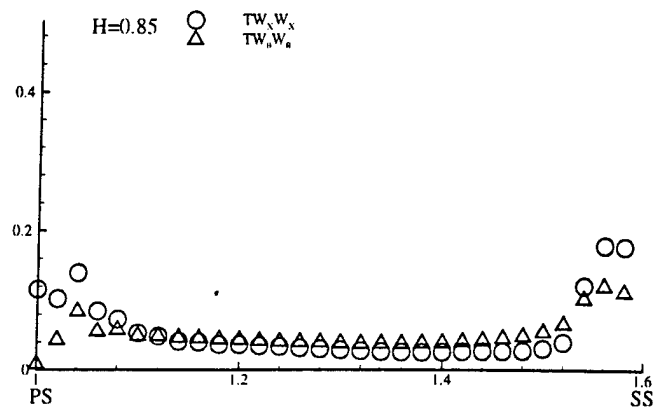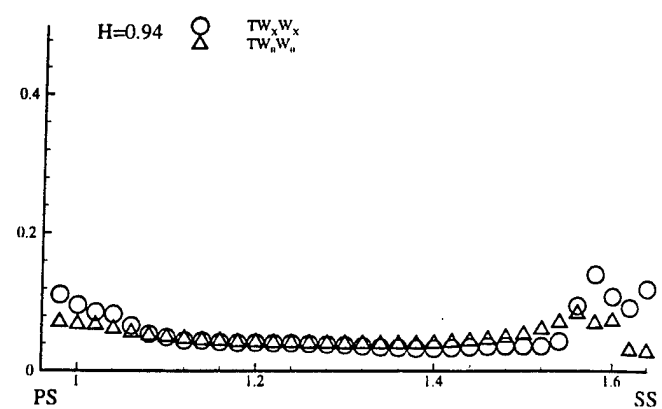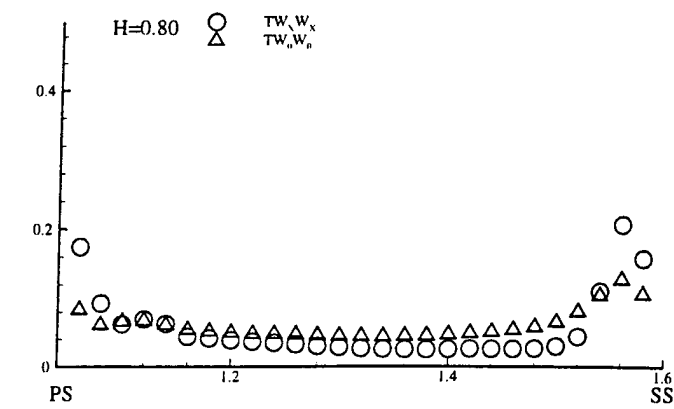
Figure 6.33 The distribution of the velocity fluctuation correlations from pressure surface to suction surface at the X/C_{ax} =0.40
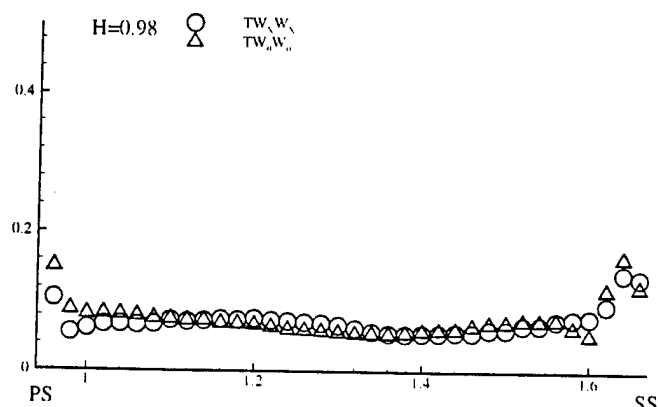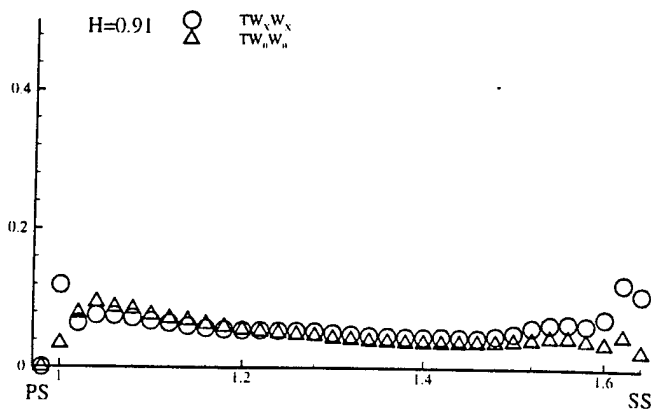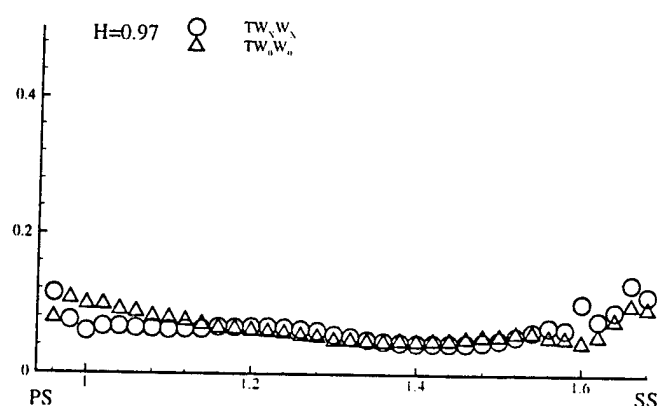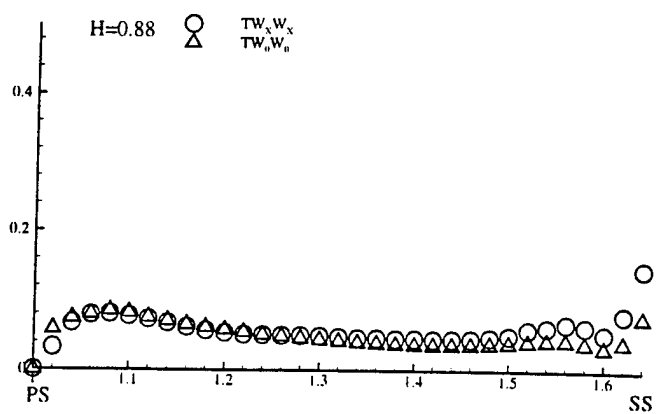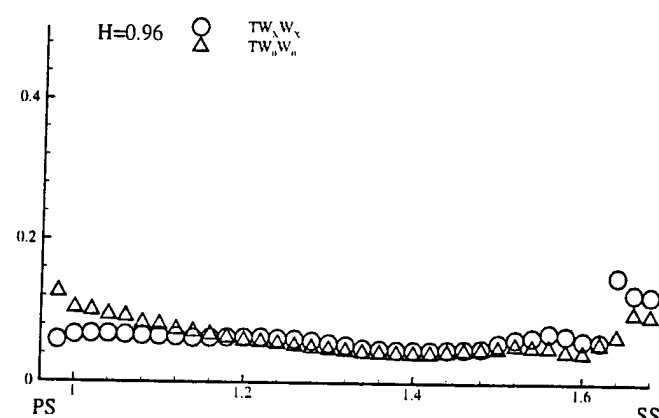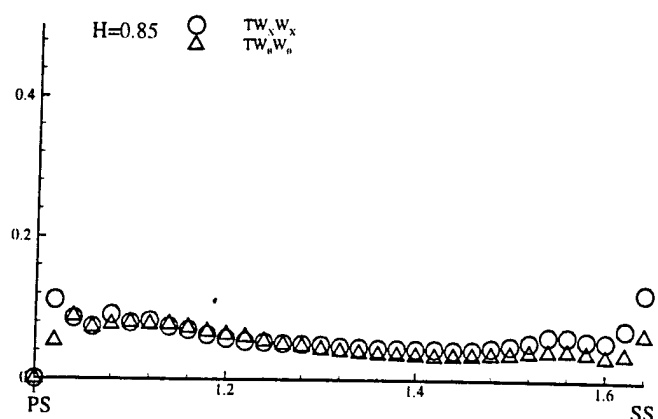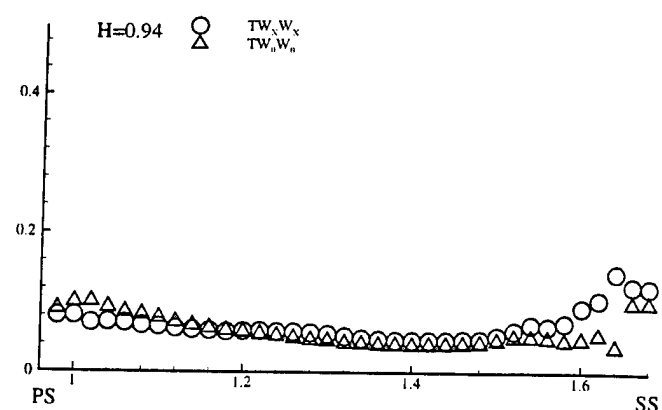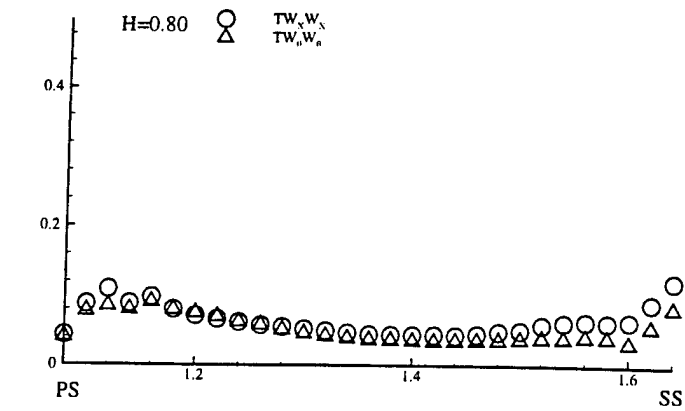
Figure 6.34 The distribution of the velocity fluctuation correlations from pressure surface to suction surface at the $X/C_{ax}=0.50$

88
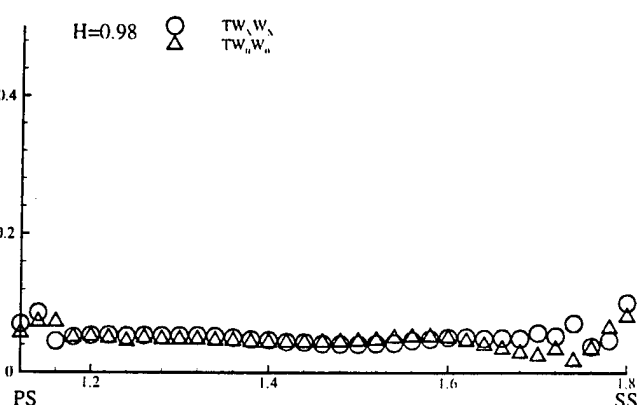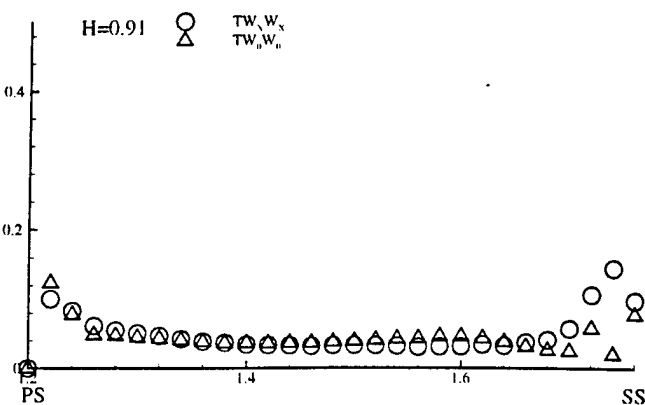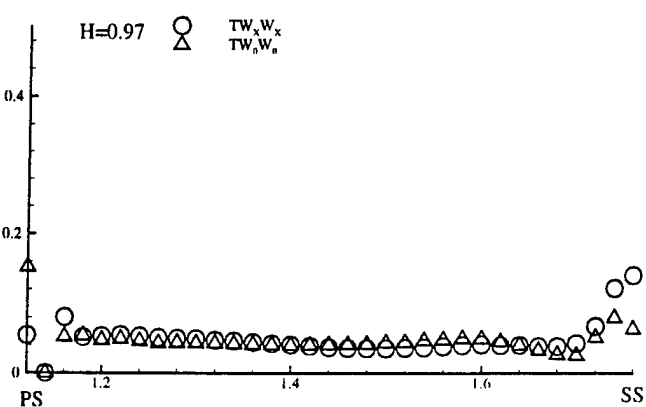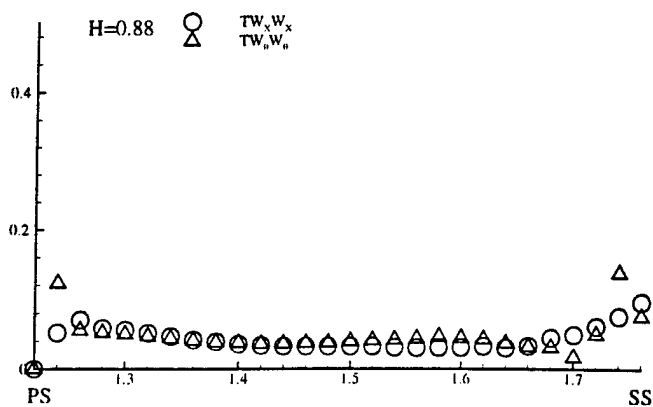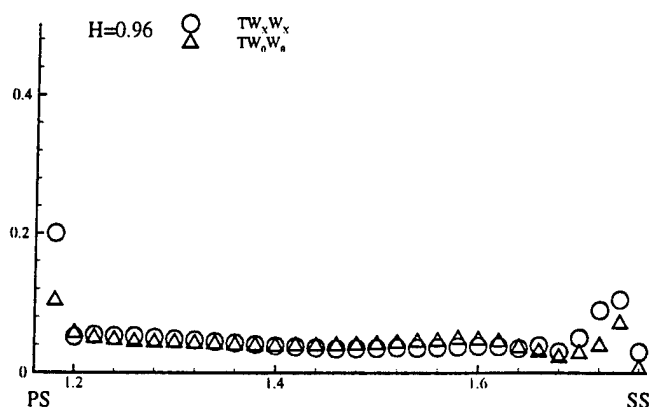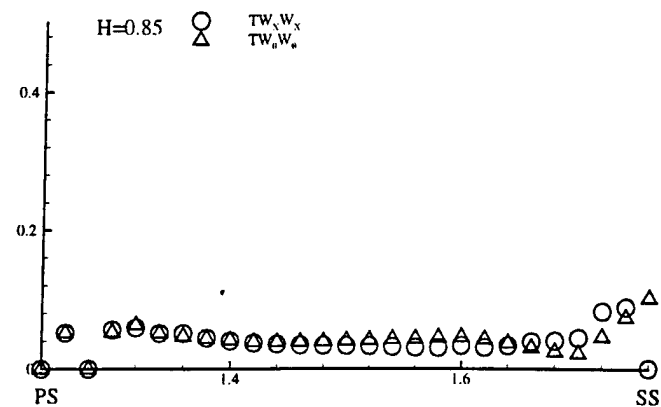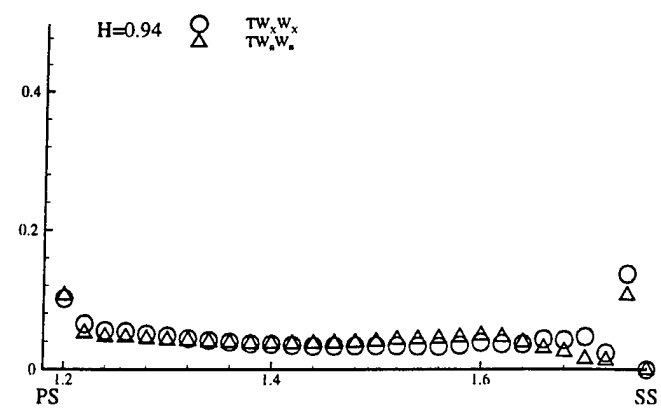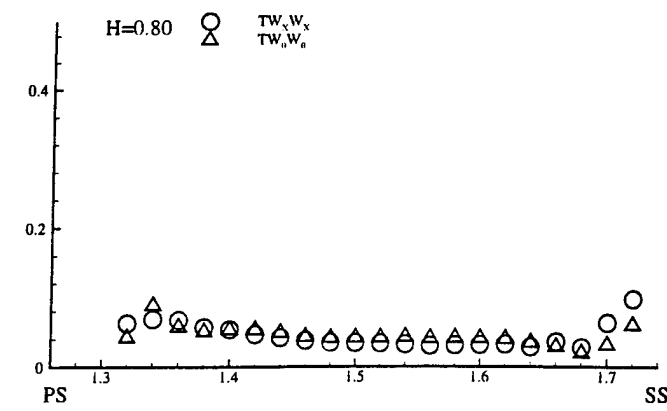
Figure 6.35 The distribution of the velocity fluctuation correlations from pressure surface to suction surface at the X/C$_{ax}$=0.60
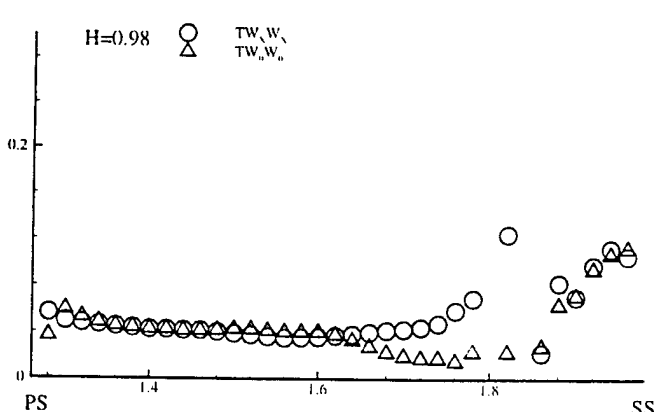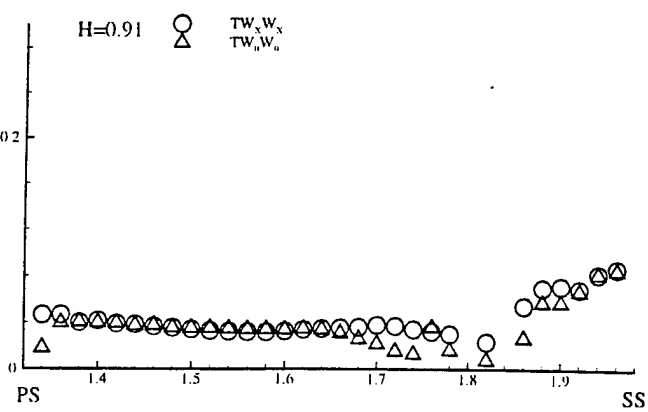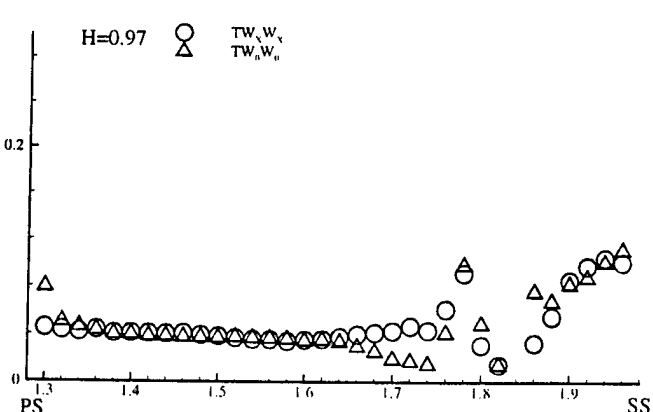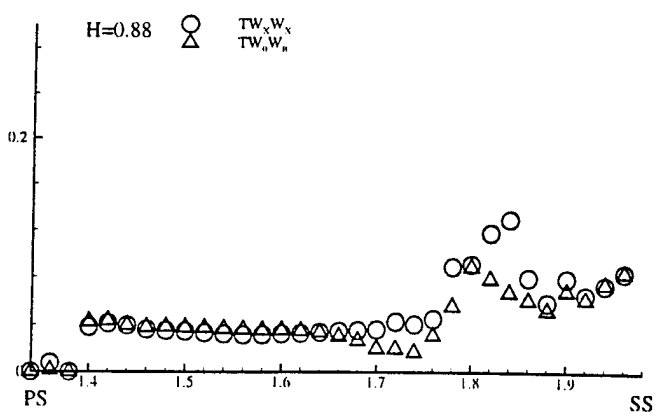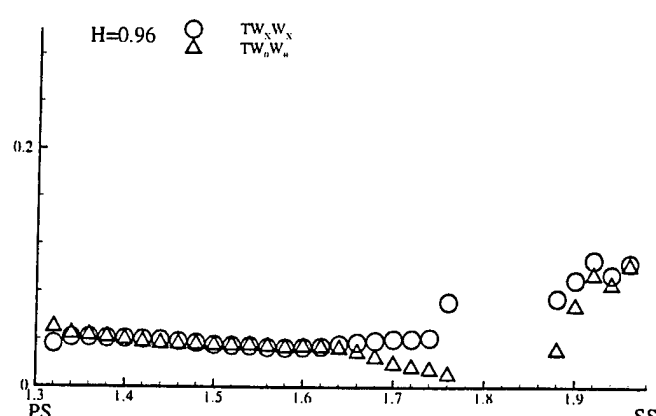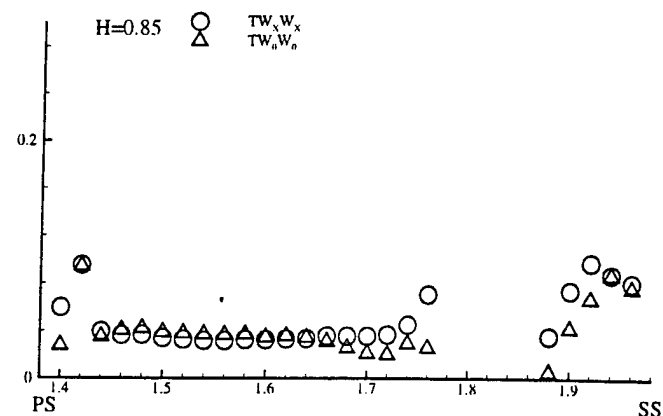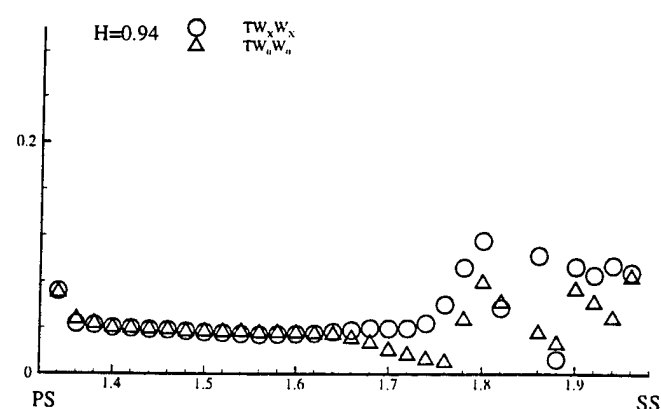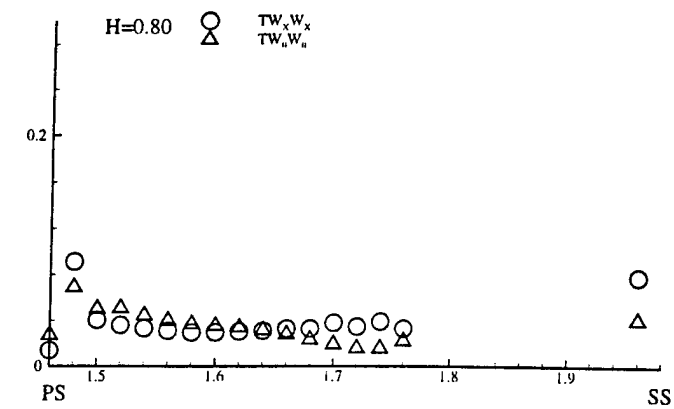
Figure 6.36 The distribution of the velocity fluctuation correlations from pressure surface to suction surface at the $X/C_{ax}=0.70$
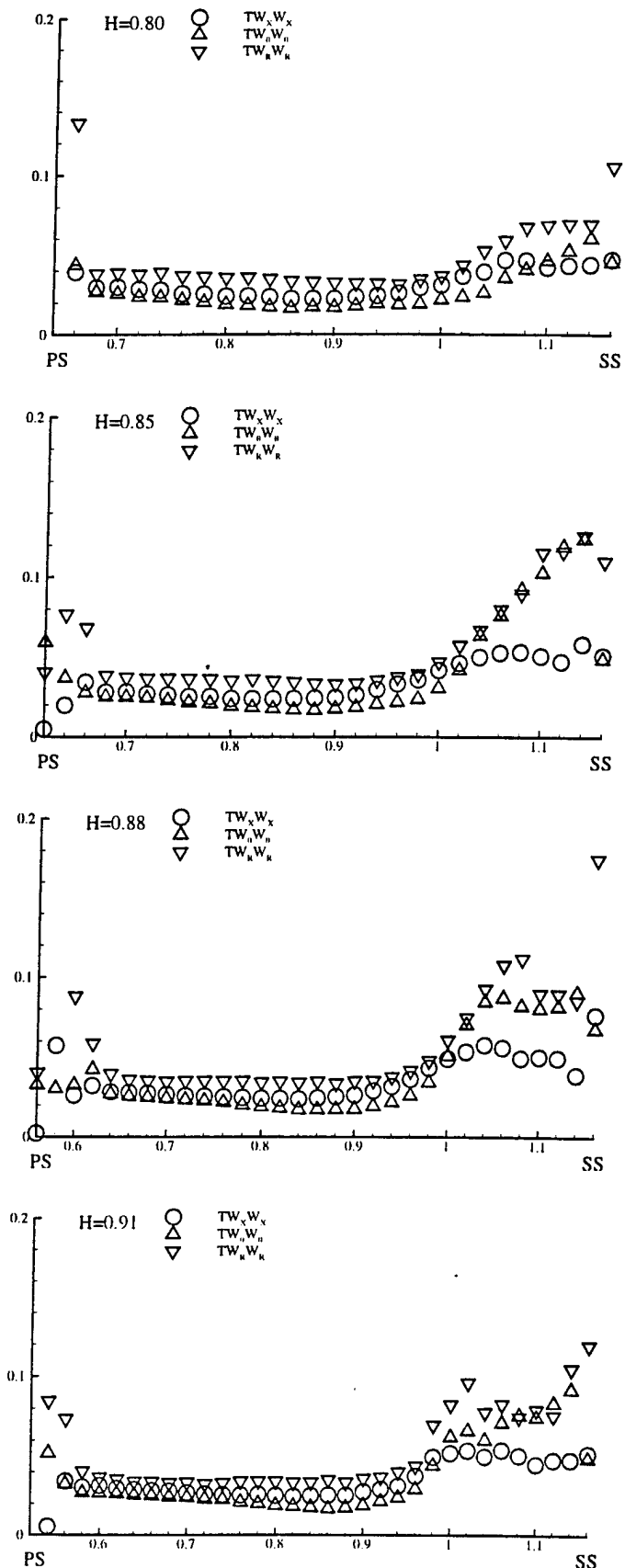
Figure 6.37 The distribution of the velocity fluctuation correlations from pressure surface to suction surface at the X/C_{ax}=0.80
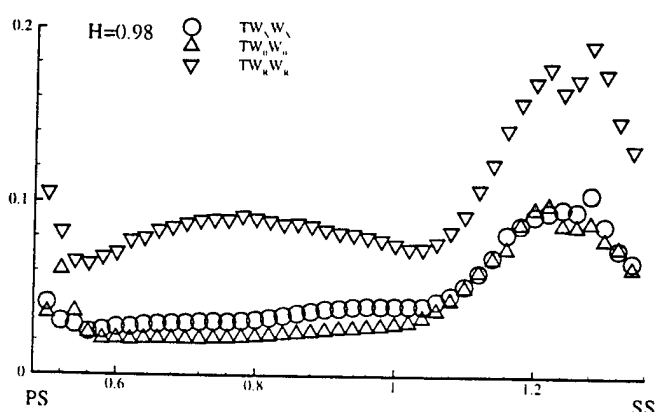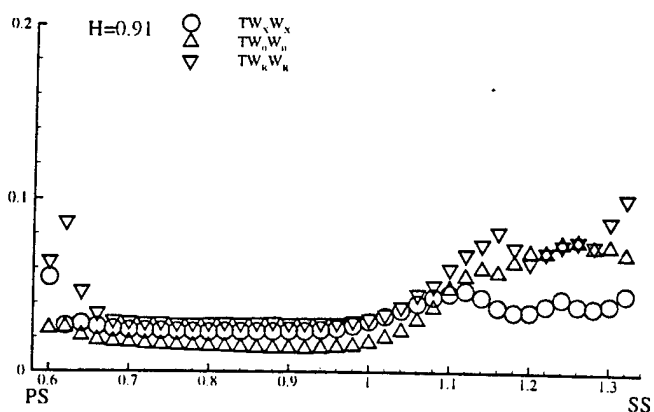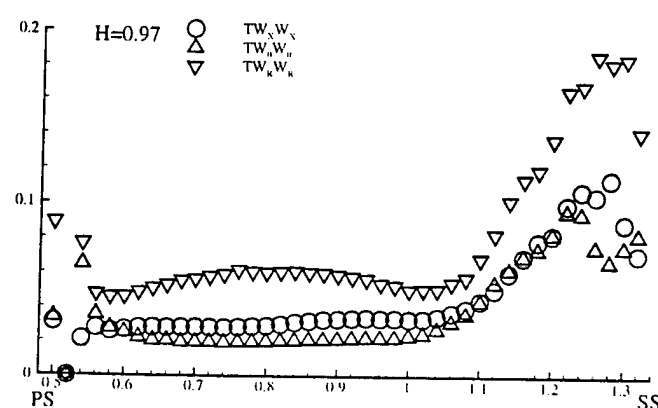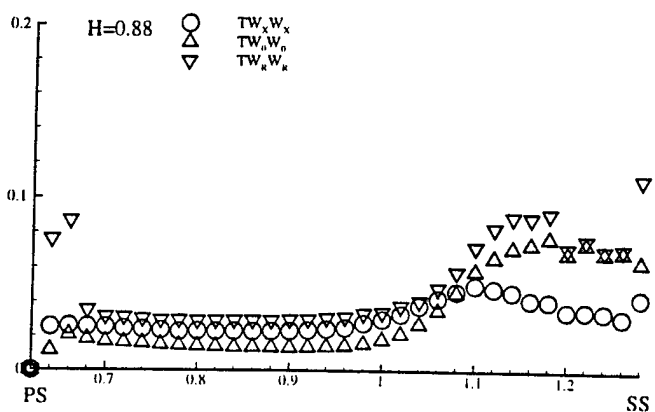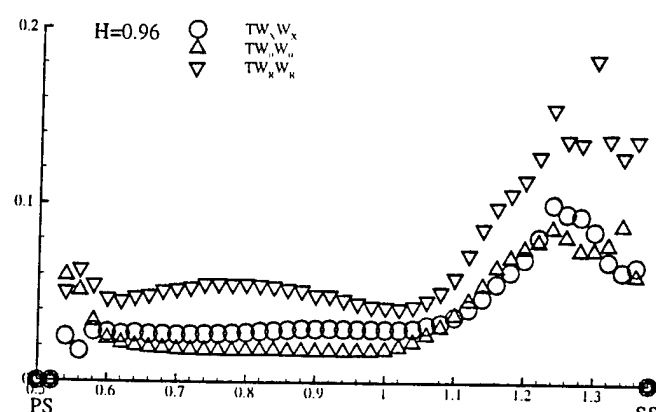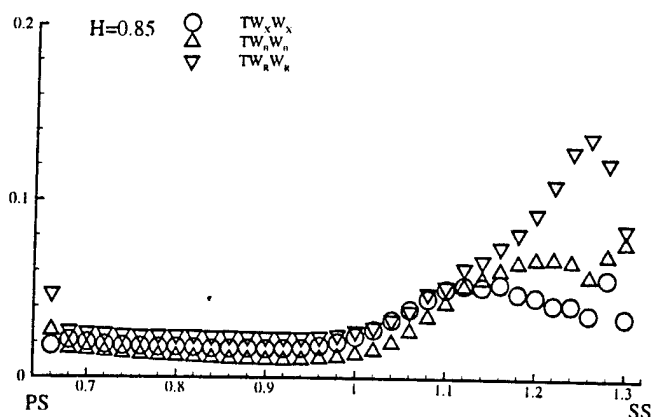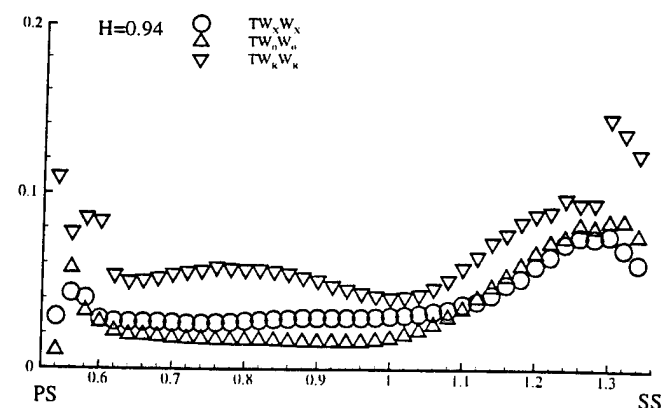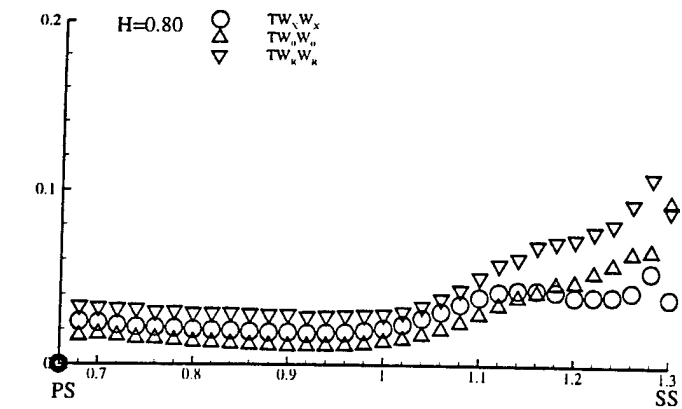
Figure 6.38 The distribution of the velocity fluctuation correlations from pressure surface to suction surface at the $X/C_{ax}=0.90$
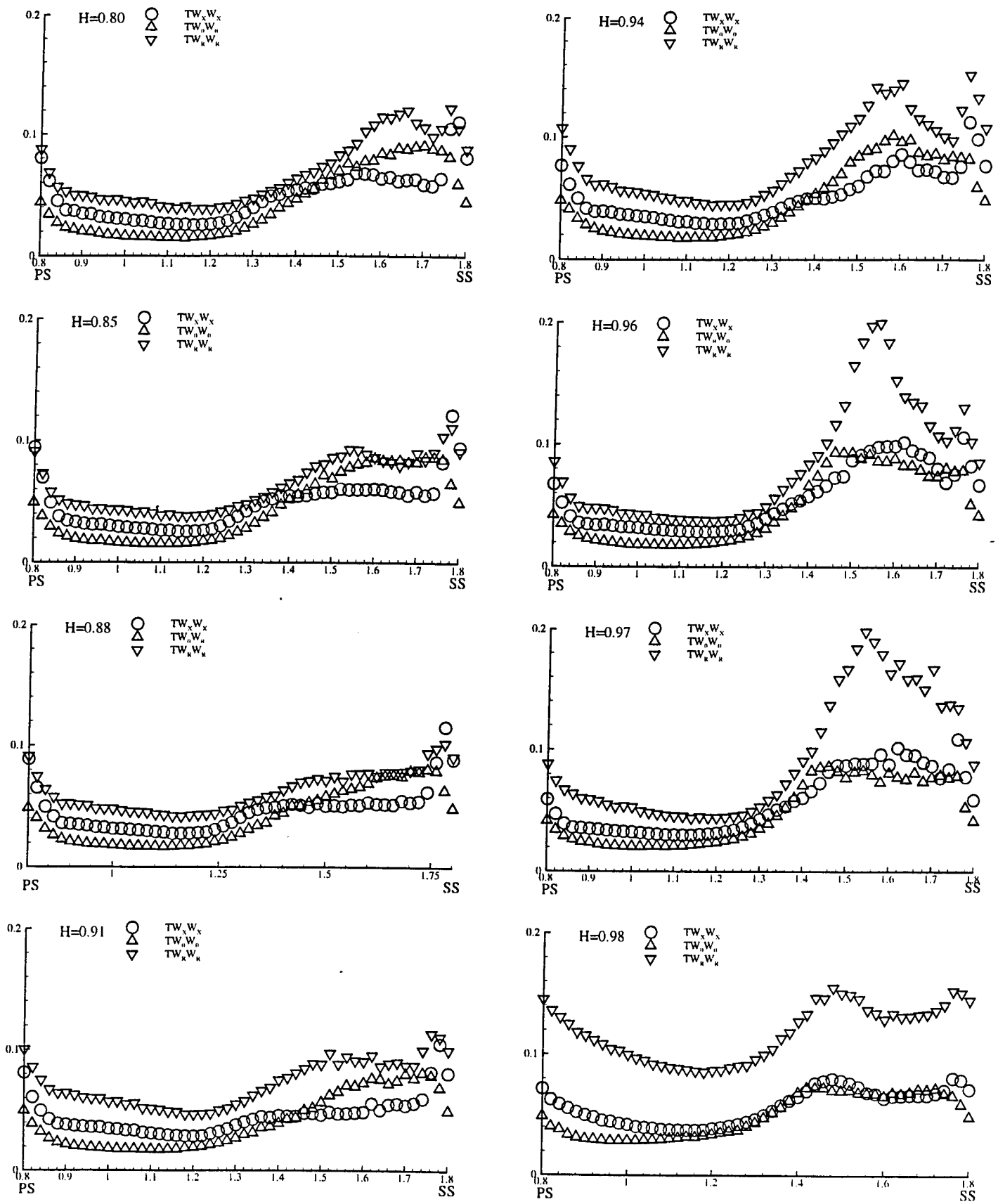
Figure 6.39 The distribution of the velocity fluctuation correlations from pressure surface to suction surface at the $X/C_{ax}=1.01$
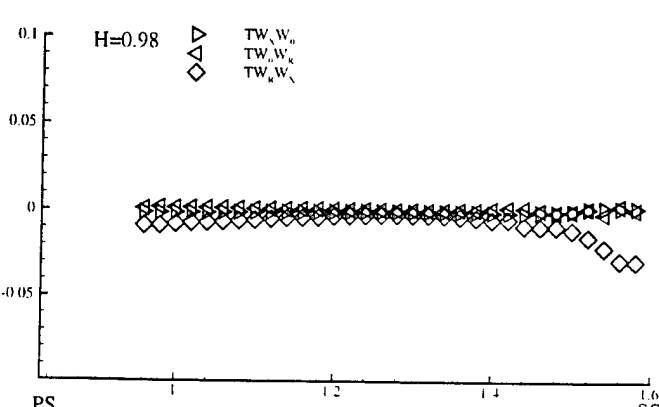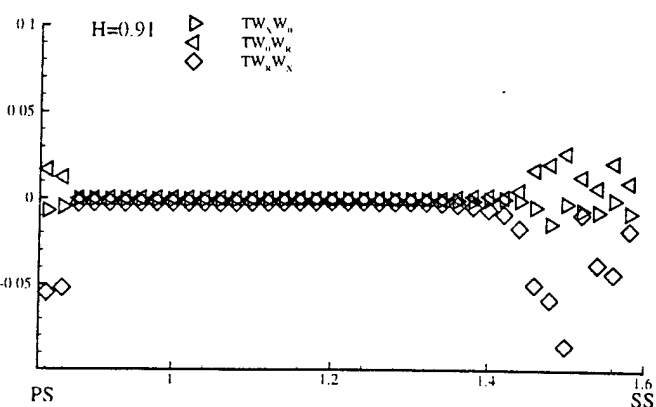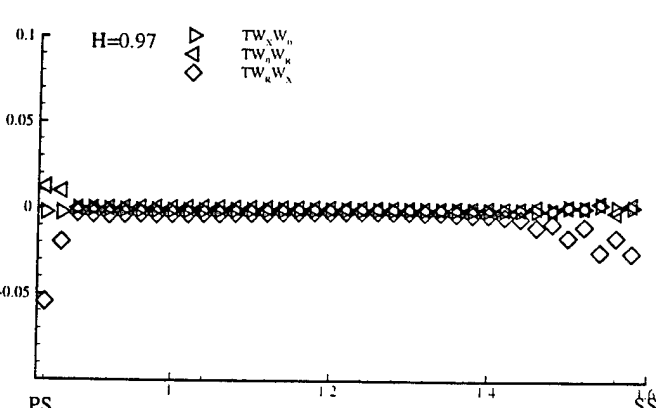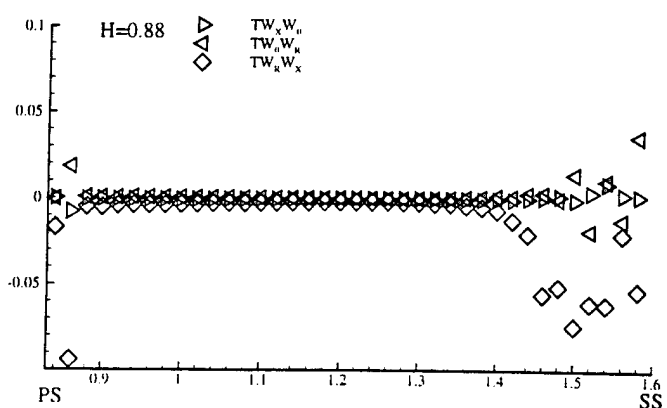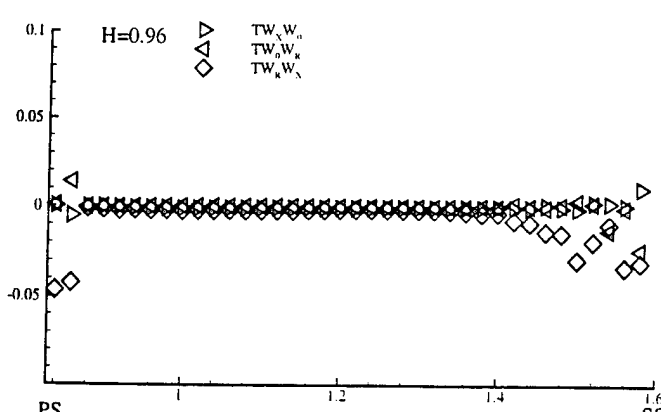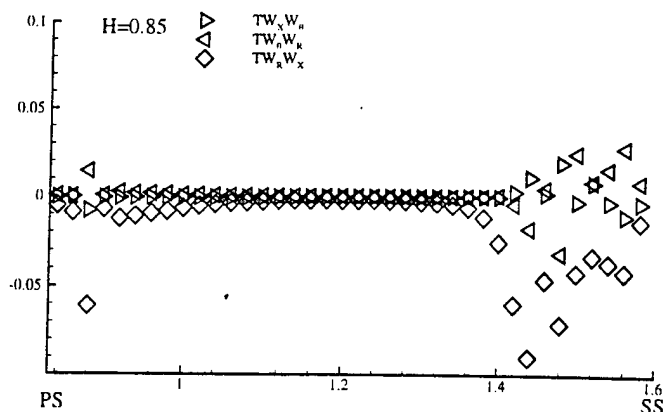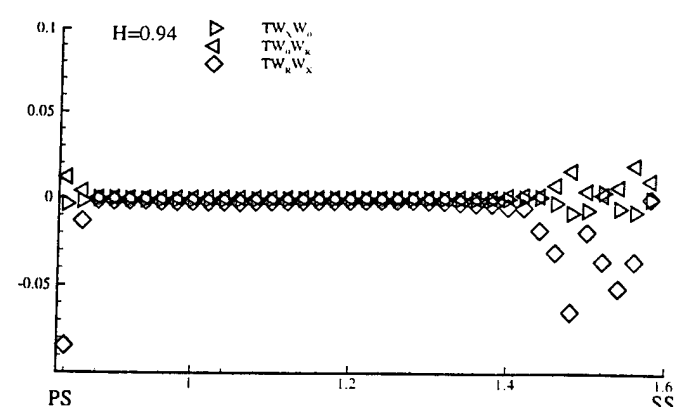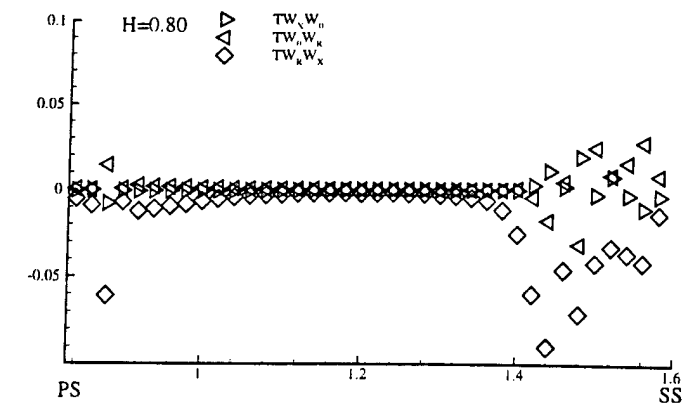
Figure 6.40 The distribution of the velocity fluctuation correlations from pressure surface to suction surface at the $X/C_{ax}=0.20$
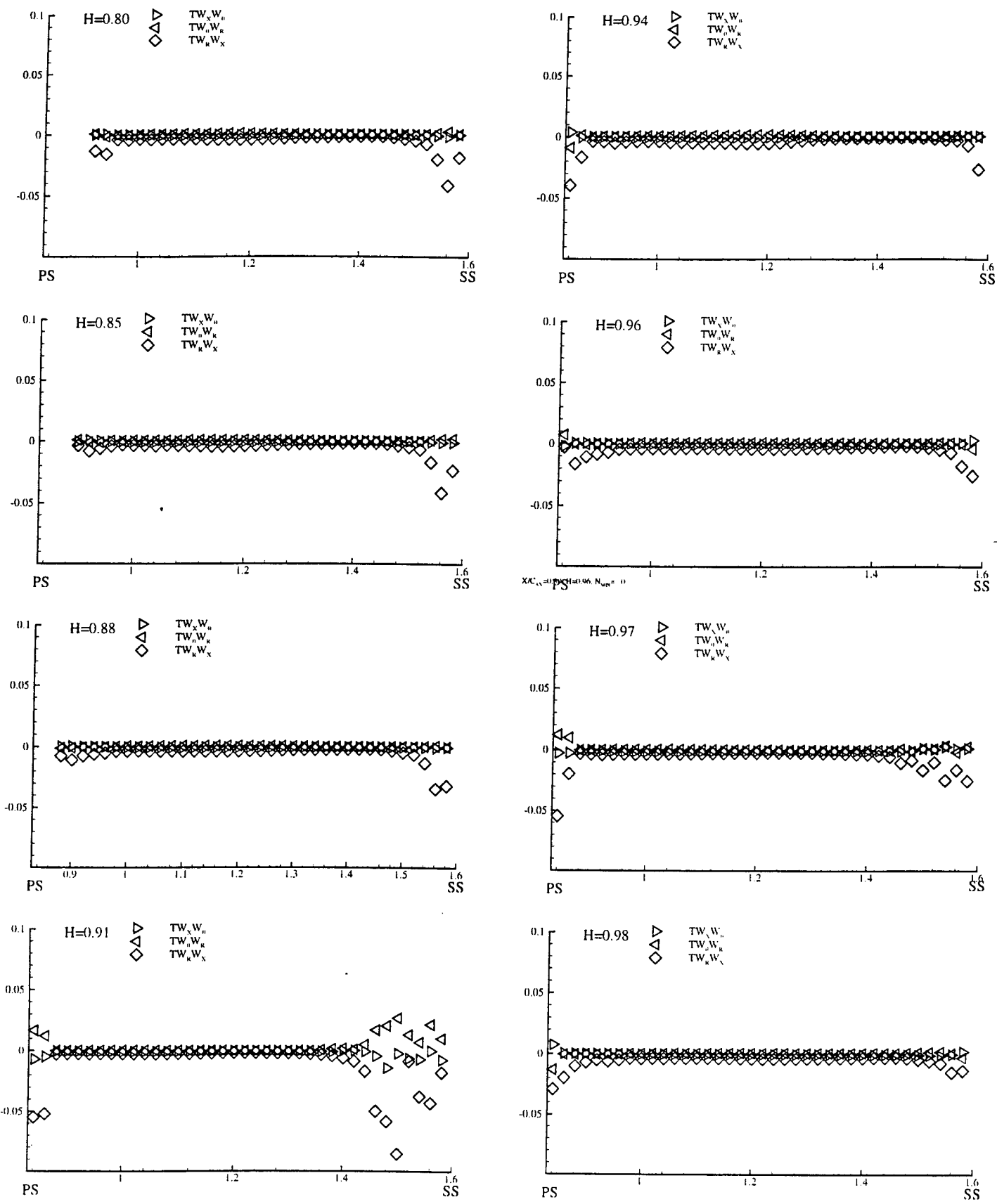
Figure 6.41 The distribution of the velocity fluctuation correlations from pressure surface to suction surface
at the X/C_{ax}=0.30
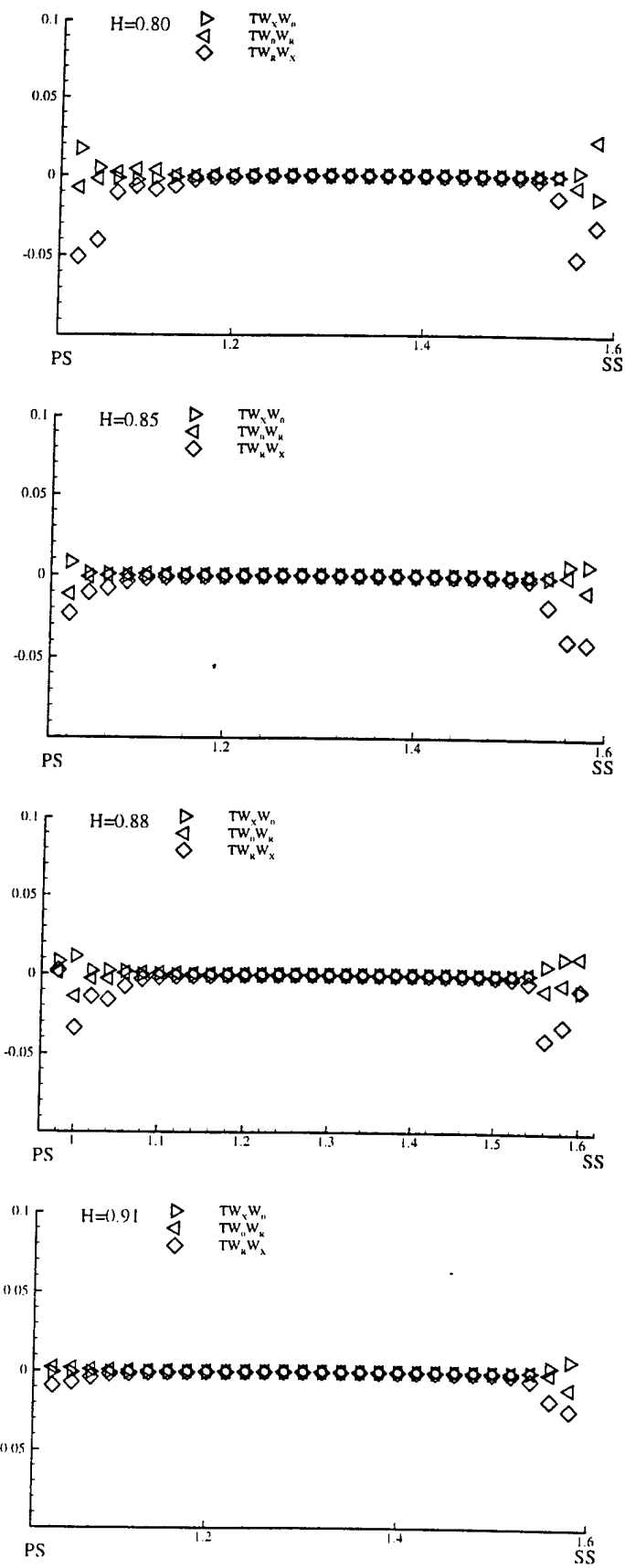
Figure 6.42 The distribution of the velocity fluctuation correlations from pressure surface to suction surface at the X/C_{ax}=0.40
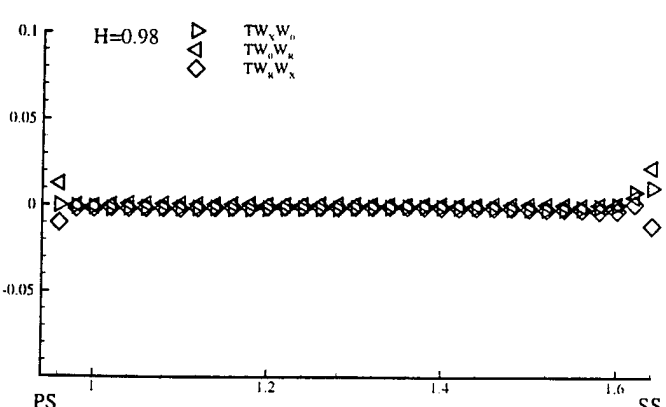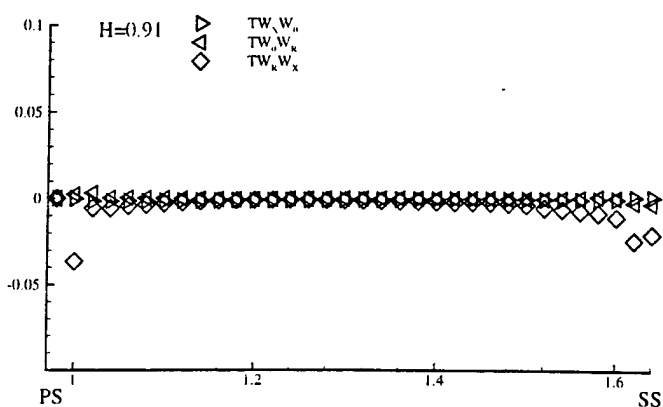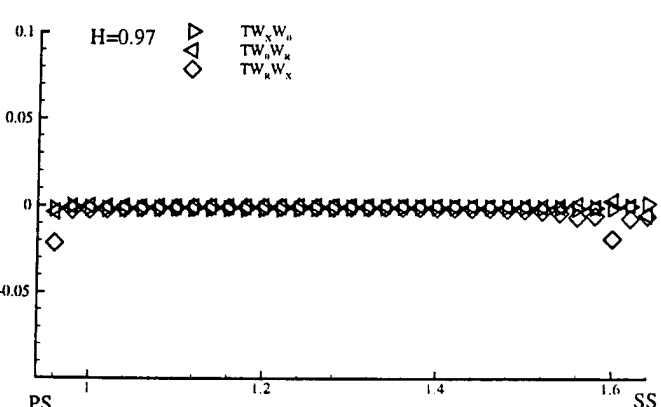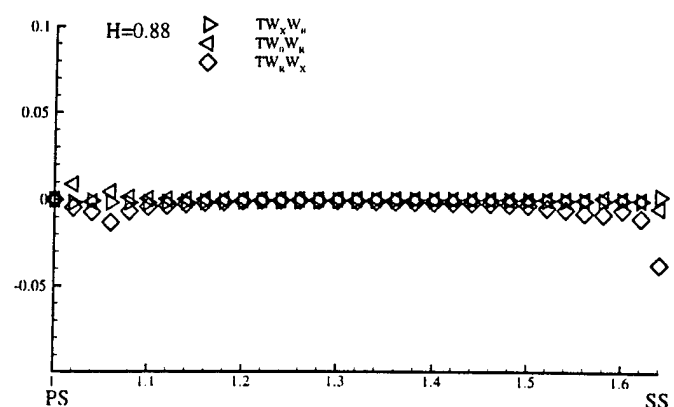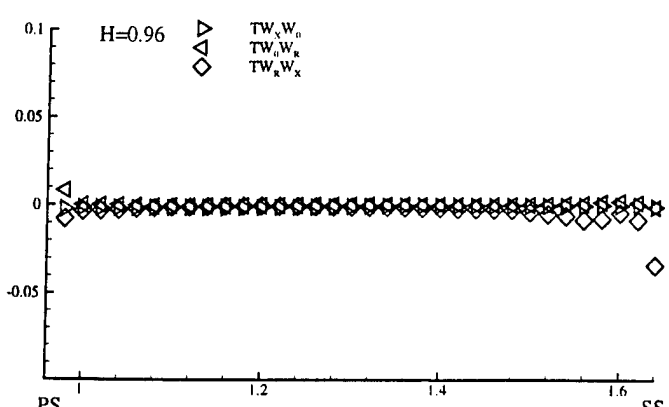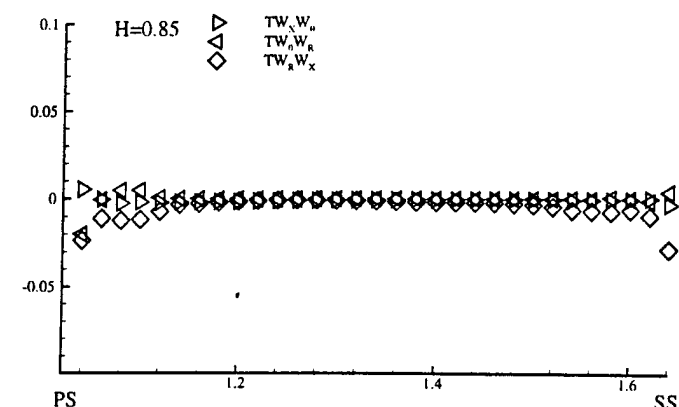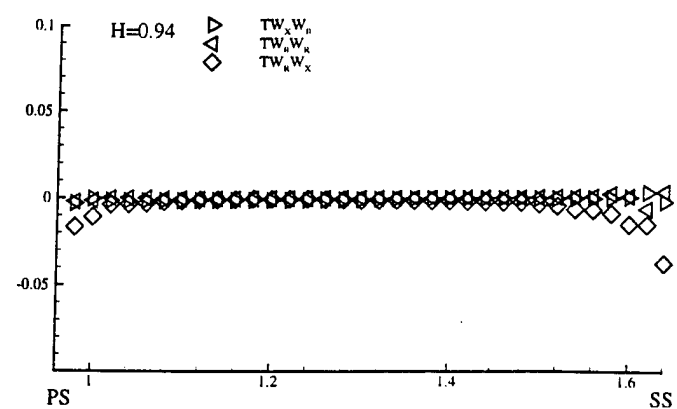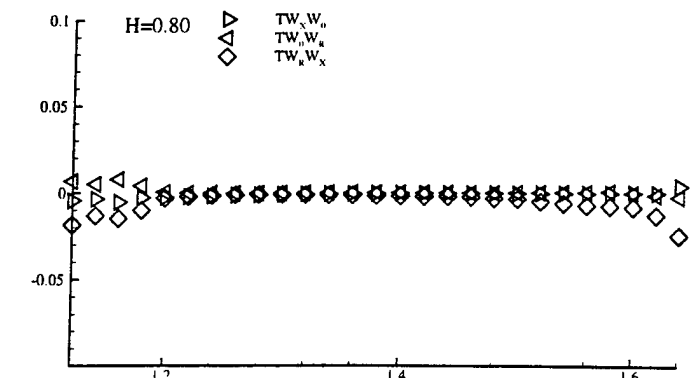
Figure 6.43 The distribution of the velocity fluctuation correlations from pressure surface to suction surface at the $X/C_{ax}=0.50$
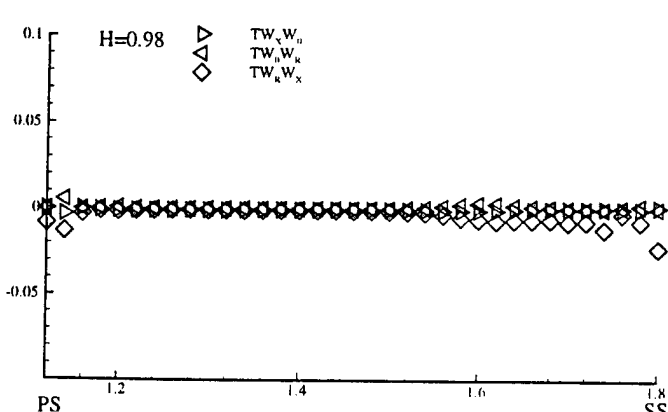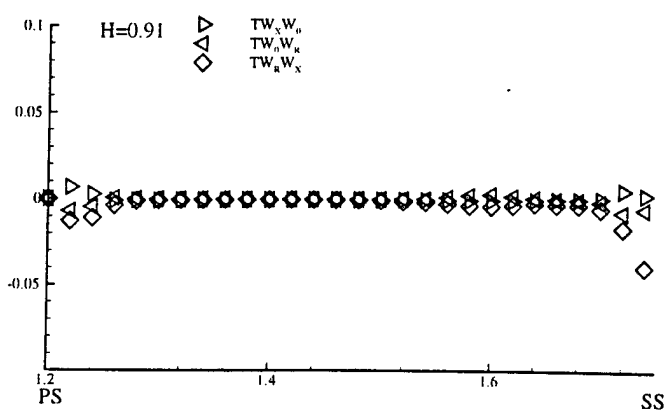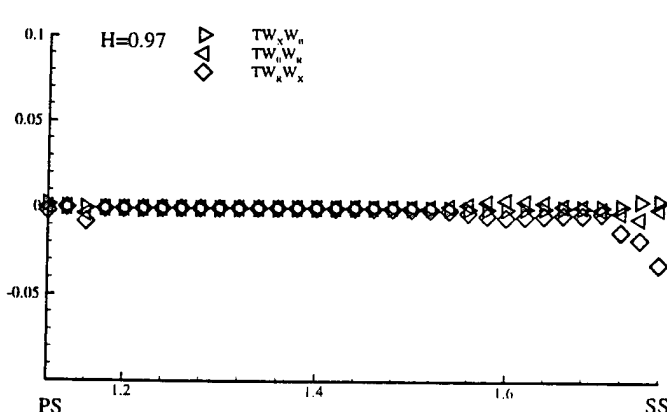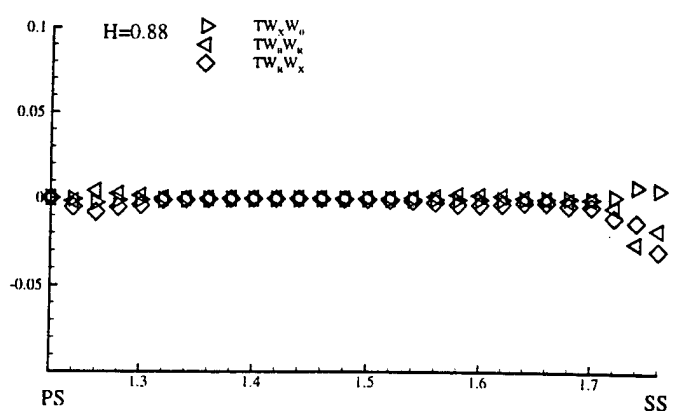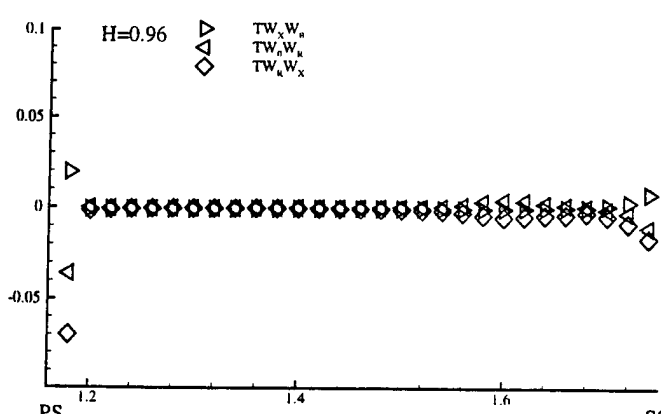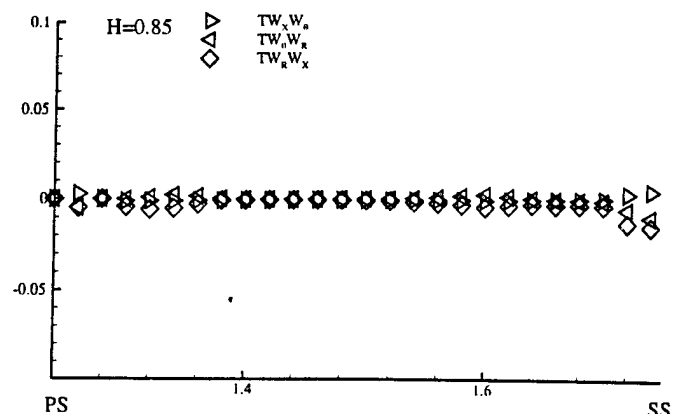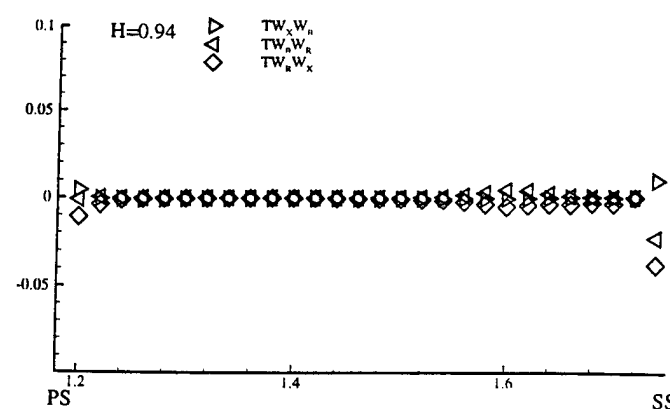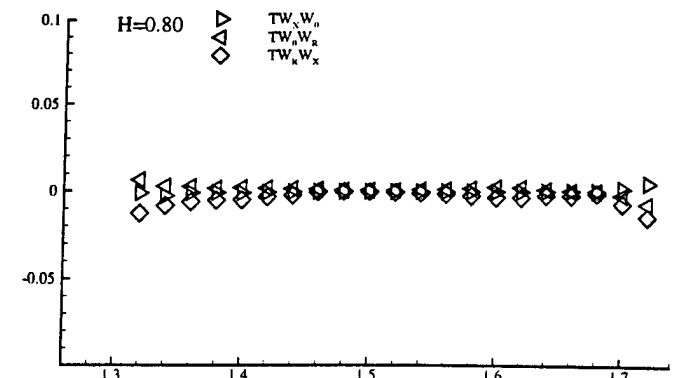
Figure 6.44 The distribution of the velocity fluctuation correlations from pressure surface to suction surface at the $X/C_{ax}=0.60$
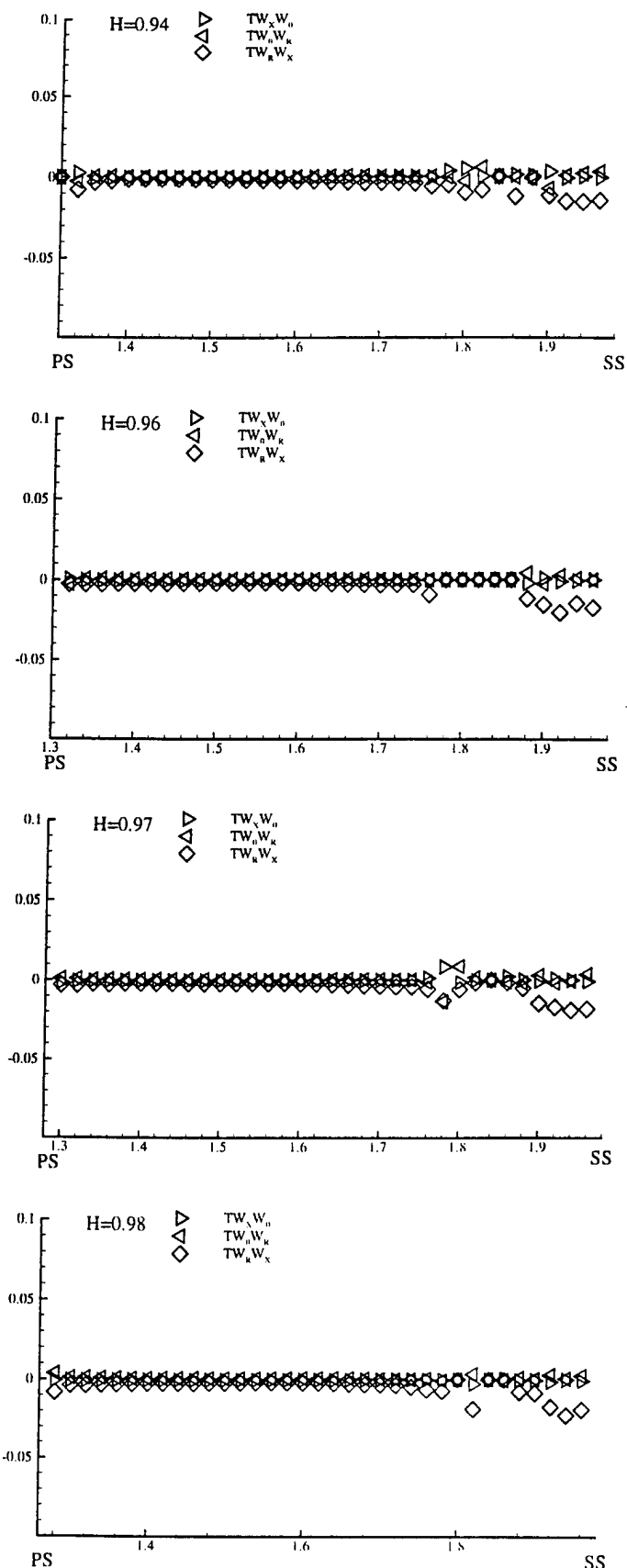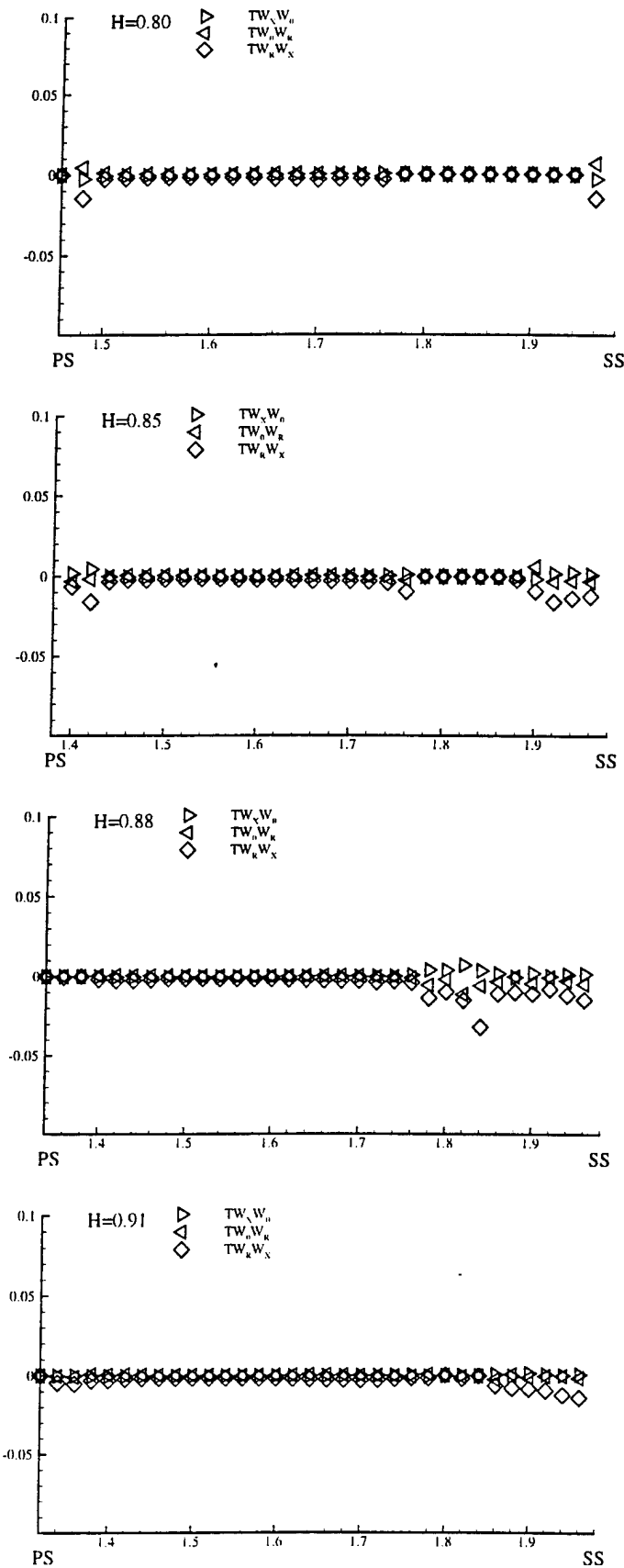
Figure 6.45 The distribution of the velocity fluctuation correlations from pressure surface to suction surface at the X/C$_{ax}$=0.70
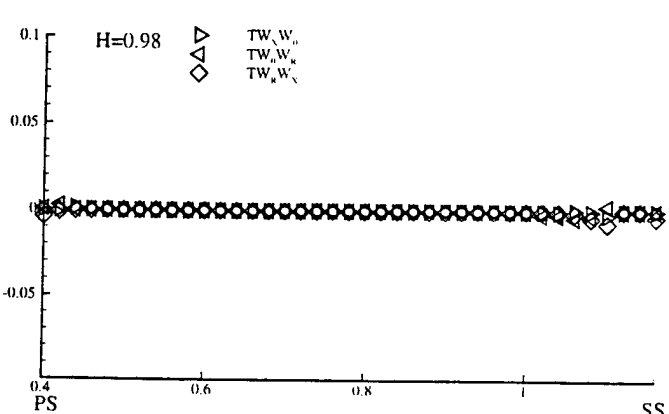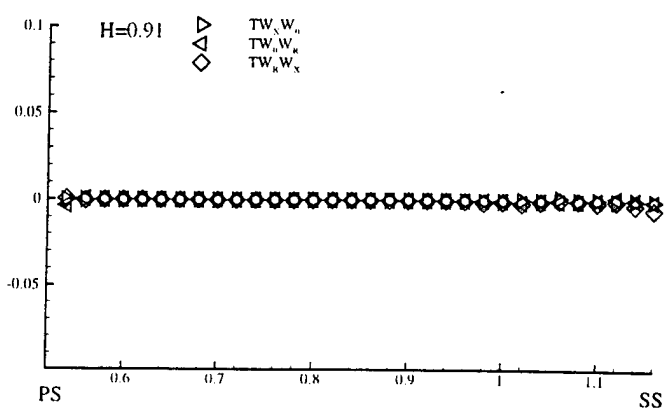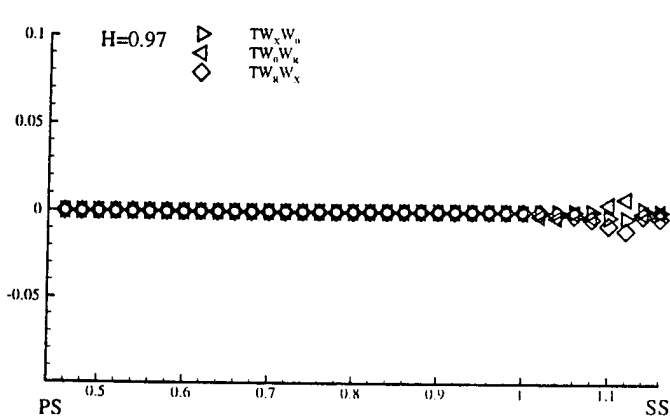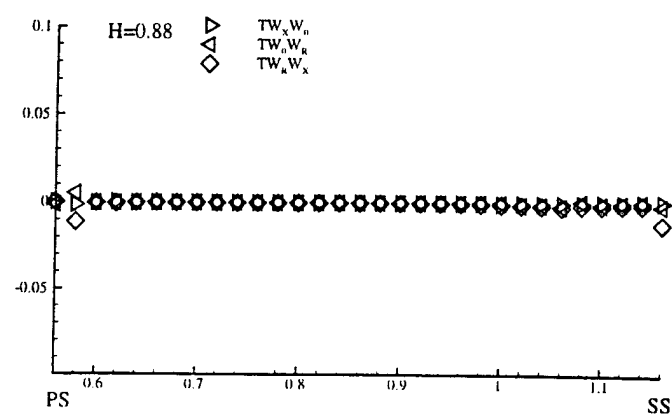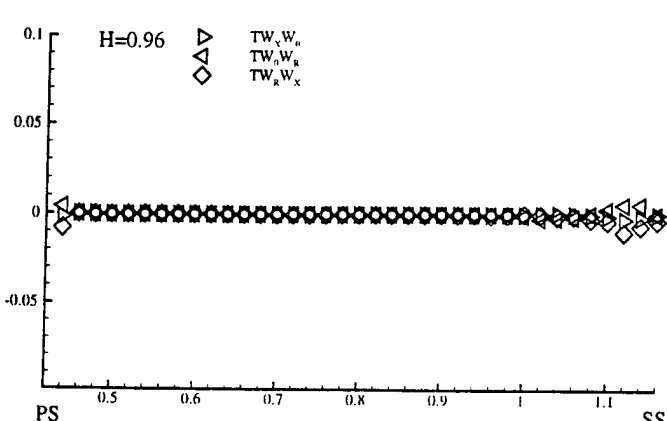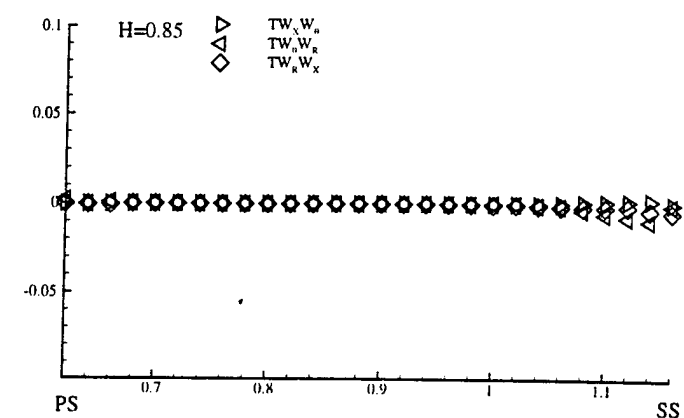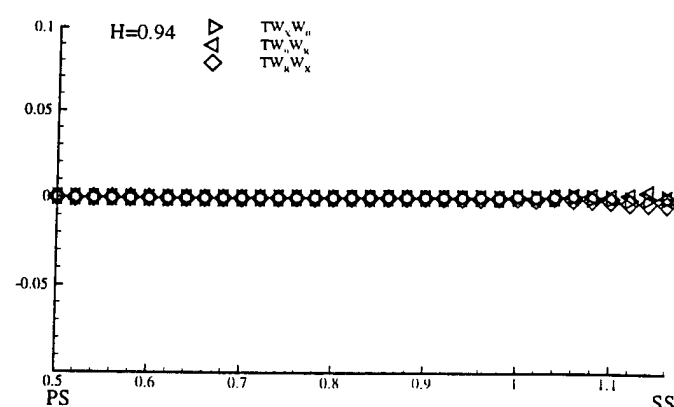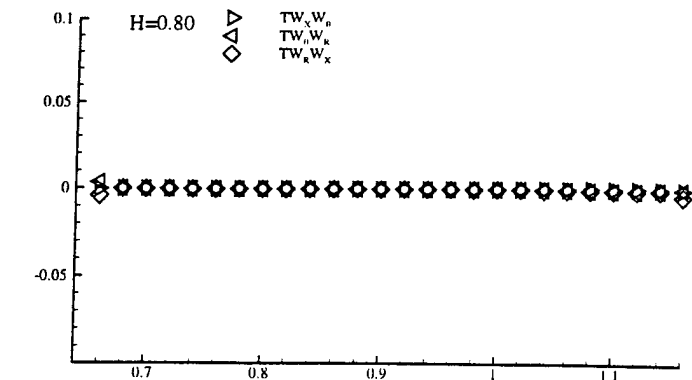
Figure 6.46 The distribution of the velocity fluctuation correlations from pressure surface to suction surface at the X/C_{ax}=0.80
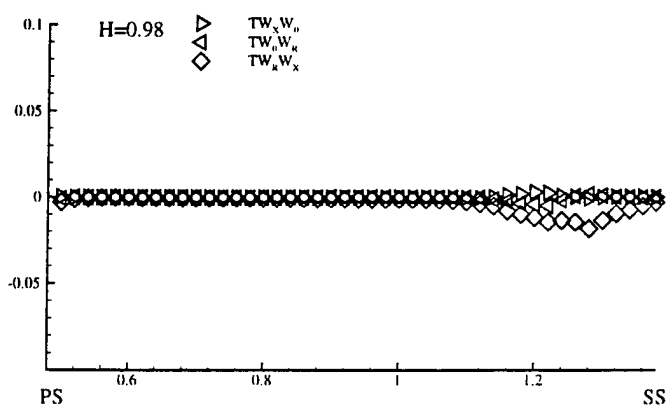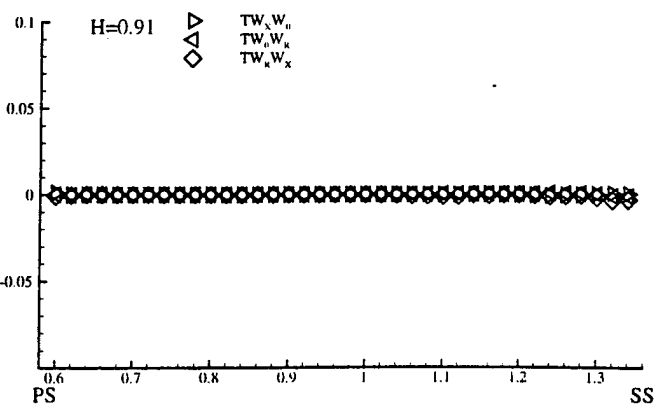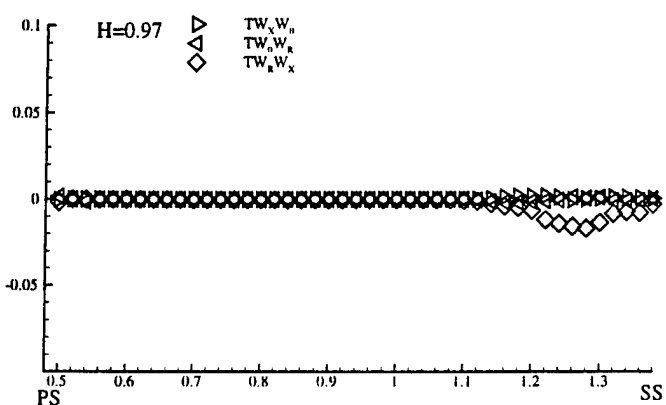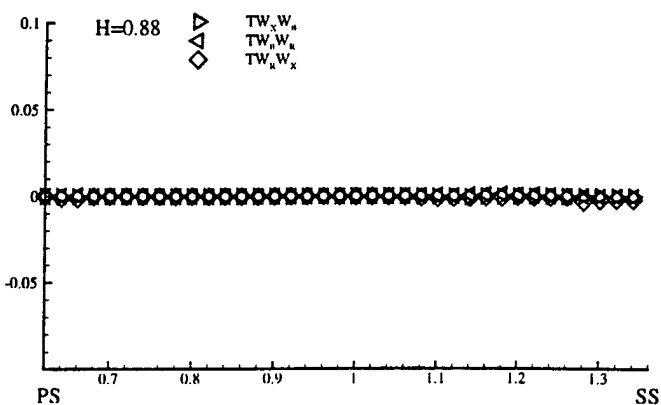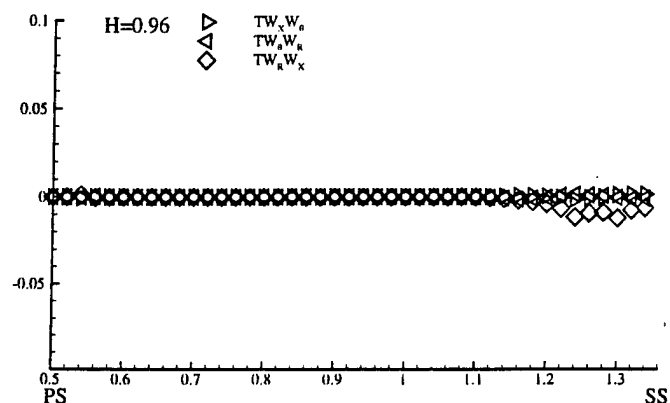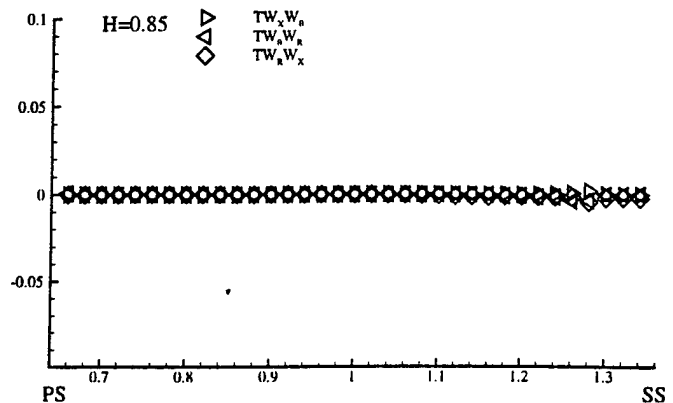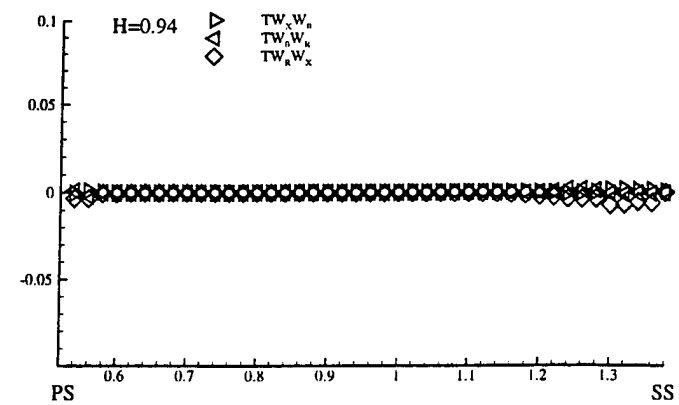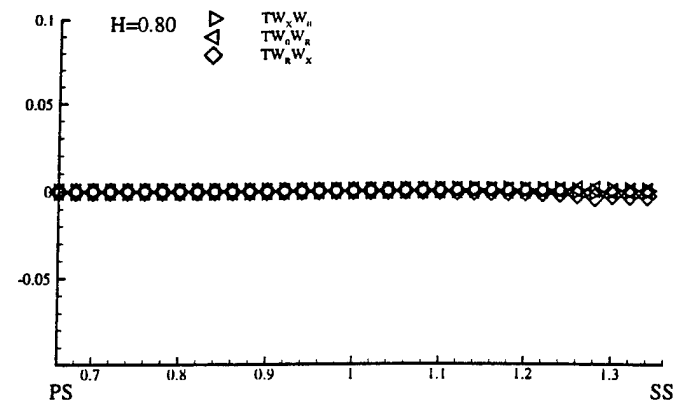
Figure 6.47 The distribution of the velocity fluctuation correlations from pressure surface to suction surface at the X/C_{ax}=0.90
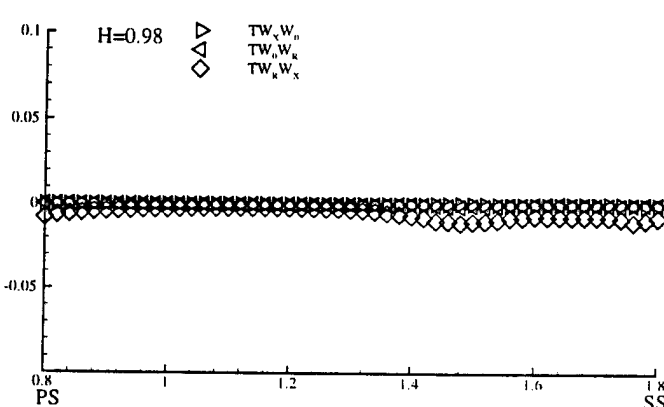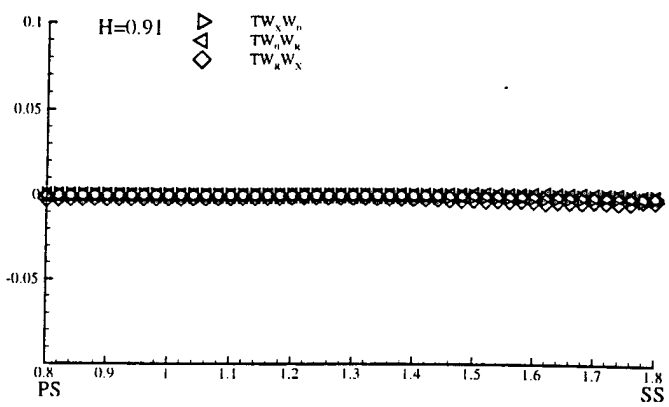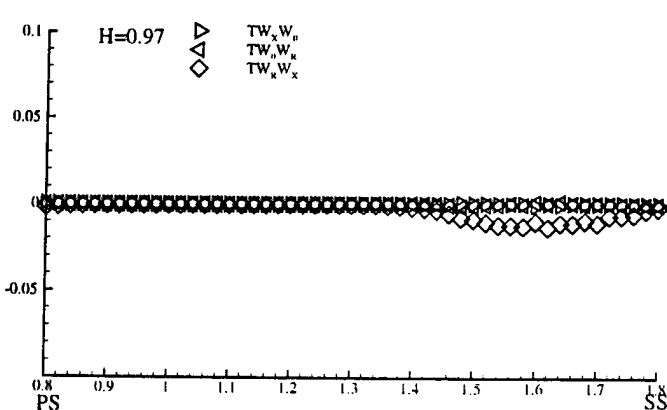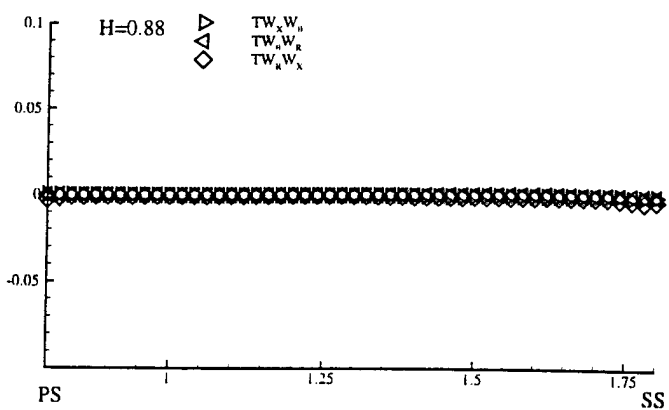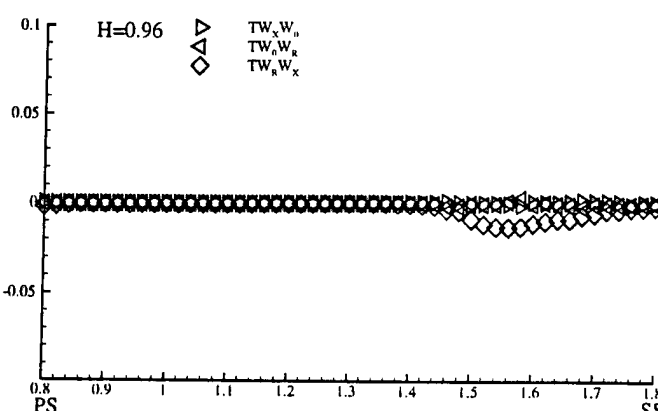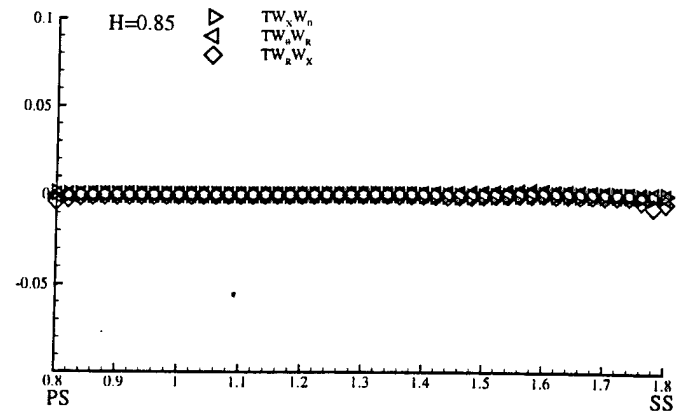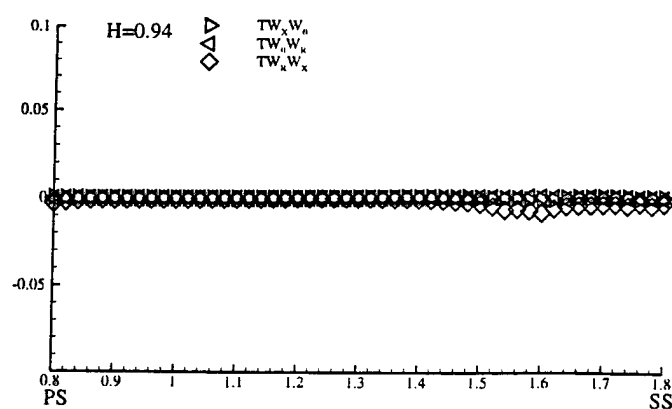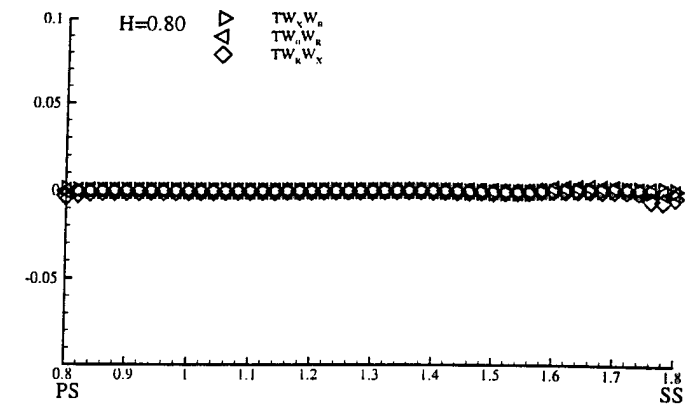
Figure 6.48 The distribution of the velocity fluctuation correlations from pressure surface to suction surface at the $X/C_{ax}=1.01$
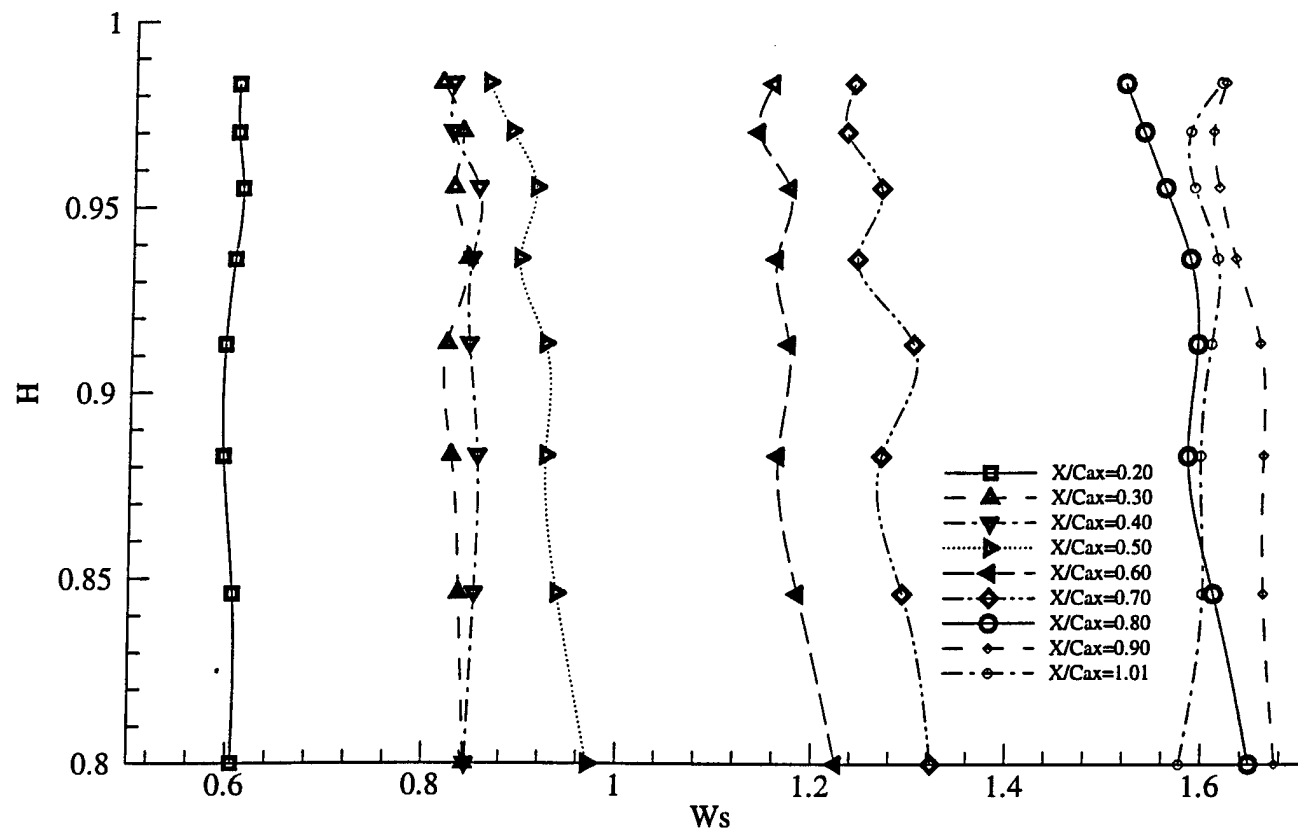
Figure 6.49 passage averaged total velocity distribution
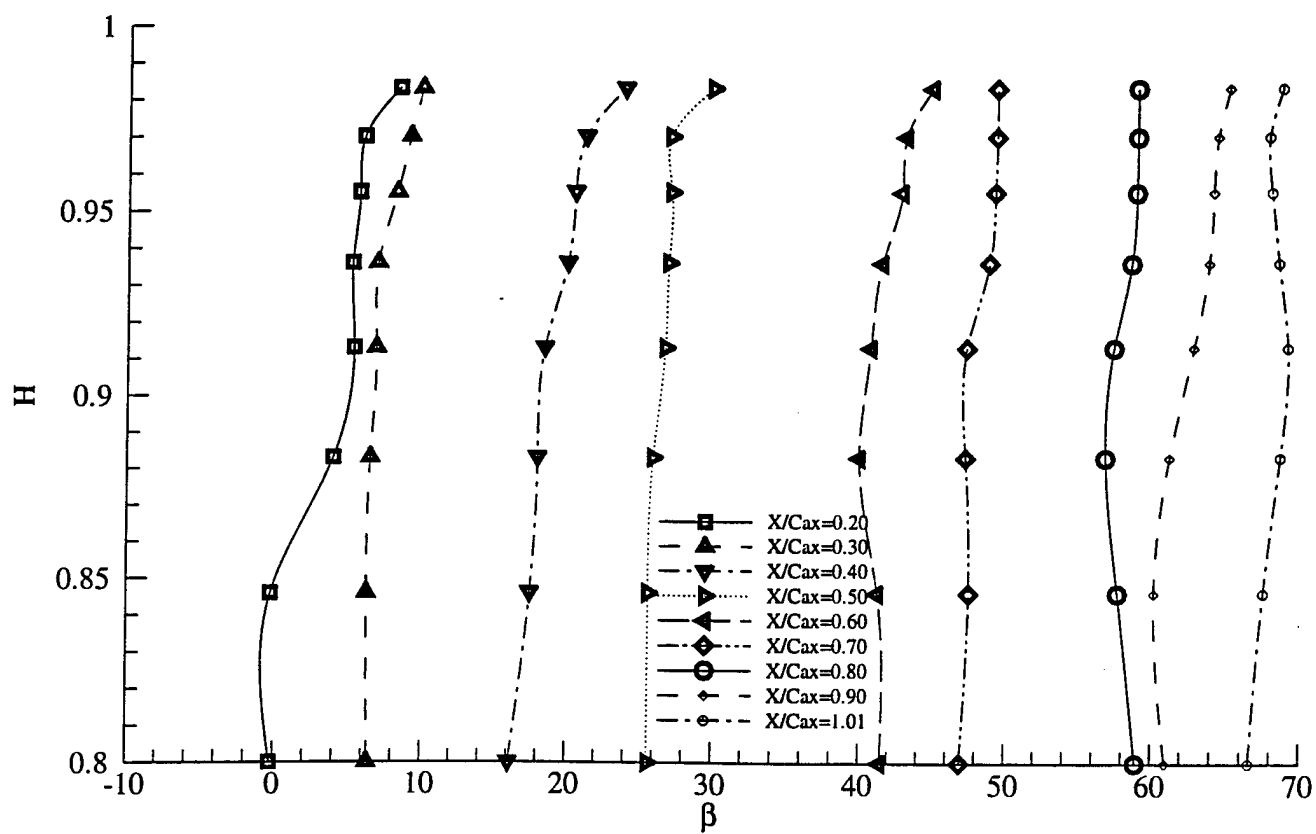
Figure 6.50 passage averaged yaw angle distribution

103
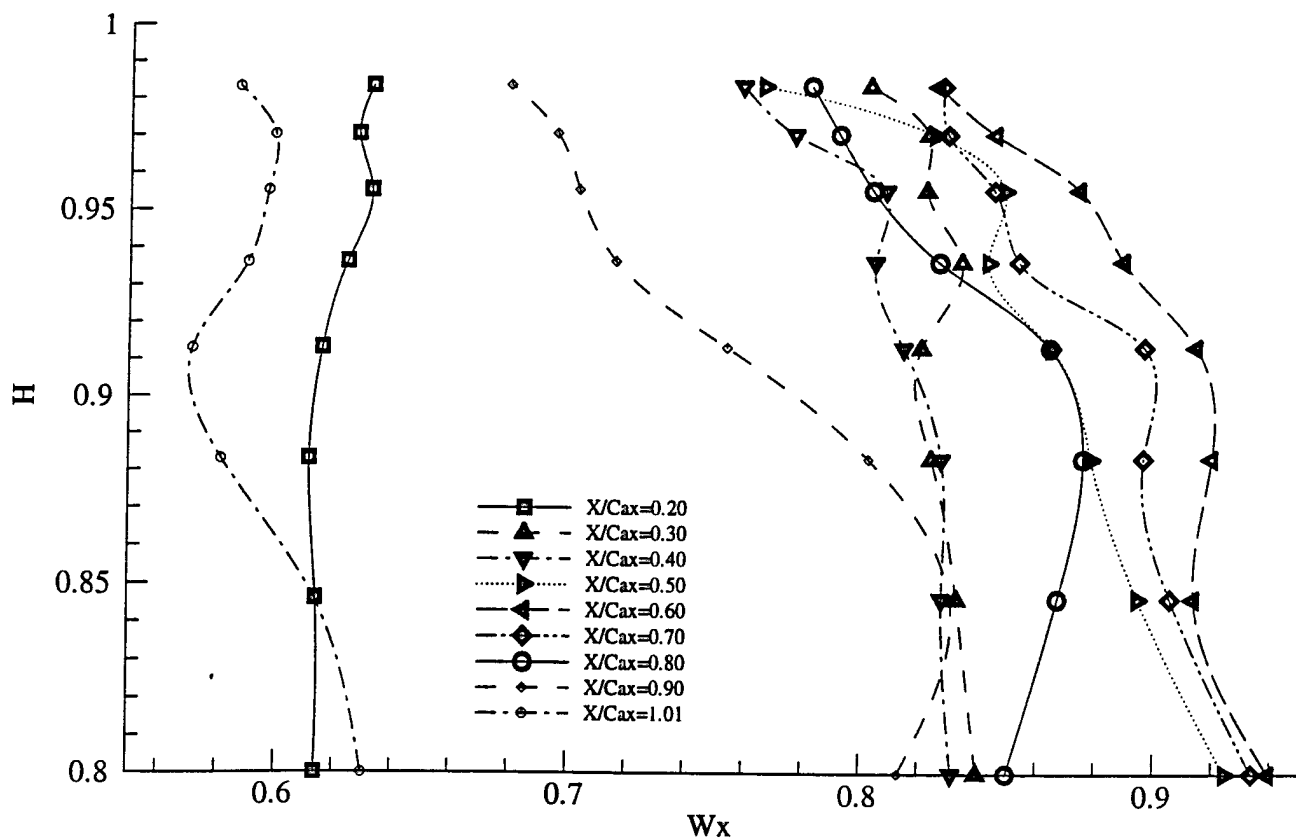
Figure 6.51 passage averaged axial velocity distribution
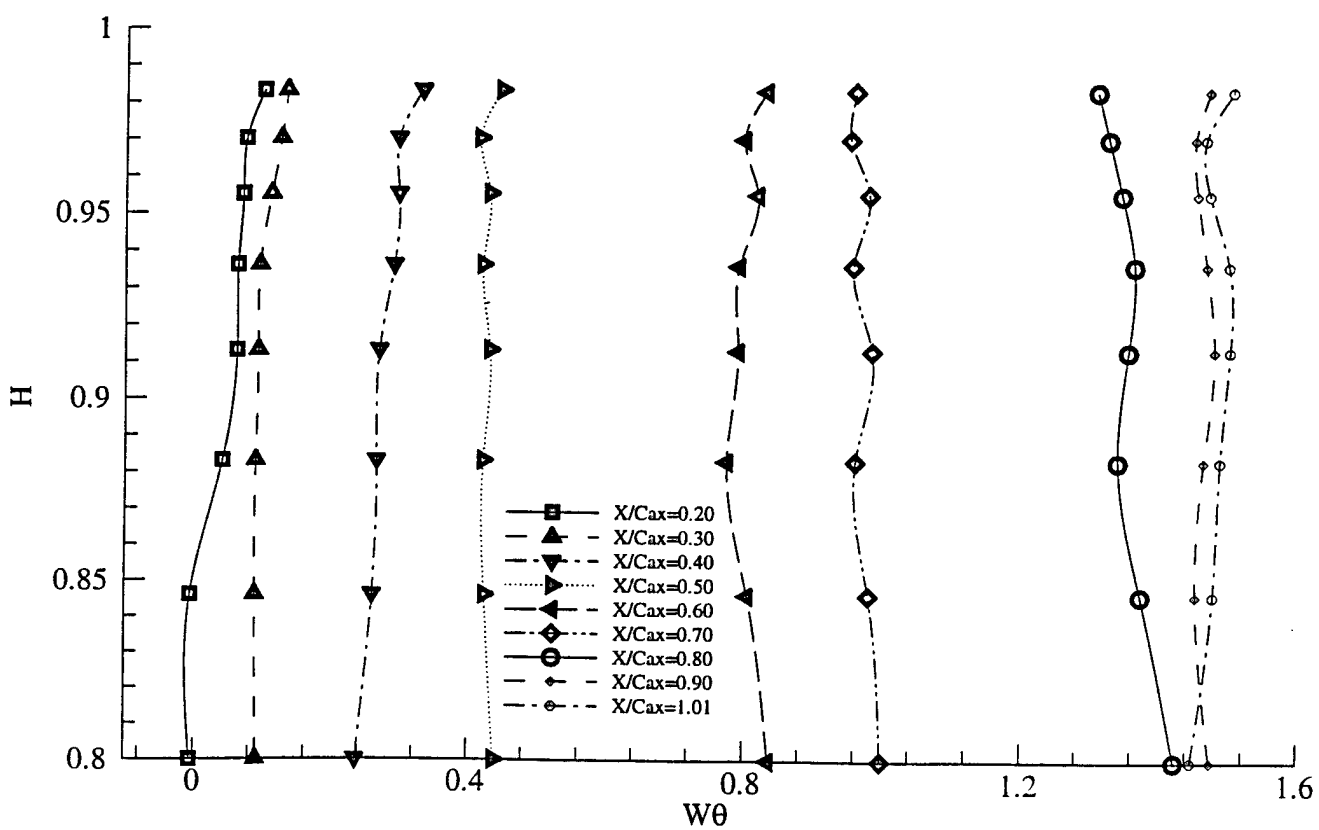
Figure 6.52 passage averaged tangential velocity distribution
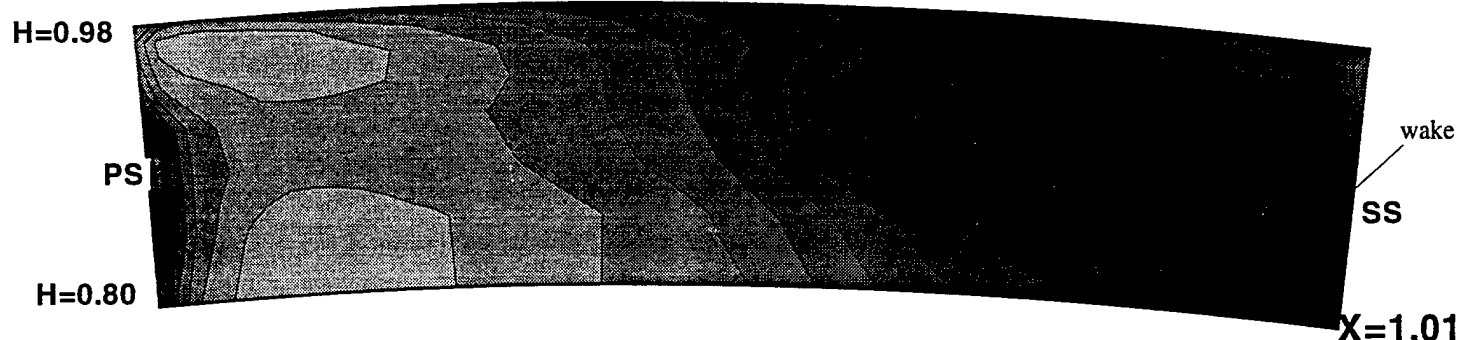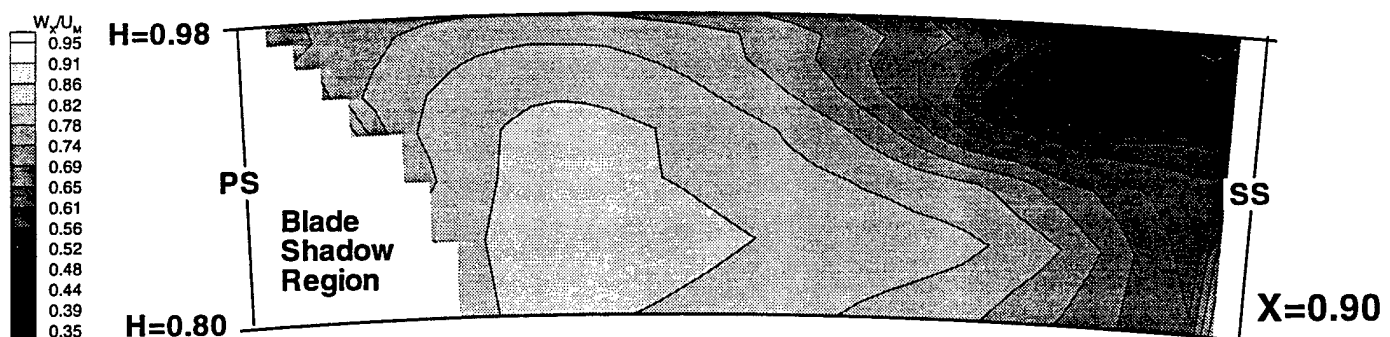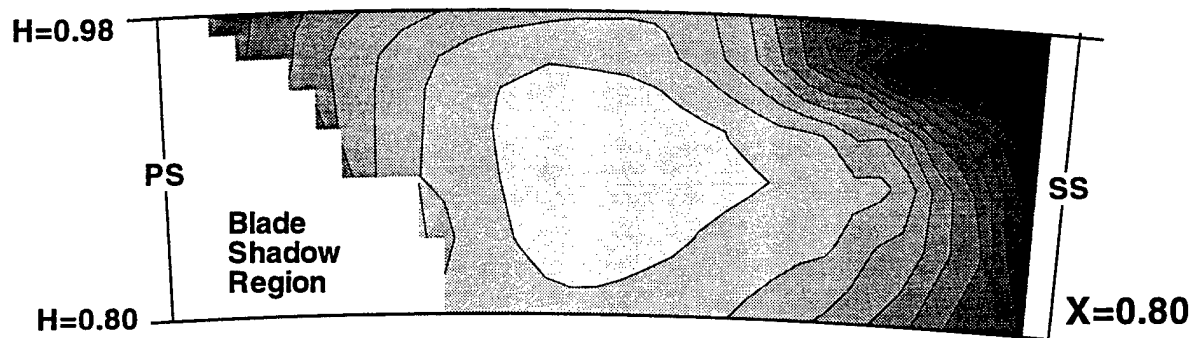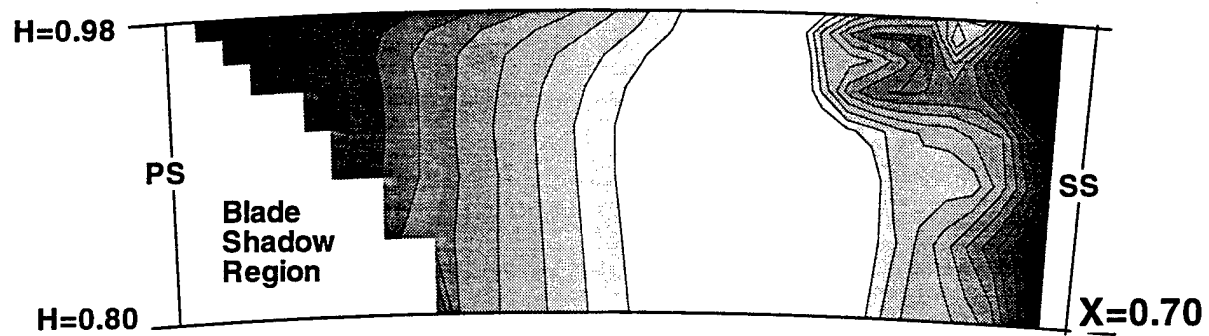
Figure 6.53 Relative axial velocity contour plots at X/Cax=0.70, 0.80, 0.90, and 1.01

ω$_x$
20.0
14.3
8.6
2.9
-2.9
-8.6
-14.3
-20.0

x/Cax=50%

x/Cax=60%

x/Cax=70%

x/Cax=80%

x/Cax=90%

x/Cax=101%
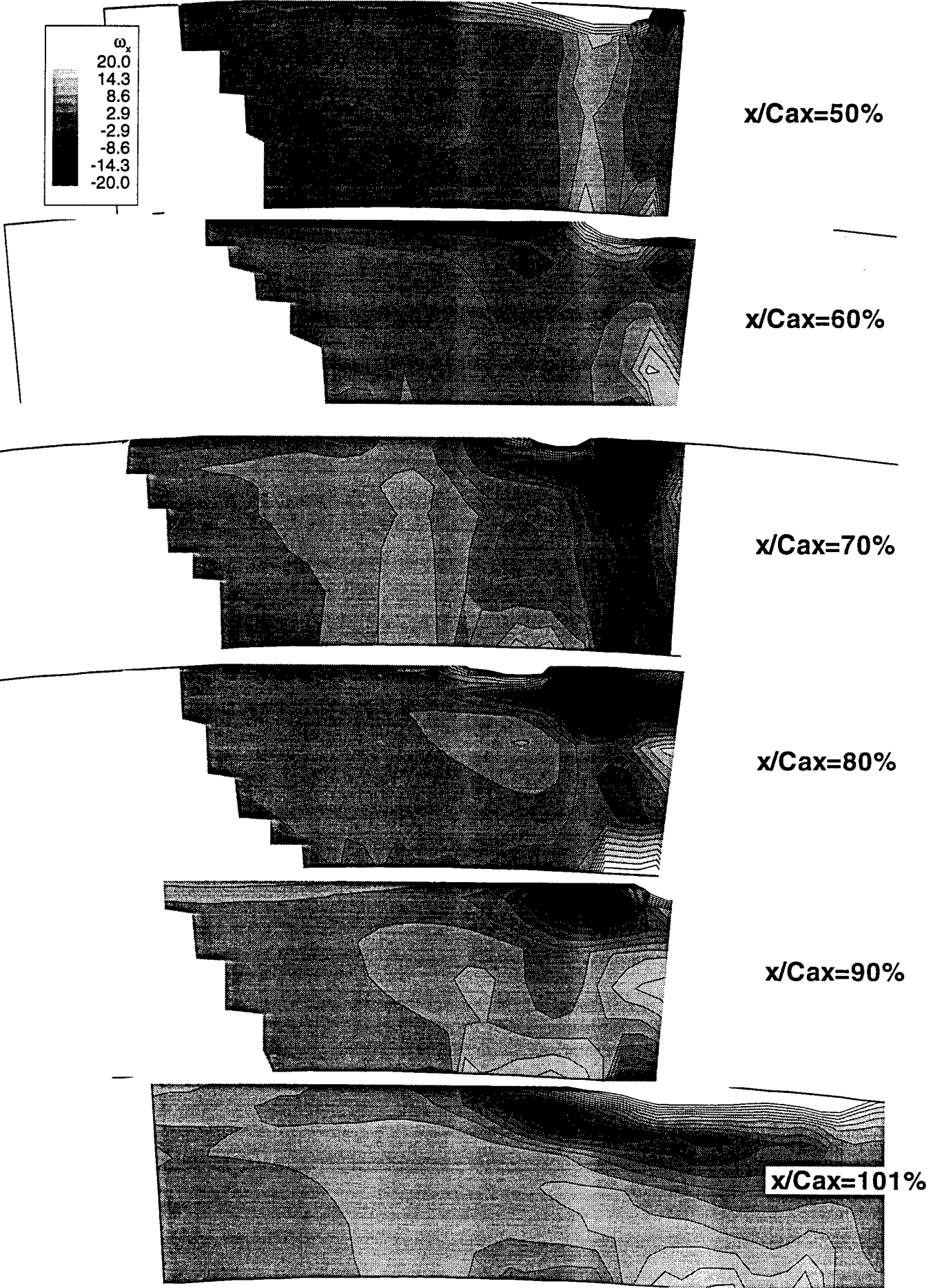
Figure 6.54 axial direction vorticity development
(black for anti-clockwise, white for clockwise)
106

7 ROTATING FIVE-HOLE PROBE DATA

7.1 Blade to Blade Profiles

Figures 7.1 through 7.10 show the blade to blade distributions of absolute pressure drop coefficient (Ψ_{03}), absolute stage pressure drop coefficient (Ψ'_{3Stage}), relative pressure loss coefficient (Ψ_{03R}), rotor static pressure drop coefficient (Ψ'_{3Rotor}), total relative velocity, axial velocity, relative tangential velocity, radial velocity, and radial and primary flow angles, respectively, for each radius given in table 7.1. Furthermore, contour plots of the same properties are presented in figures 7.11 through 7.21. Positive values for the radial flow angle and radial velocities indicate radially outward flow. The velocity profiles show the presence of a thick boundary layer and wake on the suction side of the blade, and a thinner boundary layer and wake on the pressure side. The probable cause of the thicker boundary layer on the suction side is the transport of the nozzle wake and presence of adverse pressure gradient towards the suction side. This results in the higher velocity defect on the suction side. The variations in relative tangential and radial velocities are relatively low across the passage. The wake thickness becomes consistently larger as we approach the casing due to rotational effects. Figure 7.2 shows that the absolute static pressure drop coefficient remains fairly constant throughout the entire passage.

In the region from H=0.75 to H=0.85 (figs. 7.5, 7.15) the wake width increases due to the passage vortex on the suction side interacting with the low momentum fluid in the boundary layer/wake region. There is an unexpectedly wide wake observed at H=0.85. This may be caused by the presence of nozzle secondary flow, which was observed in this region of the turbine (Zaccaria and Lakshminarayana, 1995). As we approach the tip, the radial velocity increases dramatically varying from –0.05 at H=0.60 to –0.3 in the region from H=0.75 to H=0.85 (fig. 7.8). This is due to the passage vortex. A similar trend exists in the relative tangential velocity distributions. The flow near H=0.60 is affected by the blade boundary layer and wake alone and there is little influence from the secondary flow vortex. This accounts for the lower radial and relative tangential velocities at H=0.60. Figure 7.2 shows that the absolute static pressure remains fairly constant in the area of H=0.60. There is a slight decrease in the static

pressure drop caused by the blade wake around S=0.60. The reduced velocity in the wake raises the local static pressure causing a decrease in the local absolute pressure drop.

As we move away from H=0.60 towards the tip, larger velocity gradients (fig. 7.15) are observed on the suction side due to the passage secondary flow around H=0.80. Larger decreases can also be seen in the local absolute pressure drop (fig. 7.2) in this area caused by the vortex. Figure 7.3 shows an increase in total pressure drop in the vortex area from H=0.75 to H=0.85 when compared to H=0.60. The vortex causes the low momentum fluid from the boundary layer and wake to mix further away from the blade resulting in much higher total relative pressure losses in the vortex region. The radial and tangential velocity variations then decreases around H=0.90 (figs. 7.8, 7.7) as the effects of the secondary flow decays. The relative total pressure losses at H=0.90 return to the values that they were around H=0.60 in the core flow region. The effects of secondary flow are not readily observed at H=0.90.

The data in the tip region, H=0.93 through H=0.97, shows a substantially larger velocity defect (figs. 7.5, 7.15) and larger gradients in velocities due to complex interactions between the casing boundary layer, blade wake, and tip leakage vortex. There is also a very sharp change in the radial flow direction around S=0.30 caused by the tip vortex. There is a strong inward velocity on the suction side changing quickly to a strong outward velocity indicating the presence of the tip leakage vortex. We also observe the highest relative total pressure losses in the region of the tip leakage vortex shown in figure 7.3 at H=0.95 and H=0.97. The losses here are nearly 25% higher than the losses observed near the secondary passage vortex region at H=0.80, indicating a relatively stronger leakage flow in the tip region. The plots of the primary and radial flow angles in the tip region of figures 7.9 and 7.10 also show large changes in flow angle across the center of the tip leakage vortex at H=0.93 through H=0.97. A total reversal in the radial flow angle across the tip vortex is easily observed. The significance of these changes are discussed later. It can be seen that the tip leakage has a major impact on the flow near the blade tip. This impact is shown to be stronger than that of the passage vortex.

7.2 Axial Vorticity

The axial component of vorticity was calculated from the measured data using the velocity gradients in the radial and tangential directions. The axial vorticity was calculated using the equation below.

$$\frac{\omega_x}{\Omega} = \frac{1}{r}\frac{\partial(rW_\theta)}{\partial r} - \frac{\partial W_r}{r\partial\theta} \tag{7.1}$$

The contour plot of axial vorticity is shown in figure 7.21. Counter-clockwise rotation is represented by negative vorticity values. The vorticity in the core flow is very small. Along the suction side the vorticity is very complex due to interactions of the blade wakes and secondary flows. The effects of the secondary flows dominate on the suction surface from midspan out to the casing. There is a negative vorticity in the wake region around H=0.80 to H=0.85 just away from the suction surface. This may be a result of the wake interaction with the passage vortex around H=0.80. The clockwise passage vortex can be seen a quarter of the way out from the suction side between H=0.75 to H=0.85 as the flow vorticity becomes more positive.

In the tip region, the scraping vortex is the area of clockwise vorticity close to the suction surface at H=0.97. The counterclockwise rotating leakage vortex is seen slightly further away from the suction surface than the scraping vortex. The leakage vorticity is confined to the area above H=0.93 and occupies about on quarter of the passage tangentially. The vorticity in the tip region is very complex due to the interactions of the casing boundary layer with the counter acting scraping and tip leakage vortices. The tip region vorticity is, however, much stronger than that of the passage secondary flow vorticity.

7.3 Velocity and Pressure Loss Contours

The contour plots of the absolute pressure drop coefficient (Ψ_{03}), absolute stage pressure drop coefficient (Ψ_{3Stage}), relative pressure loss coefficient (Ψ_{03R}), rotor static pressure drop coefficient (Ψ_{3Rotor}), total relative velocity, axial velocity, relative tangential velocity, radial velocity, and radial and primary flow angles, respectively, at $x/c_r=1.10$ are plotted in figures 7.12 through 7.20. In the core flow region of the passage

109

the total velocity is found to be the highest. As a result the relative total pressure losses are the lowest. As the pressure and suction side are approached, the blade boundary layer is encountered. The total velocity in the wake is reduced. As explained earlier this is due to the transport of the nozzle wake along the rotor suction side. In figures 7.13 and 7.15 higher total velocity losses and increase in pressure losses associated with the passage vortex are observed near the suction side. The highest relative total pressure losses are encountered in the tip region due to the tip clearance flow beyond H=0.93 on the suction side.

Flow characteristics in the secondary and tip leakage flow regions are complex. The tip clearance region from H=0.90 to the casing shows significantly reduced axial velocities and sharply changing radial and tangential velocities. (figs. 7.6, 7.7, 7.8, 7.16, 7.17, 7.18) The secondary flow region around H=0.8.0 show a slightly less reduced axial velocity than the tip region. Both areas also show the reduced tangential velocity and high outward gradients in radial velocity on the suction surface caused by the vortices. The relative tangential velocity shows increased gradients as we move away from the blade. The flow is underturned in this region due to the secondary tip leakage flow.

The design value of blade primary flow angles at exit is shown in table 7.1. The measured values are shown in figure 7.17.

Table 7.1   Design values of relative primary flow angle at blade trailing edge

H=	0.5	0.6	0.7	0.8	0.9	1.0
Beta =	66.64	66.94	67.26	67.55	68.87	68.15

As the figure demonstrates, in the core flow region around H=0.6 in the wake region the measured flow angle is close to design. The flow pattern is distorted towards the tip as the secondary and tip leakage flows become dominant on the suction side. The secondary and tip leakage flows in the outer region of the blade from H=0.75 to the casing has a large influence on the flow in this region.

Examining the wakes in the secondary flow regions, the total relative velocity contour shows the highest momentum fluid on the pressure side and lowest momentum

fluid on the suction side. The tip leakage flow acts to sweep the low momentum fluid from the casing wall to the suction side.

The passage vortex pulls low momentum fluid from the blade boundary layer into the flow above the suction surface. These vortices entrain fluid from surroundings as seen by the outward velocity near the pressure side and inward velocity on the suction side. The high relative total pressure losses in the tip vortex region and passage vortex region confirms the entrainment of low momentum fluid by the vortices. The losses in the tip clearance vortex are much stronger than the losses due to the passage vortex.

In the tip region from H=0.90 to the casing, the radial and axial velocity profiles show large gradients due to the interaction of the casing endwall boundary layer, tip clearance vortex, scraping vortex, and blade wake. From the primary flow angle plot in figure 7.20, and the radial velocity and radial flow angle plots in figures 7.18 and 7.19 respectively, the effects of the tip leakage vortex can be easily seen. The flow around H=0.90 is highly overturned and at H=0.97, the flow becomes highly underturned due to the leakage flow vortex . The radial velocity and radial flow angle plots in this region also show the high inward velocity on the suction side and outward flow on the pressure side associated with the tip leakage vortex. This shows a vortex in this region moving counterclockwise. The tip leakage vortex is located on the suction side of the blade centered around H=0.95 and occupies about 30% of the blade passage. The tip vortex is confined to the last 7% of the blade height in this experiment. This is unlike data obtained from cascades where the tip vortex has been shown to move further away from the casing. The secondary flows and relative motion between the blade and casing in an actual rotating turbomachinery confine the leakage vortex to the corner of the suction surface.

7.4 Pressure Loss Coefficient Analysis

Figure 7.13 shows that the secondary flow vortices account for much of the losses in the blade passage. Examining the losses in the wake region at H=0.75 through H=0.85 the relative total pressure losses are high due to the presence of the passage vortex. The losses measured include the losses due to the blade boundary layer and wake due to turbulent dissipation as well as losses from mixing and dissipation of the passage vortex.

The losses in the wake decrease around H=0.90 as the effects of the passage vortex at H=0.80 decay. The losses here are caused by the turbulent dissipation from the boundary layer and wake alone.

In the tip region from H=0.95 to H=0.97, the losses are much higher due primarily to the tip leakage vortex. The contributions to the losses include the turbulent dissipation of the blade boundary layer and wake, turbulent mixing and dissipation of the tip leakage vortex, dissipation in the casing boundary layer, and the interaction of the vortex with the casing boundary layer.
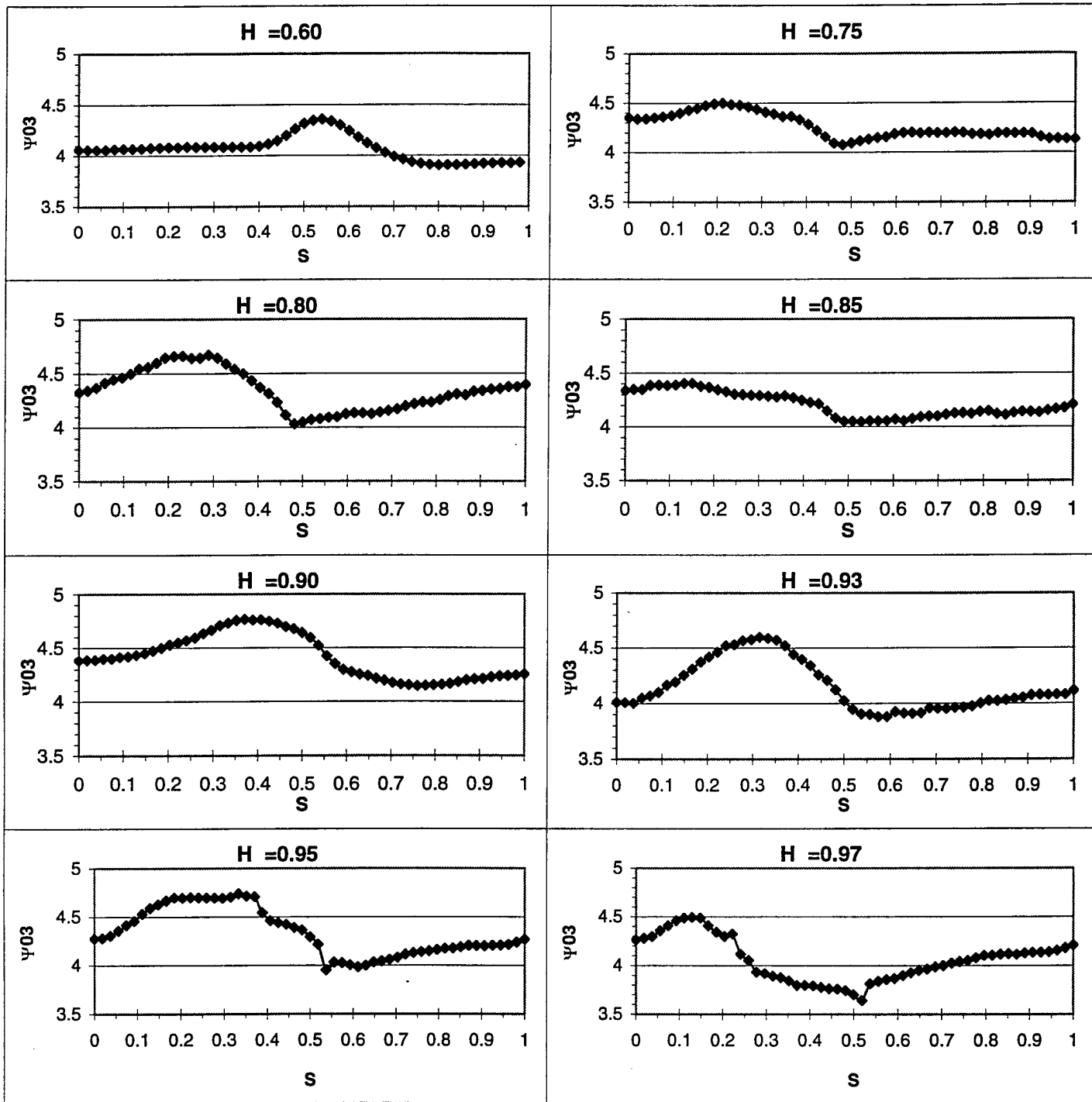
Figure 7.1 - Stage absolute total pressure drop coefficient ($\Psi 03$) distributions X/Cr = 1.10, H=0.60 through H=0.97
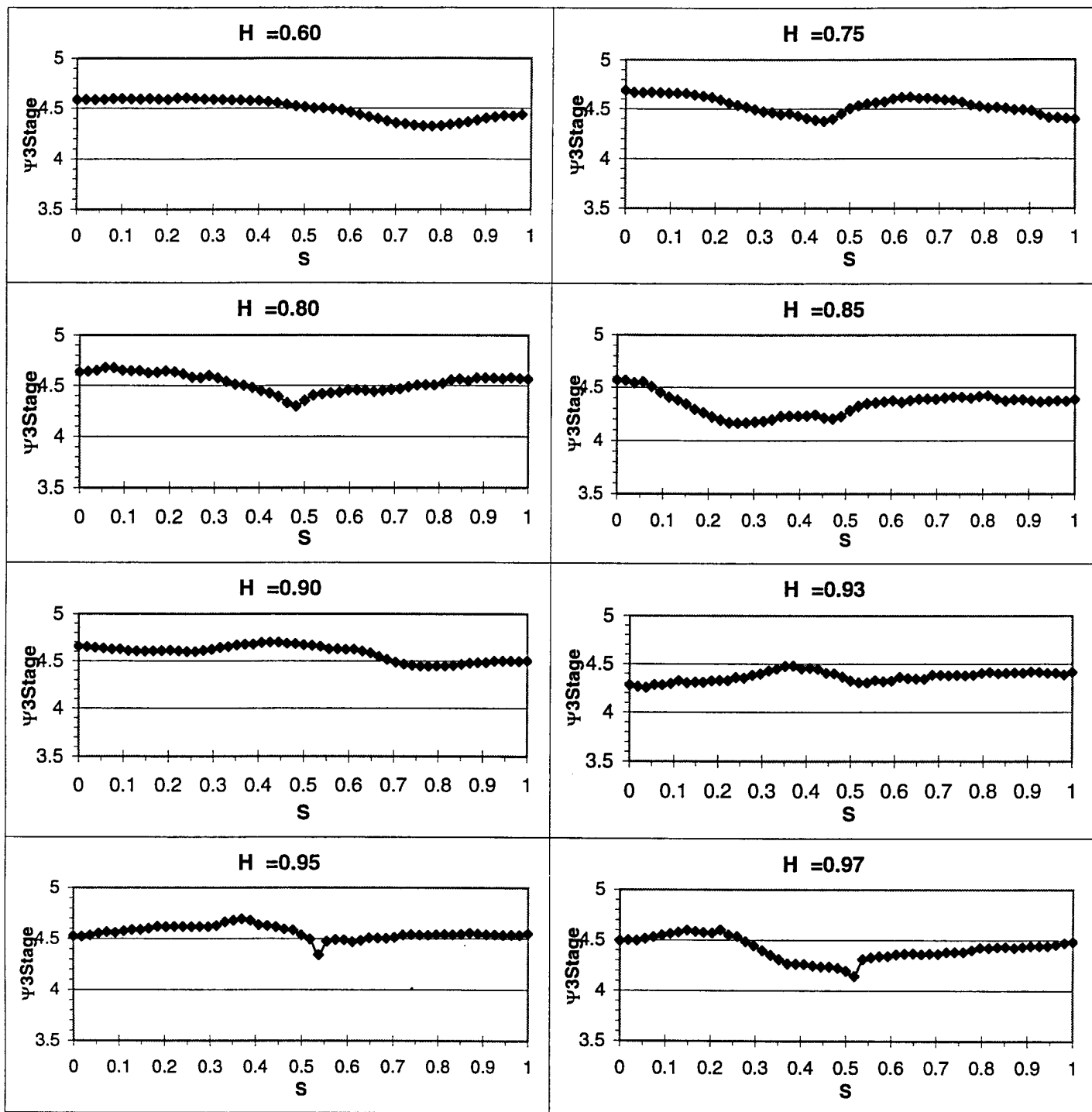
Figure 7.2 - Stage absolute static pressure drop coefficient (Ψ3Stage) distributions X/Cr = 1.10, H=0.60 through H=0.97
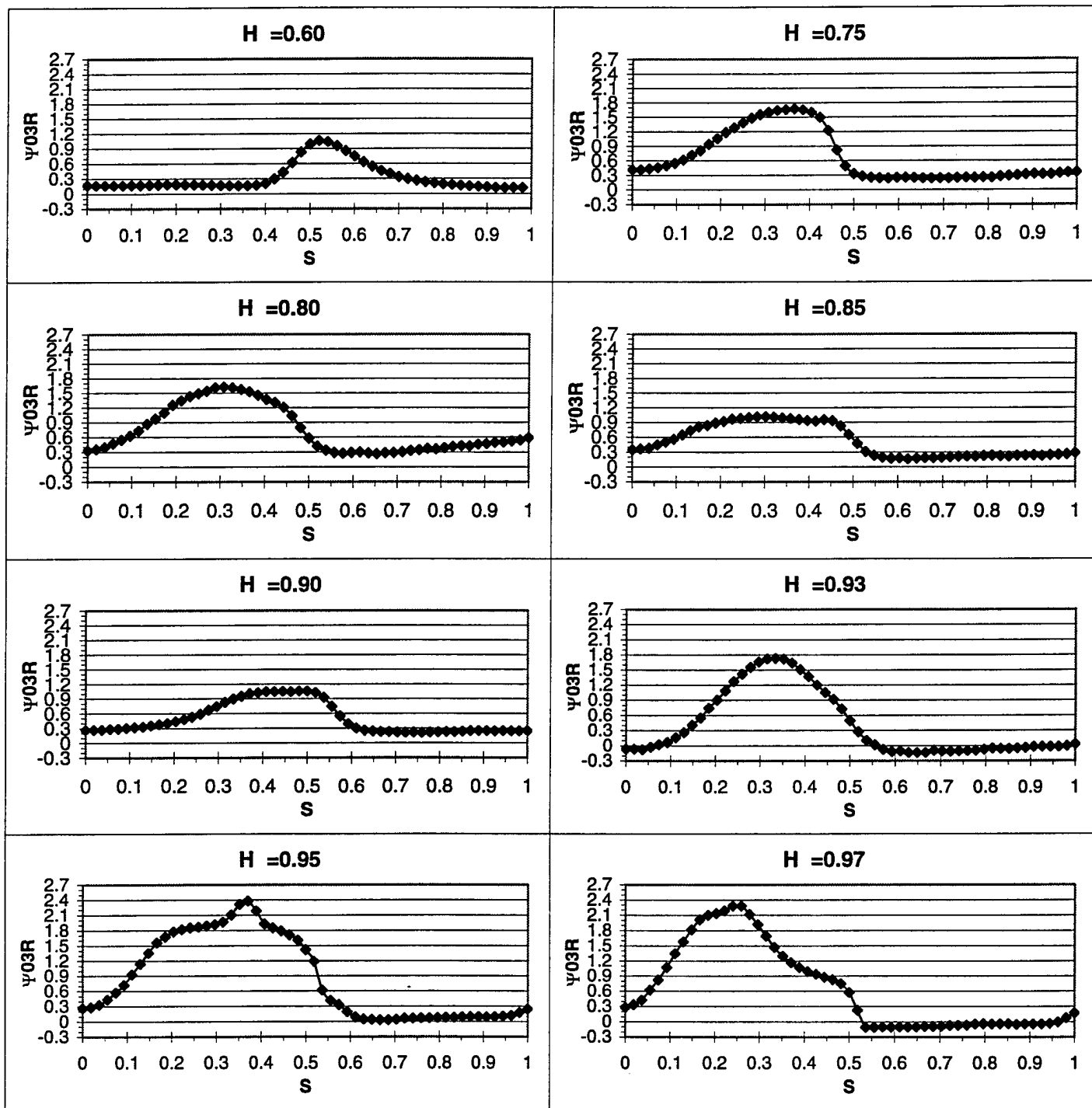
Figure 7.3 - Relative pressure loss coefficient ($\Psi 03R$) distributions X/Cr = 1.10, H=0.60 through H=0.97
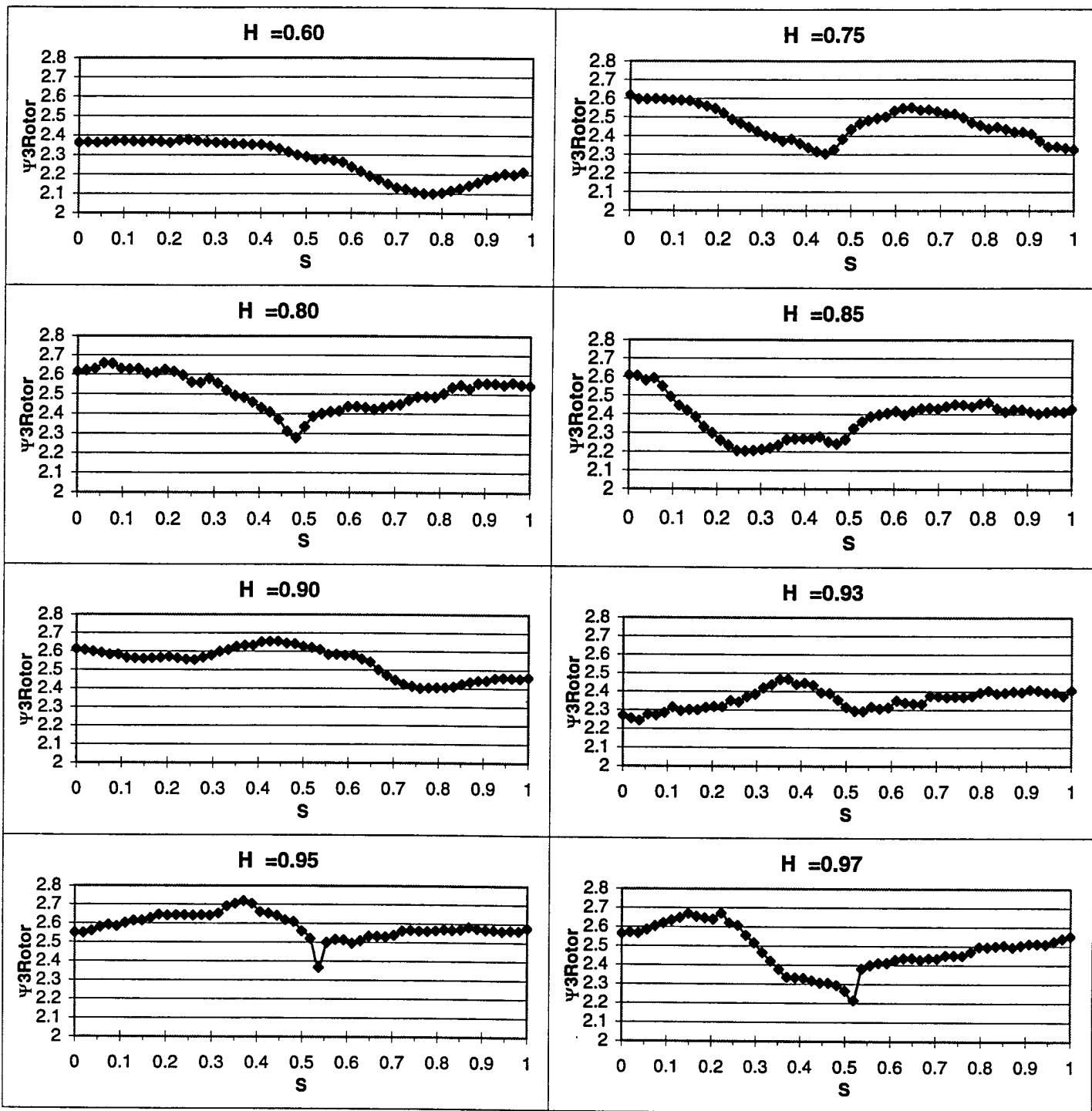
Figure 7.4 - Rotor static pressure drop coefficient (Ψ3Rotor) distributions X/Cr = 1.10, H=0.60 through H=0.97

116
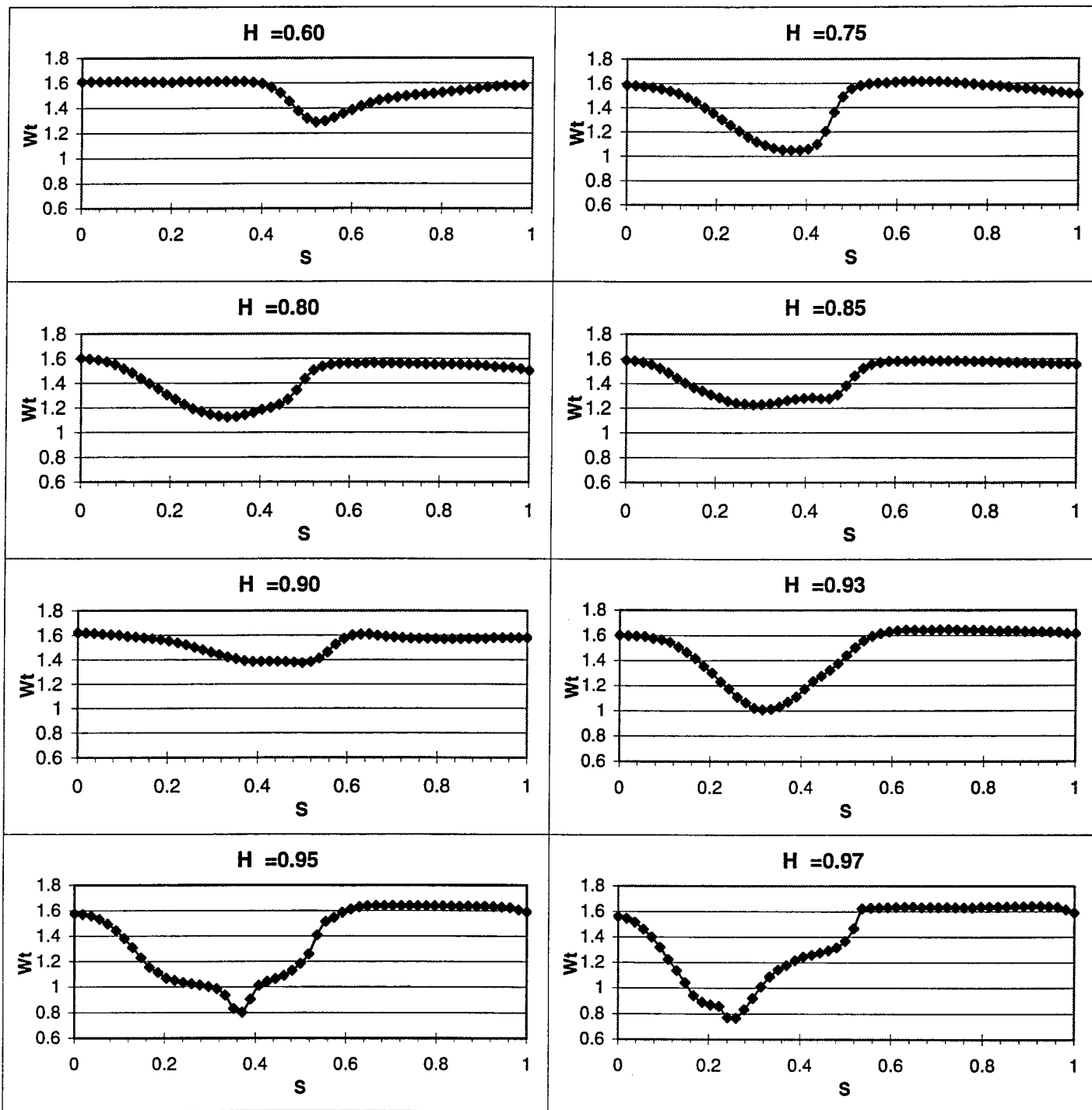
Figure 7.5 - Relative Total Velocity (Wt) Distributions X/Cr = 1.10, H=0.60 through H=0.97
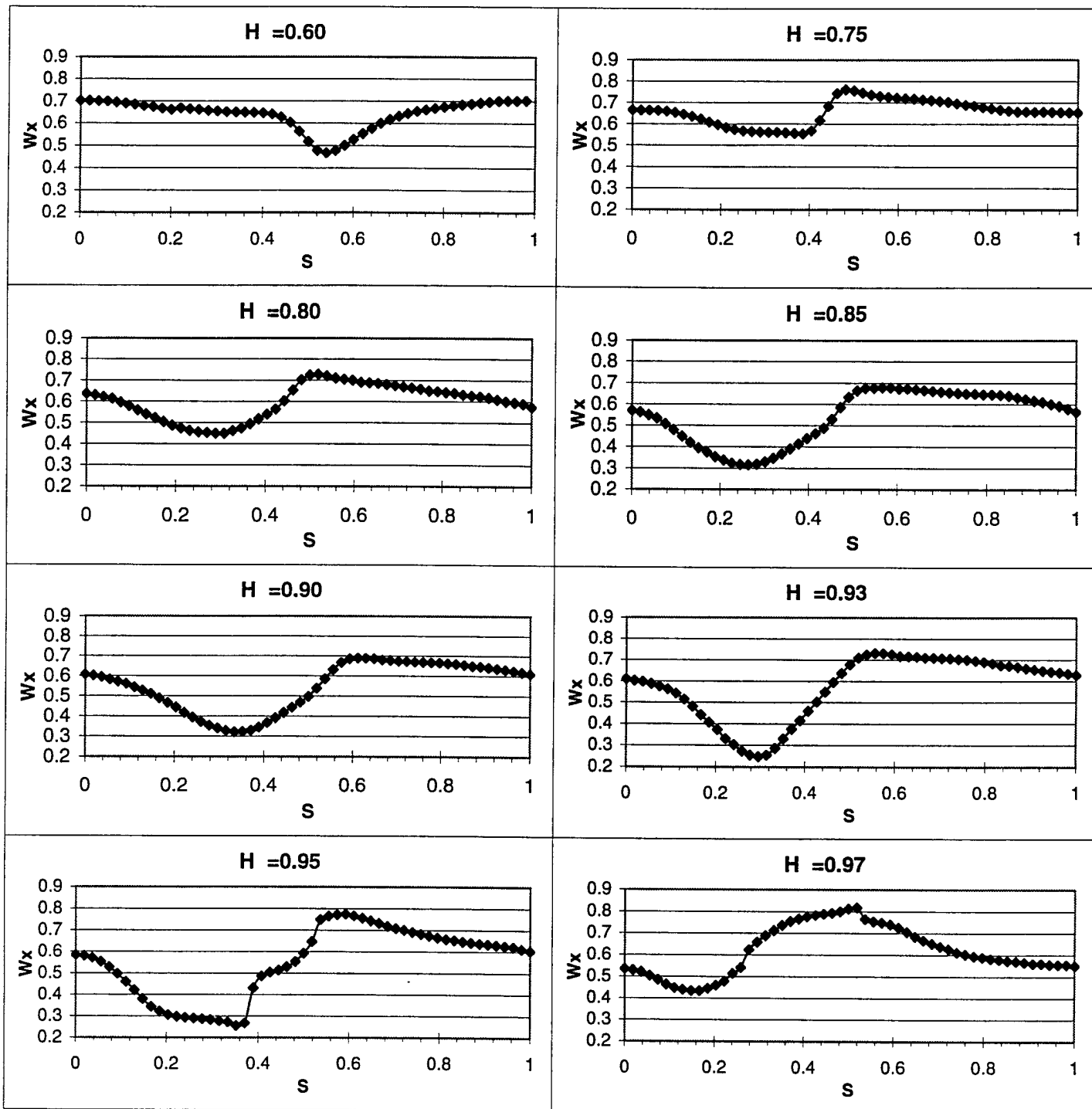
Figure 7.6 - Relative Axial Velocity (Wx) Distributions X/Cr = 1.10, H=0.60 through H=0.97

118
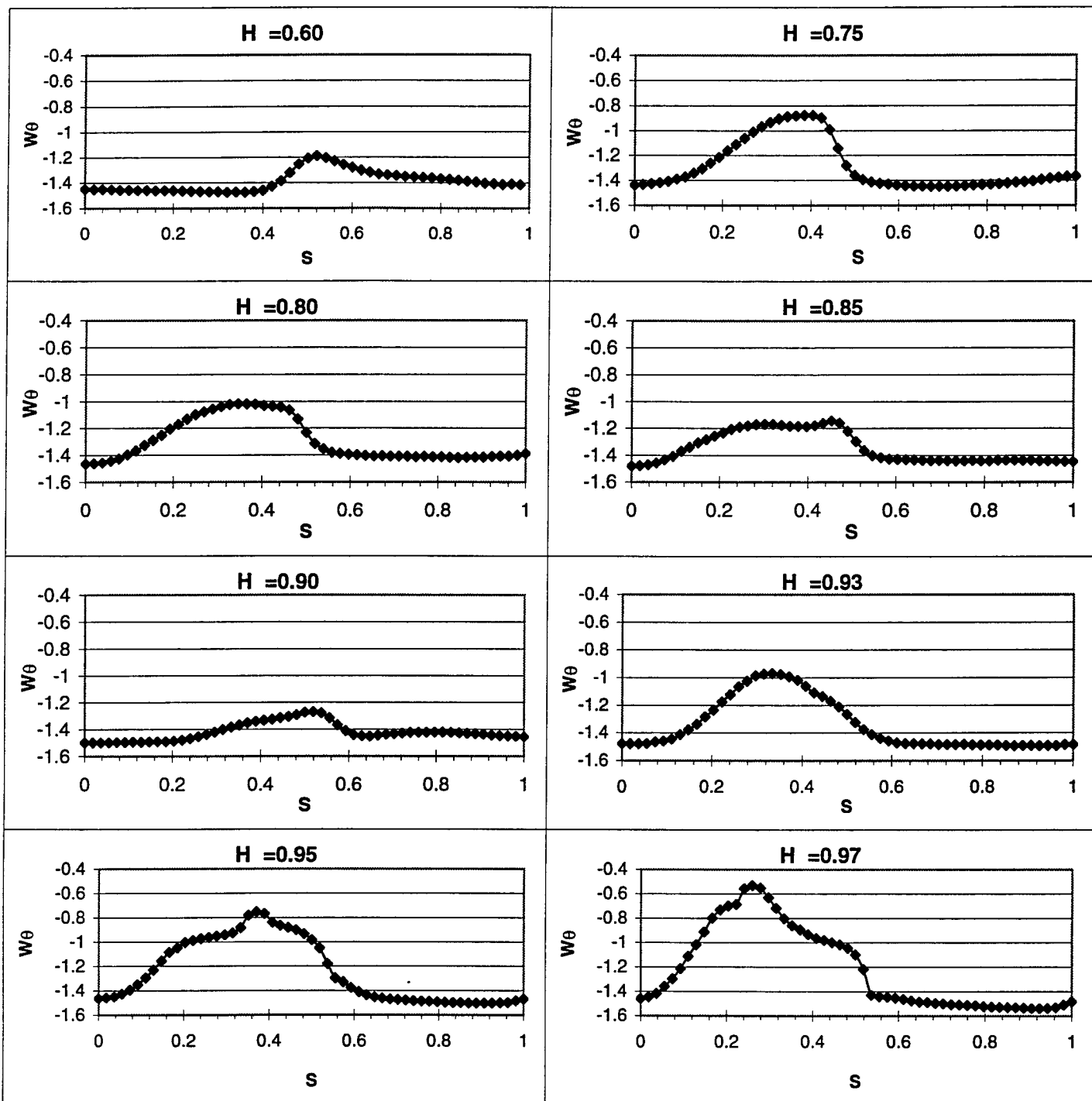
Figure 7.7 - Relative Tangential Velocity (Wθ) Distributions X/Cr = 1.10, H=0.60 through H=0.97
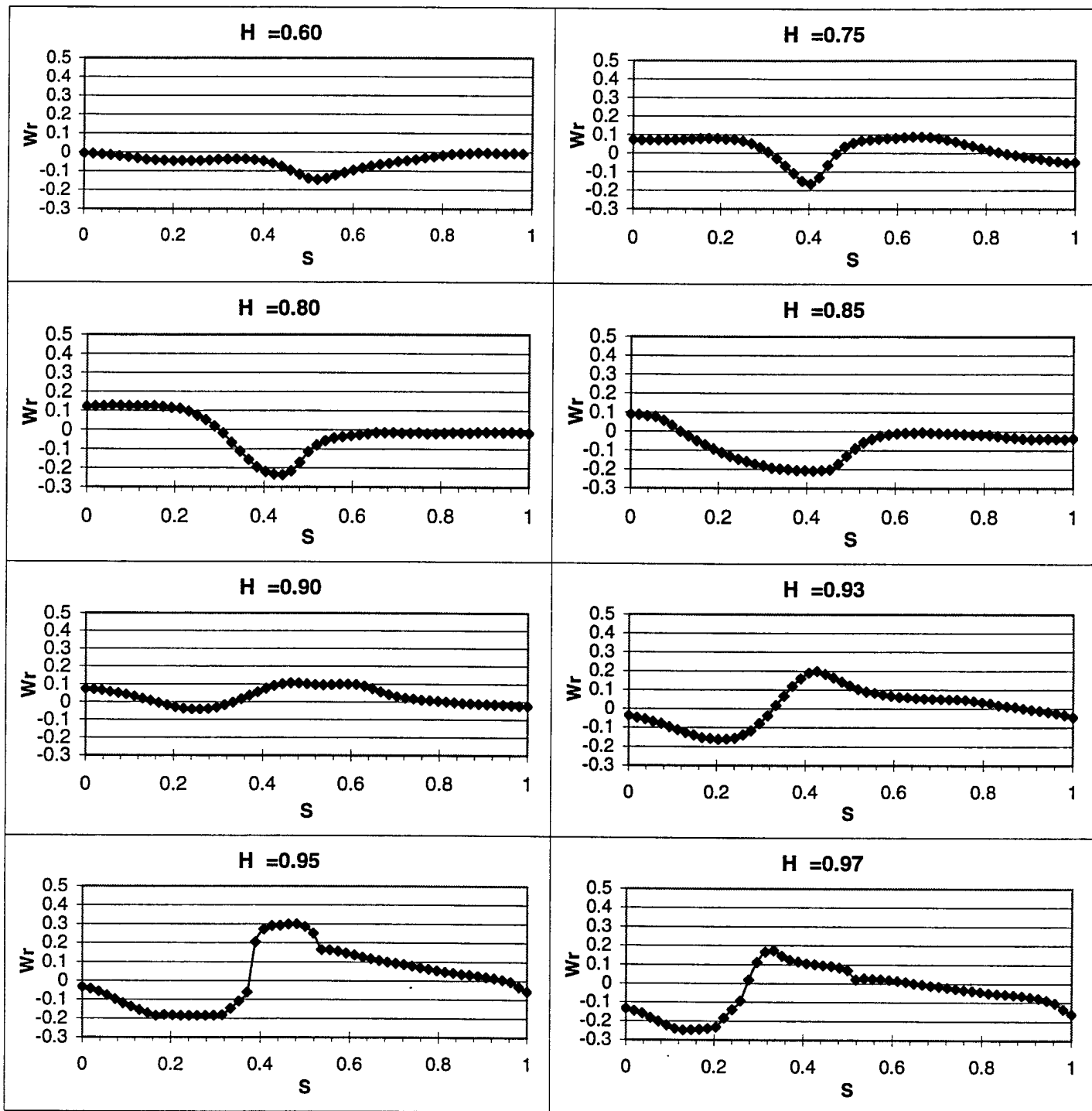
Figure 7.8 - Relative Radial Velocity (Wr) Distributions X/Cr = 1.10, H=0.60 through H=0.97
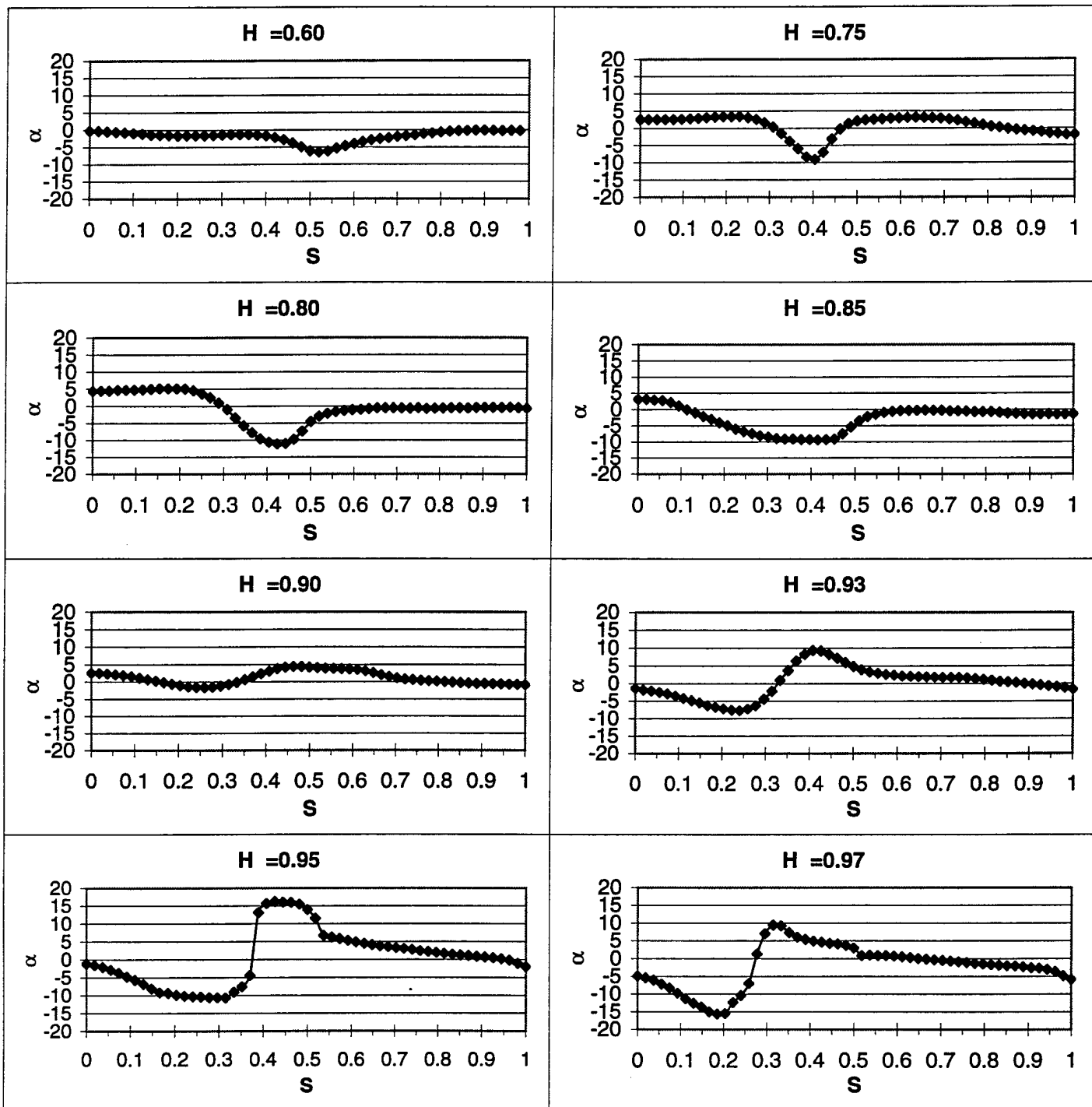
Figure 7.9 - Radial Flow Angle (α) Distributions X/Cr = 1.10, H=0.60 through H=0.97
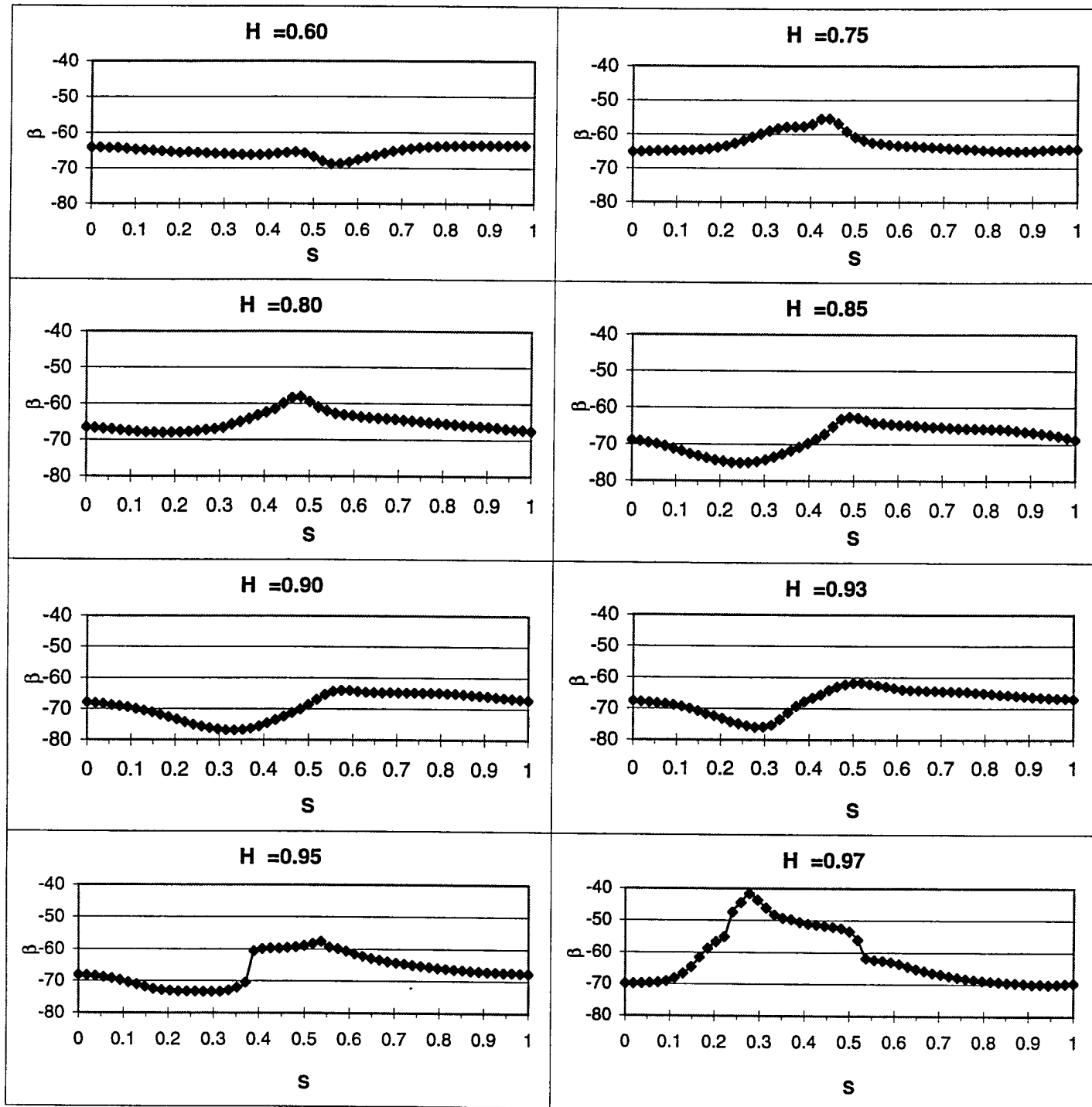
Figure 7.10 - Primary Flow Angle (β) Distributions X/Cr=1.10, H=0.60 thruogh H=0.97

Stage Absolute Total Pressure Drop Coefficient (Ψ_{03})
X/Cr = 1.10
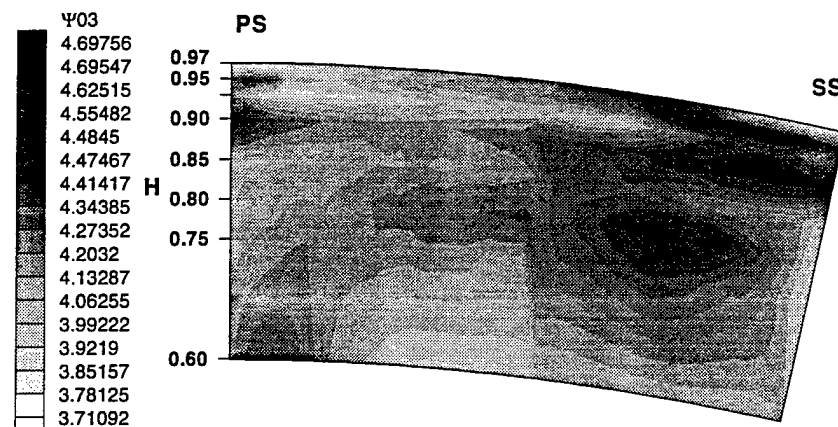
Figure 7.11

Stage Static Pressure Drop Coefficient (Ψ_{3Stage})
X/Cr = 1.10
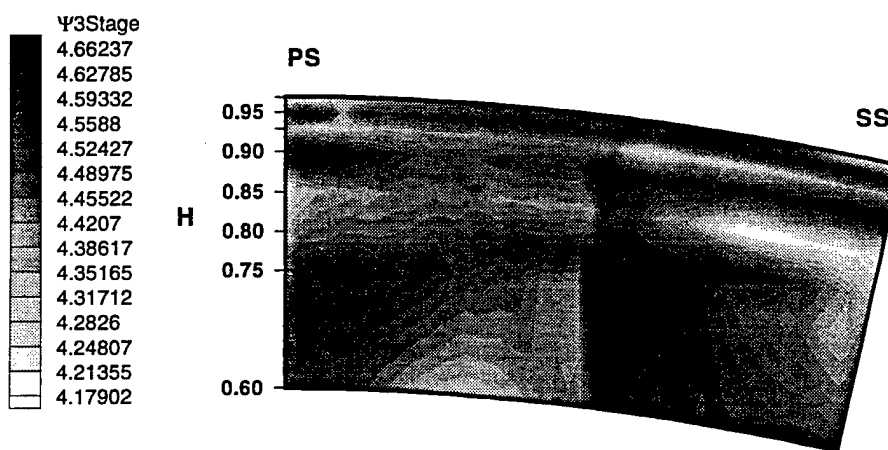
Figure 7.12

Rotor Relative Total Pressure Loss Coefficient (Ψ'_{03R})
X/Cr = 1.10
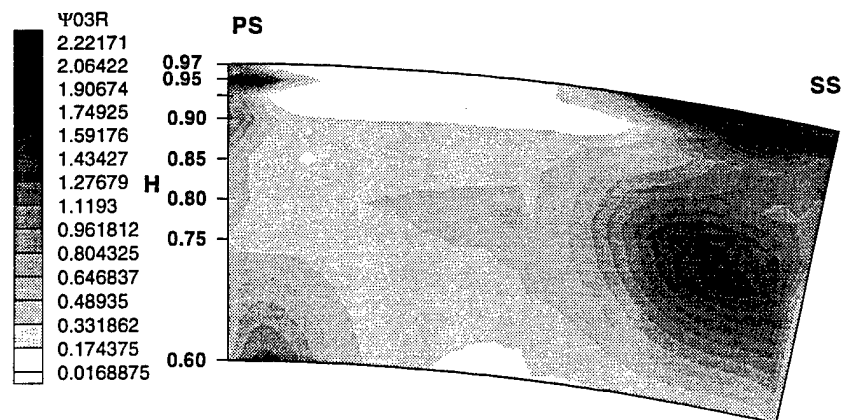
Figure 7.13

Rotor Static Pressure Drop Coefficient (Ψ_{3Rotor})
X/Cr = 1.10

Figure 7.14

Rotor Exit Total Relative Velocity Field
X/Cr = 1.10

Figure 7.15

Rotor Exit Relative Axial Velocity Field (W$_x$)
X/Cr = 1.10

Figure 7.16

Rotor Exit Relative Tangential Velocity Field (W$_\theta$)
X/Cr = 1.10

Wθ
-0.595675
-0.65865
-0.721625
-0.7846
-0.847575
-0.91055
-0.973525
-1.0365
-1.09948
-1.16245
-1.22543
-1.2884
-1.35138
-1.41435
-1.47733

PS
SS
H
0.95
0.90
0.85
0.80
0.75
0.60

Figure 7.17

Rotor Exit Relative Radial Velocity Field (W$_r$)
X/Cr = 1.10

Wr
0.265825
0.23155
0.197275
0.163
0.128725
0.09445
0.060175
0.0259
-0.008375
-0.04265
-0.076925
-0.1112
-0.145475
-0.17975
-0.214025

PS
SS
H
0.95
0.90
0.85
0.80
0.75
0.60

Figure 7.18

Rotor Exit Relative Radial Flow Angle (α)
X/Cr = 1.10
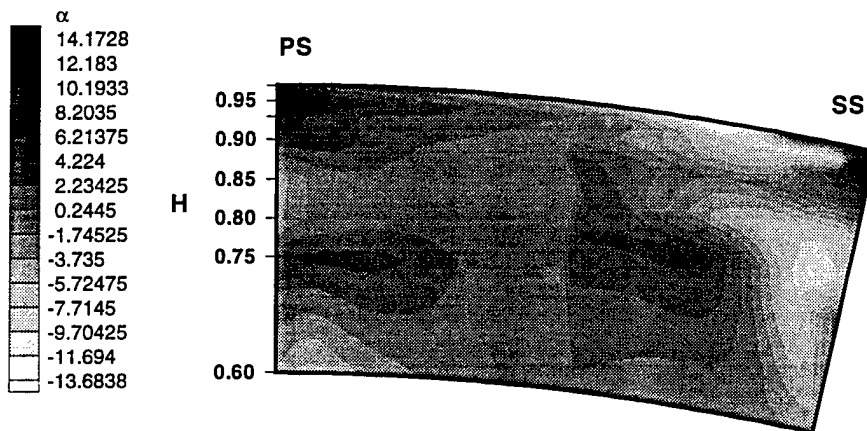
Figure 7.19

Rotor Exit Relative Primary Flow Angle (β)
X/Cr = 1.10
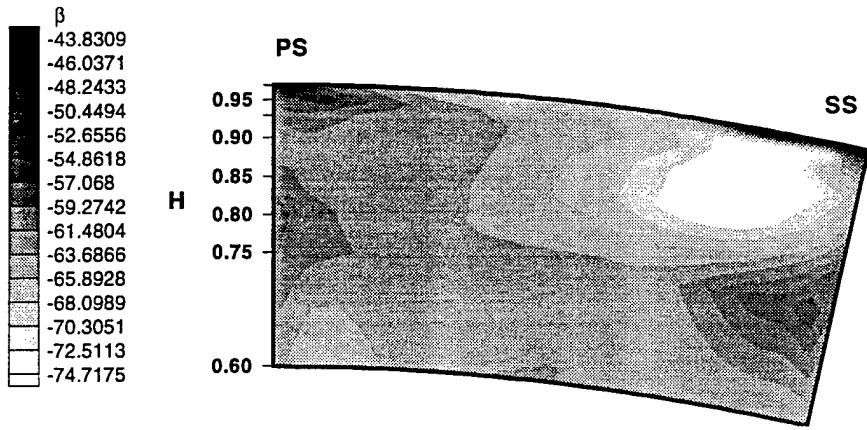
Figure 7.20

Rotor Exit Axial Vorticity Field (ω_x)
X/Cr = 1.10
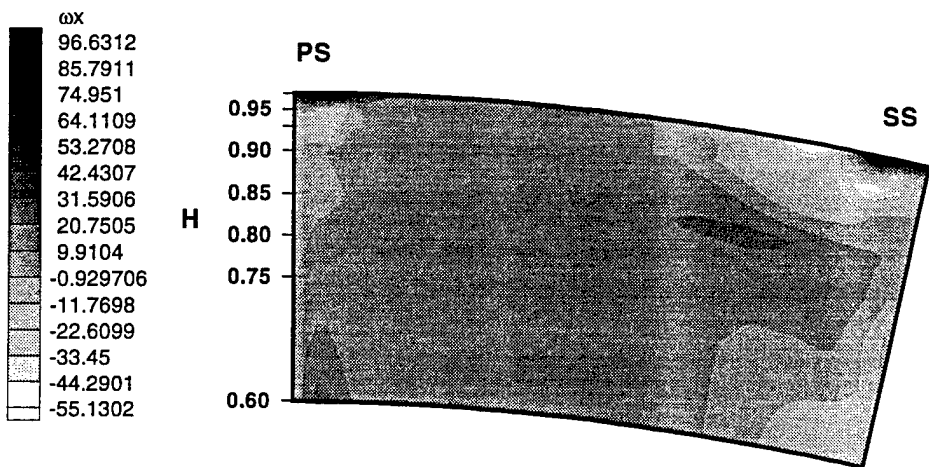
Figure 7.21

8. NUMERICAL SIMULATION

8.1 Governing Equation and Numerical Procedure

8.1.1 Governing equations and numerical procedure

Applying the Favre averaging procedure to the continuity, momentum, and energy equations, the five mean flow equations can be written in Cartesian tensor form as :

$$\frac{\partial \overline{\rho}}{\partial t} + \frac{\partial}{\partial x_j}(\overline{\rho}\tilde{U}_j) = 0$$

$$\frac{\partial(\overline{\rho}\tilde{U}_i)}{\partial t} + \frac{\partial}{\partial x_j}(\overline{\rho}\tilde{U}_i\tilde{U}_j) = -\frac{\partial \overline{p}}{\partial x_i} + \frac{\partial}{\partial x_i}\tau_{ij} - \overline{\rho}\varepsilon_{ijk}\omega_j\varepsilon_{klm}\omega_l x_m - 2\overline{\rho}\varepsilon_{ijk}\omega_j\tilde{U}_k$$

$$\frac{\partial(\overline{\rho}\tilde{e}_{0R})}{\partial t} + \frac{\partial}{\partial x_j}(\overline{\rho}(\tilde{e}_{oR} + \frac{\overline{p}}{\overline{\rho}})\tilde{U}_j) = \frac{\partial}{\partial x_j}(\tilde{U}_j\tau_{ij} - q_i) \qquad [8.1]$$

Where: $\overline{f} = \dfrac{\lim}{t \to \infty}\dfrac{1}{t}\int\limits_{t_0}^{t_0+t} f dt$ - time averaging of f

$\tilde{f} = \dfrac{\overline{\rho f}}{\overline{\rho}}$ - Favre averaging

$\tau_{ij} = \tau_{lij} - \overline{\rho u_i''u_j''}$ - effective stress tensor

$q_i = q_{li} + \overline{\rho u_i''e''}$ - effective heat flux vector

$e_{0R} = \rho(e + W^2/2 - \omega^2 r^2/2)$ -energy transport variable, assuming rotation vector is coincident with x-axis and r is a distance to the axis

Reynolds stresses and heat flux components are calculated using the eddy viscosity hypothesis or higher order turbulence closure.

For the stability analysis of the numerical scheme presented below equations [8.1] can be rewritten in a matrix form:

$$\frac{\partial Q}{\partial t} = \frac{\partial(E_i + E_v)}{\partial x} + \frac{\partial(F_i + F_v)}{\partial y} + \frac{\partial(G_i + G_v)}{\partial z} + S \qquad [8.2]$$

$Q = \begin{pmatrix} \overline{\rho} & \overline{\rho}\tilde{U}_x & \overline{\rho}\tilde{U}_y & \overline{\rho}\tilde{U}_z & \overline{\rho}\tilde{e}_{oR} \end{pmatrix}^t$ - vector of conservative variables

E_i, F_i, G_i - inviscid flux vectors,

129

E_v, F_v, G_v - vectors of viscous terms,

S - source vector.

Explicit four-stage Runge-Kutta scheme is used for time integration of both main-flow and turbulence equations. A compact second order accurate central difference flux evaluation scheme is employed for the convection terms. Diffusion terms are discretized using second order accurate central differences. For the mean flow equations a fourth order artificial dissipation is included to damp high wave number errors. Second order dissipation is used to improve the shock capturing. Eigenvalue and velocity scaling are used to optimize the amount of the artificial dissipation. Multigrid and an implicit residual smoothing are used to improve the convergence characteristics of the steady solver.

Numerical simulation of the unsteady flow requires special efforts to reduce possible reflection at the boundaries. One and two-dimensional, Giles' type, non-reflecting boundary conditions are incorporated to minimize the reflection at boundaries and to minimize the computational domain (Fan and Lakshminarayana, 1996).

8.1.2 Turbulence closure

Turbulence equations are descretized in a manner similar to those for mean flow equations. "Lagged" approach is utilized for the computation of turbulence equations, i.e., k and ε values at previous time step are used to calculate the eddy viscosity at the current step. The presence of the source term in the turbulence equation results in a stability problem during the initial convergence period. Two mechanisms are used to ensure a stable calculation; utilization of the underelaxation factor, ϕ, for k and ε equations in addition to the time step based on the mean equation and enforcement of an eddy viscosity limit. The maximum ratio of μ_t/μ_l is set equal to 10~100 during the initial convergence period with the further increase to 1000~10000 to ensure the correct solution. It was found that the utilization of ϕ=0.6 in the case of two-dimensional flow and ϕ=0.75 for the three-dimensional flow improves convergence characteristics of the solver.

8.1.3 Two-equation models

In eddy-viscosity models effective stress tensor and effective heat flux vector are defined:

$$\tau_{ij} = \tau_{lij} - \overline{\rho u_i'' u_j''} \quad \text{and} \quad q_i = q_{li} + \overline{\rho u_i'' e''}$$

Reynolds stress is calculated from

$$-\overline{\rho u_i'' u_j''} = \mu_l \left[(\frac{\partial \tilde{U}_i}{\partial x_j} + \frac{\partial \tilde{U}_j}{\partial x_i}) - \frac{2}{3} \delta_{ij} \frac{\partial \tilde{U}_k}{\partial x_k} \right] - \frac{2}{3} \delta_{ij} \overline{\rho} \tilde{k}$$

heat flux component is given

$$q_{li} = -c_p \frac{\mu_l}{\text{Pr}_l} \frac{\partial \overline{T}}{\partial x_i}$$

[8.3]

Turbulent eddy viscosity is computed using Prandtl-Kolmogorov relation

$$\mu_t = \frac{c_\mu f_\mu \overline{\rho} \tilde{k}^2}{\tilde{\varepsilon}}$$

[8.4]

Transport equations for turbulence kinetic energy and turbulence dissipation ratio (for the simplification, in subsequent equations averaging symbols are omitted)

$$\frac{\partial(\rho k)}{\partial t} + \frac{\partial(\rho U_i k)}{\partial x_i} = \frac{\partial}{\partial x_j} \left[(\mu_l + \frac{\mu_t}{\sigma_k}) \frac{\partial k}{\partial x_j} \right] + \rho P_k - \rho(\varepsilon + D)$$

[8.5]

$$\frac{\partial(\rho \varepsilon)}{\partial t} + \frac{\partial(\rho U_i \varepsilon)}{\partial x_i} = \frac{\partial}{\partial x_j} \left[(\mu_l + \frac{\mu_t}{\sigma_\varepsilon}) \frac{\partial \varepsilon}{\partial x_j} \right] + \rho \frac{\varepsilon}{k} [C_{\varepsilon 1} f_1 P_k - C_{\varepsilon 2} f_2 \varepsilon] + \rho E$$

[8.6]

Here f_1, f_2, f_μ, $c_{\varepsilon 2}$, $c_{\varepsilon 1}$, D, E are low Reynolds number functions and constants described below.

$$P_k = -\overline{u_i'' u_j''} \frac{\partial \tilde{U}_i}{\partial x_j} \quad \text{- production of turbulent kinetic energy}$$

A number of low-Reynolds number k-ε turbulence models; Chien (1982), denoted as CH, Lam-Bremhost (1981), denoted as LB, and Fan-Lakshminarayana-Barnett (1993),

131

denoted as FLB, are utilized for the turbulence closure. A summary of the constant and near wall function for different turbulence models is given in

Table 8.1 and Table 8.2. The solution of the turbulence transport equations is numerically coupled with the solution of the main flow equations. A second and fourth order artificial dissipation is included in the turbulence transport equations.

Table 8.1 Low-Reynolds-number functions used in turbulence model

Model	Code	f_μ
Chien	Ch	$1-\exp(-0.0115y^+)$
Lam-Bremhost	LB	$[1-\exp(-0.0165Re_y)]^2(1+20.5/Re_t)$
Fan-Lakshminarayana-Barnett	FLB	$0.4f_w/\sqrt{Re_t}+(1-0.4f_w/\sqrt{Re_t})[1-\exp(-Re_y/42.63)]^3$

Table 8.2 Low-Reynolds-number functions used in turbulence models

Code	f_1	f_2	D	E
CH	1.0	$1-0.22\exp(-Re_t^2/36))$	$2vk/y^2$	$-2v(\varepsilon/y^2)\exp(-0.5y^+)$
LB	$1+(0.06/f_\mu)^3$	$1-\exp(-Re_t^2)$	0	0
FLB	1.0	$1-2/9\exp(-Re_t^2/36))f_w^2$	0	0

where the near-wall function in the FLB model is given by

$$f_w = 1-\exp\left\{\frac{\sqrt{Re_y}}{2.30}+(\frac{\sqrt{Re_y}}{2.30}-\frac{Re_y}{8.89})\left[1-\exp(-\frac{Re_y}{20}\right]^3\right\}$$

Constants $C_\mu=0.09,C_{\varepsilon1}=1.44,C_{\varepsilon2}=1.92,\sigma_k=1.0,\sigma_\varepsilon=1.3$ in the LB and FLB models are the same as those used in the standard (high-Reynolds-number) k-ε model given by Launder and Spalding (1974). Chien's k-ε model has slightly different values for $C_{\varepsilon1}=1.35,C_{\varepsilon2}=1.80$.

8.1.4 Algebraic Reynolds Stress Model

Numerical simulation based on the first order turbulence closure can be applied to a wide range of cases and may improve the accuracy of the prediction in comparison with algebraic turbulence models. However, deficiency of these models associated with the Boussinesq approximation and empirical correlation used to derive these models leads to less precise solution in the case of complex flows (Lakshminarayana, 1986). Non-equilibrium flows, flows with streamwise curvature and rotation, flows with injection (e.g., film cooling) are examples when the first order turbulence closure does not provide an adequate level of accuracy. Flow computation based on a second degree closure and a subgrid turbulence modeling (LES) demonstrated the potential for the improvement in the turbulence flow prediction. Complex models generally require more CPU time. Another factor affecting the wide acceptance of more complex models is a potentially increased dependence on the numerical stability. More complex structure may lead to a less robust and, as a result, less reliable prediction. It is more difficult to develop a stable code in the case of full Reynolds Stress (FRSM) models. To overcome stability limitations many FRSM solvers utilized a simplified approach for the near wall region (wall function, one-equation models), thus decreasing the accuracy of the flow resolution near the wall.

Rodi, 1976, suggested a simplified algebraic expression for the component of the Reynolds stress tensor. This model is based on the assumption that the transport of Reynolds stress components is locally proportional to the transport of the turbulent kinetic energy. ARSM may be considered as a compromise between the two-equation and higher order models. Implementation of the ARSM does not lead to a significant increase in the CPU time and requires an inversion of the 6X6 (multidimensional case, implicit ARSM). ARSM uses the following expression to calculate Reynolds Stress component:

$$-\overline{u_i''u_j''} = -k\left[R_{ij}(2-C_2)/2 + (P_{ij} - P_{kk}\delta_{ij}/3)(1-C_2)\right]/\left[\frac{1}{2}P_{kk} + \varepsilon(C_1 - 1)\right] - \frac{2}{3}\delta_{ij}k$$

[8.7]

where: $P_{kk} = P_k = -\overline{u_i''u_j''}\dfrac{\partial \tilde{U}_i}{\partial x_j}$ - production of k

133

$$P_{ij} = -\overline{u_i'' u_k''} \frac{\partial \tilde{U}_j}{\partial x_k} + \overline{u_j'' u_k''} \frac{\partial \tilde{U}_i}{\partial x_k} \text{ - production of Reynolds stresses}$$

$$R_{ij} = -2\omega_p (\varepsilon_{ipk} \overline{u_j'' u_k''} + \varepsilon_{jpk} \overline{u_i'' u_k''})$$

$C_1=1.5$, $C_2=0.6$ - model constants

In current research, a hybrid model is utilized in a near wall region. Laminar sublayer and overlap region are calculated using k-ε equation. Matching function based on Re_y is incorporated to smooth the transition between regions calculated using k-ε and ARS models:

$$f_m = \frac{1}{2} \left(\frac{\tanh(\beta \frac{Re_y}{1.83} / y^+_{match} - 1)}{\tanh(\beta)} + 1 \right)$$

where: β is a slope constant

y^+_{match} - matching location

$$R_{vis} = f_m R_{ARSM} + (1 - f_m) R_{k-\varepsilon}$$

8.2 Computational details

The current investigation is an extension of the numerical simulation presented in Luo and Lakshminarayana (1997). The emphasis of this research is to improve the resolution of the flow in the tip region, including a detailed analysis of the tip vortex development and assessment of the utilization of an ARS turbulence model.

The embedded h-grid is utilized for the simulation of the flow in the tip region. There is a significant variation of velocity vector across the tip clearance due to the relative motion of the blade and casing. The maximum change in velocity amplitude reaches 90 m/s within 1mm distance. Thus, very dense grid is required for an accurate resolution of the tip clearance flow. A comprehensive grid dependency analysis is not feasible due to the enormous utilization of the CPU time. Only a partial grid dependency analysis has been carried out. The numerical simulation has been performed with 9, 12, and 18 grid points in the tip clearance height (0.9 mm, $\tau_c=(r_{cas}-r_{tip})/(r_{cas}-r_{hub})=0.75$). The difference between the solution based on 12 and 18 tip clearance grid points is

considerably smaller than that based on 9 and 12 grid points within the gap. All results reported are based on the grid with 18 grid points in the gap. Similar analysis has been performed for the vortex region. Twenty- six grid points in spanwise-direction are utilized across the tip vortex zone. The total grid size is 104 (axial) X 60 (blade-to-blade) X 78 (radial) (Fig. 8.1). The outlet boundary is set at $x/C_x = 2$ downstream of the leading edge to ensure that there is no influence of the outlet boundary condition on the vortex structure development. Pitchwise average flow field based on the data by Zaccaria and Lakshminarayana (1995) is used to establish the inlet boundary conditions.

8.3 Comparison with the experimental data

Predicting strong secondary flow that exists in a turbine is known to be one of the most difficult tasks in CFD analysis. Results of the numerical modeling of the ERCOFTAC turbine test cascade reveal a large variation in the position and the amplitude of the secondary vortex predicted by various codes (Gregory-Smith, 1997). Current prediction of the flow in the Penn State rotor have been compared with LDV and pressure measurements by Ristic et al. (1998) and Xiao (2000) to establish confidence in the simulated results.

A previous numerical simulation of the flow in the Penn State turbine Rotor (Luo and Lakshminarayana, 1997) showed very good correlation between the predicted surface pressure distribution and design values from H_b=0.13 to H_b=0.90. Comparison (Chapter 5) also indicates very good correlation between the experiment and predicted values. The numerical simulations presented in this report, which are based on a refined grid, variable tip gap, and a k-ε /ARSM model, show that all these factors do not affect surface pressure at the blade location away from the casing region H_b<0.94. Thus that comparison is not presented here. However, the pressure distribution in the vicinity of the blade tip is strongly affected. Grid refinement has the most profound effect on the predicted pressure distribution near the tip clearance on the pressure side (Fig. 8.2).

The comparison presented in Fig. 8.2 shows very good correlation between the predicted and measured blade pressure distribution on the pressure side. The presence of the tip clearance flow affects the pressure distribution only from 97% of span to the casing. The pressure field is essentially two-dimensional in nature (i.e., no significant

variation in radial direction) from $H_b=50\%$ to 97%. From 97% of the blade span, the velocity field undergoes sudden turning and acceleration as the flow enters the tip clearance. This leads to a rapid decrease in blade pressure near the tip from $x/C_x = 0.4$ to $x/C_x = 0.9$ in this region. This zone corresponds to the maximum tip-leakage mass flow at the pressure side of the gap. The low-pressure zone is relatively thin and extends from $Zg=(r-r_{tip})/(r_{cas}-r_{tip})=-0.2$ to $Zg = 0.5$. Grid density should be adequate not only in tip zone, but also below the blade tip to provide an accurate prediction of the flow in the flow acceleration zone. From $Zg=0.5$ to $Zg=1$ (casing) the pressure level is relaxing to the levels on the blade pressure surface. This is caused by the relative motion of the blade and casing, which generate the blockage near the casing and prevents or reduces the tip flow acceleration.

Predicted pressure distribution on the suction surface also correlates well with the experimental data (Fig. 8.3). The characteristic feature of the suction side pressure field is the development of the low-pressure zone at $x/C_x\sim0.5$ near the blade tip. This pressure decrease is caused by the development of the tip vortex. The location of the minimum pressure can be used to identify the trajectory of the tip vortex (e.g., Ho and Lakshminarayana, 1994). A comparison between the predicted and measured location of the tip vortex path reveals earlier initiation of the tip vortex development in the case of the numerical simulation ($x/C_x\sim0.58$ VS $x/C_x\sim0.64$). At the blade trailing edge, the predicted distance between the vortex location and the endwall is higher than the measured value by about 1.5–2% of the blade span. One of the potential factors contributing to this discrepancy is the variation of the tip gap in the experiment. Design tip clearance is $\tau_c=1.1\%$, while the actual clearance varies from $\tau_c= 0.61\%$ to $\tau_c=0.9\%$. Base calculations have been carried out with $\tau_c=0.75\%$. Additional simulations discussed below have been performed to assess the influence of the small variation of the tip gap height on the predicted flow field.

Distribution of the axial velocity and axial vorticity at 10% of the chord downstream of the trailing edge is shown in Fig. 8.4 and Fig. 8.5. A comparison of the velocity field with the LDV data (Ristic et al., 1998) shows that the numerical solver correctly predicts reduced axial velocity zone near the suction side caused by the secondary and leakage flows. The zone of the reduced axial velocity extends to 50% of

the pitch near casing and to 80% of the pitch near the hub. Both, the experimental data and the prediction reveal the zone of the reverse flow in the center of the tip vortex (Fig. 8.4). Distribution of the axial vorticity field shown in Fig. 8.5 may be used to identify major vortices; 1) casing wall passage vortex, 2) hub wall passage vortex, 3) tip leakage vortex, 4) scraping vortex (i.e. vortex caused by the relative motion of blade tip and casing) and 5) wake axial vortices. High flow turning results in the development of the passage vortices of significant strength. The hub wall passage vortex core is located at $H_b= 0.3$ and spreads one third of pitch in tangential direction. LDV data has two zones of the positive vorticity near the casing; 1a and 1b. A similar distribution can be observed in the predicted flow field (Fig. 8.5). However, measured axial vorticity in Zone 1a is significantly higher in comparison with the axial intensity in Zone 1b. Predicted axial vorticity distribution has an opposite trend. Normalized helicity, $\dfrac{\overline{\omega} \cdot \overline{W}}{|\overline{\omega}| \cdot |\overline{W}|}$, can be utilized to analyze vortex development (e.g., Kunz and Lakshminarayana, 1992). Normalized helicity tends to unity at the vortex center disregarding the vortex intensity. The distribution of the predicted normalized helicity indicates that at $x/C_x{\sim}0.8$ the core of the casing wall passage vortex (defined as region with normalized helicity equal to unity) is separating into two parts. One is located closer to the casing and can be tracked to Zone 1a. The other part is transported downward and can be tracked to Zone 1b. Based on this analysis, both 1a and 1b are considered as elements of the casing wall passage vortex. A comparison between the predicted flow field in the rotor with tip clearance and without tip clearance indicates that this separation of the casing passage vortex into two zones exists even in the absence of the leakage flow. Both, the prediction and the experimental data, clearly show that the tip vortex is confined to the suction side tip corner. The maximum leakage vorticity occurs at $H_b= 92\%$ (prediction) and 94% (experiment). This correlates with the zone of low pressure on the suction side of the blade, which is discussed above. The tip clearance vortex extends to 20% in the pitchwise direction. The numerical simulation predicts a narrower tip clearance vortex. The wake development downstream of the trailing edge is three-dimensional in nature with a negative axial vorticity from 60 to 80% of the span and a positive axial vorticity in the lower 45% of the span. Interaction between the secondary flow and the wake, augmented by the rotation

effects, is the primary mechanism responsible for the axial vorticity generation in the wake. Predicted wake axial vortices are more narrow than those observed in the experiment. This can be attributed to the interaction of the upstream nozzle wake with the rotor wake. This interaction makes the suction side of the rotor wake significantly thicker. The current simulation assumes a steady flow, thus the rotor wake-nozzle wake interaction effect is not captured.

A comparison between the predicted flow field with the preliminary results of the LDV measurements (Xiao, 2000) is shown in Fig. 8.6-Fig. 8.9. The axial vorticity field is mostly two-dimensional distribution at $x/C_x = 50\%$, with the exception of the narrow zone near the casing, which corresponds to the development of the casing wall passage vortex. Presence of a small zone of negative vorticity close to the blade tip indicates the inception of the tip clearance vortex. A comparison of the surface pressure distribution, presented earlier, indicates that the numerical simulation predicts earlier inception of the tip leakage vortex in comparison with the experiment. Therefore, predicted axial vorticity field at $x/C_x=50\%$ of the chord has a larger zone of high axial vorticity. At $x/C_x = 80\%$ (Fig. 8.9), the tip leakage vortex has grown significantly. The predicted axial velocity field indicates the presence of a stagnation zone in the core of the tip leakage vortex. This effect is weaker in the experimental data. However, the experimental data downstream of the leading edge (Fig. 8.4) contains a significant zone of the negative axial velocity, which is similar to the predicted flow. This discrepancy can be explained through a consideration of the tip vortex development. Presence of the reverse flow in the center of the tip leakage vortex, in combination with the fact that until 80% of the chord most of tip leakage flow is not entrained by the tip vortex, may lead to fewer LDV seeding particles in the center of the tip vortex. The tip leakage flow is essentially unsteady, therefore an experimental error may occur due to the variation of the position of the vortex core.

An overall comparison between the predicted flow field and the experimental data is good and enables a certain level of confidence in the predicted flow field required for the analysis of the secondary flow development presented below. The discrepancy noted may be attributed to two factors. First is the limitation of the flow model utilized, i.e., the steady state simulation based on the circumferential average of the rotor inlet flow field. Experimental measurements (Lakshminarayana et al.,1998) and two-dimensional

138

unsteady simulation reveal a profound effect of the unsteady interaction on the flow field in rotor. Therefore, a steady state assumption may not capture some of the time-averaged features of the flow. The second factor is associated with deficiencies of the turbulence model. Ristic et al. (1998) measured strong anisotropy of the turbulence field downstream of the trailing edge. A further analysis is required to analyze the potential influence of non-isotropic turbulence on the accuracy of the prediction.

8.4 Vortex field development

Endwall boundary layers upstream of the rotor undergo strong modification as they enter the blade passage. Low momentum fluid located closer to the wall is transported towards the suction surface due to the blade-to-blade pressure gradient and streamline curvature. After the flow reaches the suction side, it develops into a passage vortices. Streamline and streamwise vorticity distribution (Fig. 8.10) illustrates the development of the secondary vortices in the rotor passage. Hub wall secondary flow impinges on the suction side of the blade at about 50% of the chord. At this location, it merges with the weak suction side horse shoe vortex. Further downstream, the hub wall passage vortex is transported away from the hub wall. At the trailing edge crossplane, the center of the hub vortex is located at 35% of the span. Development of the casing wall passage vortex is affected by the blade casing relative motion and by the leakage flow. Relative motion of the tip endwall contributes to a more intense transport of the casing boundary layer to the suction surface, in comparison with cascade flow. Casing boundary layer starts its final transformation into the passage vortex at $x/C_x = 40\%$ of the chord near the suction surface (Fig. 8.10). Starting at $x/Cx=50\%$ of the chord, the development of the tip leakage vortex affects the casing wall passage vortex intensity and pushes it away from the suction surface.

Relative motion of the casing wall results in a flow blockage (in pitchwise direction), preventing a development of the leakage flow within the first 30% of the chord and this strongly reduces the leakage flow further downstream. At $x/C_x = 20\%$, the tangential transport of the casing boundary layer fluid results in a reverse leakage flow from the suction surface to the pressure surface (Fig. 8. 11, streamlines originated at $x/C_x=20\%$ of the chord and Fig. 8.13). The fluid, located closer to the blade tip, is

transported along the blade centerline and leaves the tip gap only at x/C_x = 50% of the chord (Fig. 8.14). This observation is supported by the distribution of the accumulated mass flow rate through the gap plotted in Fig. 8.12. There is a weak negative tip leakage mass flow rate up to 30% of the chord. Vector field at Z_g = 0.33 indicates that the leakage flow entering the gap at the pressure surface near the leading edge leaves clearance only at x/C_x = 50%. Within 60% of the blade, a significant part of tip leakage flow originates at the suction surface rather than at the pressure side of the blade tip as a result of the casing wall crossflow boundary layer. Near the casing, this zone extends from the leading edge to x/C_x = 60% (Fig. 8.13) of the tip suction side. It shrinks to about 20% of the chord, from x/C_x =40% near the blade tip (Fig. 8.14). Further downstream, an increasing pressure gradient across the tip gap confines a zone of the reverse leakage flow to less than 5% of the tip clearance height near the casing wall. At x/C_x=55% of the chord, all streamlines initiated inside the gap propagates to the suction side of the blade, an indication of the normal pattern of the tip leakage flow (Fig. 8.11). The tip clearance flow originating at this location mixes with the main stream without rolling up into a vortex.

A strong interaction between the leakage flow and the casing wall boundary layer immediately turns the leakage flow downwards and streamwise as it leaves the clearance at x/C_x = 60% (Fig. 8.14 and Fig. 8.16a). An analysis of the secondary velocity field indicates the presence of a vortex inception between the blade surface and the leakage flow. Further downstream, this vortex is transformed into a full scale tip leakage vortex (Figs.8-16). However, streamlines paths clearly show the absence of the tip leakage fluid inside this vortex at x/C_x = 60% (Fig. 8.11 and Fig. 8.16).

The inception of the tip leakage vortex occurs around 50% of the chord, caused by the interaction between the tip leakage flow and the main flow. Increasing leakage mass flow expands tip leakage jet penetration into the main flow (Fig. 8.16). However, as stated above, the leakage flow does not start to roll up into the vortex until 80% of the chord. An enlargement of the crossflow area between the leakage jet and the blade suction surface leads to a significant de-acceleration of the flow in this zone. Ultimately, the zone of weak reverse flow develops at the center of the vortex zone. Streamlines initiated at the location of the flow separation zone shown in Fig. 8.17 indicate that the

core of the tip vortex comprises of the main stream fluid rather than the tip leakage fluid until 85% of the chord. The stagnation zone in the core of the tip leakage vortex grows steadily from its initiation up to the trailing edge (Fig. 8.16). Downstream of the trailing edge, the zone of the reverse velocity disappears rapidly as a result of intense entrainment of the tip leakage flow into the core of the tip leakage vortex.

From 80% of the blade chord to the trailing edge, there is a continuous change in the amount of the leakage flow entrained by the tip leakage vortex and the tip leakage flow mixing with the main stream as a plain jet. At $x/C_x = 80\%$ of the chord, only 10% of the tip leakage mass flow ends in the tip leakage vortex (Fig. 8.16 and Fig. 8.18). At this location, most of the tip leakage fluid undergoes a quarter rotation as the outer layer of the tip leakage vortex and is then pushed downwards into the main stream. Near the trailing edge, this part of the leakage flow is merging with the rotor wake (Fig. 8.18). Within the last 7% of the blade chord, practically all the tip leakage flow rolls up into the tip leakage vortex. The only exception is a thin zone near the casing wall. In this region, the scraping vortex prevents the flow from merging with the tip leakage vortex.

Accumulated mass flow through the gap grows rapidly from 40% of the chord (Fig. 8.12). Maximum mass flow rate is achieved from $x/C_x = 70\%$ up to the 90% of the chord. The percentage of the leakage flow, which is entrained by the tip vortex, increases nearly linearly from $x/C_x = 80\%$ of the chord to the trailing edge. Thus, the combined leakage mass flow is equally split between the fluid, which is entrained by the tip vortex and the fluid which interacts with the main stream as a plain jet.

8.4.1 Secondary and leakage flow losses

The complex structure of the vortices in the rotor and their interaction has a major influence on flow losses. There are three major sources of three-dimensional losses. The first source of losses is due to the presence of strong casing and hub passage secondary vortices. The second contributor is additional losses associated with the development of the tip leakage flow. The last source is the increased or, in some cases, decreased losses due to the interaction between the tip leakage vortex, secondary vortices, and the rotor wake.

The various zones of loss generation due to the leakage flow can be classified as:

141

1. Loss generation inside the tip gap, including losses due to the sudden contraction of the flow, tip and casing boundary layers, and a potential development of the separation zone;

2. Mixing losses inside the blade passage. These losses occur due to the dissipation of the tip leakage vortex and "plain" leakage jet-main stream mixing loss;

3. Loss production associated with tip vortex development downstream of the trailing edge.

The numerical simulation is a valuable tool in the investigation of the sources of additional losses, as well as their distribution. However, the predicted losses based on CFD modeling are not very reliable in terms of their absolute values. No experimental data is available at this time; therefore, predicted losses can not be verified. Nevertheless, the author's experience and the information presented in literature show that CFD analysis provides reliable information in predicting the trend in loss distribution.

Axial distribution of the mass averaged loss coefficient, $(\varsigma = (\overline{P_{01}} - P_0)/(\rho_1 \overline{W_1}^2 / 2)$, is presented in Fig. 8.19. A comparison with the loss coefficient based on the two-dimensional simulation shows that the secondary flow and tip leakage losses are responsible for about 50% of total rotor losses. This conclusion correlates well with experimental observations (e.g., Booth, 1985).

The presence of the secondary flow and the development of the tip leakage flow (Fig. 8.20) results in increased losses downstream of the trailing edge, while the presence of the axial vortices in the wake contributes to the increased level of losses in this zone. This observation is similar to those made by Ho and Lakshminarayana (1994), for the turbine cascade. Inside the blade passage, increased rate of loss generation, in comparison with two-dimensional flow, is observed from 50% of the chord as a result of the final entrainment of the casing and hub wall secondary boundary layers into corresponding passage vortices. Intensified loss production from $x/C_x = 90\%$ correlates well with the changing pattern of tip leakage – main stream mixing. At this location, most of the leakage flow is entrained by the tip leakage vortex, resulting in additional losses.

Losses inside the tip clearance gap[1] are responsible for about 6-7% of the total additional losses (Fig. 8.19). This low value may be attributed to the absence of the flow

---

[1]Gap losses are calculated as the difference in the mass average stagnation pressure between the suction

separation inside the gap and on the blade pressure surface in the vicinity of the gap. However, the prediction of the separation zone is sensitive to the characteristics of the turbulence model used.

The secondary flow vortex structure is directly related to the distribution of the loss coefficient presented in Fig. 8.20. Development of tip and hub secondary vortices, which can be observed at $x/C_x = 60\%$ results in a zone of the low pressure near the tip and the hub wall respectively. Farther downstream, mixing of the secondary vortex is the primary source of losses up to the trailing edge. In the case of Penn State rotor, the presence of the tip leakage flow does not affect the loss generation due to the casing and hub passage vortices. This conclusion is based on a comparison of the loss coefficient distributions for the cases with and without tip clearance (Fig. 8.20 and Fig. 8.21). At $x/C_x = 80\%$, the loss coefficient distribution has a zone of the decreased total pressure located between the tip vortex center and the boundary layer (Fig. 8.20). Tip leakage flow streamlines initiated at x/C_x at 70% of the chord inside the gap indicate that these losses are due to the mixing of the tip leakage jet (i.e., part of tip leakage flow mixing with main flow without entrainment into the tip leakage vortex). Beyond this zone there is no indication of the additional losses caused by the mixing of the leakage flow outside the tip leakage vortex.

The development of the tip leakage vortex results in an extended zone of low pressure near the blade tip. The presence of the reverse flow in the vortex core minimizes the contribution of the zone of low total pressure inside the tip leakage vortex into overall losses. Downstream of the leading edge, mass flow associated with the zone of the tip leakage vortex is higher. Therefore, the contribution of this zone in loss generation is more profound downstream of the trailing edge.

Due to the complex interaction between secondary vortices, leakage flow, and wake, it is very difficult to calculate contribution of various sources to total loss. It is estimated that the tip and the hub secondary vortices contribute 50% of the additional losses (i.e., losses in addition to the profile and plain wake mixing losses), while losses due to the tip leakage flow account for about 35% of the additional losses. The rest of the

---

and the pressure sides of the gap, normalized by the ratio of tip leakage mass flow to the total mass flow

additional losses is due to the interaction of secondary vortex, the leakage flow and the wake (i.e., loss due to the presence of wake axial vortices, etc.).

8.4.2 Influence of the tip clearance height on the tip leakage vortex development.

A numerical simulation of the turbine rotor with different tip clearance heights has been carried out. The main objective of this investigation is to study the influence of clearance height on the amplitude and the structure of the secondary and leakage flows. In addition to gaining a better understanding, this simulation is useful in establishing a better interpretation of the comparison between the numerical and experimental results. This study will also provide guidance to the designer in optimizing the tip leakage effect. In the experimental rotor, the blade-to-blade variation of tip clearance is about 30% of its average value. Three cases have been investigated: with $\tau_c=1.1\%$, $\tau_c=0.61\%$, and no clearance (in addition to the base case with $\tau_c=0.75\%$). Even though zero clearance is physically not realizable, the relative motion of the blade and casing is preserved. A comparison of the leakage mass flow at different tip clearances (Fig. 8.12) shows a nonlinear relation between the clearance height and the leakage mass flow. The blade tip boundary layer and the casing boundary practically merge for the case of $\tau_c=0.61\%$. Therefore, leakage mass flow at $\tau_c=0.61\%$ is equal to less than one-third of those observed at the design value of tip clearance ($\tau_c=1.1\%$, Fig. 8.12).

There is no significant difference (beyond the moderate change in amplitude of vortices and position of the tip leakage vortex core) between the axial velocity and axial vorticity fields at $x/C_x = 110\%$ of the chord (Fig. 8.22 b,d and Fig. 8.4, Fig. 8.5) at various tip clearances. The position of the tip vortex center is located farther from the casing for the flow with $\tau_c=1.1\%$. This is due to the earlier inception of the tip leakage vortex caused by increased leakage flow. Based on the results of the numerical modeling, it is possible to estimate that 0.1% increase in clearance results in 1% change in the spanwise position of the tip leakage vortex. Despite the significant change in the size and amplitude of the tip vortex, as well as in the extent of the tip leakage vortex core reverse flow, the overall pattern of the secondary and leakage flows in the case of $\tau_c=0.61\%$ is similar to the base case (Fig. 8.22). However, there is a significant redistribution between the leakage flow entrained by the tip leakage vortex. For the case with $\tau_c=0.61\%$, about

75% of the leakage flow is entrained into the vortex, while the base case has only 50% of the leakage flow rolled up into it. Mixing of the tip leakage vortex results in higher losses in comparison with "plain" jet mixing.
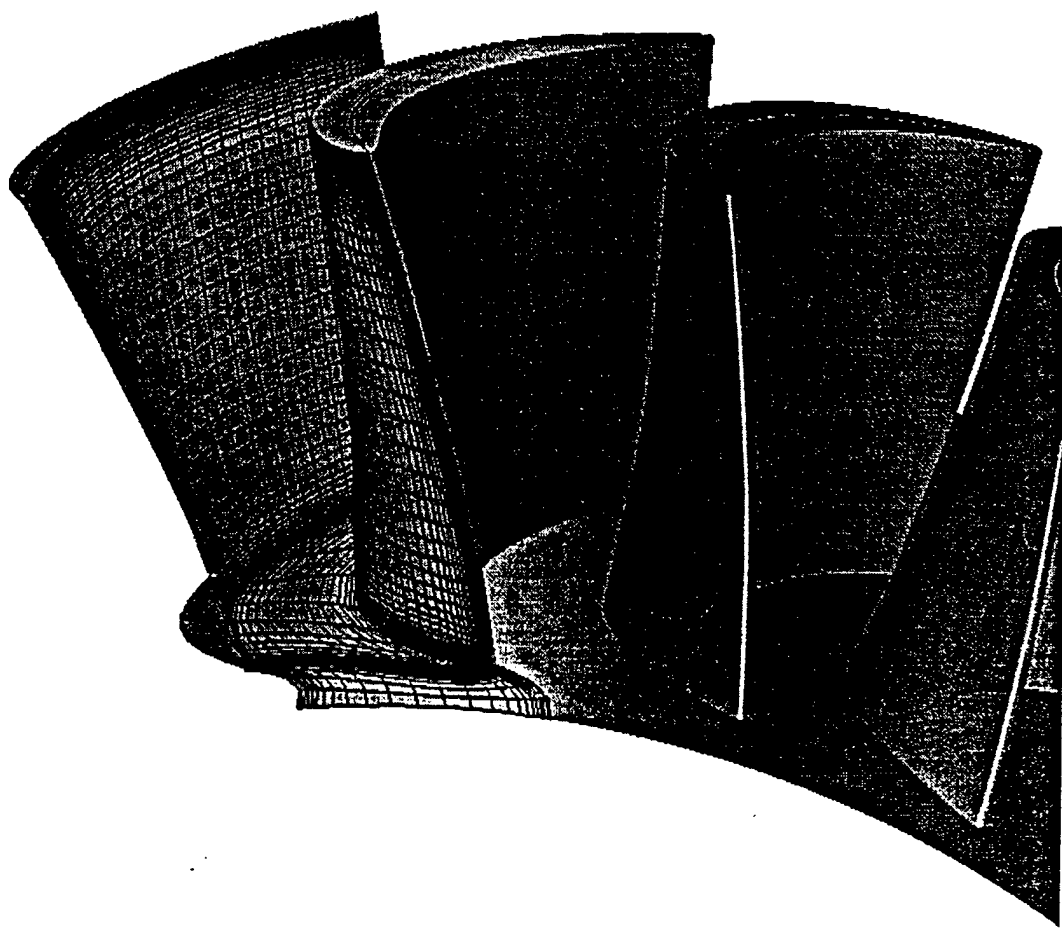
Fig. 8.1 Penn State rotor, computational grid

prediction
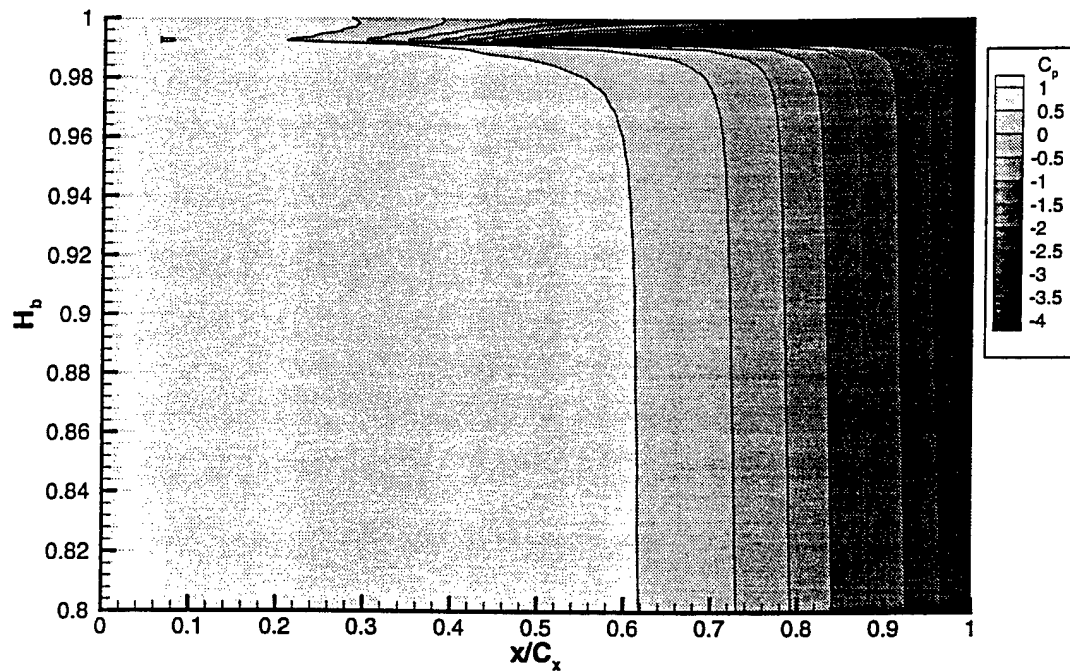
experiment
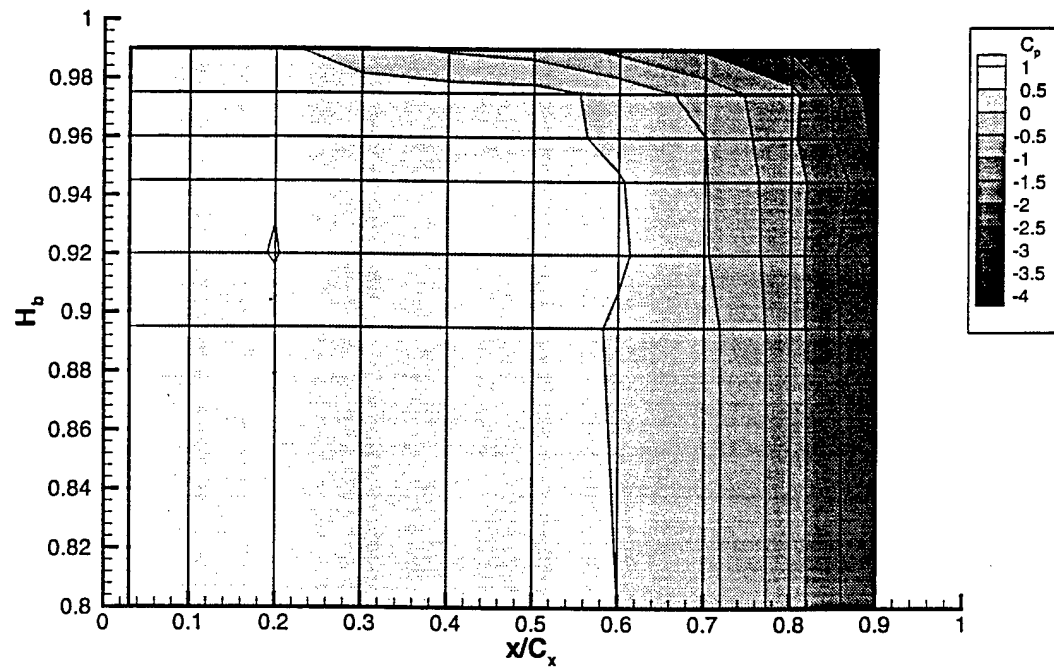
Fig. 8.2Pressure distribution, pressure surface (tip clearance zone is also shown in the prediction)
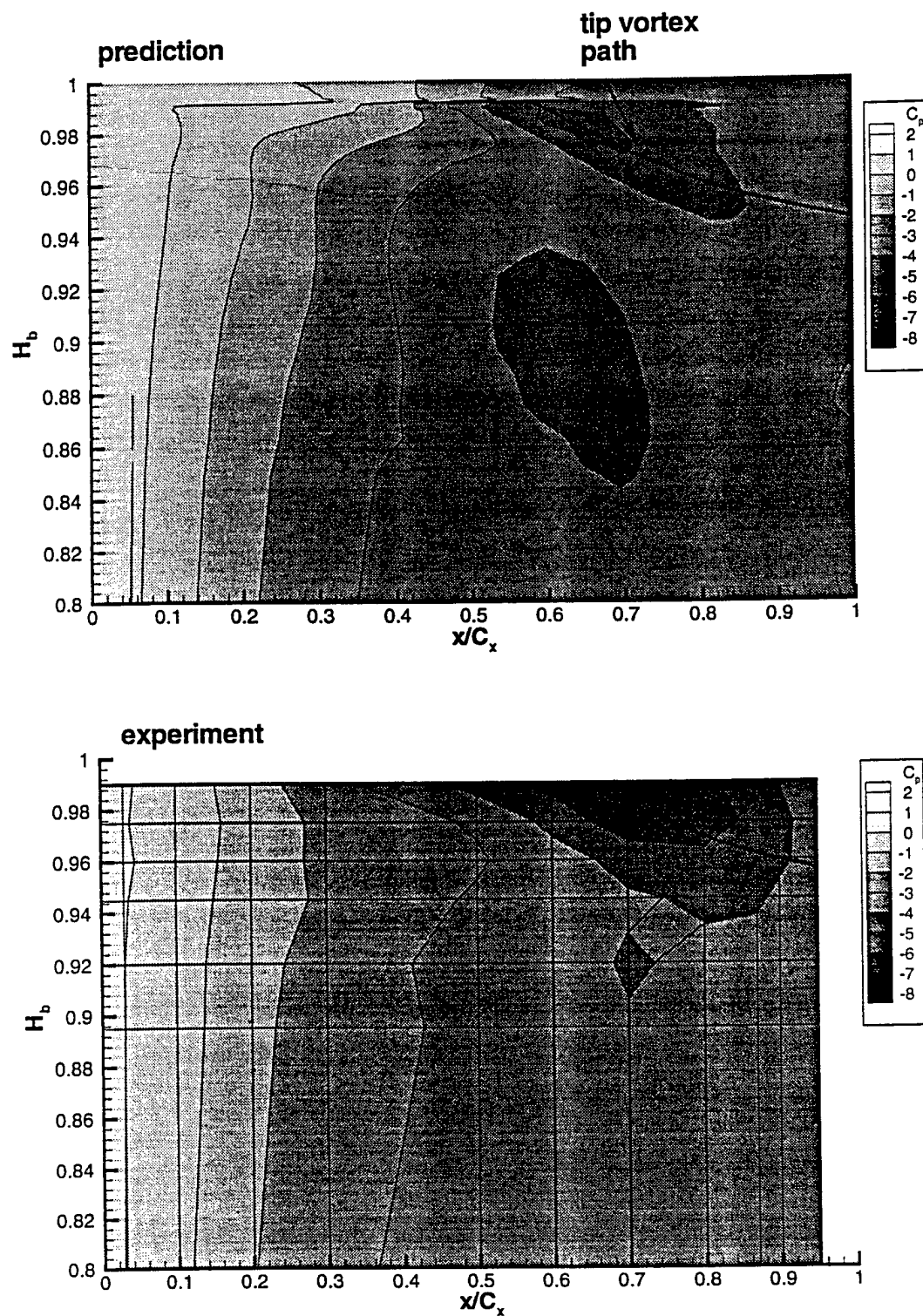
Fig. 8.3 Pressure distribution , suction surface (tip clearance zone is also shown in the prediction)
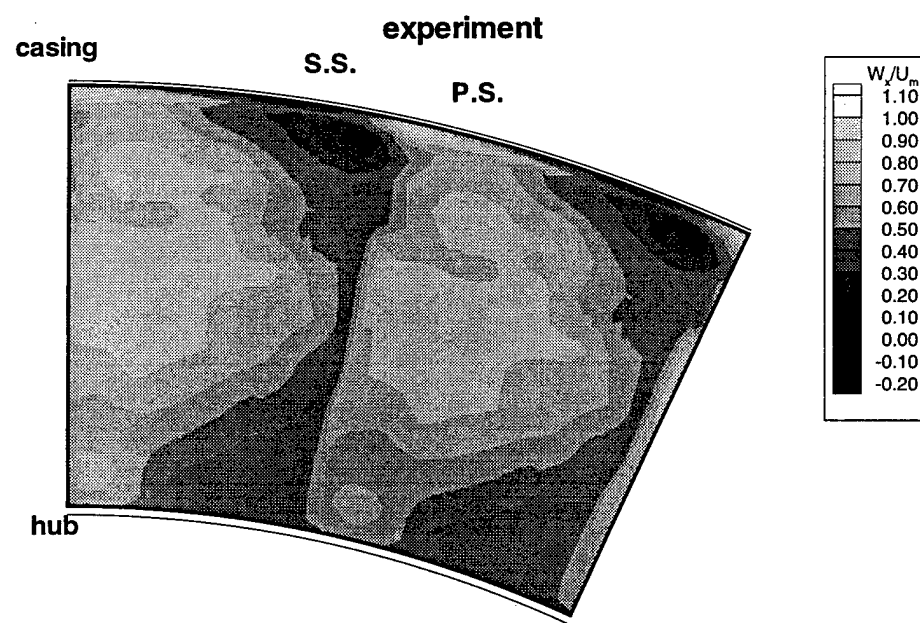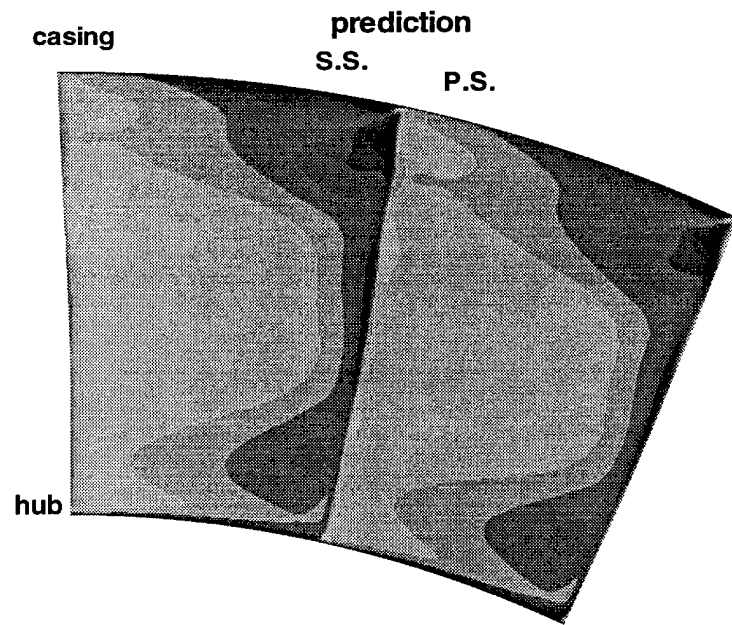
Fig. 8.4 Normalized axial velocity field at x/C_x=1.10
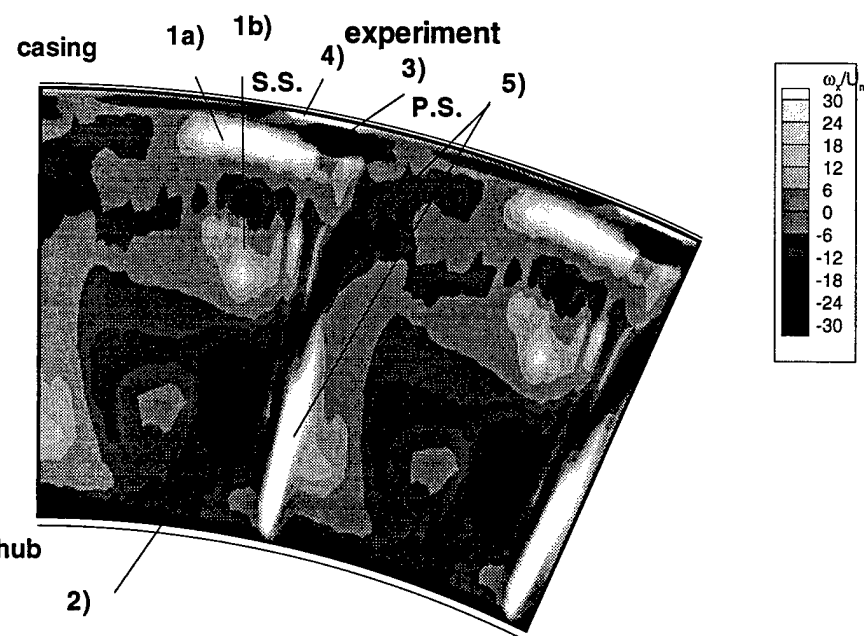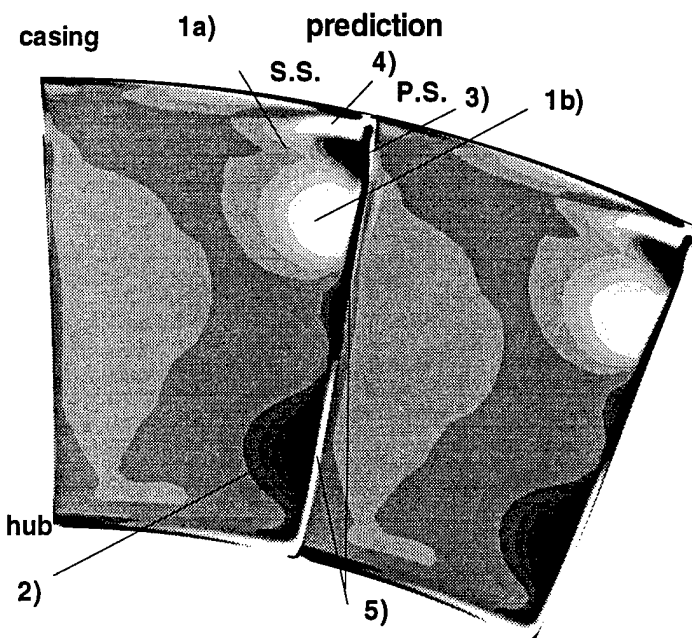
Fig. 8.5 Normalized axial vorticity at x/C$_x$=1.10
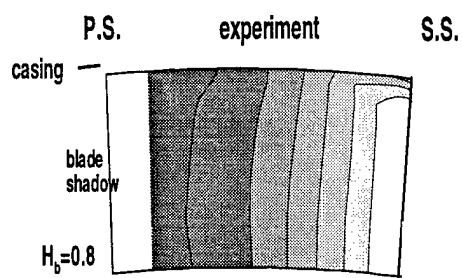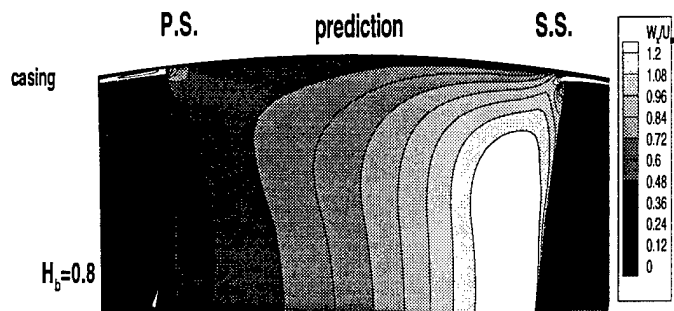
Fig. 8.6 Normalized axial velocity at x/C$_x$=50%
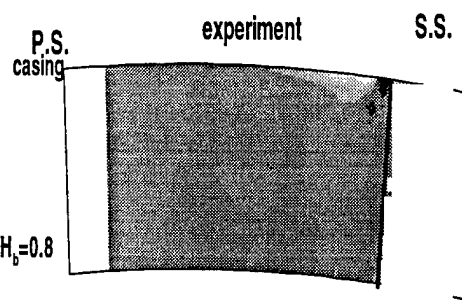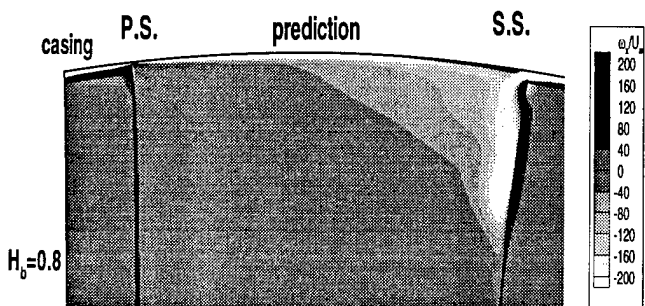
Fig. 8.7 Normalized axial vorticity at x/C$_x$=50%
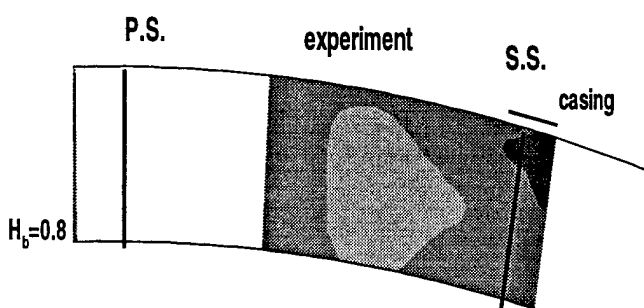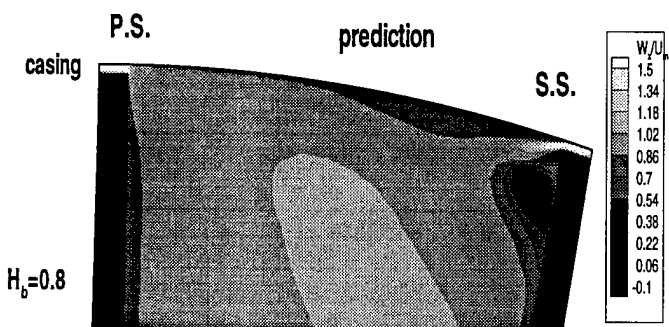
Fig. 8.8 Normalized axial velocity at x/C$_x$=80%
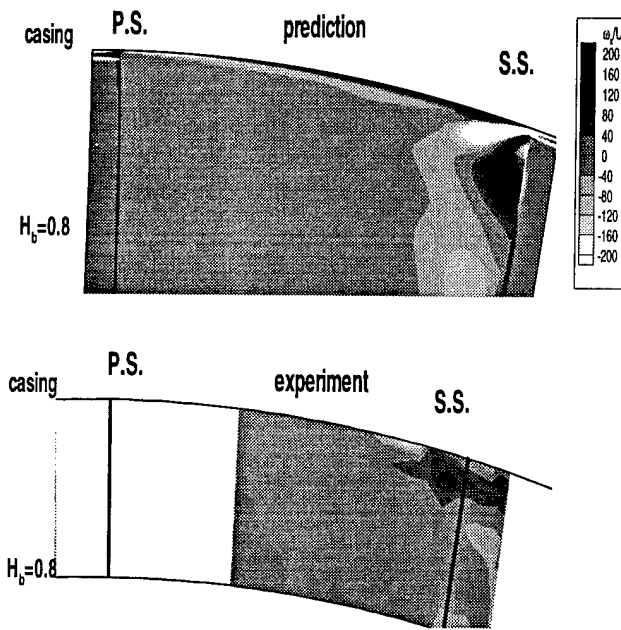
Fig. 8.9 Normalized axial vorticity at x/C$_x$=80%
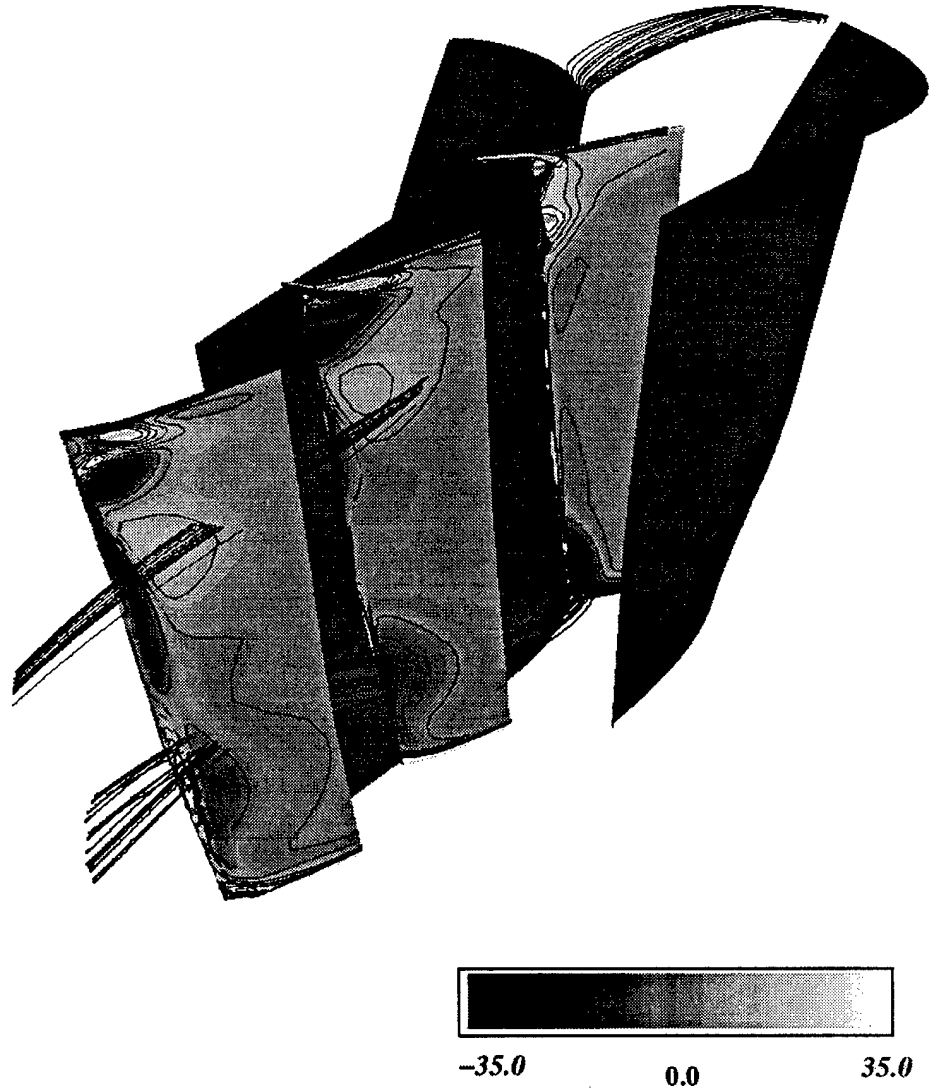
Fig. 8.10 Streamline vorticity ($\omega_s/2\omega$), crossflow planes are located at x/C_x=60%, x/C_x=80%, and x/C_x=110% respectively, streamlines are initiated 5% of the chord upstream of the leading in hub and casing boundary layers
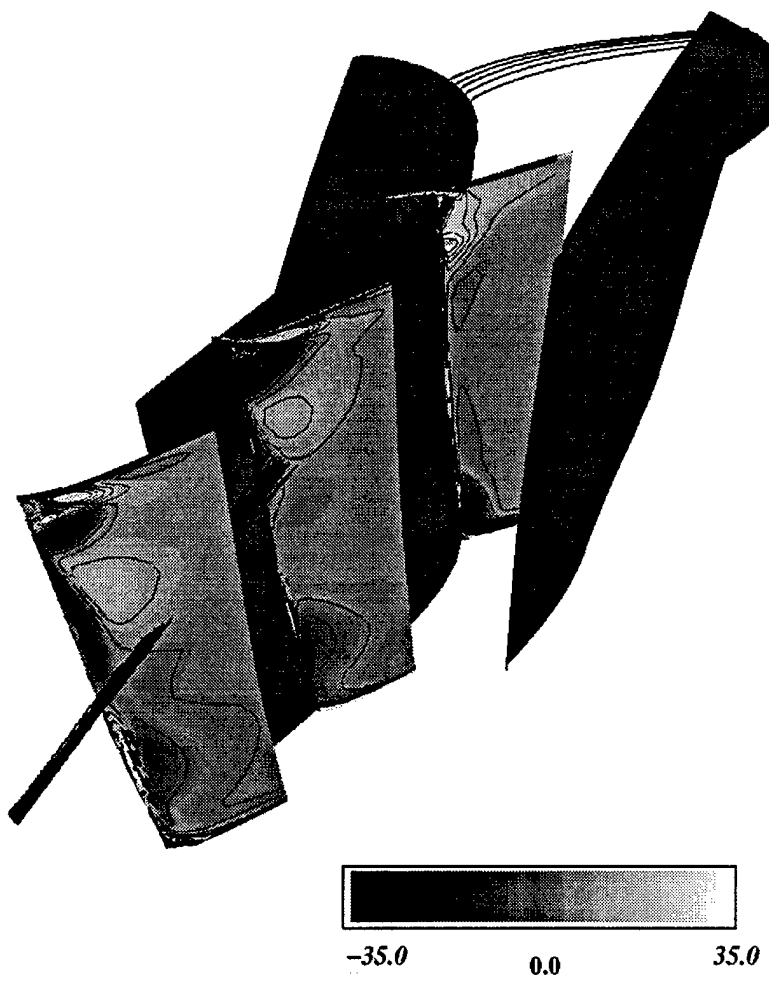
Fig. 8.11 Streamline vorticity ($\omega_s/2\omega$), crossflow planes are located at x/C$_x$=60%, x/C$_x$=80%, and x/C$_x$=110%, streamlines are initiated inside tip gap at 20% and 55% of the cord
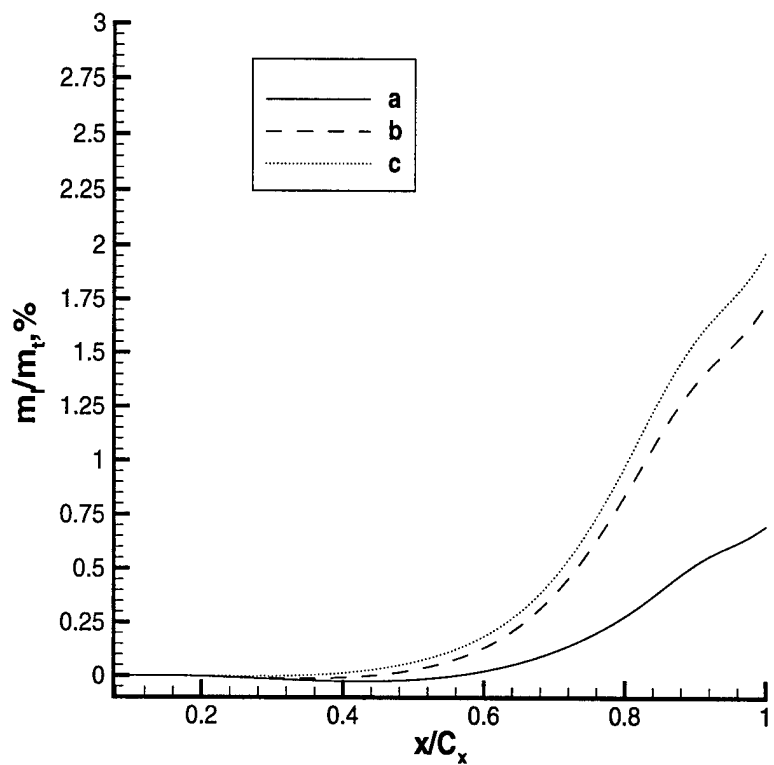
Fig. 8.12 Mass flow through the tip gap a) case with τ_c=0.61%. b) case with τ_c=0.75%. c) case with τ_c=1.1%.
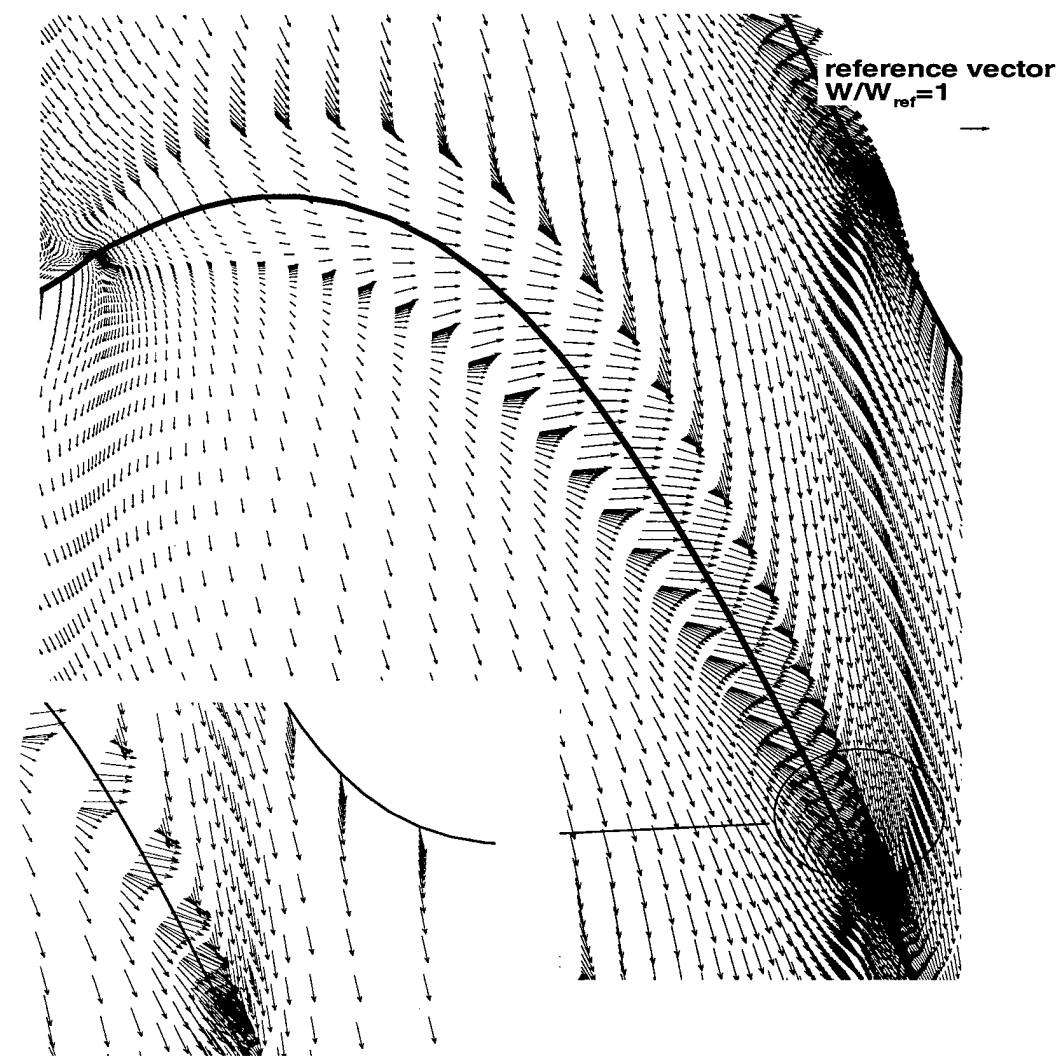
Fig. 8.13 Velocity field at Z_g=0.75
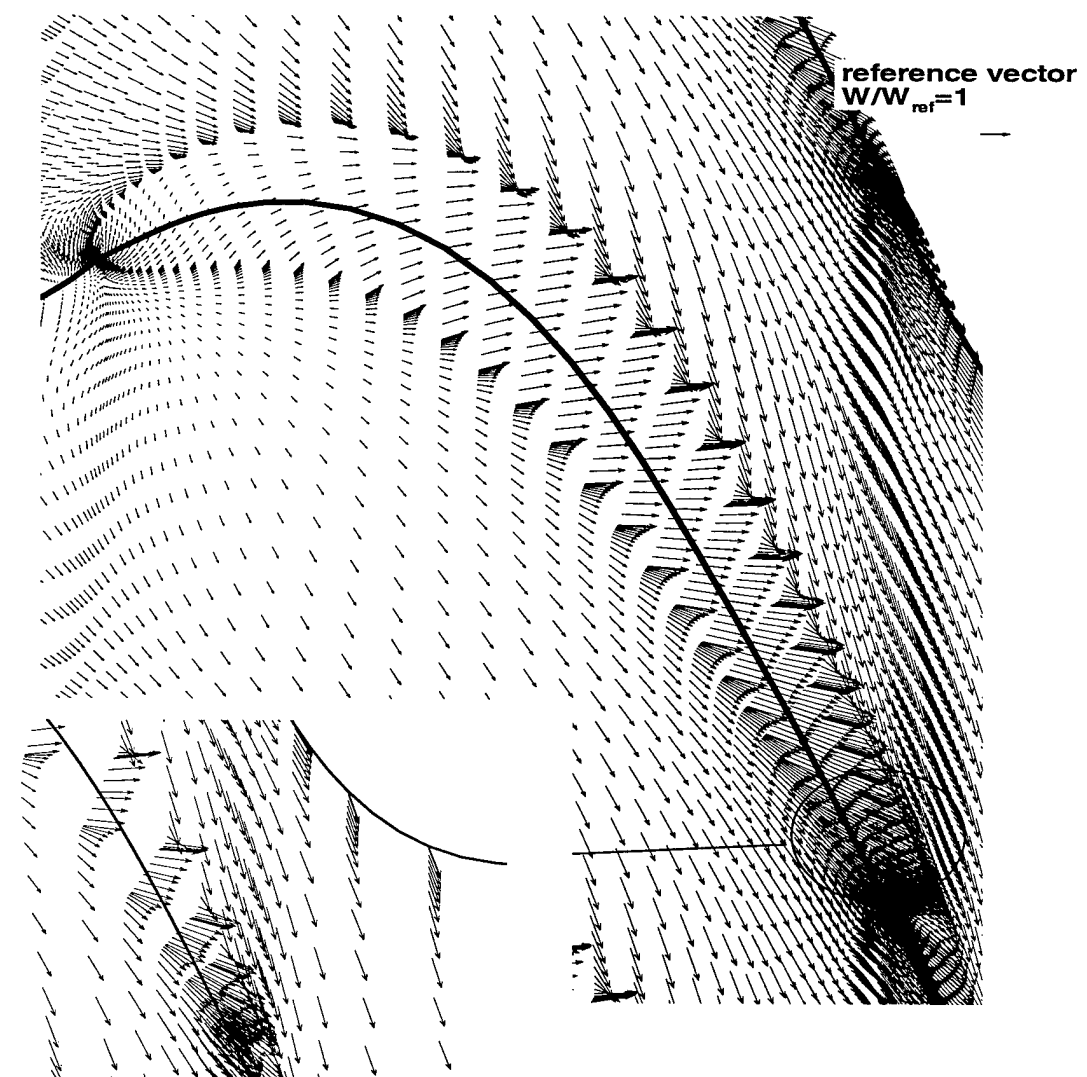
Fig. 8.14 Velocity field at Z_g=0.33

reference vector
$W/W_{ref}=1$
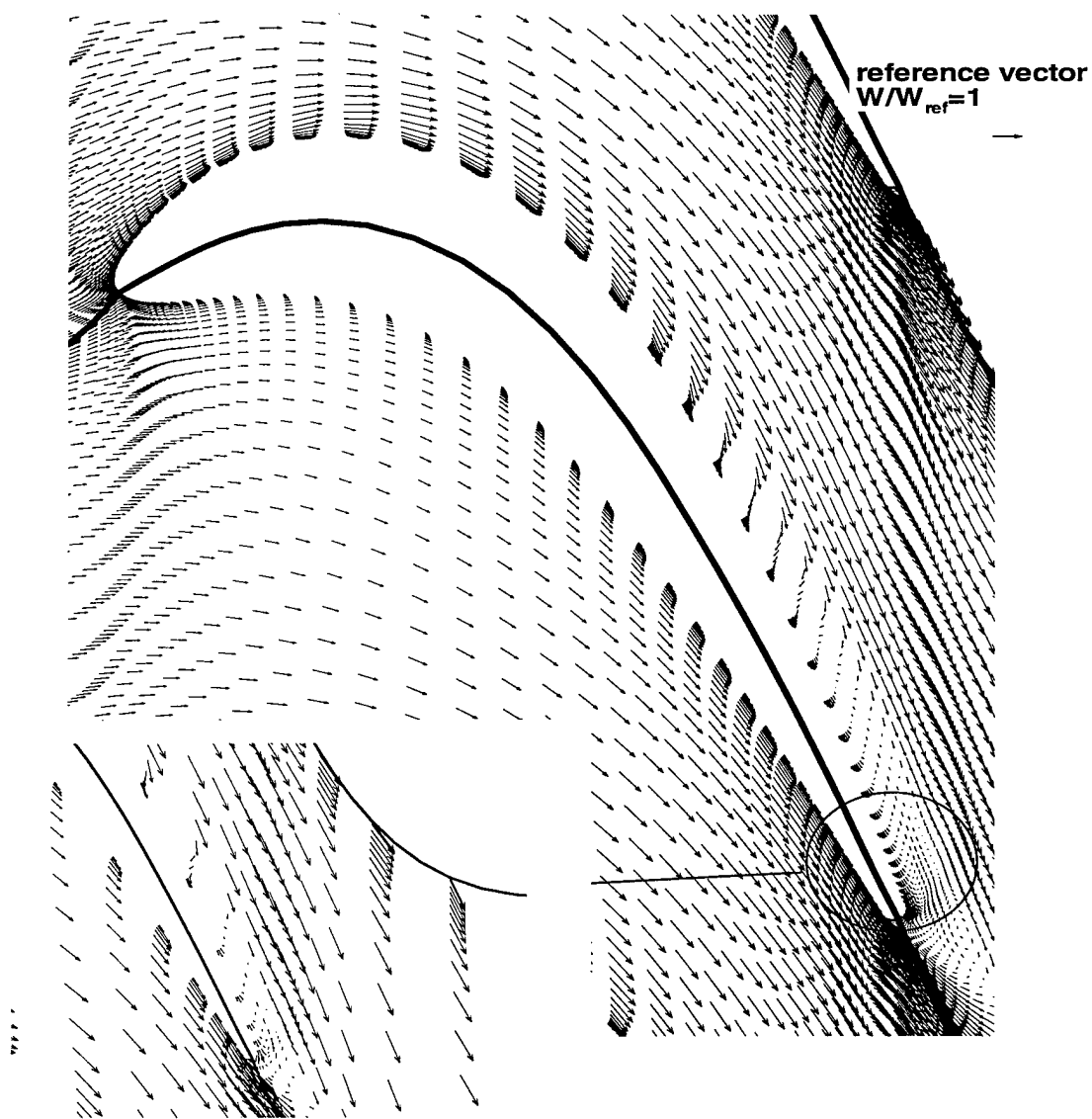
Fig. 8.15 Velocity field at Z_g=-10
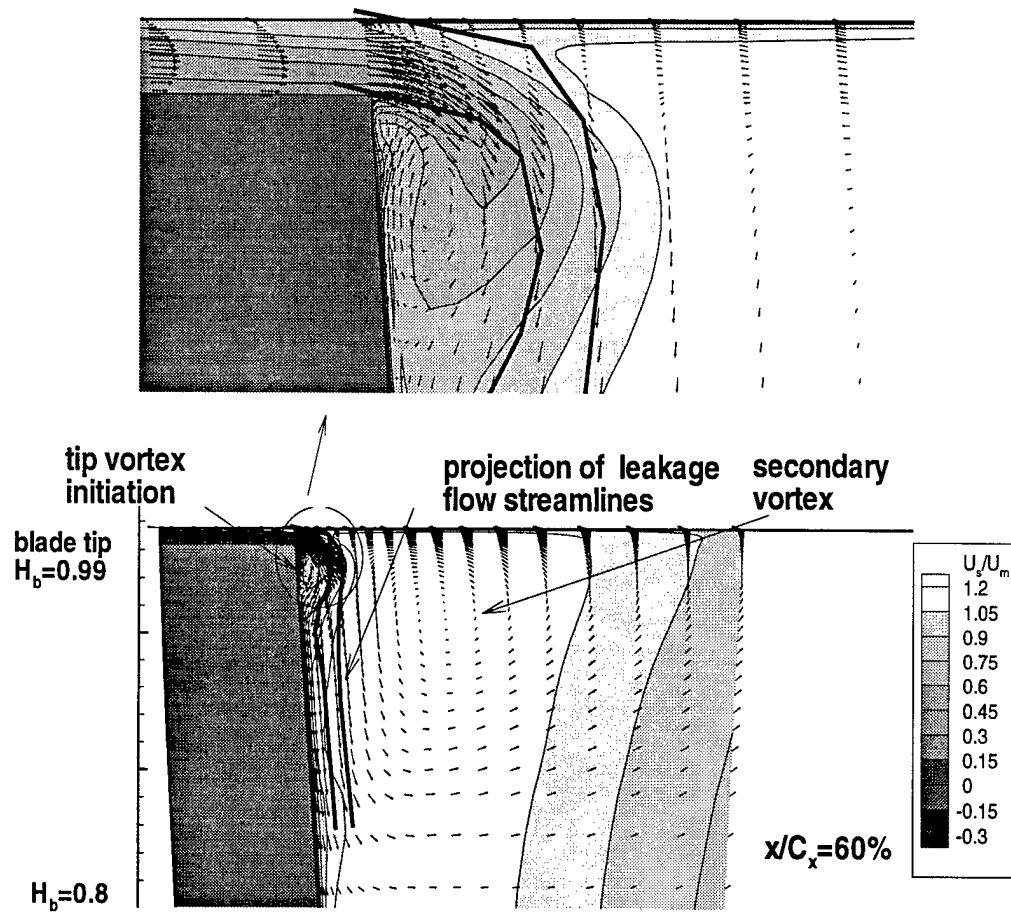
Fig. 8.16a Secondary velocity (calculated as velocity vector consisting of normal to the 2d design streamlines component and radial component), background contours - streamline velocity
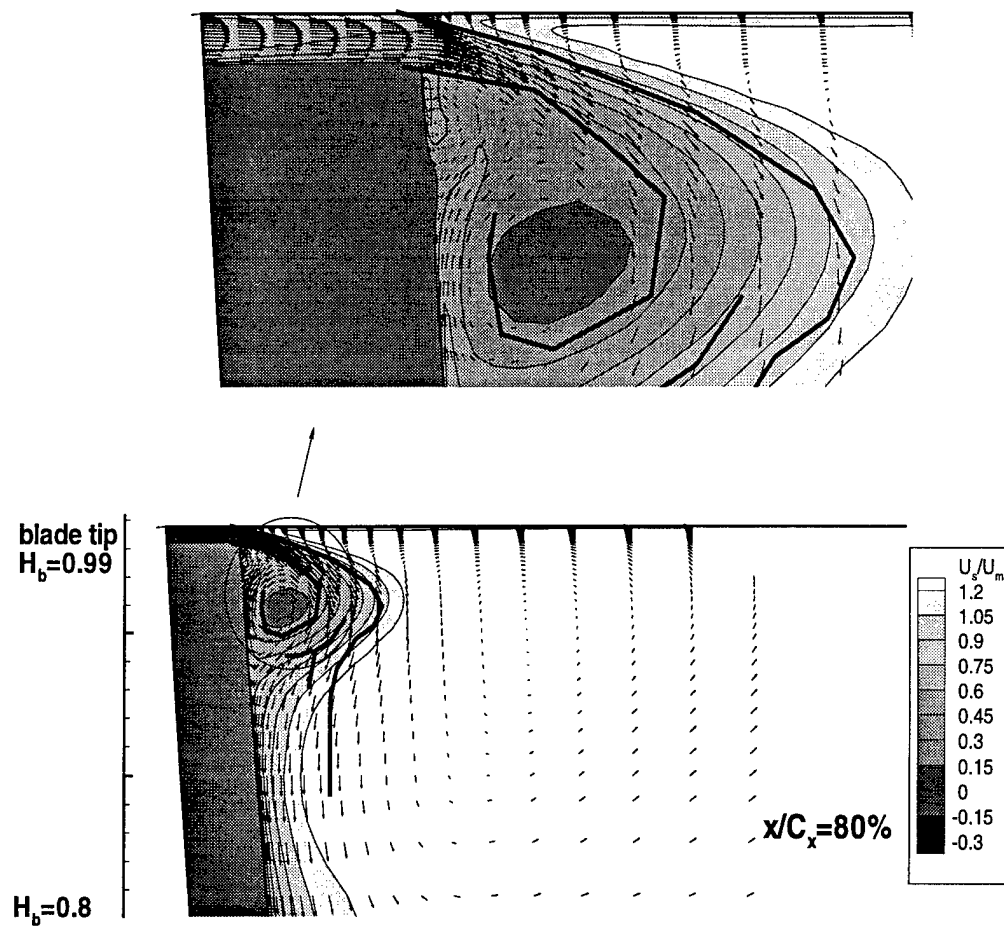
Fig. 8.16b Secondary velocity, background contours - streamline velocity
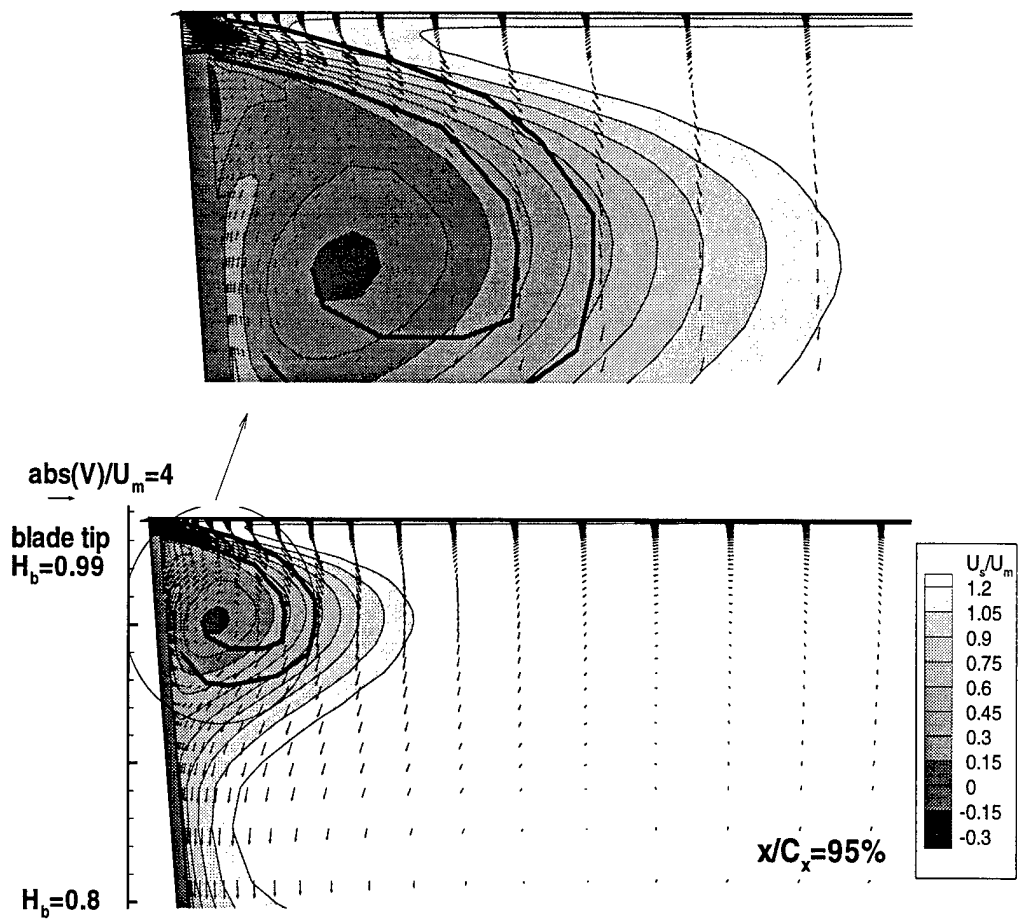
Fig. 8.16c Secondary velocity, background contours - streamline velocity
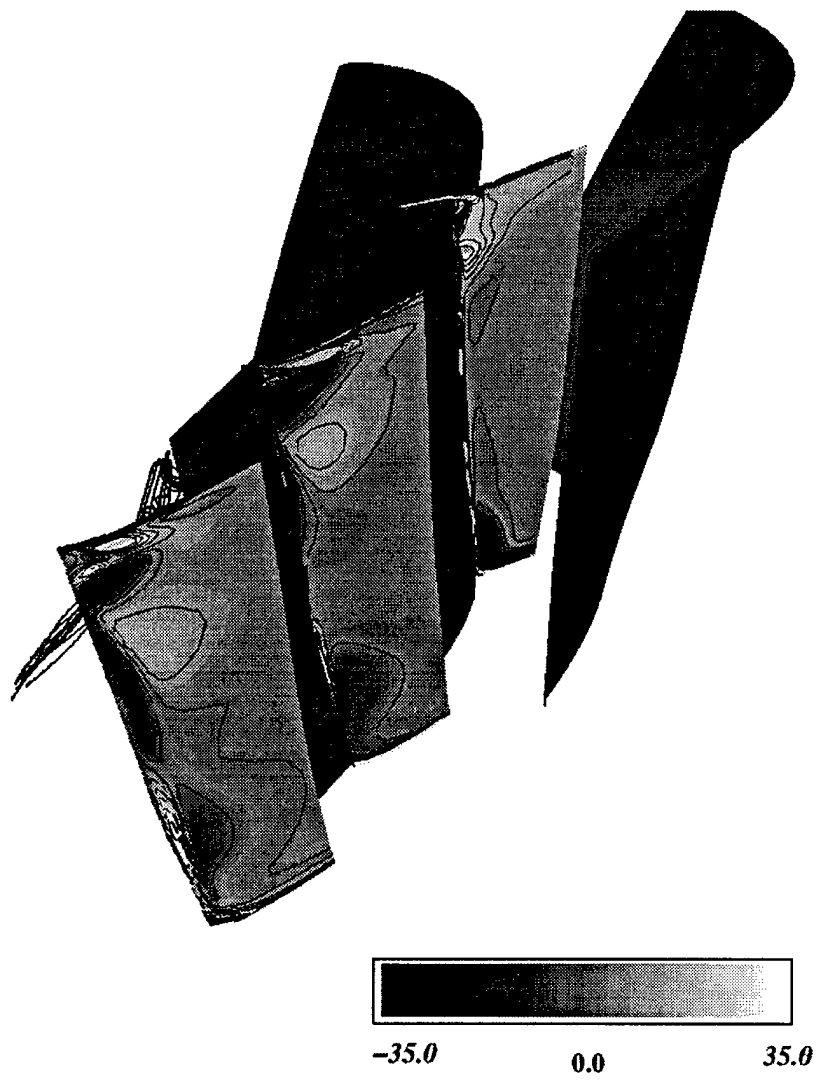
Fig. 8.17 Normalized streamline vorticity ($\omega_s/2\omega$), crossflow planes are located at x/C_x=60%, x/C_x=80%, and x/C_x=110%, streamlines are initiated at the location of the tip vortex inception and represent mean flow fluid particles
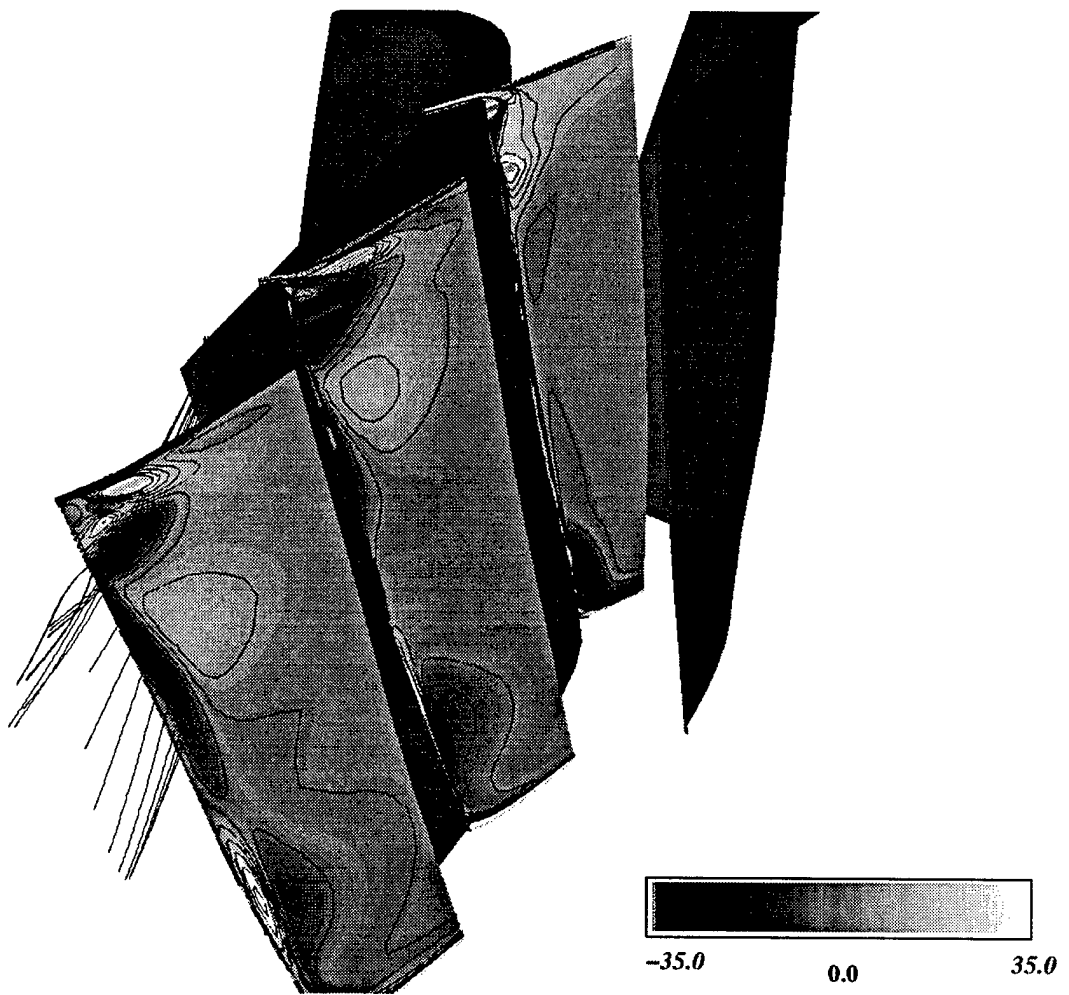
Fig. 8.18 Normalized streamline vorticity ($\omega_s/2\omega$), crossflow planes are located at $x/C_x=60\%$, $x/C_x=80\%$, and $x/C_x=110\%$, streamlines are initiated inside tip gap at 70% and 90% of the chord
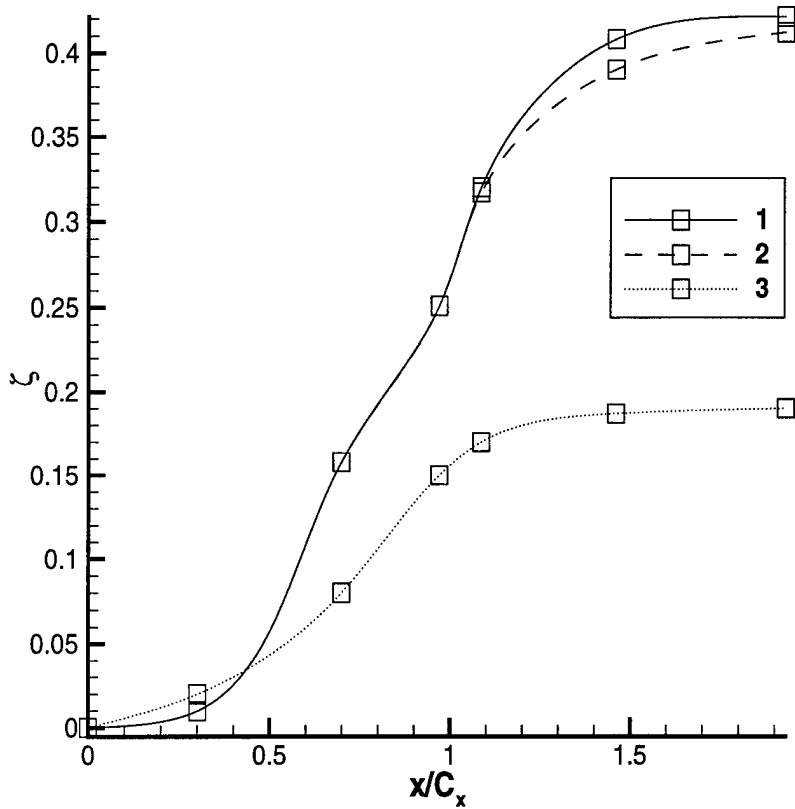
Fig. 8.19 Loss coefficient 1) case with τ_c=1.1%. 2) case with τ_c=0.75%. 3) Two-dimensional simulation
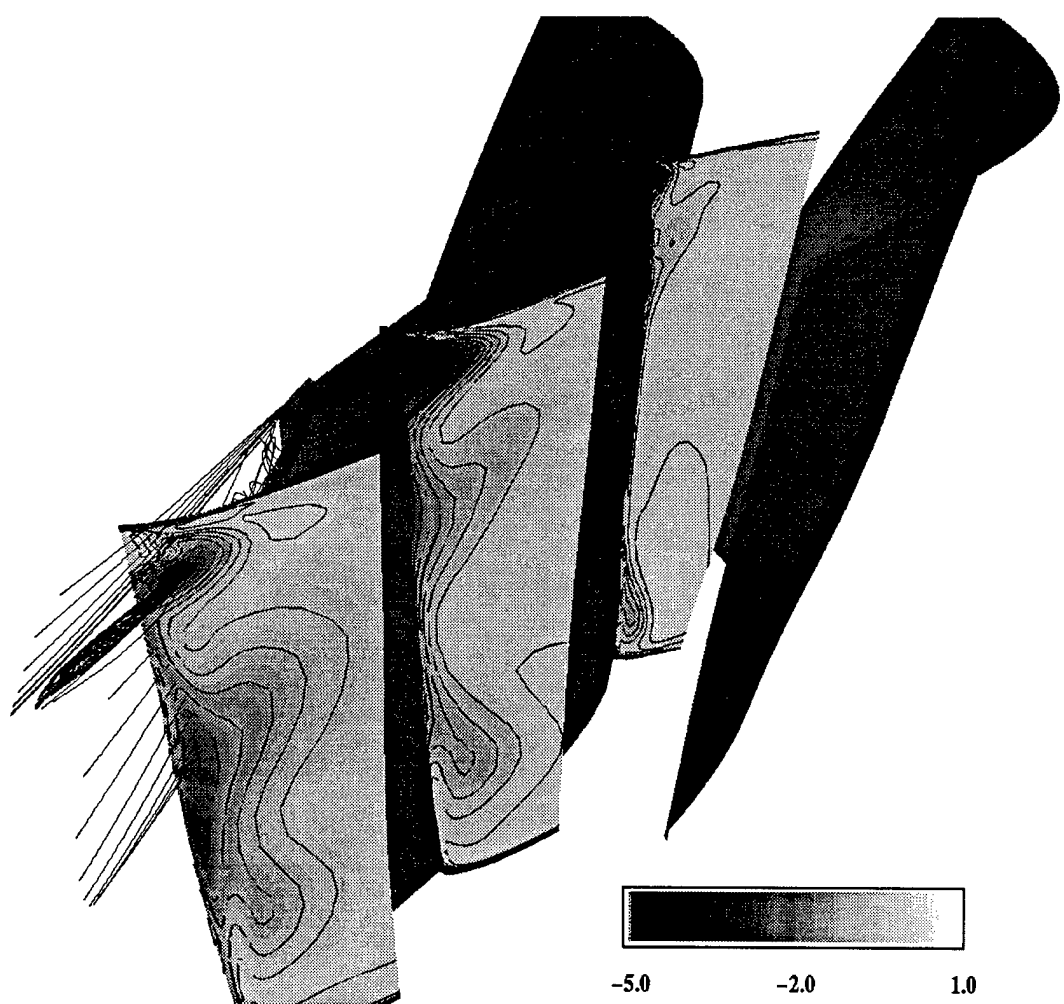
Fig. 8.20 Loss coefficient, ζ

5.00   2.00   −1.00
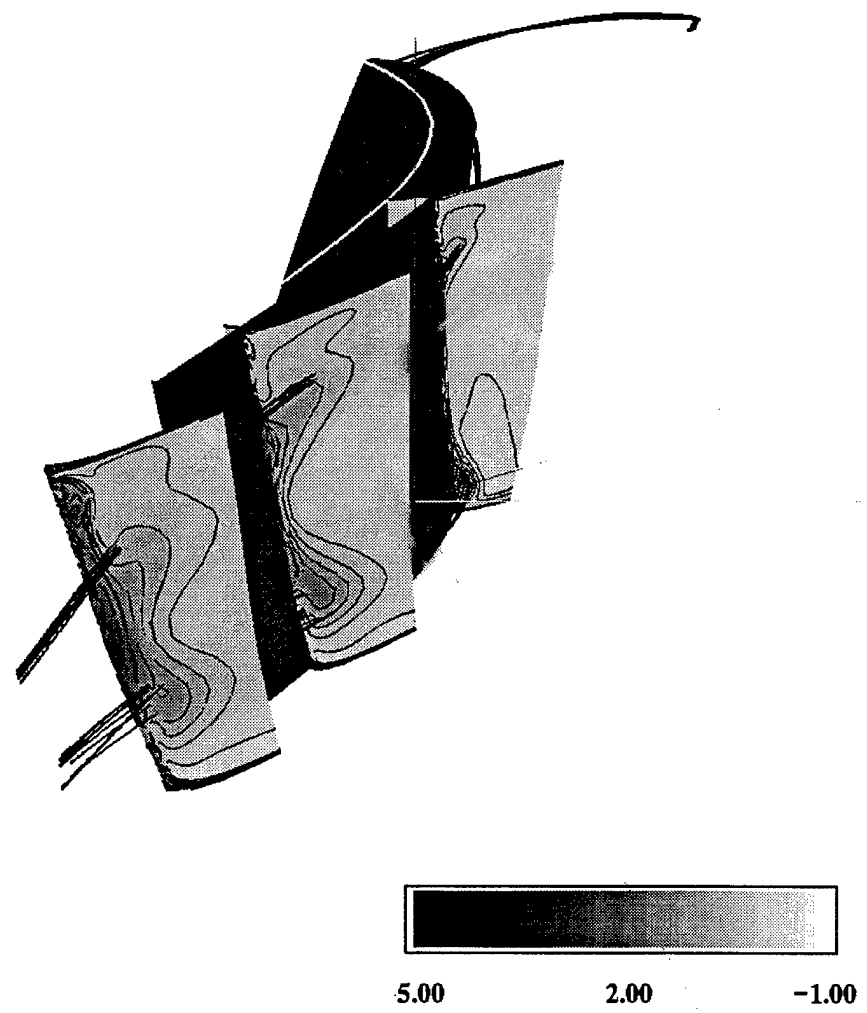
Fig. 8.21 Loss coefficient, ζ, no tip clearance
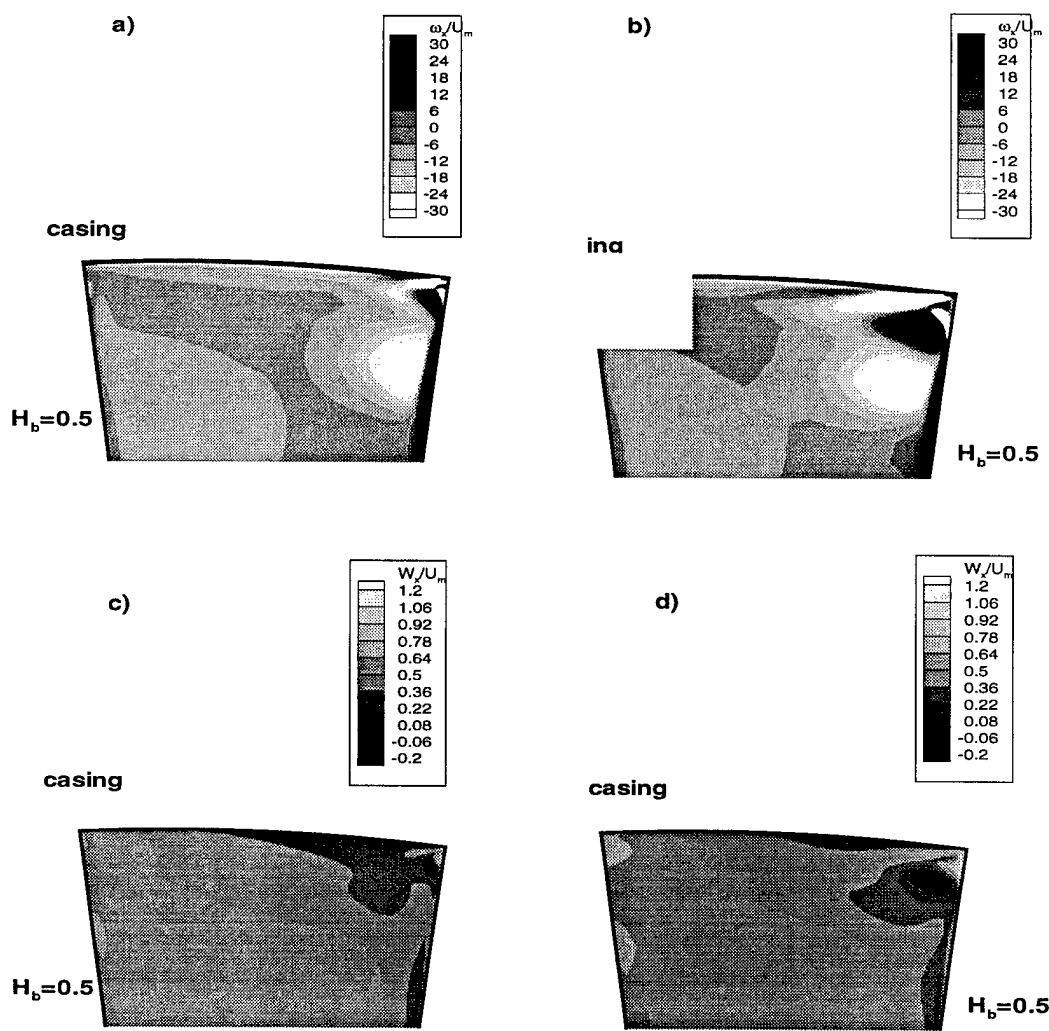
Fig. 8.22 a)-d) Flowfield at x/C_x=110%, influence of tip clearance height a) Normalized vorticity, 0.61% clearance a) Normalized vorticity, 1.1% clearance, c) Normalized axial velocity, 0.61% clearance, d) Normalized axial velocity, 1.1% clearance

e)

casing

ω_x/U_m
30
24
18
12
6
0
-6
-12
-18
-24
-30

$H_b=0.5$

f)

RHO-U
1.2
1.06
0.92
0.78
0.64
0.5
0.36
0.22
0.08
-0.06
-0.2

casing

$H_b=0.5$
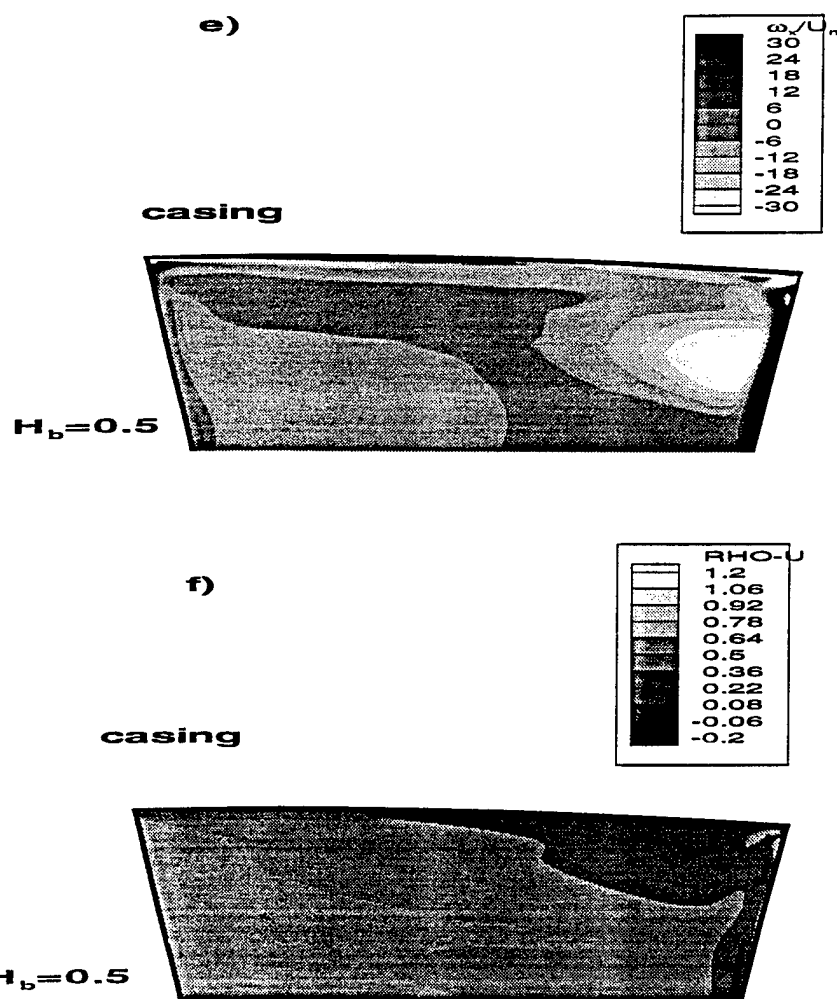
Fig 8.22 e)-f) Flowfield at x/C_x=110%, influence of tip clearance height e) Normalized vorticity, no tip clearance, f) Normalized vorticity, no tip clearance

169

9. CONCLUSIONS

9.1 Experimental investigation

Three low-pressure regions are found from the casing static pressure measurements. One of them is located inside the tip gap and is caused by a sharp edge of the blade on the pressure side. Similar low pressure cores have been found in turbine cascades. The second low-pressure area observed is caused by the horseshoe vortex. The third low-pressure area measured is caused by the tip leakage vortex, which results from interactions between the tip leakage flow and the mainstream. The tip leakage vortex formation starts near 50% of the blade chord. The vortex develops along the blade and diffuses beyond 80% of the axial chord. The pressure difference across the blade tip drops drastically beyond 80% chord. This reduces the leakage flow and allows the tip leakage vortex to diffuse.

The LDV measurements indicate that the inviscid effects dominate the flow field over the first 50% of the blade chord. The tip leakage vortex is observed to originate near 50% of the blade chord, becoming stronger until 80% of the blade chord. The tip vortex is small and is confined to the region very close to the suction surface of the casing corner. The vortex follows the suction side of the blade. The tip leakage vortex entrains portions of the suction surface boundary layer fluid. The boundary layer thickness on the suction surface of the blade increases sharply beyond 80% chord due to an adverse pressure gradient. At the same time, the tip vortex entrains appreciable amounts of fluid and hence develops very rapidly.

The passage vortex at 80% span and the tip leakage vortex at the blade tip cause the highest losses measured at the exit of the rotor flow field. The tip leakage vortex was found to be relatively stronger than the passage vortex, and causes larger losses in relative total pressure. The tip leakage vortex also has a larger impact on the flow field. The flow field along the suction surface in the tip region is dominated by the tip leakage vortex and scraping vortex. These effects are limited to an area on the suction surface in the outer 7% of the blade span and to about 30% of the blade passage above the suction surface. The data from this experiment differs from similar experiments in cascades

carried out by other investigators. The tip clearance vortex in cascade tests move further away from the casing. The secondary flows and relative motion between the blade and casing in actual rotating turbomachinery confines the leakage vortex to the corner of the suction surface.

9.2   Computational simulations

Development of the tip leakage flow is characterized by significant velocity and pressure gradients that exist in the tip gap and its vicinity. According to the result of the grid refinement analysis, it is essential to have at least 15 grid points within the gap for an adequate numerical resolution of the flow. The sudden contraction of the flow generates a low-pressure zone below the blade tip on the pressure surface. Therefore, grid also should be highly clustered at least two tip gap heights below the blade tip.

There is a good correlation between the predicted and the measured blade pressure distribution. The comparison between the predicted flow-field and the LDV data also reveals good correlation downstream of the trailing edge. However, the numerical prediction indicates an earlier development of the tip leakage vortex. Pitchwise width of the tip leakage vortex is smaller in comparison with the experiment. These discrepancies can be attributed to the limitation of the physical model, especially to the steady state approximation and isotropic nature of the turbulent model.

Development of the leakage flow in the rotor significantly differs from that observed in a cascade. Relative motion of the blade and casing blocks the development of the tip leakage flow. Mass flow through the tip gap reaches its maximum at 85% of the chord. Leakage flow leaving the tip clearance is only partially rolled up into the tip leakage vortex. At 50% of the chord, all the leakage flow mixes with the main stream as a "plain" jet, while at 93% all leakage flow leaving the gap is entrained by the vortex. Tip vortex starts at around 50% of the chord as a radial separation zone on the suction surface. It immediately moves away from the blade surface and grows steadily until the trailing edge. The core of the tip leakage vortex mostly consists of the main stream fluid entrained at the vortex inception up to the 90% of the blade. In the case of the intense tip

leakage vortex growth, a zone of reverse flow develops in the core of the tip leakage vortex, increasing the flow blockage due to the tip leakage flow.

A comparison between the three-dimensional prediction, and two-dimensional prediction of pitchwise mass average loss coefficient shows that the secondary and leakage flow losses are responsible for about 50% of total losses. The prediction shows a relatively small contribution of the tip leakage flow (less then 30% of the additional losses). This can be attributed to the relatively small clearance (less then 1% of the blade span) in Penn State rotor. Most of the losses due to the tip leakage flow occur downstream of the trailing edge through the tip vortex mixing.

A smaller tip clearance results in decreased leakage flow. It also leads to an increased percentage of the tip leakage fluid entrained by the tip leakage vortex. Therefore, the decrease in losses is less prominent, because of higher losses associated with the flow entrained by the tip leakage vortex.

References

Bindon, J.P., 1987, "Pressure Distributions in the Tip Clearance Region of an Unshrouded Axial Turbine as Affecting the Problem of Tip Burnout," ASME Paper 87-GT-230.

Bindon, J.P., and Morphis, G., 1990, "The Development of Axial Turbine Leakage Loss for Two Profiles Tip Geometries Using Linear Cascade Data," ASME Paper No. 90-GT-152.

Booth, T. C., Dodge P. R., Hepworth, H. K., 1991, "Rotor Tip Leakage Part I --- Basic Methodology," ASME Paper 91-GT-71.

Booth, T.C., 1985, "Importance of Tip Clearance Flows in Turbine Design," VKI Lecture Series 1985-05, "Tip Clearance Effects in Axial Turbomachines".

Chernobrovkin, A., "Computation for Complex Turbomachinery Flow," Ph.D. thesis, Pennsylvania State University, 1999.

Chien, K-Y., 1982, "Predictions of Channel and boundary-Layer Flows With a Low-Reynolds-Number Turbulence Model," *AIAA Journal*, Vol. 20, No. 1, pp. 33- 38.

Dean, R. C. Jr., 1954, "The Influence of Tip Clearance on Boundary-Layer Flow in a Rectilinear Cascade," Gas Turbine Laboratory MIT, Cambridge, Massachusetts, Report No. 27-3.

Dishart, P. T. and Moore, J., 1989, "Tip Leakage Losses in a Linear Turbine Cascade," ASME 89-GT-56.

Fan, S., and Lakshminarayana, B., and Barnett, M., 1993, "Low-Reynolds-Number k-ε Model for Unsteady Turbulent Boundary-Layer Flows," *AIAA Journal*, Vol. 31,

No. 10, pp. 1777-1784.

Fan, S., and Lakshminarayana, B., 1996 "On the prediction of wake Generated Unsteady pressure and boundary layers in Turbomachinery Cascades," *J. of Turbomachinery* Vol. 118, No1, pp. 96-122.

Fan, S., and Lakshminarayana, B., 1996, " Time Accurate Euler Simulation of Interaction of Nozzle Wake and Secondary Flow in an Axial Turbine Stage Using Non-reflecting Boundary Conditions," *J. of Turbomachinery*, Vol. 118, No. 4, pp. 663-678.

Graham, J. A. H., 1986, "Investigation of a tip Clearance Cascade in a Water Analogy Rig," Journal of Engineering for Gas Turbines and Power," Vol. 108, pp. 38-46

Gregory-Smith, D.G., et al. 1988, "Turbulence Measurements and Secondary Flows in a Turbine Rotor Cascade," ASME Paper 88-GT-244.

Gregory-Smith, D.G., 1997, "Secondary and Tip-Clearance Flows in Axial Turbines," "CFD Modelling of Secondary Flows," *von Karman Institute for Fluid Dynamics*, Lecture Series 1997-01.

Heyes, F.J.G., Hodson, H.P., 1993, "Measurement and Prediction of Tip clearance flow in Linear Turbine Cascades," ASME Journal of Turbomachinery, Vol. 115, pp. 376-382

Ho, Y.H. and Lakshminarayana, B., 1994 "Computational Modeling of Three-Dimensional Endwall Flow through a Turbine Rotor Cascade with Strong Secondary Flows," *J. of Tturbomachinery*, Vol 118, No2, p250-261.

Hunter, I. H. and Cumpsty, N. A., 1982, "Casing Wall boundary Layer Development in an Isolated Compressor Rotor," Journal of Engineering for Power, Vol. 107, pp.

872-879Joslyn, D., and Dring, R., 1992, "Three-Dimensional Flow in a Axial Turbine: Part 1- Aerodynamic Mechanisms," ASME *J. of Turbomachinery*, Vol. 114, pp.61-70.

Inoue, M. and Kuroumaru, M., 1984, "Three Dimensional Structure and Decay of vortices Behind an Axial flow rotating Blade row," Journal of engineering for Gas Turbines and Power, vol. 108, pp. 7-14

Inoue, M. and Kuroumaru, M., 1986, "Behavior of Tip Leakage Flow Behind an Axial Compressor rotor," Journal of Engineering for Gas Turbine and Power, Vol. 108, pp. 7-14

Inoue, M. and Kuroumaru, M., 1988, "Structure of Tip Leakage Flow in an Isolated Axial compressor Rotor," Journal of Turbomachinery, Vol. 111, pp. 250-256

Kunz, R., and Lakshminarayana, B., 1992, "Three-dimensional Navier-Stokes Computations of Turbomachinery Flows Using an Explicit Numerical Procedure and a Coupled k-ε Turbulence Model", *J. of Turbomachinery*, Vol.114, pp. 627-642, July.

Lakshminarayana, B., Horlock, J. H., 1967, "Leakage and Secondary flow in Compressor Cascades," British A.R.C. Report and Memorandum 3483

Lakshminarayana, B., 1970, "Methods of Predicting the Tip Clearance Effects in Axial Flow Turbomachinery," *J. of Basic Engineering*, Sept., pp. 467-482.

Lakshminarayana, B., 1970, "Methods of Predicting the Tip Clearance Effects in Axial flow Turbomachinery," Journal of Basic Engineering, pp. 467-482

Lakshminarayana, B., 1982, "Triple Sensor Hot Wire/Film Technique for Three Dimensional Mean and Turbulent Flow Field Measurements," TSI Quarterly, Vol. 8, pp. 3-13

Lakshminarayana, B., Murthy, K. N. S., Pouagare, M. and Govindan, T. R., 1983, "Annulus Wall Boundary Layer Development in a Compressor Stage, Including the Effects of Tip Clearance," AGARD CP-351, pp. 21-1 to 21-17

Lakshminarayana, B., Pandya, A., 1984, "Tip Clearance Flow in a Compressor rotor Passage at Design and Off-Design conditions," Journal of Engineering for Gas Turbine and Power, Vol. 106, pp. 570-577

Lakshminarayana, B., 1986, "Turbulence Modeling for Complex Shear Flow," AIAA Journal, Vol. 24, No. 12, 1900-1917

Lakshminarayana, B., Zaccaria, M. and Marathe, B., 1995, "Structure of Tip Clearance Flow in Axial compressors," Journal of Turbomachinery, Vol. 117, pp. 336-347.

Lakshminarayana, B., Camci, C., Halliwell, I., Zaccaria, M., 1996, "Design and Development of a Turbine Research Facility to Study Rotor-Stator Interaction Effects", International Journal of Turbo and Jet Engines, Vol. 13, pp.155-172.

Lakshminarayana, B., Posada, J.A., Ristic, D., and Chu, S., 1997, "Tip Clearance Flow Fields & Methods of Desensitizing the Tip Clearance Effects in Turbines," Progress Report to ARO

Lakshminarayana, B., Chernobrovkin, A., and Ristic, D., 1998, "Experimental and Numerical Study of Unsteady Viscous Flow Due to Rotor Stator Interaction in Turbines. Part 1: Data, Code, and Pressure Field", ASME Paper 98-3595, p. 1-15.

Lakshminarayana, B. and Xiao, X., 1998, "Static pressure investigation on blade surface", Progress report of the Center of the Turbomachinery and Power, Pennsylvania State University

Lam, C.K.G., and Bremhost, K., 1981 "A Modified Form of the k -ε Model for Predicting Wall Turbulence," *Journal of Fluids Engineering*, Vol. 103, September, pp. 456 - 460.

Langston, L.S., Nice, M.L., and Hooper, R.M., 1977, "Three-Dimensional Flow Within a Turbine Blade Passage," ASME *J. of Engineering for Power*, Vol. 99, pp. 21-28.

Launder, B.E., and Spalding, D.E, 1974, "The Numerical Computation of Turbulent Flows" *Computer Methods in Applied Mechanics and Engineering,* Vol. 3, pp. 269-289.

Luo, J., Lakshminarayana, B., 1997, " Three Dimensional Navier-Stokes Analysis of Turbine Rotor and Tip Leakage Flow Field," ASME 97-GT-421, 1997.

Luo, J. and Lakshminarayana, B., 1997 "Three-Dimensional Navier-Stokes Analysis of turbine rotor and Tip-Leakage Flow Field", 43rd ASME/IGTI Meeting, ASME Paper 97-GT-42.

Menon, R., 1987, "Three Component Velocity Measurements in the Inter blade Region of a Fan," ASME 87-GT-207.

Moore, J., Tilton, J. S., 1988, "tip Leakage flow in a Linear Turbine Cascade," Journal of Turbomachinery, Vol. 110, pp. 18-26.

Moore, J., et al., 1989, "flow and Heat Transfer in Turbine for Gas," Journal of Turbomachinery, Vol. 111, pp. 301-309.

Pandya, A. and Lakshminarayana, B., 1983, "Investigation of Tip Clearance flow Inside and Exit of a Compressor rotor Passage," Journal of Engineering for Power, Vol. 105, pp. 1-17

Ristic, D., Lakshminarayana, B., and Chu, S., 1998, "Three-Dimensional Flow Field Downstream of an Axial Flow Turbine Rotor," AIAA 98-3572.

Rodi, W., 1976, " New Algebraic Relation for Calculation of the Reynolds Stresses," ZAMM Vol. 56, p.219.

Rogo, C., 1968, "Experimental Aspect Ratio and Tip Clearance Investigation on Small Turbines," SAE paper, No. 680448

Schaub, U.W., Vlasic, E., and Moustapha, S.H., 1993, "Effect of Tip Clearance on the Performance of a Highly Loaded Turbine Stage," AGARD-CP-537, "Technology Requirements for Small Gas Turbines," Paper 29, October 1993.

Schmidt, M. J. P., Agnew, b., and Elder, R. L., 1987, "Tip Clearance Flows --- Part I: Experimental Investigation of an Isolated Rotor; Part II: Study of Various Models and Comparison with Test Results," Proceedings of Eighth ISABE Conference, Cincinnati, Ohio.

Senoo, Y., and Ishida, M., 1987, "Deterioration of Compressor Performance Due to Tip Clearance of Centrifugal Impellers," *J. of Turbomachinery*, Vol. 109, p.55.

Sjolander, S.A., Amrud, K.K., 1987, "Effects of Tip Clearance on blade Loading in a Planar Cascade of Turbine Blades," ASME Journal of Turbomachinery, Vol. 109, pp. 237-245.

Sjolander, S.A., 1997, "Secondary and Tip-Clearance Flows in Axial Turbines," "Overview of Tip-Clearance Effects in Axial Turbines," *von Karman Institute for*

Fluid Dynamics, Lecture Series 1997-01.

Stauter, R. C., 1992, "Measurement of the Three Dimensional Tip Region Flow Field in an Axial Compressor," ASME 92-GT-211.

Storer, J. A., Cumpsty, N.A., 1991, "Tip Leakage Flow in Axial Compressors," ASME Journal of Turbomachinery, Vol. 113, pp. 252-259.

Suder, L.L., et al., 1987, "Measurements of the Unsteady Flow Fields within the Stator Row of a Transonic Axial Flow Fan, Part I: Measurements and Analysis Techniques," ASME paper 87-GT-226

Treaster, A. L., and Yocum, A. M., (1979), "The Calibration and Application of Five-hole Probes," ISA Transactions, Vol. 18, No. 3.

Wadia, A. R., Booth, T. C., 1982, "Rotor Tip Leakage Part II --- Design Optimization Through Viscous Analysis and Experiment," Journal of Engineering for Power, Vol. 104, pp. 163-169.

Xiao, X., 2000, "An Experimental Investigation on the Tip Clearance Effects in an Axial Flow Turbine Rotor," (Thesis in preparation).

Yamamoto, A., Takahara, K., Nouse, H., Mimura, F., Inoue, s. and Usui, H., 1982, "An Experimental and Analytical Study of blade tip-clearance Effects on an Axial Flow Turbine Performance," NAL, Japan, Report TR-466T.

Yamamoto, A., 1987a, "Interaction Mechanisms Between tip Leakage flow and Passage vortex in a Linear Turbine Rotor Cascade," Journal of Turbomachinery, Vol. 109.

Yamamoto, A., 1987b, "Production and Development of Secondary Flows and Losses in tow Types of straight Turbine Cascades: Part 1 – A Stator Case, and Part 2 – A

Rotor Case," Journal of Turbomachinery, Vol. 109, pp. 186-200.

Yamamoto, A., 1988, "End wall Loss Mechanisms in a Linear Turbine Cascade with Tip Clearance," ASME Paper 88-GT-235.

Yamamoto, A., 1989, "Endwall Flow/Loss Mechanisms in a Linear Turbine Cascade with Blade Tip Clearance," ASME *J. of Turbomachinery*, Vol. 111, pp.264-275.

Yaras, Mi. I., Yingkang, Z. and Sjodlander, S. a., 1988, "Flow Fluid in the Tip Gap of a Planar Cascade of Turbine blades," ASME 88-GT-29.

Yaras, M. I. and Sjolander, S. A., 1990, "Prediction of Tip Leakage Losses in Axial turbines," ASME 90-GT-154.

Yaras, M. I. and Sjolander, S. A., 1991, "Effects of Simulated Rotation on Tip Leakage in a Planar cascade of Turbine blade; Part I: Tip Gap Flow," ASME 91-GT-127.

Zaccaria, M., and Lakshminarayana, B., (1995), "Investigation of Three-Dimensional Flow Field at the Exit of a Turbine Nozzle," Journal of Propulsion and Power, Vol. 11, No. 1, pp. 55-63.

Zaccaria, M.A., Lakshminarayana, B., 1997, "Unsteady Flow Field due to Nozzle Wake Interaction with the Rotor in an Axial Flow Turbine: Part 1: Rotor Passage Flow Field," ASME Journal of Turbomachinery, Vol. 119.